(12)

Solidification Processing and Phase Transformations

in

Ordered High Temperature Alloys

Final Technical Report
submitted to
Defense Advanced Research Projects Agency (DoD)
for the period
March 30, 1990 through September 30, 1992

Contractor: Metallurgy Division
National Institute of Standards and Technology
Gaithersburg, MD 20899

Principal Investigator: William J. Boettinger
301-975-6160

Senior Project Scientists: Leonid A. Bendersky
Ursula R. Kattner

Effective Date of Contract: March 30, 1990

Contract Expiration Date: September 30, 1992

Amount of Contract: $750,000

ARPA Order Number: 7469

Date of this report: January 20, 1993

Notice: Approved for public release. Distribution unlimited

UNCLASSIFIED

SECURITY CLASSIFICATION OF THIS PAGE

REPORT DOCUMENTATION PAGE				Form Approved OMB No. 0704-0188
1a. REPORT SECURITY CLASSIFICATION UNCLASSIFIED			1b. RESTRICTIVE MARKINGS None	
2a. SECURITY CLASSIFICATION AUTHORITY N/A			3. DISTRIBUTION/AVAILABILITY OF REPORT Approved for Public Release Distribution Unlimited	
2b. DECLASSIFICATION/DOWNGRADING SCHEDULE N/A				
4. PERFORMING ORGANIZATION REPORT NUMBER(S) N/A			5. MONITORING ORGANIZATION REPORT NUMBER(S)	
6a. NAME OF PERFORMING ORGANIZATION Metallurgy Division, NIST	6b. OFFICE SYMBOL (If applicable)		7a. NAME OF MONITORING ORGANIZATION	
6c. ADDRESS (City, State, and ZIP Code) I-270 & Quince Orchard Road Gaithersburg, Maryland 20899			7b. ADDRESS (City, State, and ZIP Code)	
8a. NAME OF FUNDING/SPONSORING ORGANIZATION DARPA	8b. OFFICE SYMBOL (If applicable)		9. PROCUREMENT INSTRUMENT IDENTIFICATION NUMBER	
8c. ADDRESS (City, State, and ZIP Code)			10. SOURCE OF FUNDING NOS.	
			PROGRAM ELEMENT NO.	PROJECT NO. / TASK NO. / WORK UNIT ACCESSION NO.

11. TITLE (Include Security Classification)
Solidification Processing & Phase Transformations in Ordered High Temperature Alloys

12. PERSONAL AUTHOR(S)
W.J. Boettinger, L.A. Bendersky, U.R. Kattner

13a. TYPE OF REPORT	13b. TIME COVERED	14. DATE OF REPORT (Year, Month, Day)	15. PAGE COUNT
Final Technical	FROM 3/30/90 TO 9/30/92	January 20, 1993	

16. SUPPLEMENTARY NOTATION

17. COSATI CODES			18. SUBJECT TERMS (Continue on reverse if necessary and identify by block number)
FIELD	GROUP	SUB. GR.	Intermetallics, Ti-Al-Nb Alloys, Phase Diagrams, Phase Transformations, Ti-Al-Ta Alloys, $MoSi_2$ Alloys

19. ABSTRACT (Continue on reverse if necessary and identify by block number)

Useful high temperature alloys generally have microstructures consisting of more than one phase. Multiphase microstructures are necessary to develop acceptable toughness and creep strength in high temperature intermetallic alloy matrices. The optimum microstructures must be developed by a careful selection of processing path that includes both solidification and solid state heat treatment. Research has been conducted on the rapid solidification of selected intermetallic alloys and on the phase transformation paths that occur during cooling, primarily in the Ti-Al-Nb system. This report describes research performed in the Metallurgy Division at NIST under DARPA order #7469 between 1/1/89 and 12/31/92. Various research tasks were completed and the results have been published or have been submitted for publication.

20. DISTRIBUTION/AVAILABILITY OF ABSTRACT	21. ABSTRACT SECURITY CLASSIFICATION
XX UNCLASSIFIED/UNLIMITED ☐ SAME AS RPT. ☐ DTIC USERS	UNCLASSIFIED

22a. NAME OF RESPONSIBLE INDIVIDUAL	22b. TELEPHONE (Include Area Code)	22c. OFFICE SYMBOL
W.J. Boettinger	301-975-6160	855

DD Form 1473, JUN 86 *Previous editions are obsolete.* UNCLASSIFIED

SECURITY CLASSIFICATION OF THIS PAGE

Solidification Processing and Phase Transformations

in

Ordered High Temperature Alloys

Final Technical Report
submitted to
Defense Advanced Research Projects Agency (DoD)
for the period
March 30, 1990 through September 30, 1992

Contractor: Metallurgy Division
National Institute of Standards and Technology
Gaithersburg, MD 20899

Principal Investigator: William J. Boettinger
301-975-6160

Senior Project Scientists: Leonid A. Bendersky
Ursula R. Kattner

Effective Date of Contract: March 30, 1990

Contract Expiration Date: September 30, 1992

Amount of Contract: $750,000

ARPA Order Number: 7469

Date of this report: January 20, 1993

Table of Contents

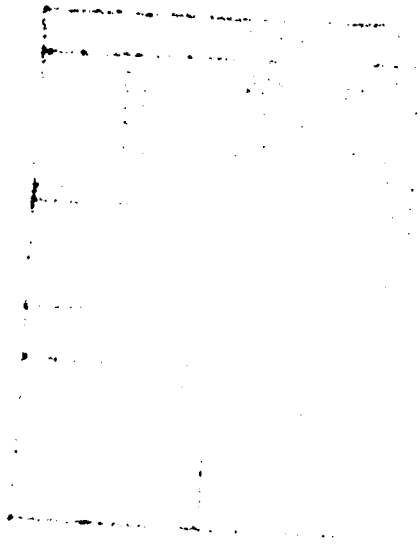

Summary

The development of acceptable toughness and creep strength in high temperature intermetallic alloy matrices is closely related to the formation of proper distributions of second phase particles in the alloy microstructures. Second phases are needed both to arrest crack growth at low temperatures and to resist creep at high temperatures. The possibility of developing new processing strategies for high temperature alloys based on intermetallic compounds has been investigated. In particular rapid solidification and/or rapid solid state quenching followed by controlled heat treatment can provide a broad range of multiphase microstructures. This report describes research performed in the Metallurgy Division at NIST under DARPA order #7469 between 1/1/89 and 12/31/92. Various research tasks were completed and the results have been published or have been submitted for publication.

- A predictive model based on thermodynamic constraints was developed for the formation of disordered intermetallics by rapid solidification. Experimental tests were performed on Ni_2TiAl.
- A unified approach, which uses crystallographic symmetry group/subgroup relations between phases, was developed to predict the complex transformation paths that change the high temperature BCC and ordered BCC into the low temperature hexagonal, orthorhombic and omega-type phases in the Ti-Al-Nb system.
- A thermodynamic calculation of the Ti-Al-Nb ternary phase diagram was completed that is consistent with most experimental observations.
- The phase constitution of alloys near the composition Al_2TiTa was determined. The

equilibrium phases present in this oxidation resistant alloy with 25at%Ti, 25at%Ta, and 50at%Al at temperatures between 1200°C and 1550°C were determined experimentally and possibilities for heat treatment elucidated.

- Phase diagrams of $MoSi_2$ alloys with additions of $TiSi_2$ and $TaSi_2$ were measured and possible composition ranges for two-phase structures determined.

Short research highlights in each of these areas follow. In the Appendix, copies of the 12 published and/or submitted papers resulting from this research are attached.

Research Highlights - Rapid Solidification of Intermetallics

One of the major processing paths to produce high temperature intermetallic alloy composites with microstructures designed for specific performance utilizes atomized powers. Powders are being combined with reinforcing fibers and particulate through various consolidation processes such as HIP to produce components. A paper published earlier under DARPA Order# 6065, Acta Met. 37 (1989) 3379-3391, has placed the prediction of alloy microstructure of atomized (rapidly solidified) intermetallics on a firm theoretical basis. The as-solidified microstructure of the powders determines the path of microstructure evolution during subsequent processing.

The research treats the chemically ordered nature of the freezing solid and predicts the range of solidification rates required to achieve certain ideal microstructures. These ideal microstructures consist of solids without the normal segregation found in more slowly frozen material and also the possibility of forming a chemically disordered form of the intermetallic (disorder trapping). The thermodynamic constraints on the range of nonequilibrium order and solubility extension were determined under the current program (see paper #1).

An experimental test of the disorder trapping model was conducted on Ni_2TiAl alloys. Using laser surface melting test performed in collaboration with Prof. M. J. Aziz (Harvard University) the Heussler order normal for this composition was suppressed by rapid solidification and the alloy formed a metastable B2 structure (see Paper #2).

Research Highlight - Phase Transformations and Equilibria in the Ti-Al-Nb System

Phase transformations in $(Ti_{(1-x)}Nb_x)_3Al$ $(0<x<0.34)$ alloys - Phase transformations in $(Ti_{(1-x)}Nb_x)_3Al$ $(0<x<0.34)$ alloys have been studied using TEM and crystallographic space group analysis (Papers 3-6). These composition include many which are currently being used for the fabrication of titanium aluminide intermetallic matrix composites. Upon cooling from the β/B2 phase field, these alloys exhibit a complex transformation path into hexagonal and orthorhombic phases which depends on composition and cooling rate. As with most Ti alloys the properties are very sensitive to the heat treatment schedule employed. The transformation path establishes a hierarchy of microstructural scales which allows one to trace the transformation sequence. A method that considers reductions in symmetry according to the crystallographic group/subgroup relations between the involved phases was applied to this system for the first time. The group/subgroup relationships together with considerations of minimum elastic energy enables one to predict the transformation path and the main microstructural features of the domain structures formed by chemical and displacive ordering. Knowledge of these paths permits an optimization of the heat treatments used for these alloys. Three phases (high temperature BCC, low temperature ordered hexagonal α_2 (DO_{19}), and orthorhombic Ti_2AlNb) are involved in the microstructures. For example, the Ti-25Al-12.5Nb (at%) alloy upon cooling from the β phase field exhibits a complex transformation path that begins with a martensitic transformation from cubic to hexagonal and ends with a transformation, from α_2 to Orthorhombic phase. During these stages a complex domain structure is formed. Characteristic of the this transition, is a small transformation strain between the two phases which can be accommodated by platelet form and symmetric arrangement of rotational domains of the

ower symmetry orthorhombic phase.

The Crystal Structure of the Ti_2AlNb Orthorhombic Phase - The results of a neutron diffraction study, performed in collaboration with B. Mozer, Reactor Radiation Division, NIST, confirm and refine the structure of the orthorhombic phase in the Ti-Al-Nb system (Paper #7). The structure is Cmcm (HgNa or Cd_3Er) with a=0.6089 nm, b=0.9569 nm, and c= 0.4667 nm. Ti(Nb) fills the 8g site, Al fills one 4c site, and Nb(Ti) fills another 4c site. The structure involves ternary ordering of the hexagonal DO_{19} phase. The ordering causes a break of the hexagonal symmetry and corresponding distortion of the unit cell; viz., contraction of the b and expansion of the a parameters. The c parameters of the two phases are essentially identical. Compared to a random mixture of Ti and Nb on the Ti sites of α_2, the ternary ordering, coordinate change, and distortion to the orthorhombic phase permit an increase of Al-Nb distances from 0.285-0.289 nm to 0.302-0.306 nm while slightly reducing the Al-Ti distances to 0.280-0.285 nm. These distances are consistent with estimates of L-J potentials for Al-Ti and Al-Nb which yield minima at interatomic distances of 0.279 and 0.292 nm.

Two-phase structures of orthorhombic and nonshearable omega structures in Ti-Al-Nb Intermetallic Alloys - Based upon research involving the ordered omega phase developed under previous DARPA Order #6065 and continued under the present program (Paper #8), a series of Ti-Al-Nb alloys in the following composition range: 48-52 at% Ti, 28-32 at% Al, 16-20 at% Nb were investigated (Paper #9). The alloys are intended to have low density, room temperature ductility and high-temperature strength and stability for possible aerospace applications. The high strength and microstructural stability is achieved when these alloys are induced by proper heat treatment to form a natural (in

thermodynamic equilibrium) composite of relatively ductile orthorhombic Ti_2AlNb and plastically unshearable omega-type $B8_2$ intermetallic phases.

Ti-Al-Nb Phase Diagram Calculation - In order to interpolate and extrapolate the above data and those of other researchers to other compositions and temperatures in a thermodynamically consistent manner, calculation of the Ti-Al-Nb system has been performed (Paper #10). The description of the Nb-Al binary recently developed at NIST was used together with the descriptions of the Ti-Al system by Chang and co-workers and Nb-Ti by Kaufman and Nesor. From experiments it is known that the intermetallic compounds that exhibit wide ranges of homogeneity in the Nb-Al and Ti-Al binaries also reveal wide ranges of homogeneity in the ternary Nb-Ti-Al system. Also, the isomorphous compounds $NbAl_3$ and $TiAl_3$ form a continuous solid solution. In order to model the ternary ranges of the intermetallic compounds Nb_3Al, Nb_2Al, Ti_3Al and TiAl ternary interaction energies were necessary. The calculated diagram generally produced the correct lines of two fold-saturation for the liquidus surface and reproduced all solid equilibria within the precision of the experimental data except for phase fields involving the orthorhombic phase. The diagram provides valuable and useful data for subsequent alloy development and suggests experiments to be carried out in critical compositional and temperature ranges in order to elucidate more fully the phase equilibria in this important system.

search Highlight - Investigation of Al_2TiTa and $MoSi_2$-based

ase Equilibrium in Alloys of Composition Al_2TiTa - Research at Lockeed and Pratt Whitney has monstrated that the composition Al_2TiTa has good oxidation resistance at temperatures proaching 1500°C. The ternary phase diagram of this system is not known. In order to provide sound data base for heat treatment and further alloy development, the phases present in this alloy tween 1200 and 1550°C have been determined. The solidus for this alloy is ~1575°C. Below e solidus the alloy lies in a broad BCC solution phase region that extends into the ternary from e binary BCC (Ti,Ta) solid solution phase. Between 1500 and 1425°C, the alloy consists of BCC d HCP. The HCP phase region extends into the ternary from the Ti HCP phase. At 1400°C the loy consists of BCC, HCP and σ phases. The σ phase extends into the ternary from the binary phase based on the composition Ta_2Al. Between 1375° and 1350°C the alloy is two-phase HCP d σ. At 1330°C the alloy is composed of three phases: HCP, σ, and γ. The γ phase extends om the binary TiAl phase. Below 1325°C the alloy consists of σ and γ (Paper # 11).

$MoSi_2$- based alloys - One candidate material for high temperature applications surpassing e capability of Ni-based superalloys is $MoSi_2$. Despite its excellent oxidation resistance due to the rmation of a continuous SiO_2 scale, it is clear that monolithic $MoSi_2$ lacks adequate mechanical operties. A paper was presented (jointly with J.H Perepezko, University of Wisconsin-Madison) the First Disilicides Workshop (Paper #12) that reviewed the literature on ternary phase diagram ta for a number of systems involving $MoSi_2$. Ternary diagrams are necessary to understand the actions that occur in various composites based on $MoSi_2$ and are very useful to develop strategies r alloy design. For example, the high temperature stability of various artificially introduced

reinforcements were examined, such as Nb or SiC in a $MoSi_2$ matrix, the former being prone to reaction products while the latter is a stable composite. Parts of the $MoSi_2$ - $TiSi_2$ and $MoSi_2$ - $TaSi_2$ quasibinary diagrams were measured experimentally to determine the possibility for developing two-phase structures of the $C11_b$ and C40 crystal structures. The phase equilibria exhibited in these systems lead to the conclusion that there is no C40 high temperature polymorph in pure $MoSi_2$.

List of publications produced with full or partial support under DARPA Order #7469

1/1/90 to 12/31/92

Rapid Solidification of Intermetallics

1. "Thermodynamic Constraints on Non-Equilibrium Solidification of Ordered Intermetallic Compounds", W. J. Boettinger, Mat. Sci and Eng. A133 (1991), 438-442.

2. "Disorder Trapping in Ni_2TiAl", W. J. Boettinger, L. A. Bendersky, J. A. West, M. J. Aziz and J. Cline, Mat. Sci and Eng., A133 (1991), 592-595.

Phase Transformations and Equilibria in Ti-Al-Nb Alloys

3. "Crystallography and Thermodynamics of Heirarchical Structures of $(Ti,Nb)_3Al$ Alloys", L. A. Bendersky, W. J. Boettinger, and A. Roytburd, in Proceedings of International Symposium on Intermetallic Compounds - Structure and Properties - (JIMIS-6), ed. by O. Izumi, The Japan Institute of Metals, Sendai, Japan, 1991, pp. 845-849.

4. "Crystallography of Hierarchical Structures of $(Ti,Nb)_3Al$ Alloys involving both Displacive and Chemical Ordering", L. A. Bendersky, W. J. Boettinger and A. Roytburd, ICOMAT-6 (Sixth International Conference on Martensite), in press.

5. "Transformation of BCC and B2 High Temperature Phases to HCP and Orthorhombic Structures in the Ti-Al-Nb System. Part I: Microstructural predictions based on a subgroup relation between phases", L.A.Bendersky, A.Roytburd and W.J.Boettinger, Acta Met., submitted.

6. "Transformation of BCC and B2 High Temperature Phases to HCP and Orthorhombic Structures in the Ti-Al-Nb System. Part II: Experimental TEM Study of Microstructures", L.A.Bendersky, W.J.Boettinger and A.Roytburd, Acta Met., submitted.

7. "Neutron Powder Diffraction Study of the Orthorhombic Ti_2AlNb Phase", B. Mozer, L. A. Bendersky, W. J. Boettinger, and R. G. Rowe, Scripta Met. 24 (1990), 2363-2368.

8. "Ordered Omega Derivatives in a Ti-37.5Al-20Nb at% Alloy", L. A. Bendersky, B. P. Burton, W. J. Boettinger, and F. S. Biancaniello, Scripta Met. 24 (1990) 1541-1546.

9. "Intermetallic Ti-Al-Nb Alloys based on Strengthening of the Orthorhombic Phase by ω-type Phases", L.A. Bendersky, W.J. Boettinger, and F. S. Biancaniello, Mat. Sci. and Eng. A152 (1992), 41-47.

10. "Thermodynamic Calculation of the Ternary Ti-Al-Nb System", U. R. Kattner and W. J. Boettinger, Mat. Sci. & Eng.A152 (1992), 9-17.

Al_2TiTa - based Alloys

11. "Investigation of the Phase Constitution of Al_2TiTa", W. J. Boettinger, A. J. Shapiro, J. P. Cline, F. W. Gayle, L. A. Bendersky and F. S. Biancaniello, Scripta Met. Mat. 25, 1991, 1993-1998.

$MoSi_2$ - based Alloys

12. "Application of Ternary Phase Diagrams to the Development of $MoSi_2$-based Materials", W. J. Boettinger, J. H. Perepezko, and P. S. Frankwicz, Mat. Sci. & Eng. A155 (1992) 33-44.

V. Fiscal Status

Amount provided for contract program

$250,000 for period March 30, 1990 to March 29, 1991.
$250,000 for period March 30, 1991 to March 29, 1992.
$250,000 for period March 30, 1992 to September 30, 1992.

Expenditures and commitments to date

$250,000 for period March 30, 1990 to March 29, 1991.
$250,000 for period March 30, 1991 to March 29, 1992.
$250,000 for period March 30, 1992 to September 30, 1992.

APPENDIX

Reprint/preprints of Papers resulting from this research

Materials Science and Engineering, A133 (1991) 438–442

Thermodynamic constraints on non-equilibrium solidification of ordered intermetallic compounds

William J. Boettinger

Metallurgy Division, National Institute of Standards and Technology, Gaithersburg, MD 20899 (U.S.A.)

Abstract

Thermodynamic constraints on permissible values of temperature, liquid composition, solid composition and long-range order parameter at the freezing interface during non-equilibrium solidification of intermetallic phases are defined in terms of the liquid and solid free energy functions.

1. Introduction

Any solidification process involving solute trapping and interface undercooling must involve a free energy decrease. Baker and Cahn [1] have used this fact to describe the domain of possible solid compositions that can form for various liquid compositions at a given temperature during rapid solidification. The free energy change for solidification is given by

$$\Delta G = G_m^S - (\mu_A^L x_A^S + \mu_B^L x_B^S) \quad (1)$$

where G_m^S is the solid molar free energy, μ_A^L and μ_B^L are the liquid chemical potentials for components A and B, and x_A^S and x_B^S are the mole fractions of A and B in the solid. Equation (1) is the basis for the usual "tangent to curve construction" to graphically show the change in free energy for a given phase change. G_m^S is evaluated for the composition of the solid phase at the interface and μ_A^L and μ_B^L are evaluated for the composition of the liquid phase at the interface. Figure 1(a) shows this construction for one temperature and Fig. 1(b) shows the allowable range of solid compositions that can form from a given liquid composition at various temperatures [2].

Non-equilibrium solidification of *intermetallic* phases that are normally ordered to the solidus also must satisfy thermodynamic constraints. The long-range order parameter and composition are constrained as a function of the interface values of the liquid composition and temperature. Indeed the observations of rapidly solidified phases with high densities of antiphase domains when the phase is normally ordered to the melting point is a clear indication that disorder has been trapped by the process of rapid solidification [3–7]. The antiphase boundaries (APBs) result from the ordering of a disordered phase made by the solidification process during post-solidification cooling. The present paper defines the thermodynamic constraint on long-range order and composition during the rapid crystallization of intermetallic phases.

2. Method

The method of Baker and Cahn can be generalized to treat chemically ordered solid phases [8] using a free energy for the solid phase, which includes the dependence on long-range order parameter as well as the composition and temperature. The condition $\Delta G < 0$ yields domains of the allowable order parameter and solid composition that can solidify from various liquid compositions at a given temperature. Any prediction of a kinetic model must yield values of order, solid composition, and temperature for each liquid composition and growth velocity consistent with these domains.

Quantitative predictions of this constraint require good thermodynamic models for the phases of interest. The data base for thermo-

0921-5093/91/$3.50

dynamic modelling is poor. Measurements of the equilibrium order parameter are often not available, especially for materials of technological interest with high melting points. Additionally *separate* thermodynamic free energy functions are often used for the ordered and the disordered phases in phase diagram modelling. The present theory requires a single potential that represents both the ordered and disordered phases. It is important to note that many complex ordered phases, such as σ phases, bear no resemblance to simple disordered structures such as b.c.c. and thus no single solid free energy can represent both the ordered and disordered phases. This theory is not applicable to cases where such complex phases are eliminated by rapid solidification and replaced by a simpler disordered phase.

3. Results and discussion

The conditions of equilibrium between a liquid and an ordered solid phase [8] can be given in terms of the molar free energies of the liquid G_m^L, which is a function of temperature T and liquid composition x_B^L, and of the solid G_m^S, which is a function of T, solid composition x_B^S, and long-range order parameter η as

$$\partial G_m^S/\partial\eta = 0 \tag{2}$$

$$G_m^S - x_B^S \frac{\partial G_m^S}{\partial x_B^S} - \eta \frac{\partial G_m^S}{\partial} = G_L - x_B^L \frac{\partial G_m^L}{\partial x_B^L} \tag{3}$$

$$G_m^S + (1 - x_B^S) \frac{\partial G_m^S}{\partial x_B^S} - \eta \frac{\partial G_m^S}{\partial \eta}$$

$$= G_L - (1 - x_B^L) \frac{\partial G_m^L}{\partial x_B^L} \tag{4}$$

Equation (2) expresses the condition of equilibrium order in the solid, while eqns. (3) and (4) give the liquid–solid equilibrium.

These conditions are depicted geometrically in Fig. 2 for some fixed temperature. The solid free

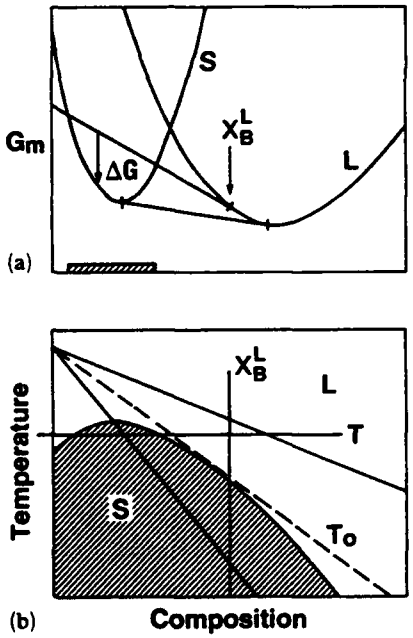

Fig. 1. (a) Schematic free energy *vs.* composition diagram at the temperature indicated on the phase diagram (b) showing the "tangent to curve" construction to obtain ΔG for the phase change from liquid of composition x_B^L to solid of various compositions. The cross-hatched region superimposed on the phase diagram defines those solid compositions at the various temperatures where $\Delta G < 0$. Only these states are thermodynamically possible non-equilibrium products of solidification.

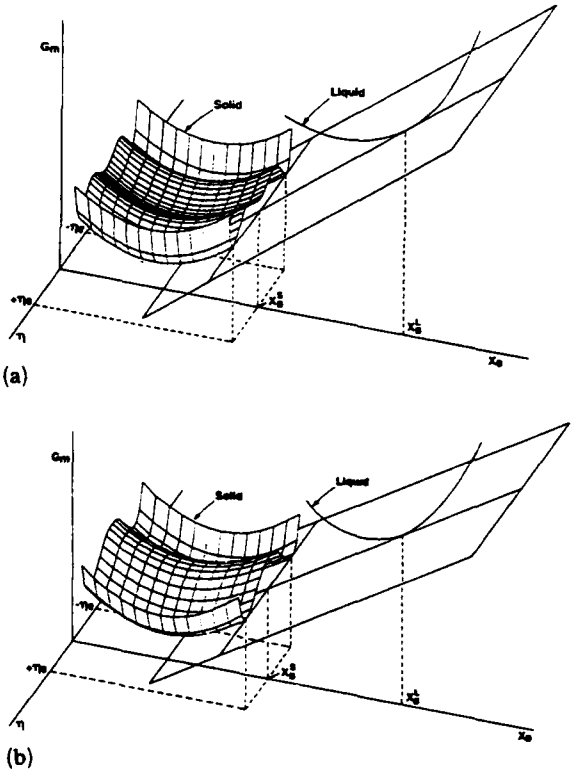

Fig. 2. Equilibrium between an ordered solid and a liquid is given by a plane with $\partial G_m/\partial\eta = 0$ that is tangent to the free energy surface for the ordered solid and the usual curve for the liquid. The tangent plane defines the equilibrium solid and liquid compositions, x_B^S and x_B^L, as well as the equilibrium value of the order parameter η_e. (a) and (b) represent solids with and without a minimum along $\eta = 0$ corresponding to solids which would undergo metastable first-order or second-order ordering transitions above their solidi. The solid free energy surface is shown truncated at the tangent.

energies shown are even functions of η ($+\eta$ and $-\eta$ are equivalent in energy) and have two general shapes depending on whether the solid state ordering reaction, which for these considerations occurs above the solidus, is first order or second order. Figure 2(a) shows the case of a first-order ordering reaction with a minimum along $\eta = 0$, while Fig. 2(b) shows a second-order ordering reaction with a maximum along $\eta = 0$. Both have their lowest extrema at $\pm\eta \neq 0$, which correspond to the equilibrium order for each composition of solid. The liquid free energy lies only in the $G_m - x_B$ plane. Equilibrium is given by the lowest plane tangent to the solid free energy surface and the liquid free energy curve. The plane must have $\partial G_m/\partial\eta = 0$ independent of whether $G_m{}^S$ is even in η.

To inspect the range of allowable solid composition and order parameter for a fixed temperature and liquid composition one merely constucts the tangent plane (with $\partial G_m/\partial\eta = 0$) to the liquid curve at the liquid composition of interest, as shown in Figs. 3(a,b). The intersection curve of this plane with the solid free energy surface defines the condition $\Delta G = 0$ according to eqn. (1). Solid compositions and order parameters inside this curve (values where $G_m{}^S$ is below the tangent plane) define thermodynamically allowable ($\Delta G < 0$) solid conditions.

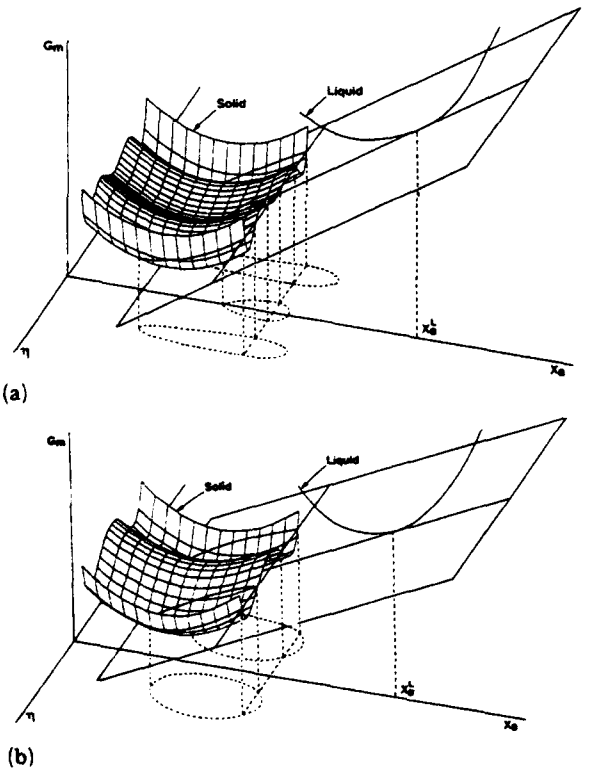

Fig. 3. Curves of solid compositions and order parameters where $\Delta G = 0$ for a given temperature and liquid composition $x_B{}^L$ are given by the intersection of the solid free energy surface with a plane tangent to the liquid free energy curve at $x_B{}^L$ with $\partial G_m/\partial\eta = 0$. The regions inside the projection of these curves onto the composition-order parameter plane correspond to possible non-equilibrium solidification states where $\Delta G < 0$. The solid free energies are as in (a) and (b) of Fig. 2.

Quantitative results will be given for hypothetical alloys with phase diagrams having a congruently melting ordered phase at $x_B = 0.5$ using the following form of the solid free energy $G_m{}^S$ [8]. This form will also permit predictions when the order–disorder transition is first order or second order

$$\begin{aligned} G_m{}^S = {} & G_A{}^S(1 - x_B{}^S) + G_B{}^S x_B{}^S \\ & + \Omega_1\{x_B{}^S(1 - x_B{}^S) + \tfrac{1}{4}\eta^2\} + \Omega_2\eta^4 \\ & + \tfrac{1}{2}RT\{(x_B{}^S - \tfrac{1}{2}\eta)\ln(x_B{}^S - \tfrac{1}{2}\eta) \\ & + (x_B{}^S + \tfrac{1}{2}\eta)\ln(x_B{}^S + \tfrac{1}{2}\eta) \\ & + (1 - x_B{}^S - \tfrac{1}{2}\eta)\ln(1 - x_B{}^S - \tfrac{1}{2}\eta) \\ & + (1 - x_B{}^S + \tfrac{1}{2}\eta)\ln(1 - x_B{}^S + \tfrac{1}{2}\eta)\} \end{aligned} \tag{5}$$

where $G_A{}^S$ and $G_B{}^S$ are the free energies of pure solid A and B and Ω_1 and Ω_2 are constants. If $\Omega_2 = 0$ and $\Omega_1 < 0$, eqn. (5) describes a Bragg–Williams phase with near neighbor interaction Ω_1 and ideal entropy. If $\Omega_2 < 0$ and $\Omega_1 \geq 12\Omega_2$ the transition between the ordered and disordered phases is a first-order phase transition.

Figures 4(a) and 5(a) show calculated phase diagrams using an ideal liquid and solids with the constants given in Table 1 with

$$G_A{}^L - G_A{}^S = G_B{}^L - G_B{}^S = S(T_m - T) \tag{6}$$

where $G_A{}^L$ and $G_B{}^L$ are the free energies of pure liquid A and B and where S and T_m are the entropy of fusion and melting point of the pure components (assumed equal).

Figures 4(b,c) show curves of $\Delta G = 0$ for liquids of composition 0.5 (at the congruent melting maximum) and 0.4 respectively projected onto the x–η plane for various temperatures of solidification. The area inside the curves satisfies the condition $\Delta G < 0$. At the liquidus temperature of the phase diagram (equilibrium) only a single solid composition and order parameter are permitted. At lower temperatures the range expands as shown.

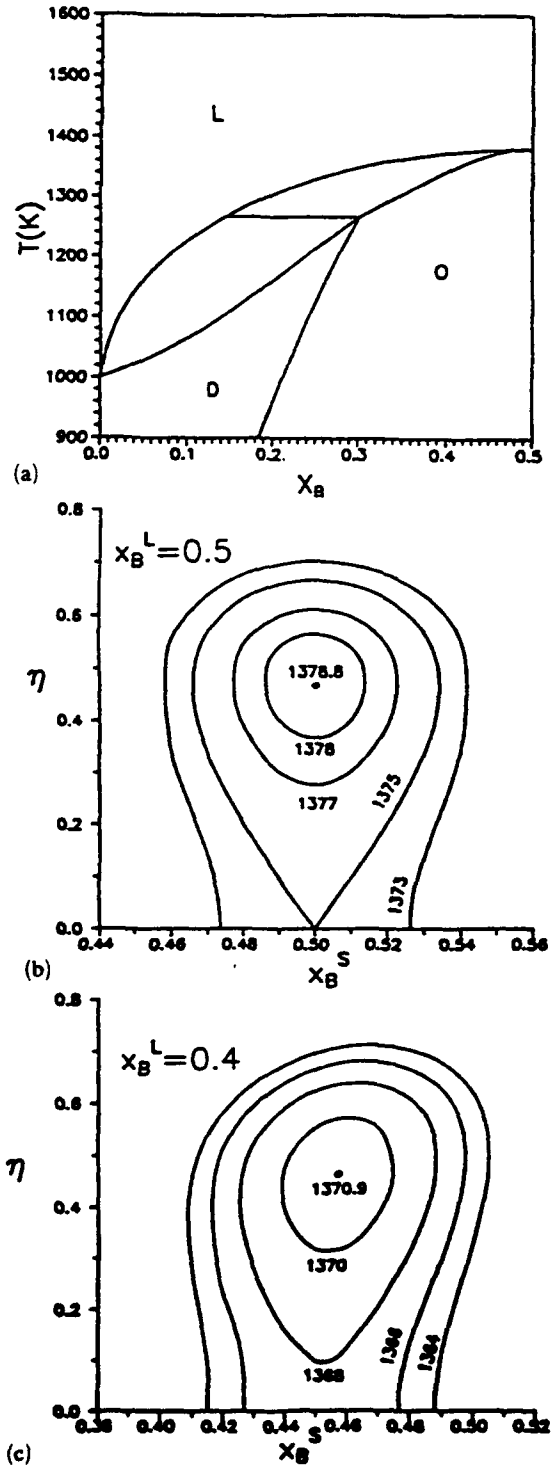

Fig. 4. (a) Calculated phase diagram between liquid L, ordered solid 0, and disordered solid D, and curves for $\Delta G=0$ at various temperatures for a Bragg-Williams solid and an ideal liquid for a composition (b) at the congruent melting maximum for the ordered phase 0 in the phase diagram ($x_B^L=0.5$) and (c) away from the maximum ($x_B^L=0.4$). Regions inside the curves define solid compositions and order parameters where $\Delta G<0$. There is no metastable liquidus and solidus for the disordered phase.

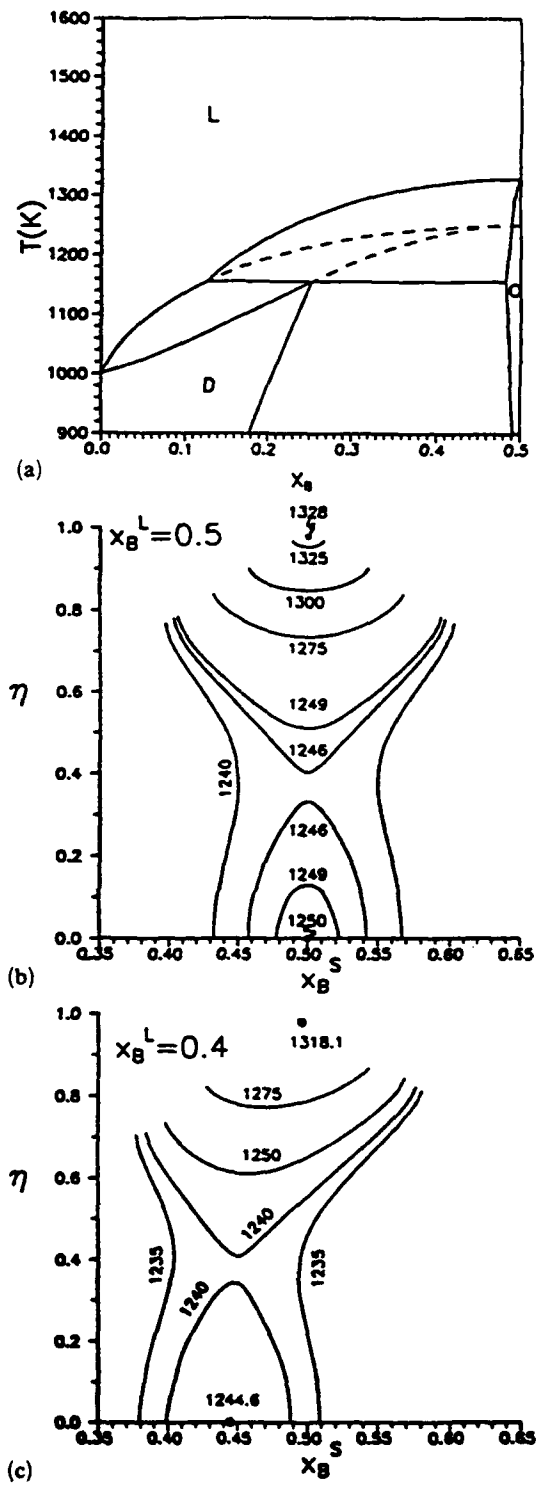

Fig. 5. (a) Calculated phase diagram and curves for $\Delta G=0$ at various temperatures for a solid with a first-order ordering reaction and an ideal liquid for a composition (b) at the congruent melting maximum in the phase diagram ($x_B^L=0.5$) and (c) at $x_B^L=0.4$. Regions inside the curves define solid compositions and order parameters where $\Delta G<0$. The dashed curves in (a) are the metastable liquidus and solidus of the disordered phase.

TABLE 1

Choice of thermodynamic parameters

Solid thermo.	T_m (K)	S/R	Ω_L/R (K)	Ω_1/R (K)	Ω_2/R (K)
First order	1000	2	0	−2000	−566.2
Second order	1000	2	0	−3000	0

For kinetic reasons, the portions of these curves that are most important involve the regions of η and x_B^S that are closest to zero and x_B^L, respectively. Such states are favored under rapid solidification conditions because they require the minimum of diffusional sorting of the components in the liquid prior to crystallization. In the case of Figs. 4(b,c) (second-order ordering reaction), the minimum value of the order parameter allowed decreases towards zero continuously as the temperature of solidification is decreased. For a liquid composition away from the congruent melting maximum (Fig. 4(c)) one can see that at some temperatures of solidification (*e.g.* 1366 K) a solid can form with zero-order parameter but not with the same composition as the liquid. Only at temperatures lower than those shown is the formation of a disordered solid with the same composition as the liquid possible.

For a first-order ordering reaction for the solid, curves of $\Delta G = 0$ are shown for liquid compositions of 0.5 and 0.4 in Figs. 5(b,c). The tops of the curves are omitted and lie very close to the limiting values of the order parameter possible at each composition ($|\frac{1}{2}\eta| < x_B^S$ and $|\frac{1}{2}\eta| < 1 - x_B^S$). In addition to the range around the equilibrium, an island of states surrounding the zero-order parameter appears as the temperature is reduced below the metastable liquidus of the disordered phase, shown as the dashed line in Fig. 5(a). The presence of this island permits a discontinuous jump in the order parameter and composition of the freezing solid as the solidification temperature drops. For a liquid composition away from the congruent melting maximum (Fig. 4(c)) one can see that at some temperatures of solidification (*e.g.* 1250 K), a solid can form with the same composition as the liquid yet still be ordered, contrary to the case above. Clearly these details depend on the shape of the free energy surfaces.

4. Conclusion

For a liquid–solid interface that is at local equilibrium, the interface temperature and liquid composition uniquely define the solid compositions at the interface as well as the long-range order parameter of the growing solid. For departures from equilibrium this uniqueness is lost. For example, for a fixed liquid composition at the interface, a range of solid compositions and order parameters are allowed thermodynamically depending on the interface temperature. The highest temperature where the solid can have the same composition as the liquid (the T_0 temperature) and the highest temperature where the solid can have zero long-range order parameters are identified. The results depend on the shape of the solid free energy surface as a function of composition and order parameter. In particular the constraints are quite different for solids whose order–disorder transitions are first order or second order.

Acknowledgments

The author wishes to thank J. W. Cahn for many helpful discussions. This work was supported under DARPA Order # 6065.

References

1 J. C. Baker and J. W. Cahn, *Solidification*, ASM, 1971, p. 23.
2 W. J. Boettinger, in B. H. Kear, B. C. Giessen and M. Cohen (eds.), *Rapidly Solidified Amorphous and Crystalline Alloys*, Elsevier, 1982, p. 15.
3 C. C. Koch, J. A. Horton, C. T. Liu, O. B. Cavin and J. O. Scarbrough, in R. Mehrabian (ed.), *Rapid Solidification Processing: Principles and Technologies, Vol. 3*, National Bureau of Standards, Washington, DC, 1982, p. 264.
4 A. Inoue, T. Masumoto, H. Tomioka and N. Yano, *Int. J. Rapid Solidification, 1* (1984) 115.
5 S. C. Huang, E. L. Hall, K. M. Chang and R. P. Laforce, *Metall. Trans., A17* (1986) 1685.
6 W. J. Boettinger, L. A. Bendersky, F. S. Biancaniello and J. W. Cahn, *Mater. Sci. Eng., 8* (1988) 273.
7 E. L. Hall and S. C. Huang, *Acta Metall., 38* (1990) 539.
8 W. J. Boettinger and M. J. Aziz, *Acta Metall., 37* (1989) 3379.

Materials Science and Engineering, A133 (1991) 592–595

Disorder trapping in Ni_2TiAl

W. J. Boettinger, L. A. Bendersky and J. Cline
National Institute of Standards and Technology, Gaithersburg, MD (U.S.A.)

J. A. West and M. J. Aziz
Harvard University, Cambridge, MA 02138 (U.S.A.)

Abstract

Pulsed laser melting and rapid resolidification can induce disorder trapping in Ni_2AlTi at the solidification interface. The alloy formed from the melt with the nonequilibrium B2 structure and subsequently transformed to the equilibrium $L2_1$ Heusler structure during cooling to room temperature.

1. Introduction

We consider here experiments in which an ordered intermetallic alloy forms a related and less (chemically) ordered phase during rapid solidification [1–6], *e.g.* b.c.c. instead of B2 or f.c.c. instead of $L1_0$. In this case, the transition to the nonequilibrium phase can be described theoretically by a decrease in the long-range order parameter of the growing crystal to zero. A model of interface kinetics [6] predict this decrease with increasing interface growth speed for a simple AB compound. A critical velocity V_T above which the alloy must form the disordered phase (complete disorder trapping) is approximately given by

$$V_T \simeq V_D[(T_C/T_M)-1] \quad (1)$$

where V_D is the ratio of the interface diffusivity to the jump distance, T_C is the critical temperature for the order–disorder transition and T_M is the solidus temperature of the compound. Only phases that are ordered at their solidus point are considered, *i.e.* $T_C/T_M > 1$. Large values of T_C, which relate directly to the strength of ordering, require large velocities to trap complete disorder.

In experiments it is usually difficult to retain the disordered phase. Typically the microstructural signature of complete disorder trapping is a high density of antiphase boundaries (APBs) in the ordered phase. These occur because the disordered phase produced by the solidification process usually transforms to the equilibrium ordered phase quite rapidly during solid state cooling to room temperature. Although one might speculate that such APBs occur as growth defects directly at the interface, rapidly solidified alloys in general do not have a high density of structural defects such as dislocations, stacking faults or twins. The high density of APBs may be important technically as a way to alter the path of microstructural change that occurs during subsequent heat treatment [7].

The present paper examines experimentally the case where the equilibrium phase has two levels of disorder. We will determine whether the Heusler alloy, Ni_2AlTi, with the $L2_1$ (DO_3) crystal structure will form a less ordered related crystal structure, B2 or even possibly b.c.c., after laser surface melting and rapid resolidification. This composition has a congruent melting maximum [4, 8] in the phase diagram at (1513 ± 5)°C [9]. Previous research on a series of NiAl–NiTi alloys [4] has shown that melt spinning can produce the B2 structure at compositions near the eutectics of Ni_2AlTi with both NiAl and NiTi.

2. Experimental procedure

Arc-melted material of composition Ni_2TiAl was homogenized by heat treatment at 1400 °C in gettered argon for 6 h. The grain size was ~0.2 mm. Disks 3 mm in diameter and 1 mm thick were prepared by diamond sawing and spark cutting. Laser surface melting and resolidification

0921-5093/91/$3.50

of metallographically polished disks was performed using a pulsed eximer (XeCl, $\lambda = 308$ nm) laser with a 40 ns pulse duration with 300–400 mJ of pulse energy. Melting was performed with either a spatially uniform beam using a commercial beam homogenizer or with a focused beam. In the first case, one-dimensional heat flow is obtained and simultaneous measurement of reflectivity with an Ar^+ ion ($\lambda = 488$ nm) probe laser was used to determine the time that the specimen surface was molten. This measurement permits an estimation of the solidification velocity by way of heat flow calculations. For the specimens examined by TEM a focused beam was used to generate a range of solidification velocities in the single laser shot.

TEM samples were prepared by back grinding and one-sided electropolishing and ion milling to preserve the thin (~ 1 μm) melted region. The melted side was protected with lacquer. Sample preparation was quite difficult because of microcracking in the melted regions, as shown in Fig. 1.

High-temperature X-ray powder diffraction studies were also performed on the homogenized material to be certain of the presence of $L2_1$ order up to the melting point. Diffraction samples, 3 mm diameter × 1 mm, were made from homogenized alloy, ground to ~ 160 μm powder, and cold pressed in a WC die at 4 GPa. During high-temperature diffraction, samples were supported on a horizontal tantalum strip heater coated with a thin Y_2O_3 layer and were equilibrated for 50 min at each temperature before the data collection. Temperature was measured with a Pt–Rh thermocouple welded to the back side of the heater. Sample temperatures were checked with an optical pyrometer. Diffraction was performed in gettered helium.

3. Results and discussion

High temperature X-ray diffraction profiles (Fig. 2) show the presence of the 111 and 200 peaks of the $L2_1$ structure at the nominal temperatures of 600 °C, 975 °C, 1375 °C and 1500 °C ($a = 5.92$ A, 5.95 A, 5.98 A and 5.99 A respectively). This indicates the presence of Heusler $L2_1$ order at all measured temperatures under equilibrium conditions. The disappearance of the 111 peak would have indicated a transition from $L2_1$ order to B2 order. The disappearance of the 200 peak would have indicated a transition from B2 order to b.c.c. Optical pyrometry indicates that sample temperatures were approximately 75 °C lower than the nominal temperatures and thus the highest temperature measured was ~100 °C below the melting point. Examination of integrated intensities for the 111 peak corrected for the Debye–Waller factor shows little decrease in $L2_1$ order as a function of temperature, as might have been expected if the alloy were to disorder just below the melting point. (This transition is crystallographically permitted to be second order with a continuous decrease in order parameter to zero with increasing temperature.) Thus one concludes that Ni_2TiAl has $L2_1$ order at its melting point.

Figure 3(a) shows the reflectivity of a sample measured with the probe laser during surface melting and resolidification for a case with a laterally uniform homogenized beam with a measured fluence of 4.2 J cm^{-2} from the pulsed laser. The time the surface is molten is seen to be ~80 ns.

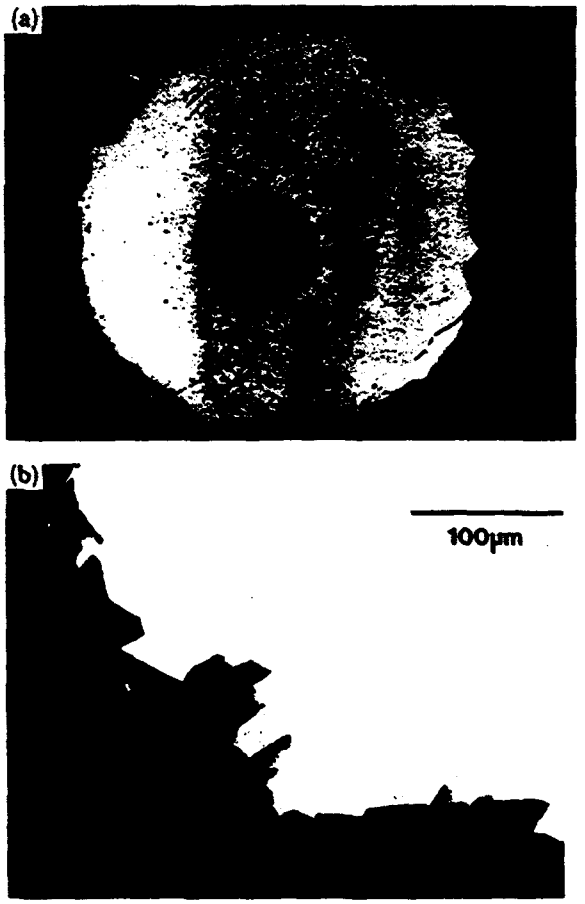

Fig. 1. (a) Optical micrograph of an ion-milled TEM sample showing melt zone and the location of the perforation. (b) Low magnification TEM view of perforation showing cracking in sample.

Using values of the thermophysical properties of nickel [10] to approximate those of the intermetallic except for the melting point, and an energy reflectivity for the pulsed laser of 0.76 and 0.71 for the solid and liquid respectively, a good fit to the measured melt duration *vs.* fluence data (Fig. 3(b)) is obtained. These same calculations yield estimates for the solidification velocity of 8–20 m s^{-1} and estimates of the melt depth of 0.8–0.2 μm for fluence values between 6 J cm^{-2} and 3 J cm^{-2} respectively. For this pulsed laser and this material, these values serve as practical limits to the range of solidification velocities. Surface vaporization would limit heat imput for higher values of the fluence while the length of the laser pulse limits velocities at lower values of the fluence. The estimated velocity scales approximately as the ratio of conductivity to the latent heat so that as better thermophysical data become available, these estimates may be revised accordingly.

For the samples examined by TEM, the laser was intentionally focused to cover a range of energy densities in a single shot and growth velocities following the above discussion were between 8 m s^{-1} and 20 m s^{-1}. Figure 4(a) is a bright field micrograph from the melted region showing a ~0.3 μm grain size which is 10^3 times finer than the starting material. This refinement of grain size indicates that the growth was not epitaxial from the underlying alloy. However, estimates of the regrowth velocity discussed above remain reasonable because the grain size is comparable with the calculated melt depth.

The inset in Fig. 4(b) shows the SAD, which confirms the presence of 111 reflections indicating the presence of $L2_1$ order in the grains. However, the grains contain a high density of antiphase boundaries in the $L2_1$ structure, as shown in the 111 dark field image of Fig. 4(b). These domain boundaries have ⟨100⟩ displacements indicating that they result from the occurrence of a B2 to $L2_1$ transition. No evidence of APBs with ⟨111⟩ displacements was detected in dark field images using 200 reflections indicating the absence of a b.c.c. to B2 transition. These observations strongly suggest that the rapid solidification produced the B2 structure and that subsequent cooling to room temperature produced the $L2_1$ structure and the fine domains. Thus we conclude that solidification velocities

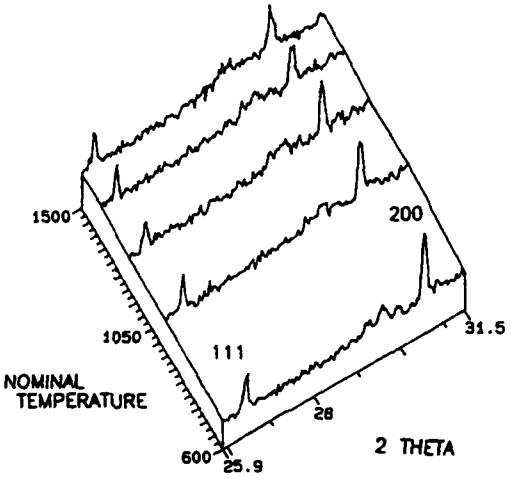

Fig. 2. High temperature X-ray diffraction profiles showing the presence of 111 and 200 peaks at the nominal temperatures of 600 °C, 975 °C, 1350 °C and 1500 °C indicating the presence of Heusler $L2_1$ order at all temperatures under equilibrium conditions. Optical pyrometry indicates that sample temperatures were approximately 75 °C lower than the nominal temperatures.

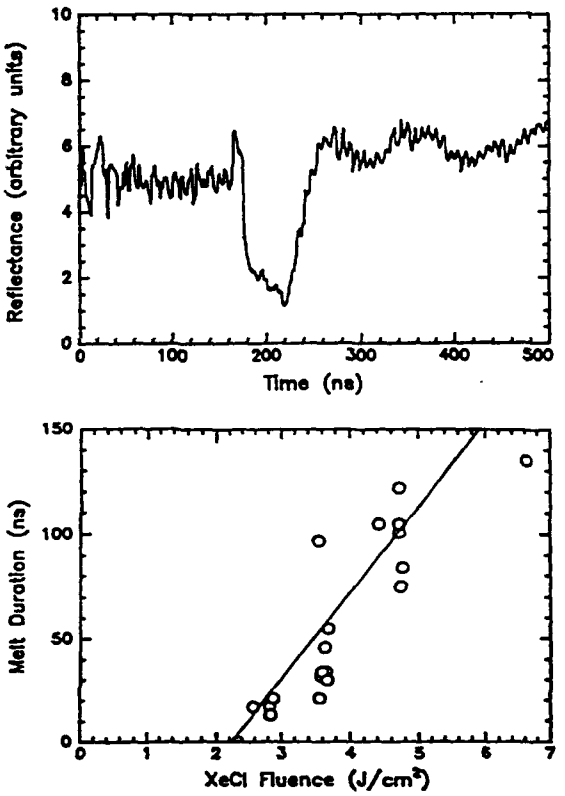

Fig. 3. (a) Reflectivity *vs.* time measured by an Ar^+ ion probe laser from the surface of a Ni_2TiAl sample during surface melting and resolidification with a XeCl laser with a measured fluence of 4.2 J cm^{-2}. (b) Measured melt duration *vs.* fluence data and fit obtained using heat flow model with pulsed laser reflectances of 0.76 and 0.71 for the solid and liquid respectively.

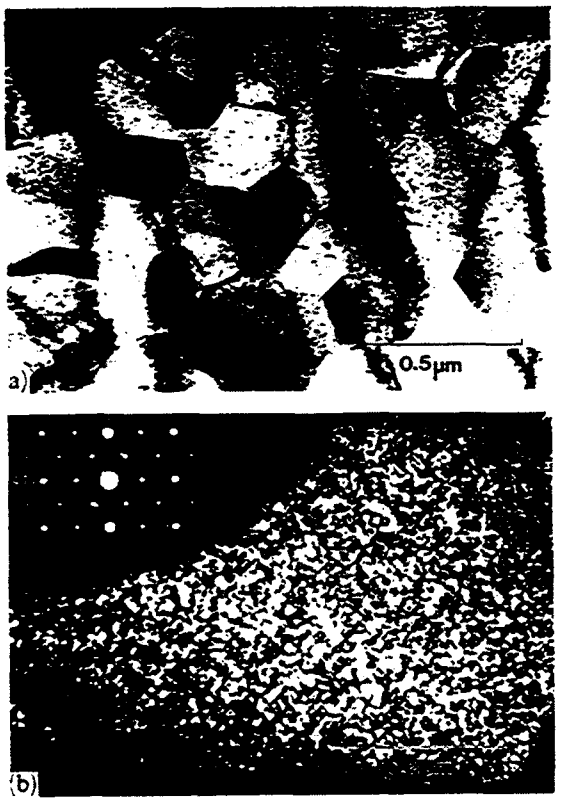

Fig. 4. (a) TEM bright field micrograph showing the grain size in the surface melted and resolidified region. (b) 111 dark field TEM micrograph showing fine APBs in the surface melted and resolidified region. Under these imaging conditions the APBs can be identified as ⟨100⟩ type which occur during solid state B2 and $L2_1$ ordering. SAD shows the presence of $L2_1$ order.

between 8 m s^{-1} and 20 m s^{-1} are sufficient to suppress the formation of the equilibrium $L2_1$ phase and produce the B2 phase. At present it has not been determined experimentally whether higher solidification rates might suppress the B2 phase and produce the b.c.c. structure.

For comparison with eqn. (1), values for T_c for the B2 to $L2_1$ transition and for the b.c.c. to B2 transition are estimated using the cluster variation method (CVM) as ~2925 K and 5000 K respectively [11]. This yields values for V_T of 0.6 V_D and 1.8 V_D to suppress $L2_1$ and B2 order respectively. A value for V_D of 12 m s^{-1} would provide consistency between theory and experiment. This is of the same order of magnitude as the value of V_D determined in solute trapping experiments in metallic systems [12].

4. Conclusion

Rapid solidification at velocities in the range of 8–20 m s^{-1} are sufficient to suppress the formation of the equilibrium $L2_1$ ordered structure but not the less ordered B2 structure in Ni_2TiAl.

Acknowledgments

This research was supported by DARPA Order —6065 (NIST) and ONR —N00014-88-K-0548 (Harvard). G. Q. Lu and J. T. Manos (Harvard) provided technical assistance.

References

1 C. C. Koch, J. A. Horton, C.T. Liu, O. B. Cavin and J. O. Scarbrough, in R. Mehrabian (ed.), *Rapid Solidification Processing: Principles and Technologies, Vol. 3*, National Bureau of Standards, Washington, DC, 1982, p. 264.
2 A. Inoue, T. Masumoto, H. Tomioka and N. Yano, *Int. J. Rapid Solidification, 1* (1984) 115.
3 D. Shectman, W. J. Boettinger, T. Z. Kattamis and F. S. Biancaniello, *Acta Metall., 32* (1984) 749.
4 W. J. Boettinger, L. A. Bendersky, F. S. Biancaniello and J. W. Cahn, *Mater. Sci. Eng., 8* (1988) 273.
5 E. L. Hall and S. C. Huang, *Acta Metall., 38* (1990) 539.
6 W. J. Boettinger and M. J. Aziz, *Acta. Metall., 37* (1989) 3379–3392.
7 L. A. Bendersky, P. W. Voorhees, W. J. Boettinger and W. C. Johnson, *Scr. Metall., 22* (1988) 1029–1034.
8 P. Nash and W. W. Liang, *Met. Trans., 16A* (1985) 319.
9 D. Anton, unpublished research, United Technology Research Center, Hartford, CT, USA, 1987.
10 S. C. Hsu, S. Chakravorty and R. Mehrabian, *Metall. Trans., 9B* (1978) 221.
11 B. P. Burton, J. E. Osburn and A. Pasturel, *Calphad XIX*, Noordwijkerhout, Netherlands, 1990.
12 P. M. Smith, J. A. West and M. J. Aziz, *Mater. Res. Symp. Proc., 205* (1991), to be published.

CRYSTALLOGRAPHY AND THERMODYNAMICS OF HIERARCHICAL STRUCTURES OF $(Ti,Nb)_3Al$ ALLOYS

L.A.Bendersky, W.J.Boettinger and A.Roytburd*

Metallurgy Division, NIST, Gaithersburg MD, USA
* Dept. of Chemical and Nuclear Engineering
University of Maryland, College Park, MD, USA

Upon cooling from the β or B2 phase field, Ti-Al-Nb alloys exhibit a complex transformation path depending on composition and cooling rate. The transformation path establishes a hierarchy of microstructural scales which allows one to trace the transformation sequence. Another hierarchy appears as a change of crystallographic symmetry according to subgroup and supergroup relations between the phases. The subgroup relations establish the main features of the domain structure.

In the present work the microstructure and transformation of two alloys cooled from 1100°C were investigated. For a Ti_2AlNb alloy, a B2 ordered phase transforms directly to the orthorhombic low temperature phase. For a Ti_5Al_2Nb alloy, the BCC phase transforms to a hexagonal phase preceding the orthorhombic phase formation. The small transformation strain between the latter two phases can be accommodated by a platelet morphology and a symmetric arrangement of rotational domains of the lower symmetry orthorhombic phase.

1. Introduction

The need for low density structural materials with high temperature strength and low temperature ductility has stimulated much interest in Ti-Al-Nb alloys. In particular alloys near the Ti_3Al-Nb_3Al pseudobinary section with Nb levels up to 30 at.% have been investigated [1-3]. In a recent review [3] it has been shown that the alloys have very promising combinations of specific strength and rupture life at high temperature (< 800°C). Equilibria along this pseudobinary section in this temperature range involve four phases, high temperature BCC (β) and ordered B2 along with low temperature ordered hexagonal DO_{19} (Ti_3Al or α_2) and orthorhombic Ti_2AlNb. All of these phases are structurally related to each other, and the structural relations are reflected in the observed orientation relationships between the different phases.

Because of this structural relationship, a correspondence between atom sites in these phases can be found, and the structures can be described by common Wyckoff positions of the lowest symmetry phase which is the orthorhombic Ti_2AlNb phase. With this approach, possible transformations between the phases that occur without long-range diffusion (change of composition) can be considered as order/disorder transformations of a displacive or chemical nature with, in principle, a single thermodynamic potential and paths which can be analyzed using subgroup/supergroup symmetry relations [4,5]. Transitions involving homogenous (Bain) deformations, shuffle transitions and chemical ordering can be treated with this approach. Such analysis can preclude certain transformation paths, and assist in the interpretation of observed paths [4]. Domain microstructures after transformation, i.e. the distribution of orientational (twin) and translational variants and their interfaces can also be predicted assuming coherency of the transformations. Such coherency produces morphologies that minimize strain energy, mostly with invariant plane strain boundaries.

2. Experimental

Two alloys with compositions Ti_5Al_2Nb and Ti_2AlNb were prepared by arc melting, and were homogenized at 1400°C. Samples were subsequently heat treated at 1100°C for 4 hrs. and at 700°C for up to 30 days with either water quenching or slow cooling at ~400°C/min.

3. Crystallographic structures and their subgroup/supergroup relationship.

The orthorhombic Ti_2AlNb phase was first discovered by Banerjee et al.[1] and involves ternary ordering of the hexagonal DO_{19}-Ti_3Al phase. This structure with Cmcm space group was confirmed and refined by neutron diffraction [6]. With the ternary ordering the hexagonal lattice gets small orthorhomic distortion of the (0001) plane. The orthorhombic structure has three Wyckoff positions, $4c_1$,$4c_2$ and 8g, each of them occupied mostly with Nb, Al or Ti atoms, respectively, as is presented in Table 1 (x_i and y_i are measured coordinates of the Wyckoff positions).

Letting $4c_2$ and 8g have the same occupancy (mixed Ti and Nb), the structure becomes the hexagonal DO_{19} (with lattice parameters in the ratio $b/a=\sqrt{3}$), Table 1. The $P6_3/mmc$ space group of the hexagonal phase is a maximal supergroup of the orthorhombic Pmcm.

TABLE 1 - Description of Various Phases Based on Common Sites in the Cmcm Space Group

Structures	Special Conditions	Occup.	Wyck.	x	y	z
Ti_2AlNb,	$y_1=0.163$; $y_2=0.623$	A	$4c_1$	0	y_1	1/4
HgNa, Cmcm	$y_3=0.904$; $x_3=0.231$	B	$4c_2$	0	y_2	1/4
		C	8g	x_3	y_3	1/4
Ti_3Al, DO_{19}	$b/a=\sqrt{3}$	A	$4c_1$	0	1/6	1/4
Ni_3Sn, $P6_3/mmc$		B	$4c_2$	0	2/3	1/4
		B	8g	1/4	11/12	1/4
αTi, A3	$b/a=\sqrt{3}$	A	$4c_1$	0	1/6	1/4
Mg, $P6_3/mmc$		A	$4c_2$	0	2/3	1/4
		A	8g	1/4	11/12	1/4
Ti-Nb, A20	$y_1=0.1$	A	$4c_1$	0	y_1	1/4
αU, Cmcm		A	$4c_2$	0	$1/2+y_1$	1/4
		A	8g	1/4	$3/4+y_1$	1/4
Ti-Ni, B19	$y_1=0.156$	A	$4c_1$	0	y_1	1/4
AuCd, Pmam(Pmma)	$y_2=0.906$	A	$4c_2$	0	$1/2+y_1$	1/4
		B	8g	1/4	y_2	1/4
βTi, A2	$b/a=\sqrt{2}$	A	$4c_1$	0	1/8	1/4
W, Im3m	$c/a=\sqrt{2}/2$	A	$4c_2$	0	5/8	1/4
		A	8g	1/4	7/8	1/4
TiNi, B2	$b/a=\sqrt{2}$	A	$4c_1$	0	1/8	1/4
CsCl, Pm3m	$c/a=\sqrt{2}/2$	A	$4c_2$	0	5/8	1/4
		B	8g	1/4	7/8	1/4

The BCC and B2 structures can also be described within the Cmcm space group assuming a correspondence between the atoms in 110 of the cubic and 004 of the orthorhombic structure (the correspondence fits the observed Burgers orientation relationship). The lattice parameters have

restricted ratios and the position of atoms are fixed and significantly different from the orthorhombic phase. For the BCC all three site are disordered, whereas for B2 $4c_1$ and $4c_2$ have mixed occupancy of Al and Nb atoms and 8g is filled with Ti atoms [1] (Table 1).

A path of maximal subgroup or supergroup symmetry relations [5] between the BCC and the orthorhombic phase involves a few intermediate structures not described above. These structures, the disordered HCP (A3), orthorhombic disordered α-U prototype (A20) and ordered AuCd prototype (B19), are all known as martensitic phases in various other Ti-based alloys and may well be metastable or unstable phases in the Ti-Al-Nb system (see Table 1). Homogeneous distortions expected in the course of transformation will be represented by two additional intermediate space groups. Fig.1 summarizes these relations along disordered and ordered branches. From here three transformation paths from the Im3m to the ordered Cmcm seem likely:

(1) $Im\bar{3}m \rightarrow$ [I4/mmm,Fmmm] $\rightarrow$ Cmcm(disord) $\rightarrow$ $P6_3/mmc$(disord) $\rightarrow$ $P6_3/mmc$(ord) $\rightarrow$ Cmcm(ord);
(2) $Im\bar{3}m \rightarrow Pm\bar{3}m \rightarrow$ [P4/mmm,Cmmm] $\rightarrow$ Pmma $\rightarrow$ Cmcm(ord);
(3) $Im\bar{3}m \rightarrow$ [I4/mmm,Fmmm] $\rightarrow$ Cmcm(disord) $\rightarrow$ Pmma $\rightarrow$ Cmcm(ord).

The microstructure resulting from such a sequence will consist of a hierarchy of interfaces (interdomain boundaries), decreasing in scale with each subgroup transformation step with details depending on kinetics and elastic accommodation of the coherent phases.

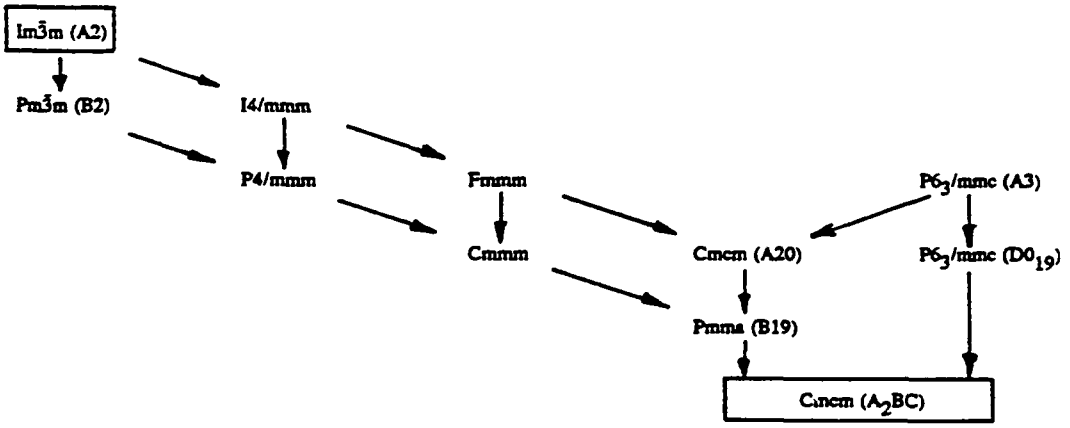

Fig.1. Subgroup/supergroup symmetry relations between the high temperature high symmetry BCC($Im\bar{3}m$) phase and the lower temperature lower symmetry orthorhombic Ti_2AlNb(Cmcm) phase. Vertical and oblique paths are chemical and displacive ordering respectively.

4. Microstructure after cooling from the BCC/B2 field.

When the cooling rate from 1100°C is high (water quenching), it is possible to suppress most of the low temperature transformations. The quenched-in phase has B2 order for both alloys, however observation of a high density of anti-phase boundaries (APBs) for the Ti_5Al_2Nb suggests that it is disordered BCC at 1100°C. For both phases annealing prior to quenching establishes 10^{-1} cm sized grains.

A microstructure in the μm range is observed for slower cooled specimens. It consists of a martensite-type structure, coarser and needle-like type for the Ti_5Al_2Nb alloy, and much finer and plate-like for the Ti_2AlNb alloy (Fig.2). For the Ti_2AlNb alloy the transformation to that structure

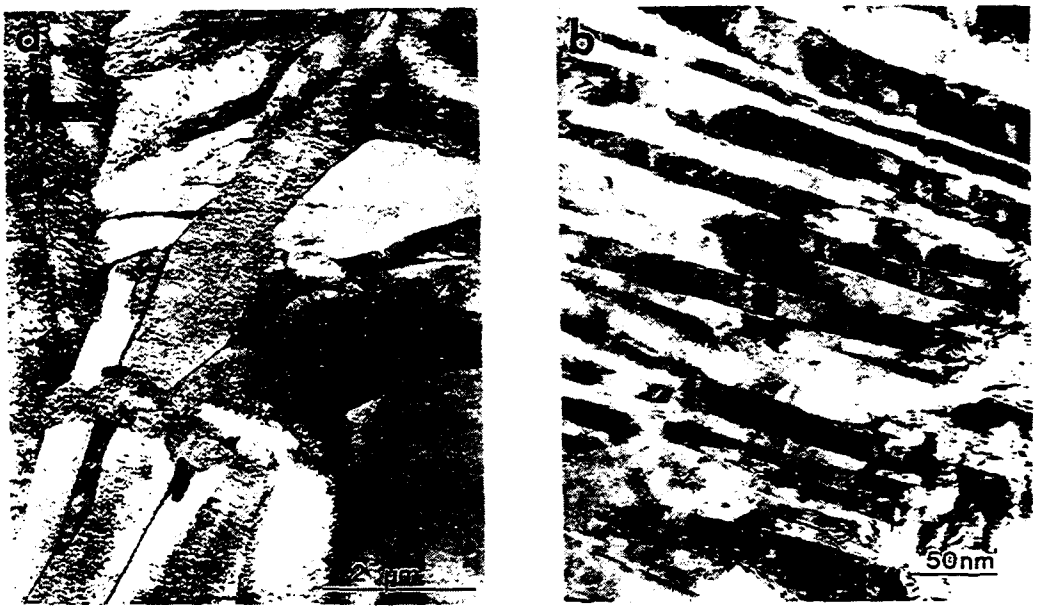

Fig.2 Martensite-type structure (μm structural scale) observed for slow-cooled specimens. (a) Coarser and needle-like type for the Ti_5Al_2Nb alloy, and (b) much finer and plate-like type for the Ti_2AlNb alloy.

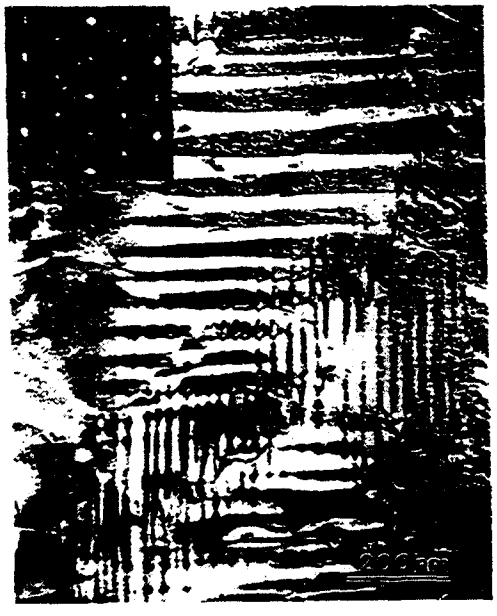

Fig.3 The Ti_5Al_2Nb alloy substructure (submicron structural scale) of the needles consisting of orthonormal pairs of the orthorhombic phase parallel plates. The plates are in a twin relation according to the SAD pattern.

Fig.4 The Ti_5Al_3Nb alloy after annealing at 700°C for 26 days. The annealing results in re-precipitation of the DO_{19} phase as a modulation of the orthorhombic phase plates.

is very sluggish, and requires either very slow cooling (e.g. furnace cooling) or additional isothermal treatment. Selected area electron diffraction (SAD) and convergent beam (CB) electron diffraction of several major zone axes from a single plate of the Ti_2AlNb alloy confirms that its structure has orthorhombic Cmcm symmetry, in accord with results of Banerjee and co-authors [2]. The microstructure exhibits an elastically accommodated domain structure, with most domains in a twin relation consisting of (110) mirror planes of the cubic symmetry. The crystallographic orientation of the domains with respect to cubic axes and to each other and the type of APB and stacking faults observed inside the plates suggest that transformation path (2) took place.

Close examination of SAD patterns from the Ti_5Al_2Nb alloy reveals similar patterns as above but with spot splitting and streaking. Streaking is the result of the presence of parallel interfaces from the plate-like substructure (submicron structural scale) of the needles (Fig.3). Analysis of the spot splitting indicates that the domains of the orthorhombic phase being are in a twin relation. In contrast to the Ti_2AlNb alloy, the twinning operation is by mirror planes which are symmetry elements of the 6/mmm point group and not a part of symmetry group of the contacting variants. Such domain structure will have three sets of orthonormal pairs of parallel plates in order to minimize elastic energy [7], which is indeed observed (Fig.3). Therefore, the intermediate hexagonal phase must be part of the transformation path. From the orientation of the domains and the type of APB and stacking faults, we conclude that transformation path (1) occurred for the Ti_5Al_2Nb alloy.

5. Microstructure after annealing at 700°C.

Annealing of the Ti_2AlNb alloy at 700°C results in coarsening of the plate-like structure in earlier stages, and then in complete recrystallization. Since the Ti_5Al_3Nb alloy is in an equilibrium two-phase field, the 700°C annealing results in reprecipitation of the DO_{19} phase. The DO_{19} phase appears as a modulation inside the orthorhombic phase domains (Fig.4). Formation of such structure could be by mechanism of conditional spinodal decomposition where the orthorhombic phase first separates to Nb dilute / reach regions, and then the dilute regions disorder spontaneously to the DO_{19} phase. The habit plane of the interfaces satisfies the condition for an invariant plane between the phases in order to minimize elastic energy.

6. Conclusion

During cooling from 1100°C, the high temperature cubic phase of $(Ti,Nb)_3Al$ alloys decomposes into low temperature orthorhombic phase by two different paths depending on Nb content. One involves the intermediate formation of a hexagonal precursor while the other involves the formation of precursor B2 phases. These two different paths are seen as feasible after an examination of subgroup/supergroup relation between the various phases. This research was performed under DARPA Order #7469.

References.

1. D. Banerjee, A.K. Gogia, T.K. Nandi, and U.A. Toshi, Acta. Met., 36, 871 (1988).
2. H. T. Kestner-Weykamp, C. H. Ward, T. F. Broderick and M. J. Kaufman, Scr. Met. 23, 1697 (1989).
3. R.G.Rowe, Proceeding of TMS Symposium, Detroit (1990).
4. J. W. Cahn, Acta Met.25(1977) 721.
5. International Tables of Crystallography, Vol.A, T.Hahn, ed., Reidel Publishing Co., Dordrecht (1978).
6. B.Mozer, L.A.Bendersky, W.J.Boettinger and R.G.Rowe, Scr. Met., 24, 2363 (1990).
7. J. Sapriel, Phys. Rev. B. 12,5128 (1975).

CRYSTALLOGRAPHY OF HIERARCHICAL STRUCTURES OF $(Ti,Nb)_3Al$ ALLOYS INVOLVING BOTH DISPLACIVE AND CHEMICAL ORDERING

L. A. Bendersky (a), W. J. Boettinger (a) and A. Roytburd (b)

(a) Metallurgy Division, NIST, Gaithersburg MD 20899 USA

(b) Department of Materials and Nuclear Engineering, University of Maryland, College Park, MD, USA

ABSTRACT

In the present work the microstructure of rotational domains of the orthorhombic O phase in continuously cooled Ti-25Al-12.5Nb (at%) and Ti-25Al-25Nb (at%) alloys were investigated. For the Ti-25Al-25Nb alloy the domains form from the B2 phase through a transient B19 structure and have a stress accommodating polytwin structure. For the Ti-25Al-12.5Nb alloy the domains form from the disordered BCC phase by (1) the formation of hexagonal phase domains and subsequently (2) their transition to the O phase by ordering. The stress accommodating morphology occurs in the second step. The configuration of the domain interfaces can be understood on the basis of strain energy minimization.

1.INTRODUCTION

Upon cooling at sufficiently high rates from the β/B2 phase field $(Ti_{(1-x)}Nb_x)_3Al$ $(0>x>0.35)$ alloys exhibit complex diffusionless transformations with morphologies resembling martensite [1-4]. From recent work [2,4] it follows that five phases, high temperature BCC (β) and B2, low temperature disordered hexagonal α and ordered hexagonal DO_{19} hexagonal (Ti_3Al, or α_2) and orthorhombic (Ti_2AlNb) O phase are involved in equilibrium microstructures of these alloys. All five phases are structurally related to each other. The structural relations are reflected in the maximal crystallographic group/subgroup relations as described in [4]. According to this scheme, different transformation paths from the high ($Im\bar{3}m$) to low (Cmcm) symmetry structure can be deduced. Different hierarchies of interfaces will be established in the microstructure for different paths (each type of interface corresponding to a particular group/subgroup transition of displacive or chemical ordering). It has been shown for the Ti-25Al-25Nb (at%) alloy that the B2 phase transforms to the O phase through a transient B19 structure [4]. For the Ti-25Al-12.5Nb (at%) alloy the formation of the hexagonal phases precedes the O phase formation [4]. The two paths for the transformation are: $Im\bar{3}m \rightarrow [I4/mmm,Fmmm] \rightarrow Cmcm(disord) \rightarrow P6_3/mmc(disord) \rightarrow P6_3/mmc(ord) \rightarrow Cmcm(ord)$ for the 12.5%Nb alloy and $Pm\bar{3}m \rightarrow [P4/mmm,Cmmm] \rightarrow Pmma \rightarrow Cmcm(ord)$ for the 25%Nb alloy.

In the present work strain accommodating microstructures of Ti-25Al-12.5Nb (at%) and Ti-25Al-25Nb

(at%) alloys established by continuous cooling from 1100°C were investigated. Usually for coherent transitions with a change in the symmetry of the lattice, i.e., for rotational domain formation, an accommodation of transformation strain occurs by the formation of alternating plates of two variants with planar strain-free interfaces (SFI) [5,6]. For rotational domains the elastic energy has a larger contribution to the total energy than does the interface energy. For the Ti-25Al-12.5Nb (at%) alloy transformation path, the rotational domains form in the $Pm\bar{3}m \rightarrow$ [P4/mmm,Cmmm] → Pmma step (from the cubic to the orthorhombic lattice). For the Ti-25Al-25Nb (at%) alloy, the rotational domains form in two steps: $Im\bar{3}m \rightarrow$ [I4/mmm,Fmmm] → [Cmcm(disord) → $P6_3$/mmc(disord)] (cubic to orthorhombic/hexagonal lattice) and $P6_3$/mmc(ord) → Cmcm(ord) (hexagonal to orthorhombic lattice). SFI's for these transitions are calculated using the small strain approximation, and the results are compared with experimental observations.

2. EXPERIMENTAL

Two alloys with compositions Ti-25Al-12.5Nb (at%) and Ti-25Al-25Nb (at%) were prepared by arc melting and 1400°C homogenization, as described in [4]. The homogenized specimens were heat treated at 1100°C for 4 days and subsequently cooled to room temperature at 400°/min. The microstructure of the alloys were studied by optical and transmission electron microscopy (TEM).

3. CALCULATION OF SFI's.

We only consider the features of rotational domain structures which minimize elastic energy while ignoring their interfacial energy. The most important characteristic which determines a domain structure is self-strain, e_{ij}. Different variants of a step in the transformation sequence are characterized by different self-strain tensors according to the different orientations of the crystal axes of the variants. *The self-strain tensor of two different variants, 1 and 2, are connected by the following relation:*

$$e_{ij}(2) = g_{ik}g_{jl}e_{kl}(1) \tag{1}$$

where g_{ik} is a matrix representing one of the symmetry operations lost from the space group of the parent after transformation. If the variants remain coherent and if the transformation strains are small, the orientation of each SFI plane, given by a vector x_i lying in the plane, can be predicted [6] using

$$x_i(e_{ij}(2) - e_{ij}(1))x_j = 0 \tag{2}$$

The equation reflects the conditions of strain compatibility along the planar interface between variants 1 and 2. This quadratic equation can be factored into the product of two linear forms whose zeros determine the coordinates of two SFI planes. Besides the solutions corresponding to the rational mirror planes in the parent phase, Equation 2 also has solutions that depend on the lattice parameters of the product phase, and therefore yield orientations that are generally irrational and depend on the effective transformation temperature and the alloy composition.

For the transitions considered here, namely for BCC to orthorhombic/hexagonal and for HCP to orthorhombic, solutions of Equation 2 are as follows. For the HCP → O phase transformation, there are only symmetric SFI's of the $\{1\bar{1}00\}_h$ and $\{11\bar{2}0\}_h$ types. Each pair of variants (taken from the three possible variants) has two SFI's of the two types that are normal to each other. For the BCC → orthorhombic (or HCP) transformation, there are three SFI's of the $\{100\}_c$ type, six of the $\{110\}_c$ type, and six irrational $\{hhk\}_c$ types with an h/k ratio depending on the lattice parameters of the orthorhombic (or hexagonal) phase ($h/k = 2(2c_o - b_o)/(b_o + 2c_o - 2a_o\sqrt{2})$. For the lattice parameters of the DO_{19} and O phases taken from the literature [3], the {hhk} interfaces are close to $\{155\}_c$ and $\{144\}_c$, respectively. For each pair of variants (taken from the six possible variants) there is a pair of

orthogonal interfaces, and each interface can exist for different pairs of variants. Figure 1 shows the SFI traces, as they would be seen when viewed along the $[011]_c$ zone axis. Such a drawing will be useful in analyzing the interfaces as observed in TEM specimens. Figure 1a presents traces of the symmetric {001}- and {110}-type interfaces and Figure 1b presents traces of the non-symmetric {hhk}-type interfaces. The labeling of variant pairs is given in [4].

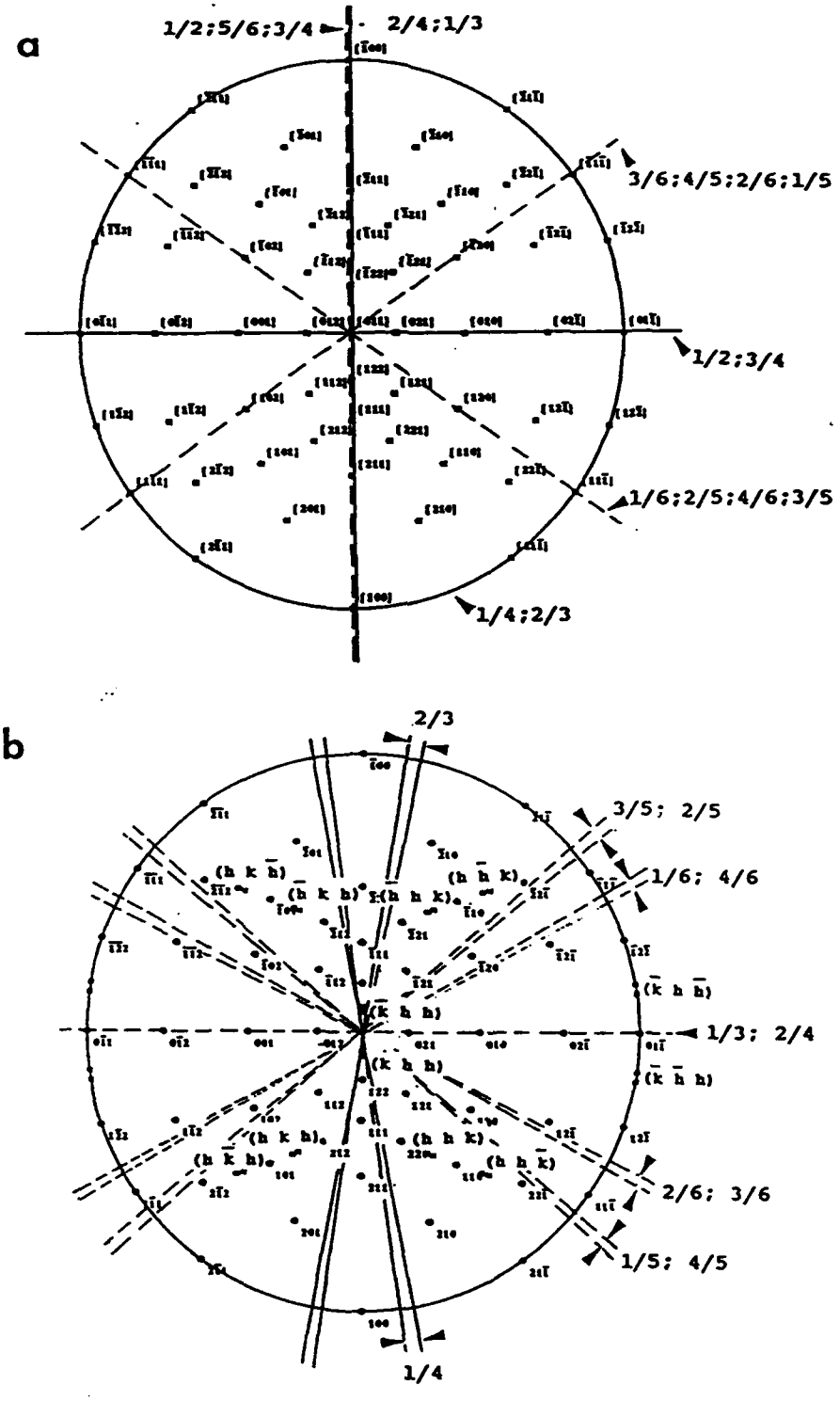

Figure 1. The directions of the SFI traces superimposed on the $[011]_c$ stereographic projection. (a) traces of the symmetric {001}- and {110}-type interfaces. (b) traces of the irrational {hhk}-type interfaces showing a range of orientations for lattice parameters ranging from a=0.61 nm, b=0.96 nm, c=0.47 nm (O phase) to a=0.59 nm, b=1.0 nm, c=0.47 nm (DO_{19} phase).

4. MICROSTRUCTURE OF THE ROTATIONAL DOMAINS IN ALLOYS CONTINUOUSLY COOLED FROM THE BCC/B2 FIELD.

4.1 Ti-25Al-25Nb alloy

For the Ti-25Al-25Nb alloy the transformation of the B2 to the O phase is very sluggish. For cooling rates of ~400°C/min, the transformation proceeds by copious nucleation of O-phase regions that grow outward uniformly until impingement. From the TEM observations of partially transformed structures (figure 2) it is evident that the O-phase regions consist of a complex microstructure identified by selected area electron diffraction as platelets of the O phase in a Burger's orientation relationship (OR): $[001]_O // <110>_c$ and $<110>_O // <111>_c$.

Figure 2. Low magnification TEM image of the microstructure of the slowly cooled, partially transformed Ti-25Al-25Nb alloy showing islands of transformed material, surrounded by a B2 phase matrix. The islands consist of a complex plate-like structure of the O phase.

The microstructure has features of an elastically accommodated domain structure. A typical example is shown in figure 3 where two polytwin plates with an "edge-on" A-A interface are seen in an $[011]_c$ orientation of the TEM film. Dark field imaging with the 020_o reflection (figure 3b) proves that the plates labeled 5 and 5' in figure 3a on both sides of A-A belong to the same variant oriented with $[001]_o$ parallel to $[011]_c$. The remaining plates have orientations close to $<212>_o$ and belong to other variants.

Referring to figure 1, we conclude (judged from the directions and widths of the B-B and C-C interface projections) that the B-B interface corresponds reasonably well to the $hh\bar{k}$ (or $hk\bar{h}$) SFI between variants 3/5 (or 2/5) and the C-C interface corresponds to the $hk\bar{h}$ (or $hh\bar{k}$) SFI between variants 1/5 (or 4/5). (The ambiguity as to the correct pair of variants can be resolved if one determines which side of the projected B-B and C-C interfaces intersects the upper and lower surface of the TEM foil). Since the intersection line of the B-B and C-C planes lies in the A-A plane, the polytwins are a combination of either 4/5 and 2/5 or 1/5 and 3/5 variants.

The A-A interface consists of an alternation of two structurally different segments. One segment is a $(01\bar{1})_c$ interface between 4 (or 1) and 2 (or 3) variants, and according to figure 1 is a symmetric SFI. The second segment separates plates of the same variant that are misoriented by about 10° and constitute a low angle boundary, possibly relaxed by a dislocation wall.

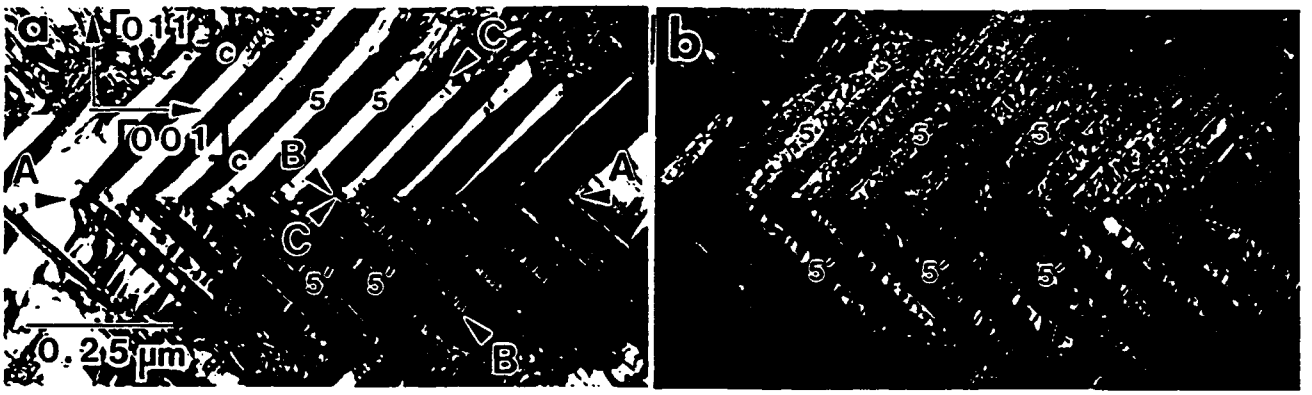

Figure 3. Typical arrangement of single variant O phase plates into a larger size secondary (polytwin) plate alternating with another polytwin plate as seen in the $[011]_c$ orientation. (a) and (b) are dark-field images with 020_O and 040_O reflections, respectively. Traces of the observed A-A, B-B and C-C interfaces correspond to SFI's, according to figure 1.

4.1 Ti-25Al-12.5Nb alloy

For the BCC to orthorhombic/hexagonal phase transition of the Ti-25Al-12.5Nb alloy, rotational domains with SFI's and morphology similar to those previously discussed in Section 4.1 are expected. However, as figure 4 shows, the microstructure for the same cooling conditions is noticeably different (even though the OR is of a similar Burger's type). Instead of a strain accommodating polytwin structure, the microstructure is needle-like with irregular interfaces. Some grains are separated by a thin layer of the BCC phase. Enrichment of Nb in the BCC layer was detected by EDS. The observed morphology suggests a diffusion controlled growth of the needles. In this condition, the ductility of the phases is apparently high enough to accommodate the transformation stresses by plastic flow. Higher cooling rates result in lowered transformation temperatures where coherent plate-type transformations occur.

Figure 4. Bright field TEM micrograph showing acicular morphology of the Ti-25Al-12.5Nb alloy. The needles have very irregular interfaces. The blocky grains between elongated needles are merely needles with their long axis normal to the TEM foil. A thin layer of the BCC phase is found between the grains.

Close examination of selected area diffraction (SAD) patterns from individual needles reveals spots splitting and streaking (figure 5a). Analysis of the spot splitting shows that they correspond to the twin related domains of the O phase. The twinning operation is by mirror planes which are symmetry

elements of the 6/mmm point group of the DO_{19} phase and not a part of the symmetry group of the contacting variants. Such twinning planes coincide with the expected SFI domain structure which have sets of orthonormal plates. Such domain structures were indeed observed as a part of the needle substructure (figure 5b).

Figure 5. (a) SAD pattern taken from an areas where only one set of parallel interfaces is present. Split spots correspond to twin-related variants of the O phase. (b) TEM dark field image, slightly off of the [0001] zone axis in order to give a different excitation error for different domains.

References.

1. S.M.L.Sastry and H.A.Lipsitt, Met. Trans., 8A, 1543 (1977)
2. K. Muraleedharan, T.K. Nandi, D.Banerjee and S.Lele, Met. Trans., 23A, 417 (1992)
3. H. T. Kestner-Weykamp, C. H. Ward, T. F. Broderick and M. J. Kaufman, Scr. Met. 23, 1697 (1989)
4. L.A.Bendersky, W.J.Boettinger and A.Roytburd, Proceeding of Sixth JIM International Symposium on Intermetallic Compounds - Structure and Properties, ed. O.Izumi, The Japan Institute of Metals, p.845 (1991); L.A.Bendersky, A.Roytburd and W.J.Boettinger, submitted to Acta Metall. Mater. (1992)
5. A.L.Roitburd, Sov. Phys. - Solid State, 10 2870 (1969)
6. A.G.Khachaturian, "Theory of Structural Transformations in Solids", J.Wiley and Sons, New York, 1983.
7. J. Sapriel, Phys. Rev. B., 12, 5128 (1975).

Submitted to Acta Met.

Transformation of BCC and B2 High Temperature Phases to HCP and Orthorhombic Structures in the Ti-Al-Nb System. Part I: Microstructural predictions based on a subgroup relation between phases.

L.A.Bendersky, A.Roytburd* and W.J.Boettinger

Metallurgy Division, NIST, Gaithersburg MD, USA
* Dept. of Materials and Nuclear Engineering
University of Maryland, College Park, MD, USA

ABSTRACT

Possible paths for the constant composition coherent transformation of BCC or B2 high temperature phases to low temperature HCP or Orthorhombic phases in the Ti-Al-Nb system are analyzed using a sequence of crystallographic structural relationships developed from subgroup symmetry relations. Symmetry elements lost in each step of the sequence determine the possibilities for variants of the low symmetry phase and domains that can be present in the microstructure. The orientation of interdomain interfaces is determined by requiring the existence of a strain-free interface between the domains. Polydomain structures are also determined that minimize elastic energy. Microstructural predictions are made for comparison to experimental results given in Part II.

1. Introduction

The need for low density structural materials with high temperature strength and low temperature ductility has stimulated much interest in Ti-Al-Nb alloys. In particular alloys near and in the Ti_3Al-Nb_3Al pseudobinary section with Nb levels from 10 to 30 at.% have been investigated [1-8]. It has been shown that alloys with 10-12 and 25 at% Nb have very promising combinations of specific strength and rupture life at room and high (<800°C) temperatures [1,6,9-14]. The mechanical properties of these alloys were found to be very sensitive to their microstructure. Most of the microstructures were formed by heat treatments that involve continuous cooling from a high temperature (>1100°C) single-phase field with subsequent heat treatment at lower temperatures. The microstructure developed during continuous cooling depends strongly on cooling rate and alloy composition [15-19] and thus affects the microstructure produced from it during the subsequent lower temperature (600 to 900°C) treatment. From a technological point of view, an understanding of the formation mechanisms of both continuously cooled and annealed microstructures is very important for processing these alloys for optimum properties, for controlling behavior during thermal cycling, and for obtaining weldability.

Equilibria along the Ti_3Al-Nb_3Al pseudobinary section with Nb<30 at% involves phases based on two distinct fundamental structures: body centered cubic (BCC) at high temperatures and hexagonal close-packed (HCP) at lower temperatures. The BCC-based phases appear over a wide range of compositions at high temperatures as either a disordered A2 or an ordered B2 (CsCl-type) structure depending on the exact temperature and composition [2-5,20]. For Ti-Al-Nb alloys the B2 ordering appears to have Ti on one site and Al/Nb on the other site [21]. For low Nb content, the HCP-based structures have a disordered hexagonal α phase at intermediate temperatures and an ordered hexagonal DO_{19} phase (Ti_3Al or α_2) at low temperatures. At higher Nb contents, the HCP-based low temperature structure is an orthorhombic O-phase (Ti_2AlNb) [2,4-6,22]. The DO_{19}

ructure involves binary ordering of the α structure with Ti/Nb occupying one site and Al the other te [23]. The O-phase structure involves further ternary ordering of the α_2 phase with Ti, Al, and b predominantly occupying three different sites [2,24]. Due to the structural relations (reflected i the observed Burger's orientation relationships between the phases [2-4,7,8,25]) it is well known iat the structural changes (transformations) from BCC- to HCP-based phases can be described as result of:

1) distortions of $\{110\}_c$ planes and changes in their interplanar distances;

2) shuffles, or relative displacement of neighboring $(110)_c$ planes;

3) reordering that changes the distribution (occupancy) of Ti, Al and Nb atoms among the lattice sites.

vhere $(hkl)_c$ refers to the cubic phase.

In the spirit of the Landau theory of phase transitions [26] a common framework is sought o describe all of the BCC- and HCP-based phases. Then in principle, a single thermodynamic otential can be identified as a continuous function of a set of order parameters that describe these hree types of structural changes. To obtain such a common framework, a site-to-site orrespondence between the structures must be found. This correspondence between atom sites in hese phases can be obtained by a single set of Wyckoff sites of the lowest symmetry phase onsidered, which in this case is the orthorhombic O-phase. Changes in the coordinates and occupancies of the Wyckoff positions are related to the three types of structural changes mentioned above. Special values of the site occupancy parameters (and lattice parameters) will correspond to changes in crystal symmetry that will follow subgroup/supergroup paths. Analysis of these paths lead to important information regarding the sequence of phase transitions, possible transient states, interconnections between the structures, and domain interface configurations.

To make this approach valid, two assumptions are required:

1) The transformations are diffusionless; i.e., no changes in compositions of phases may occur. The assumption seems to be valid considering the time scale of long-range diffusion as compared the interatomic jumps or displacements required for chemical or displacive ordering respectively;

2) The transformations are coherent; i.e., no discontinuities occur by slip or fracture in order to relieve internal stress during the phase transformation.

Both assumptions are likely to hold for the Ti-Al-Nb compositions considered either during sufficiently fast continuous cooling from the high temperature single-phase BCC or B2 field or during the initial stages of isothermal annealing of the metastable quenched-in phase. Experimental microstructural results indicate the occurrence of martensite-type ordering transitions and coherent structures under these conditions. Phase separation involving long-range compositional diffusion will be treated in Part II of this paper.

In Part I of the paper we analyze the possible continuous transformations on cooling in the Ti-Al-Nb system and the expected features of idealized coherent microstructures. The approach here is to see the transformations as a sequence of symmetry reductions, and microstructure as a collection of domains. The microstructural features determined by this analysis will be used for comparison to the actual experimental results of Part II of the paper based on microstructural studies of three Ti-Al-Nb alloys, mainly by transmission electron microscopy (TEM).

Prediction of the microstructural features relies almost entirely on the known structural and symmetry relations between the highest and lowest symmetry phases. The necessary information concerning the symmetry relations is contained in the space group tables of the International Tables for Crystallography [27, Chapter 7]. Based on this information, maximal group/subgroup symmetry

relations between phases will be established in Section 2. Each transformation step will be considered as a symmetry change, and the transformation path as sequence of subgroups. The symmetry analysis can preclude certain transformation paths, assist in an interpretation of the observed paths and also predict possible intermediate phases. From the predicted path, domain structures can be anticipated. Such domain structures will consist of a hierarchical distribution of interfaces due to the formation of orientational (twin) and translational (anti-phase domain) variants, (Section 3). It is expected that the formation of domain structures will minimize the elastic energy arises due to the coherency of transformation. Therefore, low energy, stress free interfaces (SFI) between orientational domains as well as their mutual arrangement are considered in Section 4. In Section 5 results from the previous sections will be summarized to show what microstructures are expected to be seen for different transformation paths.

2. Group/subgroup relations between BCC ($Im\bar{3}m$), HCP ($P6_3/mmc$) and ordered orthorhombic (Cmcm) phases.

2.1 Sequence of maximal subgroups.

The Landau theory of phase transition of first or higher order assumes that the symmetry of the product phase is a subgroup of the parent phase and that the atomic positions of the two structures are closely related by a set of order parameters. Usually the low temperature phase has symmetry lower than the high temperature phase and the decrease in symmetry is known as ordering while an increase in symmetry is known as disordering. The group/subgroup relationship between the parent and product phases need not be maximal[1]. However in this paper, we will search for a

[1] A subgroup H of space group G is called a maximal subgroup of G if there is no subgroup L of G such that H is a subgroup of L, i.e. $G > L > H$ [27].

sequence of maximal group/subgroup relationships in order to anticipate all possible (but not necessarily occurring) intermediate states. Such a sequence can be obtained using the International Tables for Crystallography [27], where the maximal subgroups and supergroups of all 230 crystallographic space groups are tabulated. Table 1 gives examples of such subgroup tables for (a) the $Im\bar{3}m$ space group (e.g. of the BCC structure) and (b) the $P6_3/mmc$ space group (e.g. of the HCP structure). Examples of the known structures represented by these subgroups are B2 ($Pm\bar{3}m$) in the IIa subgroups of $Im\bar{3}m$ and DO_{19} ($P6_3/mmc$) in the IIc subgroups of $P6_3/mmc$.

Often there is no apparent subgroup relation between parent and product phases. Examples are found for transitions between structures with cubic and hexagonal symmetry, like the phases in the Ti-Al-Nb system. Here the non-coinciding 3-fold <111> cubic and 6-fold [0001] hexagonal symmetry axes preclude such a relation. Usually transformations between two phases which do not have a group/subgroup relation are considered reconstructive and not treated by the Landau approach. A connection between symmetries can be restored in some cases by introducing an intermediate structure with space group G_t that is either a supergroup of both structures, G_1 and G_2, or a subgroup of both structures [28]. When G_t is a supergroup (also called a paraphase in [28]), it is at least a group union of the G_1 and G_2 groups and might not necessarily exist. Such is the case for the BCC and HCP phases considered here which already have very high symmetry. However a subgroup, G_t can always be found (and not necessarily the trivial group P1) as the intersection group of G_1 and G_2. In particular, for the disordered BCC and HCP phases with $Im\bar{3}m$ and $P6_3/mmc$ space groups and an orientation of unit cell axes according to the Burger's relationship (parallel close-packed directions $[111]_c//[11\bar{2}0]_h$ and planes $(110)_c//(0001)_h$), the intersection group G_t is the orthorhombic Cmcm, with its c-axis parallel to the $[110]_c$ direction.

The Cmcm space group (with appropriate choice of Wyckoff sites) can represent a structure

which is close to HCP but differs in symmetry and relative position of the atoms in the basal planes (Fig. 1). Such an intermediate structure was reported as a martensitic phase in some Ti alloys [29]. The Cmcm structure can also be considered as the BCC structure distorted by shuffles (relative shifts) of the $(110)_c$ planes. In this case the Cmcm group could have been found procedurally by taking the intersection of the cubic symmetry and the symmetry of the shuffle displacement wave (mmm point group symmetry for the $(110)[\bar{1}10]$-type shuffle [30,31]). Such symmetry can be locally present in the premartensitic tweed states of quenched BCC or BCC-based structures, which are also known to have the $(110)[\bar{1}10]$-type soft phonon modes (tweed BCC).[2]

Sequences of maximal subgroups were found that connect the highest symmetry cubic and hexagonal space groups to the low symmetry orthorhombic "intersection" space group (Fig. 2). This sequence includes all known equilibrium phases observed in alloys near the Ti_3Al-Nb_3Al section with less than 30 at% Nb. The figure includes sequences along disordered (BCC) and ordered (B2) branches of the high temperature phases. In the figure the space groups are connected to each other with arrows indicating symmetry decrease. The numbers shown are the indices of symmetry reductions between two neighboring subgroups (the index of a subgroup is the ratio of the number of symmetry elements in a group to that of the subgroup). These integers give the number of lower symmetry variants (domains) that would be possible if a transition from high to the low symmetry occurred. Inclined arrows indicate symmetry changes due to atomic site (Wyckoff) position changes

---

[2] The use of an intersection group to create continuity of group/subgroup relations has been successfully used in a study of the formation of ω-type phases from a B2 high-temperature phase in a different region of the Ti-Al-Nb system containing 37.5 at% Al and 12.5 at% Nb [32]. In this case the [111](111) shuffle displacement wave of the omega transition has the cylindrical ∞h symmetry (for coinciding wave and polarization vectors) [30]. The intersection point group of the $m\bar{3}m$ (BCC) and the ∞h (with the mirror plane h parallel to one of the $<111>_c$ directions) has the trigonal $\bar{3}m$ point group symmetry. The $P\bar{3}m1$ space group ($\bar{3}m$ point group) is obtained from the intersection of space groups of the two stable phases, the high-temperature B2 ($Pm\bar{3}m$) and the low-temperature hexagonal $B8_2$ ($P6_3/mmc$). The structure with the trigonal $P\bar{3}m1$ symmetry was indeed observed as an intermediate state in the transformation path.

leaving the occupancy fixed, i.e., displacive ordering. Vertical arrows indicate symmetry changes due primarily to changes in atomic site occupancy, i.e., chemical ordering. Slight adjustments of site positions and occupancies due to the new atomic environments will accompany the chemical and displacive ordering respectively. As described in Section 3, one possible transformation sequence for the formation of the lowest symmetry orthorhombic phase from BCC will involve symmetry increase (supergroup formation) from the A20 structure to the A3 structure. In this case no new variants are formed.

2.2 Intermediate subgroups and their corresponding structures.

In addition to the space groups of the Ti-Al-Nb equilibrium phases, (A2(BCC):$Im\bar{3}m$, B2:$Pm\bar{3}m$, A3(HCP):$P6_3/mmc$, DO_{19}:$P6_3/mmc$ and O-phase(Ti_2AlNb:Cmcm), several other space groups must be introduced in order to keep the subgroup relation maximal (Fig. 2). Crystallographic structures corresponding to the space groups in Fig. 2 are shown in Fig. 3 and 4 (with occupancies relevant for the ternary Ti-Al-Nb alloys). These figures assume an atom to atom correspondence between the structures. In Fig. 3 all of the structures are presented in a common projection normal to their close-packed planes. Frames of both the largest unit cell (of the O-phase) and of the particular crystal structure unit cells are also shown. Analysis of the intermediate structures lead to the following details.

The I4/mmm and Fmmm structures (obtained from the disordered BCC, $Im\bar{3}m$) and the P4/mmm and Cmmm structures (obtained from the ordered B2, $Pm\bar{3}m$) represent homogeneous strain of the cubic lattice. The I4/mmm (Wyckoff position 2a) and P4/mmm (Wyckoff positions 1a and 1d) are tetragonally distorted along the cubic <100> direction . The Fmmm and Cmmm are structures with different distortions along two orthogonal cubic <011> directions (with Wyckoff

positions 4a and 2a, 2c, respectively, and a doubled unit cell, recentered and rotated by 45° (a'=a+b; b'=a-b). The homogeneous strains of orthorhombic symmetry do not change the number of atoms per primitive cell - there remains one atom/cell for the disordered and two atoms/cell for the ordered structures (Fig. 4).

The overall orthorhombic distortion of the cubic structure, if not supported by ordering, is most probably unstable for materials with simple metallic bonding. Therefore, these structures are not expected to exist as metastable states but rather represent a homogeneous strain accompanying (and selecting the orientation of) the subsequent symmetry reduction by shuffle displacement (from Fmmm and Cmmm to Cmcm and Pmma, respectively).

Structures corresponding to the Cmcm and Pmma space groups are known in the literature as the Struckturbericht A20 (α-U prototype) and B19 (AuCd prototype), respectively. These structures can be obtained by heterogeneous shuffles of pairs of $(110)_c$ planes of either disordered or ordered cubic structure (corresponding to either 100 or 010 planes of the Fmmm and Cmmm, respectively (Fig. 4)). The amplitude of the shuffle displacement wave is reflected in the parameters of the y coordinate of Wyckoff positions: 4c (0,y,1/4) for the Cmcm structure and 2e $(1/4,y_1,0)$; 2f $(1/4,y_2,1/2)$ for Pmam. The symmetry changes do not depend on the size of the displacement. The effect of the shuffles on the disordered Fmmm (010) is that its mirror planes are changed into diagonal glide planes, and all two-fold axes disappear, as shown in Fig. 5 which compares the symmetry elements of these two space groups. The Cmcm structure (or equivalently Amam for the Fmmm coordinate system) has a shifted coordinate origin at either 0,-1/4,-1/4 or 0,1/4,1/4 (in order to have coincidence of common symmetry elements as shown in Fig. 5). Similarly, for the ordered Cmmm (010) mirror planes and two-fold axes disappear, and the symmetry became Pmam (or conventional Pmma [27] with a permutation of the b and c axes). A new coordinate origin of the

Pmma is also at $\pm$ 1/4,0,1/4.

The two origins correspond to two translational variants, with a (0,1/2,0) displacement vector. Formally, from the maximal subgroup relations [27], the translational variants are the result of a lattice decentering. Structurally, the formation of the two variants can be described by shuffle displacement waves that are out of phase by a half period in opposite directions. Because of the displacive nature of ordering, a translational interface between them has a stacking fault nature with atomic distances different from the bulk material. We will discuss details of the interface structure later.

For some special values of Wyckoff positions (y coordinates) and/or of lattice parameters, a structure can degenerate into a structure of higher symmetry. Such a higher symmetry structure, the hexagonal $P6_3/mmc$ (Fig. 3), occurs for the disordered Cmcm when the shuffles are such that Wyckoff position parameter y is 1/3 and the ratio of lattice parameters, b/a, is $\sqrt{3}$. For the ordered orthorhombic Pmma such a symmetry increase by displacement is precluded by the chemical order inherited from the B2. The disordered hexagonal $P6_3/mmc$ is expected to be more stable than the disordered orthorhombic Cmcm; in a hard sphere approximation $P6_3/mmc$ has higher entropy (due to its higher symmetry) while interaction energies are comparable. No thermodynamic barrier for the Cmcm (A20) to $P6_3/mmc$ (A3) transition is expected, and therefore the disordered Cmcm structure is believed to be unstable. This conclusion cast doubts on the existence of the truly disordered orthorhombic martensite [29]. (Nevertheless disordered Cmcm(A20) structures are known for U, Am, Ce, Ga with nonspherical electron densities). Conversely, the Pmma structure (B19) could well be a stable or a metastable phase and exist as a transient state. Indeed numerous B19 phases are known in different systems as either metastable (martensitic) or stable phases, e.g., AuCd and NiTi.

The structure with the lowest symmetry, the O-phase, also has the Cmcm space group and ternary ordering on three Wyckoff positions, $4c_1$, $4c_2$ and 8g. The O-phase translations on basal $(001)_o$ plane are twice that of the binary ordered Pmma (B19). The structure can be obtained by ordering either Pmma (B19) or $P6_3/mmc$ (DO_{19}). The DO_{19} structure itself can be obtained by binary ordering of the disordered HCP (A3) and could be in a intermediate metastable state.

2.3. Description of structures as special cases of the lowest symmetry Cmcm.

To summarize, the structures from the group/subgroup sequence can be described in terms of the lowest symmetry Cmcm space group corresponding to the Ti_2AlNb phase. The orthorhombic structure has three Wyckoff positions, $4c_1$ $(0,y_1,1/4)$, $4c_2$ $(0,y_2,1/4)$ and 8g $(x_3,y_3,1/4)$. Special values of the Wyckoff coordinates, the site occupancies, and the ratios of the orthorhombic lattice parameters can describe all the structures. The results are summarized in Table 2 where the space groups, Strucktur bericht name, prototypes, restrictions on lattice parameters (if any), occupancies (general values and measured values for Ti,Al,Nb) and coordinates of the Wyckoff sites are presented. From the schematic representation of the data in Fig. 3 one can visualize the transformation sequence as a continuous change of atomic sites occupancies and positions within the framework of the O-phase. Regardless of whether the transformations occur by a continuous mechanism, the common geometrical description of the known equilibrium phases permits the realization, in principle, of a single thermodynamic potential representing all of the phases as a function of a set of order parameters based on the site positions and occupancies.

3. Transformation paths, types and hierarchy of domains interfaces.

The formal crystallographic sequence of group/subgroup relations (Fig. 2 and 3) suggests

different ways that the coherent phase transformations from the high temperature BCC ($Im\bar{3}m$) phase might occur in reality. While the direct formation of the lowest symmetry phase by a reconstructive transformation is possible, microstructural evidence presented in Part II suggests the contrary. The transformation proceeds by steps according to the sequence which imply metastable transient phases. Each transient phase may exist over some temperature interval between upper (to the supergroup phase) and lower (to the subgroup phase) critical temperatures (or temperatures of phase instability for 1st order transitions). Each transformation step of the sequence will reduce a crystal of the higher symmetry phase into lower symmetry phase variants (except A20 → A3 where an increase of symmetry does not lead to new variants). The orientation and relative translation of the variants will be related to each other by the symmetry operations of the preceding higher symmetry phase that disappeared after the transition. Therefore a hierarchical (in a sense of both symmetry reduction and domain interface distribution) microstructure is expected. Assuming the nucleation of different low symmetry phase variants in each variant of the high symmetry phase and the absence of significant domain coarsening, a hierarchy of microstructural scale is also expected. The transformation sequence can then be recognized by the way in which the variants of the lowest symmetry phase are grouped.

Starting from the A2 (BCC) phase, the lowest symmetry O-phase can be obtained along different transformation paths (different sequences of transformation steps). Using the maximal subgroups relations in Fig. 2 and reasoning about the stability of structures discussed in 2.2, one finds that following three transformation paths are feasible:

$$\underset{[12]}{\rightarrow}\ \underset{[1]}{\rightarrow}\ \underset{[4]}{\rightarrow}\ \underset{[3]}{\rightarrow}$$

$$Im\bar{3}m(A2) \rightarrow Cmcm(A20) \rightarrow P6_3/mmc(A3) \rightarrow P6_3/mmc(DO_{19}) \rightarrow Cmcm(O) \qquad (3.1)$$

$$\overset{[2]}{\rightarrow}\ \overset{[12]}{\rightarrow}\ \overset{[2]}{\rightarrow}$$

$$Im\bar{3}m(A2) \rightarrow Pm\bar{3}m(B2) \rightarrow Pmma(B19) \rightarrow Cmcm(O) \qquad (3.2)$$

$$\overset{[12]}{\rightarrow}\ \overset{[2]}{\rightarrow}\ \overset{[2]}{\rightarrow}$$

$$Im\bar{3}m(A2) \rightarrow Cmcm(A20) \rightarrow Pmma(B19) \rightarrow Cmcm(O) \qquad (3.3)$$

where the numbers in brackets are the number of variants possible after symmetry the change .

The microstructures resulting from these sequences will consist of the same O-phase but with distinctly different hierarchies and types of interfaces. The type of interfaces, either rotational, translational or mixed, is obvious from the group/subgroup relation. Each symmetry reduction has necessarily more then one variant of the low symmetry phase. Variant generating operations and their matrices, g_{ij}, can be obtained with the help of the International Tables for Crystallography [27] from the list of Symmetry Operations of the space group, after excluding the symmetry operations of the subgroup listed in the Maximal subgroups table (see Table 1).

The number of variants in each transition is equal to the index of the subgroup (square brackets in Fig. 2 and in (3.1) - (3.3)). For a sequence of transitions the number of lowest symmetry phase variants (with respect to the highest symmetry phase) will be the product of indices for each step. For the transformation paths, (3.2) and (3.3), the number of variants is the same; viz., 48 (2x12x2 or 12x2x2). For the transformation path, (3.1), more variants occur; viz., 144 (12x1x4x3) because of the hexagonal symmetry present as an intermediate state. The index of 12 in (3.1)-(3.3) is the product (3x2x2) of indices of the individual maximal subgroups that accomplish the homogeneous distortion and the shuffles between $Im\bar{3}m$ and Cmcm or between $Pm\bar{3}m$ and Pmma.

The maximal subgroups in [27] (e.g. shown in Table 1) are divided into isomorphic and non-isomorphic subgroup classes. The isomorphic subgroups (IIc) differ from their parent group only by a translation group; i.e., an increased unit cell size (e.g., HCP to DO_{19} ordering which maintains the same rotation group but doubles the unit cell dimensions in the basal plane). The non-isomorphic class is divided into three subclasses. Class IIa, in which the unit cell is decentered, will have translational variants similar to the isomorphic subgroups (e.g. ordering of BCC ($Im\bar{3}m$) to B2($Pm\bar{3}m$)). Class IIb, in which the unit cell is decentered and enlarged, will also have only translational variants (e.g ordering in the Fe-Al system of the B2($Pm\bar{3}m$) to the DO_3 ($Fm\bar{3}m$) phase). Therefore variants of these Classes, IIa, IIb and IIc, are purely translational. The third type of non-isomorphic subgroup is Class I (t subgroups), which retain all translation, and have only rotational variants (e.g. transition in the $YBa_2Cu_3O_{7-\delta}$ high T_c superconductor from the tetragonal P4/mmm to the orthorhombic Pmmm superconducting phase). For non-maximal subgroups translational/rotational combinations are possible. In Table 3, the type of interfaces which are created in each group/subgroup transformation step of the transformation paths (3.1)-(3.3) are summarized.

In the case of coherent structure formation, the contacting volumes of the different variants, which form differently oriented or shifted lattices with respect to each other, are known respectively as rotational and translational domains. Mixed rotational/translational domains are also possible for transitions with non-maximal subgroup relation. A single rotational variant of a transformation usually has slightly different orientation of axes with respect to its parent than those following the structural correspondence. The orientation depends on the kind of variant of the surrounding domains and the interface orientation. In general, the number and orientation of coexisting domains as well as the configuration of the domain interfaces, i.e., the domain structure, depend on the thermodynamics and kinetics of the phase transformation.

Two major factors will effect the morphology and the orientation of equilibrium interfaces - their surface energy and their bulk elastic energy due to the misfit between different variants and between the matrix and different variants. For rotational domains the self-strains generate significant long range strain and one expects elastic energy minimization to dominate the selection of the interface patterns, as described in detail in section 4. For translational domains, (class II subgroup transitions) there is no change of crystal system (e.g cubic to cubic lattice in the BCC → B2 transition), and therefore only dilatational strains are expected. Thus the surface energy, or more precisely its anisotropy, controls the morphology. However, as many examples from ordered alloys show, these surface energies often have weak anisotropy and domain walls are isotropic and wavy. This is especially true for chemical (substitutional or interstitial) ordering [33]. Based on this, wavy isotropic interfaces are expected for the following transitions presented in Table 3: $Im\bar{3}m \rightarrow Pm\bar{3}m$, $P6_3/mmc(A3) \rightarrow P6_3/mmc(DO_{19})$, Cmcm(A20) → Pmma(B19) and Pmma(B19) → Cmcm(O). Less clear are two cases of translational domains in the $Im\bar{3}m \rightarrow$ Cmcm (A20) and the $Pm\bar{3}m \rightarrow$ Pmma (B19) transitions as discussed in detail in Appendix A & B.

4. Equilibrium structure of rotational domains: interfaces and their arrangement.

For rotational domains the elastic energy dominates the interfacial energy for sufficiently coarse structures. We will only consider equilibrium features of rotational domain structures which minimize elastic energy while ignoring their interfacial energy. For interfaces with equivalent elastic energy, the interfacial energy, which can be different for different types and orientations of interfaces (even for the same pair of variants), determines the relative stability.

It is convenient to subdivide the elastic problem into two steps. First, we will consider the simplest domain structure - two domains of two different variants. Secondly, using results for the

domain pairs, we will discuss the domain structures consisting of more than two domains. The results, first discussed in general terms, will be applied to two transformations in the Ti-Al-Nb system involving rotational domains: cubic to orthorhombic ($Im\bar{3}m \rightarrow Cmcm$, $Pm\bar{3}m \rightarrow Pmma$) and hexagonal to orthorhombic ($P6_3/mmc \rightarrow Cmcm$).

4.1 Pairs of Domains.

The most important characteristic which determines a domain structure is <u>self-distortion</u>, S_{ij}, or its symmetric part, <u>self-strain</u>, e_{ij}. The self-strain is a homogeneous macroscopic strain that accompanies each phase transformation. The inhomogeneous strains associated with shuffles can be neglected since their effects cancel over a few atomic dimensions. Different variants of each transformation are characterized by different self-strain tensors according to different orientations of the crystal axes of the variants, and therefore of the principal axes of the tensor. The self-strain tensors of two different variants, e.g. 1 and 2, are connected by the following relation:

$$e_{ij}(2) = g_{ik}g_{jl}e_{kl}(1) \tag{4.1}$$

where g_{ik} is the matrix of one of the parent phase space group symmetry operators which are not a part of the space groups of the two variants. Operating on the self-strain tensor of one variant with these lost symmetry elements generates the self-strain tensors for the other variants. Examples of these matrices for the hex → O-phase and the BCC → O-phase transformations are given in the Appendix A.

In a coherent crystalline system incompatibility of the self-strains on both sides of the interface between domains creates internal stress originating from the interface. Such stress will not

arise, and a stress-free interface (SFI) will result if

1) the interface is planar, and

2) the self-strains on both sides are compatible; i.e., no discontinuity of displacements occurs at the interface.

To meet the requirement of compatibility it is necessary and sufficient that the difference between two self-strains can be represented as the symmetric part of a diadic product of two unit vectors, m and n,:

$$\Delta e_{ij} = e_{ij}(2) - e_{ij}(1) = \tfrac{1}{2}s(m_i n_j + n_i m_j) \tag{4.2}$$

where m_i is a vector normal to the planar interface considered, n_j is a vector orthogonal to the m_i, and s is a scalar measure of self-strain difference [33]. The rotation of the variants necessary to maintain contact between the domains is given as

$$\omega_{ij} = \pm \tfrac{1}{2}s(m_i n_j - n_i m_j). \tag{4.3}$$

When the strain difference given in Eq.(4.2) is combined with the relative rotation of domains given in Eq.(4.3), a simple shear will describe the relationship between the two domains. The distortion tensor describing this simple shear is either sn_im_j along a plane with m normal in the direction n or sm_in_j along the plane with n normal in the direction m. These simple shears are twin shears, and the domains can be considered as twins with two twinning planes, m or n, normal to each other. One of these twinning planes coincides with a mirror plane of the parent crystal structure (which is not a symmetry element of the variants under consideration) and therefore has rational indices. The other one can be a plane with irrational indices in coordinates of the parent crystal. The rational mirror plane corresponds to type I twinning, whereas the second, irrational plane, corresponds to

type II twinning [34]. Using a simple two-dimensional example of a square to a rectangle (p4mm to p2mm) transition, Fig. 6 illustrates the operations described above. (Only Type I twinning occur in this example.)

The orientation of SFI's as well as the domain misorientations can be found directly from Eq.(4.2) in the coordinate system of the principle axes of the strain difference tensor Δe_{ij} [33,35]. For all other coordinate systems it is convenient to transform Eq(4.2) by multiplying it by $x_i x_j$, where x_i is an arbitrary vector belonging either to the m ($x_i m_i = 0$) or n ($x_i n_i = 0$) SFI planes to obtain [36]

$$x_i(e_{ij}(2) - e_{ij}(1))x_j = 0 \tag{4.4}$$

This quadratic equation splits into the product of two linear equations whose solutions determine the coordinates of two SFI planes. (The absence of a solution of Eq. (4.4) implies that the difference between the self-strains of the variants can not be represented in the diadic form of Eq. (4.2), and therefore a domain pair generated by these variants cannot have a SFI.)

Both equivalent equations, (4.2) and (4.4), were obtained with the assumption that the self-strains are small [33, 36]. However, Eq.(4.4) can be easily generalized to avoid the small-strain approximation using standard finite deformation analysis. A plane belonging to the parent phase becomes a SFI if any vector x_k in that plane, after being transformed, will have the same length in both variants. In variant (1) the vector x_k becomes $X_i(1) = (\delta_{ik} + S_{ik}(1))x_k$, where δ_{ik} is a unit matrix, $S_{ik}(1)$ is a self-distortion tensor of the variant 1. The variant (2) transforms the same vector x_k into $X_i(2) = (\delta_{ik} + S_{ik}(2))x_k$. The equality of the lengths ($X_i^2(1) = X_i^2(2)$) leads to an equation similar in its form to Eq.(4.4) but where

$$e_{ij} = \tfrac{1}{2} (S_{ij} + S_{ji}) + \tfrac{1}{2} S_{ik}S_{kj} \qquad (4.5)$$

Eq.(4.5) is a strain tensor commonly used to describe finite deformation and provides an exact definition of self-strain as a symmetric tensor based on the known self-distortion tensor of a transformations, and it includes a quadratic term of the distortion tensor, S_{ij}. For weakly first order and second order ferroelastic-type transformations, the quadratic term can be neglected in the vicinity of transformation because S_{ij} (related to the order parameter) is small. For strongly first order martensitic transformations, with large distortions, the quadratic term can be considerable.

Besides the solutions corresponding to the rational mirror planes in the parent phase, Eq.(4.4) has solutions that depend on the lattice parameters of the product phases, and therefore yield orientations that are generally irrational and depend on transformation temperature and the phase compositions. The solutions for orientations of SFIs for 94 different combinations of higher and lower point groups, relevant for ferroelastic transformation, are given by Sapriel by solving Eq.(4.4) [36]. For the transitions considered in this work, namely for BCC/B2 to orthorhombic/HCP structures ($Im\bar{3}m$(A2)→Cmcm(A20)/$P6_3/mmc$(A3) and $Pm\bar{3}m$(B2)→Pmma(B19)) and for HCP to orthorhombic ($P6_3/mmc(D0_{19})$ → Cmcm(O-phase)), specific forms of Eq.(4.4) and its solutions are given in Appendix A. For the HCP → orthorhombic transformation, there are only symmetric SFIs of the $\{1\bar{1}00\}_h$ and $\{11\bar{2}0\}_h$ types (the irrational solution degenerates into a symmetric one). The SFIs correspond to $\{110\}_o$ and $\{130\}_o$, respectively, when transformed to coordinates of the O-phase. For the BCC → orthorhombic (or similarly HCP) transformation, there are three SFIs of the $\{100\}_c$ type, six of the $\{110\}_c$ type, and six irrational $\{hhk\}_c$ types with h/k ratios depending on the lattice parameters of the orthorhombic (or hexagonal) phase. The rational SFIs correspond to $\{021\}_o$ and $\{221\}_o$, respectively, when transformed to coordinates of the O-phase. The $\{hhk\}_c$-type interfaces in the O-phase coordinates are of the form $\{1,(s-1),2(s+1)\}_o$

where s=k/h. The $\{hhk\}_c$ interfaces, when calculated for the lattice parameters of the DO_{19} or O phases taken from the literature [4], are found to be close to $\{155\}_c$ and $\{144\}_c$, respectively. The pair of orthogonal interfaces between different pairs of variants are summarized in Table 4 where the labeling of the pairs is given according to Fig. A.2.

4.2 Polydomain Structures

Two rotational domains separated by a planar SFI are a unique morphology that avoids long range elastic stress fields. Two domains cannot be bounded by the two conjugate orthogonal SFIs as shown in Fig. 7a, because the corner where these SFIs intersect each other would be a disclination, and therefore a source of a long-range distortion.

The optimal shape of one domain included inside another is a plate with a small thickness to length ratio. (Experimentally the plates usually are found lenticular.) If the wide facets of the plate are SFI's, the stress field would be concentrated only near the plate edge, in a manner similar to a dislocation loop field (Fig. 7b) [35, 37]. This long range field can be reduced if a packet of plate-like domains is formed (Fig. 7c). If the boundaries of the packets (imaginary planes through the plate edges) are aligned parallel to the conjugate SFI plane n of the SFI plane of the individual plates, m, then interference of the edge fields cancels the long-range stress field components. Such plane-parallel packets (also named in the literature as polytwins (by analogy with polysynthetic twins), or polydomains) are a typical element of domain morphology.

The polytwin as a whole can be considered as an effective "domain" of second order in a hierarchy of domain structures [33,37]. By analogy domain structures of even higher order can also be constructed. Examples of a domain structure of 2nd order for the BCC → Ort transition

consisting of 3 variants are discussed below and illustrated in Fig. 8.

The pseudo-SFIs between polytwins can be determined by the same Eqs. (4.4) and (4.5), where e_{ij} (or S_{ij}) is an average self-strain of the polytwin as a whole. For example, the equations for the SFI between the polytwin consisting of domains 1 and 2 and the polytwin consisting of 1 and 3 is

$$x_i(e_{ij}(1,2) - e_{ij}(1,3))x_j = 0 \tag{4.6}$$

The average self-distortions $S_{ij}(1,2)$ and $S_{ij}(1,3)$ are expressed through an average distortion of the polytwins

$$S_{ij}(1,2) = (1-\alpha)S_{ij}(1) + \alpha S_{ij}(2) \tag{4.7a}$$

$$S_{ij}(1,3) = (1-\beta)S_{ij}(1) + \beta S_{ij}(3) \tag{4.7b}$$

where α (or β) is the fraction of domains 2 (or 3) in polytwin (1,2) (or 1,3), and where the distortions $S_{ij}(1)$, $S_{ij}(2)$ and $S_{ij}(3)$ include the supplementary rotations (Eq. (4.3)) of the domains in the polytwins required for conserving coherency.

In general, to determine the pseudo-SFI between polytwins, the fractions α and β must be known. If $\alpha = \beta$, the stress free boundary between polytwin (1,2) and polytwin (1,3) may run along the SFI between domains 2 and 3. For that, a line of intersection of the 1,2 SFI and the 1,3 SFI has to belong to the 2,3 SFI. For the BCC → ORT transformation there are three different interfaces of this type between polytwins consisting of 3 types of domains: along $\{100\}_c$, $\{110\}_c$ and

$\{h11\}_c$ according to the three possible orientations of the SFI's between the domains given in Table 4. Using Table 4 it is not difficult to find all possible second order polydomain morphologies for the $\alpha = \beta$ case. Such morphologies for three-variant structures are represented in Fig. 8. It is very likely that such structures with $\alpha = \beta$ correspond to a minimal energy.

While interfaces between polytwins that satisfy Eqs. 7, 8 have no long-range stress field, they do have microstresses distributed in the packet boundary. Even in the case of good matching ($\alpha = \beta$), the rotation between different domains causes microstresses which can be described as fields from disclination dipoles. These microstresses at the boundary could manifest themselves during annealing as sites for further microstructural change.

The approach of packing first, second, and higher order effective domains can be applied in principle for the analysis of any hierarchy of domain structures. The scale of such hierarchical structures should be determined by the competition between the short-range microstresses distributed in the packet boundaries that tend to disperse the structure and the effective interfacial energy that tends to coarsen the structure[3]. The number of the variants in the polydomain structure which are necessary to accommodate the self strain depends on boundary conditions. For a polydomain structure inside an untransformed matrix, the simplest polytwin that has an invariant plane boundary with the matrix is sufficient [39,40]. If the boundary of the region to be transformed is fixed, e.g. it coincides with a grain boundary, minimum elastic energy corresponds to the minimum average self-strain of the region, or zero average shear. This condition can be achieved only when all

[3] As shown by [33,35,37], similar hierarchical structures can also be formed by domains consisting of different phases. For example, the structure morphologically similar to the 3-domain structure in Fig. 8 can be created by incorporating two domains of the O- phase inside of which there is one domain of the hexagonal DO_{19} phase (domain 1). The geometry of such a heterophase structure will be analyzed in Part II.

variants take part in the polydomain structure. The number of the variants determines an internal hierarchy of the polydomain structure.

5. Expected Microstructures and Transformation Paths

The present analysis suggests that three different types of domain structures are possible for a single phase microstructure of the O-phase depending on the transformation path traversed. The paths are summarized by Eqns. 3.1, 3.2 and 3.3 in the form of subgroup sequences. These paths differ primarily as to whether the hexagonal symmetry phases or the B19 phase occurs at an intermediate stage of transition. The path involving the hexagonal phases (Eqn. 3.1) involves the formation of a supergroup; i.e., the intermediate orthorhombic A20 structure transforms to the hexagonal A3 by pure displacement. In general this is impossible (as a pure displacive transformation) if the parent phase has either long or short range chemical order of a type which would have been required to adjust to form the higher symmetry [41]. Thus path 3.1 is only possible for alloys quenched from a disordered BCC phase.

For Ti-Al-Nb alloys quenched from a B2 phase field, path 3.2 is clearly expected. The path is characterized by the presence of the B19 structure as an intermediate stage of transition, which in this case forms by a purely displacive transition from B2. The B19 phase could also form from an alloy quenched from the disordered BCC field by path (3.2) or by path (3.3). This latter path involves the formation of the B19 structure from the orthorhombic A20 by a pure ordering reaction between Ti and Al/Nb. Experimentally, evidence for the occurrence of one of the three paths can be obtained with microstructural information for the transient existence of B19 or A3 phases in the final O-phase domain structure. In alloys near the Ti_3Al-Nb_3Al section of the ternary system, the

tendency towards B2 order in the high temperature BCC phase is strongest for alloys near Ti_2AlNb because the two Wyckoff sites of the B2 are known [21] to be filled with Ti and a mixture of Al and Nb. Thus paths to the O-phase involving the B19 phase are most likely for alloys with Nb contents around 25at%, while the path to the O-phase involving the hexagonal phase is expected for lower levels of Nb.

The microstructural development for the three paths is depicted in Fig. 9, starting from a large grain single phase BCC and ending with single phase orthorhombic. It is assumed that the interface configuration does not change significantly after formation at each stage of the transformation. All three paths, in their first stages, have similar microstructures composed of orthorhombic phase domains (either disordered Cmcm(A20) for path 3.1 and 3.3 or ordered Pmma(B19) for path 3.2). According to the discussion in Sec.4, the domains will form a polytwin morphology with *SFIs* parallel to either $\{100\}_c$, $\{110\}_c$ or conjugate $(hhk)_c$ planes. In path 3.2, the BCC → B2 ordering precedes the formation of the orthorhombic phase but does not influence the formation and morphology of the polytwin structure. The APBs due to this ordering (curved lines) separate either interconnected or closed volume domains and may be found continuously crossing the polytwin domains. If path 3.2 starts from the B2 phase, such APBs will be absent.

Inside the polytwin plate-like domains, as Fig. 9 shows, anisotropic planar interfaces (schematically represented as rectangles, or straight lines for interfaces connected to twin boundaries) separate two translational domains resulting from antiphase shuffles (formally due to the Fmmm → Cmcm and Cmmm → Pmma symmetry changes). The anisotropy is expected because of the stacking fault nature of the interface structure. Because of the anisotropy the interfaces are distinct for each orthorhombic phase variant orientation.

After the formation of the polytwin structure by displacive ordering, the next step in all three transformation paths is chemical ordering. For path 3.1 the ordering involves two steps. First, A3 → DO_{19} ordering of the hexagonal lattice (between Al and Ti/Nb) results in a four translational domain structure with isotropic interfaces shown in Fig. 9 as thin lines with triple junctions. Some of the interfaces are shown to coincide with previously formed translational interfaces. These coinciding segments will have a structure where changes in both atomic environment and distances are combined. Secondary ordering (DO_{19} → O-phase) between Ti and Nb results in a second polytwin domain structure with planar interfaces running through the DO_{19} APBs, which are not effected by the secondary ordering. The interfaces in the same primary plate can have different orientations (either orthogonal or 60° rotated) as discussed in Appendix A and shown in Fig. 9.

In path 3.2, the ordering (B19 → O-phase) between Al and Nb results in a two domain structure, with isotropic interconnected or closed interfaces. Due to the presumed lower temperature of transformation for this stage, the size of these antiphase domains is shown in Fig. 9 smaller then of those from the first BCC → B2 ordering. If the path starts from the B2 phase only the second type of antiphase domains will occur in the final microstructure.

In path 3.3 there are two steps of chemical ordering - the first one between Ti and Al/Nb atoms (A20 → B19) and the second one between Al and Nb (B19 → O-phase) - resulting in isotropic interfaces. Again, due to the difference in the presumed temperature of transformation, the size of these antiphase domains may be different. However the difference, as it is shown in Fig. 9, is less than for path 3.2, and this is the only difference in these two final microstructures.

Appendix A. SFIs for the $P6_3/mmc(DO_{19}) \rightarrow Cmcm(O)$ (6/mmm → mmm) transition.

The structural relation between the phases (o - orthorhombic; h - hexagonal) gives the following lattice correspondence: $a_o = a_{1h}$; $b_o = a_{1h} + 2a_{2h}$; $c_o = c_h$. Fig. A.1 shows stereographic projections of the point groups of the hexagonal and of the orthorhombic phase variants, according to the lattice correspondence. When the symmetry elements of a pair of variants are compared, we find a set of two orthogonal mirror planes which belong to the parent phase but not to the pair considered. E.g., for variants 2 and 3 in Fig. A.1, the set of lost mirror planes is $x = 0$ and $y = 0$. Similarly, for the 1/2 and 1/3 pairs of domains the sets are $y/x = \tan 30° = \sqrt{3}/3$, $y/x = \tan 120° = -\sqrt{3}$ and $y/x = \tan 60° = \sqrt{3}$, $y/x = \tan 150° = -\sqrt{3}/3$, respectively. Being mirror planes, and therefore twinning planes, the three sets are planar SFIs running parallel to the z-axis.

The same results can be obtained by solving Eqn. (4.4). For this purpose, the self-strain tensor of the three variants must be first determined. For variant 1 in Fig. A.1, the self-strain tensor will be

$$e_{ij}(1) = \begin{vmatrix} e1 & 0 & 0 \\ 0 & e2 & 0 \\ 0 & 0 & e3 \end{vmatrix} \qquad \text{(A.1)}$$

where

$$e_1 = a + a^2/2; \quad e_2 = b + b^2/2; \quad e_3 = c + c^2/2.$$

with

$$a=\frac{a_o-a_k}{a_k};b=\frac{b_o-\sqrt{3}a_k}{\sqrt{3}a_k};c=\frac{c_o-c_k}{c_k}.$$

The self-strain tensor for the other two variants will be obtained using Eqn.(4.1). The variant generating symmetry operation in that case is chosen to be the three-fold anti-clock-wise rotation ($g_{ij} = 3^-$), so that $e_{ij}(3) = 3^- 3^- e_{ij}(1)$ and $e_{ij}(2) = 3^- 3^- e_{ij}(3)$ (see Fig. A.1). In order to do calculations in orthogonal coordinates, the matrix of the three-fold rotation must be presented in the same coordinates. It is found as

$$3_{ij}^- = \begin{vmatrix} -1/2 & -\sqrt{3}/2 & 0 \\ \sqrt{3}/2 & -1/2 & 0 \\ 0 & 0 & 1 \end{vmatrix} \qquad \text{(A.2)}$$

After matrix multiplication we find that

$$e_{ij}(3) = \begin{vmatrix} \frac{a}{4}+3\frac{b}{4} & -\sqrt{3}\frac{a}{4}+\sqrt{3}\frac{b}{4} & 0 \\ -\sqrt{3}\frac{a}{4}+\sqrt{3}\frac{b}{4} & 3\frac{a}{4}+\frac{b}{4} & 0 \\ 0 & 0 & c \end{vmatrix} \qquad \text{(A.3)}$$

and

$$e_{ij}(3)-e_{ij}(1) = \frac{\sqrt{3}(b-a)}{4}\begin{vmatrix} \sqrt{3} & 1 & 0 \\ 1 & -\sqrt{3} & 0 \\ 0 & 0 & 0 \end{vmatrix} \qquad \text{(A.4)}$$

Eqn. 4 for the SI interfaces between variants 3 and 1 will be

$$[e_{ij}(3) - e_{ij}(1)]x_i x_j = x^2 - y^2 + \frac{2}{\sqrt{3}}xy = 0 \qquad (A.5)$$

or

$$(y - \sqrt{3}x)(y + x/\sqrt{3}) = 0.$$

Two solutions for the quadratic equation are $y/x = \sqrt{3}$ and $y/x = -\sqrt{3}/3$ and they do not depend on the parameters a, b and c. These are the same mirror planes found with the help of the stereographic analysis performed above. Solutions for the other variants can be found similarly, and they are the remaining mirror planes of the 6/mmm with $y/x = \sqrt{3}/3, -\sqrt{3}$ (for the 1/2 variants) and $x = 0$, $y = 0$ (for the 2/3 variants). A pair of variants can be identified unambiguously from their interface orientation.

Appendix B. *SFIs for the Im$\bar{3}$m(A2) → Cmcm(A20) and Pm$\bar{3}$m(B2) → Pmma(B19);*
i.e., the (m$\bar{3}$m → mmm) transition.

The structural relation between the phases (c - cubic; o - orthorhombic) gives the following lattice correspondence: $a_o = a_{1c}$; $b_o = a_{2c} + a_{3c}$; $c_o = a_{2c} - a_{3c}$. According to the lattice correspondence, Fig. A.2 shows the stereographic projections of the point groups and the crystallographic axes of the parent cubic (m$\bar{3}$m) and its six subgroup variants of the orthorhombic (mmm) phases. Comparing symmetry elements belonging to a pair of the variants with those of the parent cubic, we can find mirror planes of the parent (but missing in the product variants) that reflect the variants into each other. The mirror planes serve as the SFIs. For a pair of variants sharing the a_o axis (1/2, 3/4 and 5/6 pairs in Fig. A.2), there are two orthogonal mirror planes of $\{100\}_c$ type (parallel to the a_o axis). For the other pair of variants, not sharing a common direction, there is only one such mirror plane, of $\{110\}_c$ type. Orthogonal to the {110} plane is either a $\{hh\bar{l}k\}_c$ or

a $\{h\bar{h}\bar{k}\}_c$ plane, generally of an irrational orientation which depends on the ratio of the lattice parameters. In order to find h and k, eqn.(4) must be solved.

We solve Eqn. (4.4) in the coordinate system of the cubic phase shown in Fig. A.2. First, we find the self-strain tensors of the six variants using the variant generating operators, Eqn. (4.1). All variants can be generated by the mirror plane operations, starting from the first variant:

$$e(2) = m_{100}m_{100}e(1); \quad e(5) = m_{10\text{-}1}m_{10\text{-}1}e(1); \quad e(4) = m_{011}m_{011}e(1);$$

$$e(6) = m_{010}m_{010}e(5); \quad e(3) = m_{100}m_{100}e(4). \tag{B.1}$$

Matrices for the mirror planes are given in Table 11.4 of The International Tables for Crystallography [37]. The self-strain tensor for variant 1 (see Fig. A.2) in the coordinates of the variant is

$$e'_{ij}(1) = \begin{vmatrix} a & 0 & 0 \\ 0 & b & 0 \\ 0 & 0 & c \end{vmatrix} \tag{B.1}$$

where

$$a = \frac{a_o - a_c}{a_c}\ ;\ b = \frac{b_o - \sqrt{2}a_c}{\sqrt{2}a_c}\ ;\ c = \frac{c_o - \sqrt{2}a_c}{\sqrt{2}a_c}\ ;$$

and a_c, a_o, b_o, c_o are the lattice parameters of the cubic and the disordered orthorhombic phase (for the ordered O-phase half of their values of a_o and b_o should be used).

In order to obtain the $e'_{ij}(1)$ tensor in cubic coordinates, the tensor's axes must be rotated 45° around $[100]_c$, which is obtained by the rotation and permutation matrix

$$\alpha_{ij} = \begin{vmatrix} 0 & m & m \\ 0 & -m & m \\ 1 & 0 & 0 \end{vmatrix}; \; m = \frac{\sqrt{2}}{2} \tag{B.3}$$

The tensor $e_{ij}(1)$ in cubic coordinates is then

$$e_{ij}(1) = \alpha_{ik}\, \alpha_{jl}\, e'_{kl}(1) = \begin{vmatrix} A & B & 0 \\ B & A & 0 \\ 0 & 0 & C \end{vmatrix} \tag{B.4}$$

where A = 1/2(b + c); B = 1/2(c - b); C = a.

The self-strain tensors for other variants are:

$$e_{ij}(2) = \begin{vmatrix} A & -B & 0 \\ -B & A & 0 \\ 0 & 0 & C \end{vmatrix}; \; e_{ij}(3) = \begin{vmatrix} A & 0 & B \\ 0 & C & 0 \\ B & 0 & A \end{vmatrix}; \tag{B.5}$$

$$e_{ij}(4) = \begin{vmatrix} A & 0 & -B \\ 0 & C & 0 \\ -B & 0 & A \end{vmatrix}; \; e_{ij}(5) = \begin{vmatrix} C & 0 & 0 \\ 0 & A & B \\ 0 & B & A \end{vmatrix}; \tag{B.6}$$

$$e_{ij}(6) = \begin{vmatrix} C & 0 & 0 \\ 0 & A & -B \\ 0 & -B & A \end{vmatrix}. \tag{B.7}$$

Eqn.(4) for the SFI interface between variants 1 and 2 will be

$$(e_{ij}(2)-e_{ij}(1))x_ix_j = \begin{vmatrix} 0 & 2B & 0 \\ 2B & 0 & 0 \\ 0 & 0 & 0 \end{vmatrix} x_ix_j = xy = 0 \qquad \text{(B.8)}$$

Solutions are the symmetric x = 0, $(100)_c$, and y = 0, $(010)_c$, the twinning mirror planes expected from symmetry.

For variants 1 and 3 Eqn. 4 is

$$(e_{ij}(3)-e_{ij}(1))x_ix_j = \begin{vmatrix} 0 & B & -B \\ B & A-C & 0 \\ -B & 0 & C-A \end{vmatrix} x_ix_j = (y-z)[2Bx+(A-C)(y+z)] = 0 \qquad \text{(B.9)}$$

One solution of the equation is the expected symmetric case, y = z, which corresponds to the $(01\bar{1})_c$ crystallographic plane. The second, non-symmetric case, is 2Bx + (A-C)(y + z) = 0. This is the equation of a plane having a normal n where n_x = 2B, n_y = (A-C), and n_z = (A-C). This plane has $(hkk)_c$ Miller indexes, and therefore orthogonal to the $(01\bar{1})_c$. The ratio of h to k is 2B/(A-C), or 2(c-b)/(b+c-2a) and depends only on the lattice parameters of the orthorhombic phases (h/k = $2(2c_o - b_o)/(b_o + 2c_o - 2\sqrt{2}a_o)$). For the lattice parameters of the Ti-Al-Nb DO_{19} and O phases [4], the Miller indexes are close to $\{\bar{1}\ 5\ 5\}_c$ and $\{\bar{1}\ 4\ 4\}_c$, respectively.

Similarly, the solutions for all 15 pairs of domains were found. The results are given in Table 4. There are 30 (N=6x5) SFIs, of which only 21 are different orientations: 3 of the $\{100\}_c$ type, 6 of the $\{110\}_c$ type and 12 of the $\{hkk\}_c$ type.

Fig. A.3 shows the directions of the SFI traces superimposed on the $[011]_c$ stereographic projection, as they would be seen for crystals oriented for TEM at the $[011]_c$ zone axis. Such drawings are useful in analyzing the nature of interfaces observed in TEM specimens of the Ti-Al-Nb alloys, as shown in Part II of this paper. Fig. A.3a presents traces of the symmetric $\{001\}_c$- and $\{110\}_c$-type interfaces. Fig. A.3b presents traces of the non-symmetric $\{hhk\}_c$-type interfaces. Two of the $\{hhk\}_c$-type interfaces are oriented edge-on ($kh\bar{h}$ and $\bar{k}hh$), and two are inclined but with a rational trace direction $[01\bar{1}]$ (khh and $\bar{k}hh$) . Since the lattice parameter varies with temperature and composition, a range of possible orientations of the interfaces is given for the orthorhombic phase having lattice parameters ranging from those of the Ti_2AlNb O-phase (determined in [24] as a_O=0.60893 nm, b_O=0.95694 nm, c_O=0.46666 nm) to those of the hexagonal DO_{19} phase (determined in [4] as a_h=0.578 nm, b_h=1.001 nm, c_h=0.466 nm).

References.

1. S.M.L.Sastry and H.A.Lipsitt, Met. Trans., 8A, 1543 (1977)
2. D. Banerjee, A.K. Gogia, T.K. Nandi, and U.A. Toshi, Acta. Met., 36, 871 (1988).
3. R. Strychor, T.C. Williams and W.A. Soffa, Met. Trans., 19A, 1321 (1988).
4. H. T. Kestner-Weykamp, C. H. Ward, T. F. Broderick and M. J. Kaufman, Scr. Met. 23, 1697 (1989).
5. J.H. Perepezko, Y.A. Chang, L.E. Seitzman, T.C. Lin, N.R. Bonda, T.J.Jewett and J.C. Mishurda,
6. R.G. Rowe, in "High Temperature Aluminides and Intermetallics", eds. S.H.Whang, C.T.Lui, D.P.Pope and J.O.Stiegler, TMS-AIME, Warrendale PA. 1990, pp.375 -401
7. K. Muraleedharan, A.K. Gogia, T.K. Nandi, D.Banerjee and S.Lele, Met. Trans., 23A, 401 (1992)
8. K. Muraleedharan, T.K. Nandi, D.Banerjee and S.Lele, Met. Trans., 23A, 417 (1992)
9. D.A.Lukasak and D.A.Koss, Met. Trans., 21A, 1990 (1990)
10. A.K.Gogia, D.Banerjee and T.K.Nandy, Met. Trans., 21A, 609 (1990)
11. D.Banerjee, A.K.Gogia and T.K.Nandy, Met. Trans., 21A, 627 (1990)
12. W.Cho, A.W.Thompson and J.C.Williams, Met. Trans., 21A, 641 (1990)
13. R.G.Rowe and M.F.X.Gigliotti, Scr. Met., 24, 1209 (1990)
14. R.W.Hayes, Scr. Met., 23, 1931 (1989)
15. H.T.Weykamp, D.R.Baker, D.M.Paxton and M.J.Kaufman, Scr. Met., 24 445 (1990)
16. W.A.Baeslack III and T.Broederick, Scr. Met., 24, 319 (1990)
17. J.A.Peters and C.Bassi, Scr. Met., 24, 915 (1990)
18. R.S.Mishra and D.Banerjee, Scr. Met., 24, 1477 (1990)

19. M.J.Cieslak, T.J.Headley and W.A.Baeslack, Met. Trans., 21A, 1273 (1990)

20. L.A. Bendersky and W.J. Boettinger, Proc. Mater. Res. Soc. Symp., 133, (1989), p. 45.

21. D.Banerjee, T.K.Nandy and A.K.Gogia, Scr. Met., 21, 597 (1987)

22. D.Banergee, T.K.Nandy, A.K.Gogia and K.Muraleedharan, 6th World Conf. on Titanium, 1988, eds.P.Lacombe, R.Tricot and G.Beranger, J. Phys. (Les Ulis, Fr.), pp.1091

23. D.G.Konitzer, I.P.Jones and H.L.Fraser, Scr. Met., 20, 265 (1986)

24. B.Mozer, L.A.Bendersky, W.J.Boettinger and R.G.Rowe, Scr. Met., 24, 2363 (1990).

25. L.A.Bendersky, W.J.Boettinger and A.Roytburd, Acta Metall. Mater. 39 1959 (1991)

26. L.D.Landau and E.M.Lifschitz, Statistical Physics, Addison-Wesley (1958)

27. International Tables of Crystallography, Vol.A, T.Hahn, ed., Reidel Publishing Co., Dordrecht (1978).

28. Yu.A. Izyumov and V.N. Syromyatnikov, Phase Transitions and Crystal Symmetry, Kluwer Academic Publ.,1990

29. A.Bagaryatski, T.V. Tagunova and G.I. Nosova, Dokl. Akad. Nauk SSSR, 122, 539 (1958)

30. J. W. Cahn, Acta Met.25, 721 (1977)

31. R.Portier and D.Gratias, J. Physique, 43, C4-17 (1982);
M.Guymont, D.Gratias, R.Portier and M.Fayard, Phys. Stat. Sol., 38, 629 (1976)

32. L.A. Bendersky, W.J. Boettinger, B. Burton, F.S. Biancaniello, and C.B. Shoemaker, Acta. Metall. Mater, 38, 931 (1990).

33. A.L.Roitburd, Sov. Phys. - Solid State, 10 2870 (1969)

34. J. W. Christian, Theory of Phase Transformations in Metals and Alloys, Pergamon, 1975.

35. A.G.Khachaturian, "Theory of Structural Transformations in Solids", J.Wiley and Sons, New York, 1983.

36. J. Sapriel, Phys. Rev. B. 12,5128 (1975).

37. A. L. Roytburd, in Solid State Physics, vol. 33, Academic Press, 1978.

38. T.Saburi and C.M.Wayman, Acta Met., 27, 979 (1979)

39. M.S.Wechsler, D.S.Lieberman and T.A.Read, Trans. AIME, 197, 1503 (1953)

40. C.M.Wayman, "Introduction to Crystallography of Martensitic Transformations", MacMillan, New York, 1964

41. J. W. Cahn, Acta Met.25, 1021 (1977)

TABLE 1 - Subgroups and Supergroups from the International Tables of Crystallography for $Im\bar{3}m$ and $P6_3/mmc$

$Im\bar{3}m$

Maximal non-isomorphic subgroups

	I	[3] I4/m 12/m (I4/mmm)
		[3] I4/m 12/m (I4/mmm)
		[3] I4/m 12/m (I4/mmm)
→		[4] $I1\bar{3}2/m$ ($R\bar{3}m$)
		[4] $I1\bar{3}2/m$ ($R\bar{3}m$)
		[4] $I1\bar{3}2/m$ ($R\bar{3}m$)
		[4] $I1\bar{3}2/m$ ($R\bar{3}m$)
		[2] $Im\bar{3}1$ ($Im\bar{3}$)
		[2] I432
		[2] $I\bar{4}3m$
→	IIa	[2] $Pm\bar{3}m$
		[2] $Pn\bar{3}n$
		[2] $Pm\bar{3}n$
		[2] $Pn\bar{3}m$
	IIb	none

Maximal isomorphic subgroups of lowest index

	IIc	[27] $Im\bar{3}m$ ($a'=3a$, $b'=3b$, $c'=3c$)

Minimal non-isomorphic supergroups

I	none
II	[4] $Pm\bar{3}m$ ($2a'=a$, $2b'=b$, $2c'=c$)

$P6_3/mmc$

Maximal non-isomorphic subgroups

	I	[2] $P6_322$
		[2] $P6_3/m11$ ($P6_3/m$)
		[2] $P6_3mc$
		[2] $P\bar{3}m1$
		[2] $P\bar{3}1c$
		[2] $P\bar{6}m2$
		[2] $P\bar{6}2c$
→		[3] Pmmc (Cmcm)
		[3] Pmmc (Cmcm)
		[3] Pmmc (Cmcm)
	IIa	none
	IIb	[3] $H6_3/mmc$ ($a'=3a$, $b'=3b$) ($P6_3/mcm$)

Maximal isomorphic subgroups of lowest index

→	IIc	[3] $P6_3/mmc$ ($c'=3c$); [4] $P6_3/mmc$ ($a'=2a$,$b'=2b$)

Minimal non-isomorphic subgroups

I	none

TABLE 2 - Description of Various Phases Based on Common Sites in the Cmcm Space Group

Structure	Lattice Conditions	Occup.	Wyck.	x	y	z
Ti_2AlNb,	y_1=0.163; y_2=0.623	A	$4c_1$	0	y_1	1/4
HgNa, Cmcm	y_3=0.904; x_3=0.231	B	$4c_2$	0	y_2	1/4
		C	8g	x_3	y_3	1/4
Ti_3Al, DO_{19}	b/a=$\sqrt{3}$	A	$4c_1$	0	1/6	1/4
Ni_3Sn, $P6_3/mmc$		B	$4c_2$	0	2/3	1/4
		B	8g	1/4	11/12	1/4
αTi, A3	b/a=$\sqrt{3}$	A	$4c_1$	0	1/6	1/4
Mg, $P6_3/mmc$		A	$4c_2$	0	2/3	1/4
		A	8g	1/4	11/12	1/4
Ti-Nb, A20	y_1=0.1	A	$4c_1$	0	y_1	1/4
αU, Cmcm		A	$4c_2$	0	$1/2+y_1$	1/4
		A	8g	1/4	$3/4+y_1$	1/4
Ti-Ni, B19	y_1=0.156	A	$4c_1$	0	y_1	1/4
AuCd, Pmam(Pmma)	y_2=0.906	A	$4c_2$	0	$1/2+y_1$	1/4
		B	8g	1/4	y_2	1/4
ßTi, A2	b/a=$\sqrt{2}$	A	$4c_1$	0	1/8	1/4
W, $Im\bar{3}m$	c/a=$\sqrt{2}/2$	A	$4c_2$	0	5/8	1/4
		A	8g	1/4	7/8	1/4
TiNi, B2	b/a=$\sqrt{2}$	A	$4c_1$	0	1/8	1/4
CsCl, $Pm\bar{3}m$	c/a=$\sqrt{2}/2$	A	$4c_2$	0	5/8	1/4
		B	8g	1/4	7/8	1/4

Table 3

List of interfaces between domains in different group/subgroup transitions. The Class represent type of symmetry reduction [37], the interfaces are described by domain generating symmetry operation (of lowest symmetry).

Group/Subgroup	Class of Subgroup	Type of Interface
$Im\bar{3}m \rightarrow Pm\bar{3}m$	IIa	translational (APB)
$Im\bar{3}m \rightarrow Cmcm(A20)$	I+I+IIa	rotational (twins of I and II kind), translational with stacking fault mixed twin/translational
$Cmcm(A20) \rightarrow P6_3/mmc(A3)$	Supergroup	no new interface
$P6_3/mmc(A3) \rightarrow P6_3/mmc(DO_{19})$	IIc	translational (APB)
$P6_3/mmc(DO_{19}) \rightarrow Cmcm(O)$	I	rotational (compound twins)
$Pm\bar{3}m \rightarrow Pmma(B19)$	I+I+IIa	rotational (twins of I and II kind), translational with stacking fault, mixed twin/translational
$Cmcm(A20) \rightarrow Pmma(B19)$	IIa	translational (APB)
$Pmma(B19) \rightarrow Cmcm(O)$	IIb	translational (APB)

Table 4

List of SFI interfaces for all possible pairs of domain of the O-phase in the $m\bar{3}m \rightarrow mmm$ type transformation. Labeling of variants and interface indexes are given in the cubic coordinates of Fig. A.2. $s = k/h = 2B/(A-C)$

Pair of domains	Interface equation	Interface in Miller indices
1/2	x = 0;	(1 0 0)
	y = 0;	(0 1 0)
1/3	y = z;	(0 1 $\bar{1}$)
	-2Bx + (C-A)(y + z) = 0;	(s 1 1)
1/4	y = -z;	(0 1 1)
	-2Bx + (C-A)(y-z) = 0;	(s 1 $\bar{1}$)
1/5	x = z;	(1 0 $\bar{1}$)
	-2By + (C-A)(x+z) = 0;	(1 s 1)
1/6	x = -z;	(1 0 1)
	-2By + (C-A)(x-z) = 0;	(1 s $\bar{1}$)
2/3	y = -z;	(0 1 1)
	2Bx + (C-A)(y-z) = 0;	(s $\bar{1}$ 1)
2/4	y = z;	(0 1 $\bar{1}$)
	2Bx + (C-A)(y+z) = 0;	(s $\bar{1}$ $\bar{1}$)
2/5	x = -z;	(1 0 1)
	2By + (C-A)(x-z) = 0;	($\bar{1}$ s 1)
2/6	x = z;	(1 0 $\bar{1}$)
	2By + (C-A)(x+z) = 0;	($\bar{1}$ s $\bar{1}$)
3/4	x = 0;	(1 0 0)
	z = 0;	(0 0 1)
3/5	x = y;	(1 $\bar{1}$ 0)
	-2Bz + (C-A)(x+y) = 0;	(1 1 s)
3/6	x = -y;	(1 1 0)
	-2Bz + (C-A)(x-y) = 0;	(1 $\bar{1}$ s)
4/5	x = -y;	(1 1 0)
	2Bz + (C-A)(x-y) = 0;	($\bar{1}$ 1 s)
4/6	x = y;	(1 $\bar{1}$ 0)
	2Bz + (C-A)(x+y) = 0;	($\bar{1}$ $\bar{1}$ s)
5/6	y = 0;	(0 1 0)
	z = 0;	(0 0 1)

TABLE CAPTIONS:

Table 1. Examples of subgroup tables as it is presented in International Tables of Crystallography [27]. (a) the $Im\bar{3}m$ space group of the BCC structure and (b) the $P6_3/mmc$ (of both simple HCP and ordered DO_{19}) hexagonal structures. Different types of subgroups are listed according to: I - no change of translations; IIa - decentering; IIb - enlarging the conventional cell; IIc - no change of the group type. [x] - index of the subgroup which gives the number of variants. In a right side - list of symmetry elements of the group which were preserved in the subgroup.

Table 2. The structures space groups, Struckturberichte name, prototypes, restrictions on lattice parameters if such, occupancies (in general and for measured distribution of Ti,Al,Nb) and coordinates of the Wyckoff sites are presented for maximal subgroups of the BCC to O phase sequence.

Table 3. Type of domain interfaces which are created in each group/subgroup step which appears in the transformation paths (3.1)-(3.3).

Table 4. List of IS interfaces for all possible pairs of domain of the O-phase in the $m\bar{3}m \rightarrow mmm$ transformation. Labeling of variants and interface indexes are given in the cubic coordinates of Fig. A.2. Lattice parameters of the O and DO_{19} phases and indexes are according to the refs. [24] and [4].

FIGURE CAPTIONS

Fig. 1. The Cmcm space group is represented by the structure (a) which is close to both the HCP (b) and BCC (c) but nevertheless different in symmetry and the relative positions of their basal planes. The structures are shown in projections along their [001] (a,b) and [110] (c) directions. Black and white shades represent two neighboring layers of atoms.

Fig. 2. Subgroup/supergroup symmetry relations between the high symmetry $Im\bar{3}m$ (BCC) and the lower symmetry orthorhombic Cmcm (Ti_2AlNb) space groups. Space groups are connected to each other with arrows pointing in the direction of a decrease in symmetry. The number shown in square brackets next to each arrow is the index of symmetry reduction. Vertical arrows are used to indicate changes in symmetry due to displacive ordering. Angled arrows indicate that the difference in symmetry is due to changes in atomic site occupancy (chemical ordering).

Fig. 3. Structures corresponding to the Fig.2 subgroup sequence, as viewed along the $[001]_o$ ($[011]_o$) direction. Frames of the largest unit cell (of the O-phase) and of each particular crystal structure are drawn. Increasing size circles represents Al, Ti and Nb atoms, respectively. Filled and empty circles correspond to different parallel layers of atoms.

Fig. 4. Space groups and structures representing homogeneous strain distortion of the cubic lattice (a). (b) The I4/mmm and P4/mmm are structures of tetragonal distortion along cubic <100> (with Wyckoff positions 2a and 1a, 1d, respectively). (c) The Fmmm

and Cmmm are structures with orthorhombic biaxial distortion along orthogonal cubic <011> directions (with Wyckoff positions 4a and 2a,2c, respectively, and a doubled size unit cell.

Fig. 5 Comparison of the space-group diagrams of Fmmm and two translational variants of Cmcm. In order to have coincidence of common symmetry elements of these two space groups, the Cmcm diagrams must have a coordinate origin shifted to either 0,-1/4,-1/4 or 0,1/4,1/4. The translation vector between two Cmcm variants is [0 1/2 1/2].

Fig. 6. Two-dimensional example of the square to rectangular (p4mm to p2mm) transition illustrating formation of two pairs of domains, their rotations, strain-free interfaces and description by twinning.

Fig. 7. Schematic drawing of two rotational domains (white and gray shades) separated by planar SFIs and corresponding long range elastic stress fields. (a) Disclination field of a dihedral angle of a domain interface. (b) Dislocation-like field of a single domain inside another domain serving as a matrix. (c) Self-accommodated group of domains with reduced long range field.

Fig. 8. Polydomain structures of two second order polytwin plates composed of different combinations of three rotational variants (white, light and dark shades) of the orthorhombic phase as seen in the $[011]_c$ direction. The domain interfaces are either SFI (twin boundaries) or low-angle boundaries (dislocation walls). Continuous lines represent "edge-on" planes while doted lines are inclined planes. Possible

combinations of three variants are: (a) (1,3)/(2/3), (2,4)/(1,4); (b) (4,5)/(2,5), (2,6)/4,6), (3,5)/(1,5), (1,6)/(3,6); (c) (1,2)/(2,4), (3,4)/(2,4), (1,2)/(1,3), (3,4)/(1,3); (d) (1,2)/(2,3), (1,2)/(1,4), (3,4)/(2,3), (3,4)/(1,4); (e) (4,6)/(2,6), (1,6)/(3,6), (1,5)/(3,5), (4,5)/(2,5); (f) (1,2)/(2,4), (3,4)/(1,3). (The labeling of the variants follows Fig. A.2.)

Fig. 9 Graphical representation of the microstructural development for the three paths, starting from a large grain single phase BCC and ending with single phase orthorhombic. For the figure it is assumed that the interface configuration does not change significantly after formation at each stage of the transformation.

Fig. A.1 Stereographic projections of the point groups of the hexagonal (6/mmm) and of the orthorhombic phase variants (mmm's), according to their lattice correspondence. When the symmetry elements of a pair of variants are compared, a set of two orthogonal mirror planes is found that belong to the parent phase but not to the pair considered.

Fig. A.2 Stereographic projections of the point groups and the crystallographic axes of the parent cubic ($m\bar{3}m$) and its six subgroup variants of the orthorhombic (mmm) phases. Comparing symmetry elements belonging to a pair of the variants with those of the parent cubic, mirror planes that reflect the variants into each other can be found.

Fig. A.3 Directions of the SFI traces superimposed on the $[001]_c$ stereographic projections, as they would be seen for crystals oriented for TEM at the $[001]_c$ zone axes. (a) traces of the symmetric {001}- and {110}-type interfaces. (b) traces of the non-

symmetric lattice parameter depended {hhk}-type interfaces. A range of possible orientations for the orthorhombic phase having lattice parameters ranging from those of the Ti_2AlNb O-phase (determined in [24] as a=0.60893 nm, b=0.95694 nm, c=0.46666 nm) to those of the hexagonal DO_{19} phase (determined in [4] as a=0.578 nm, b=1.001 nm, c=0.646 nm) is shown as shaded area.

Fig. A.4 Directions of the SFI traces superimposed on the $[011]_c$ stereographic projections, as they would be seen for crystals oriented for TEM at the $[011]_c$ zone axes. (a) traces of the symmetric {001}- and {110}-type interfaces. (b) traces of the non-symmetric lattice parameter depended {hhk}-type interfaces. A range of possible orientations for the orthorhombic phase having lattice parameters ranging from those of the Ti_2AlNb O-phase (determined in [24] as a=0.60893 nm, b=0.95694 nm, c=0.46666 nm) to those of the hexagonal DO_{19} phase (determined in [4] as a=0.578 nm, b=1.001 nm, c=0.646 nm) is shown as shaded area.

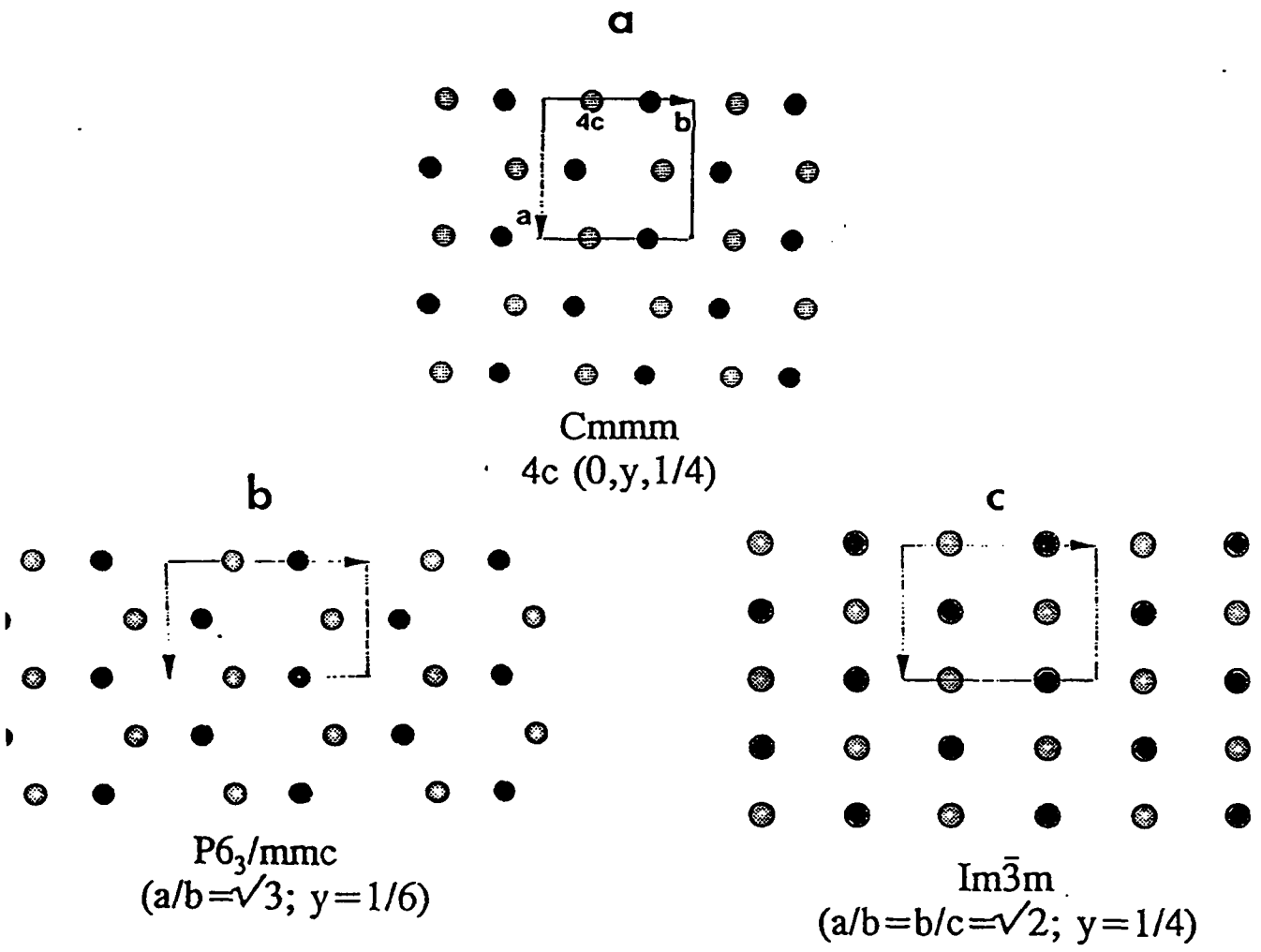

Fig. 1

Group/Subgroup Relations for BCC, HCP and Orthorhombic Phases

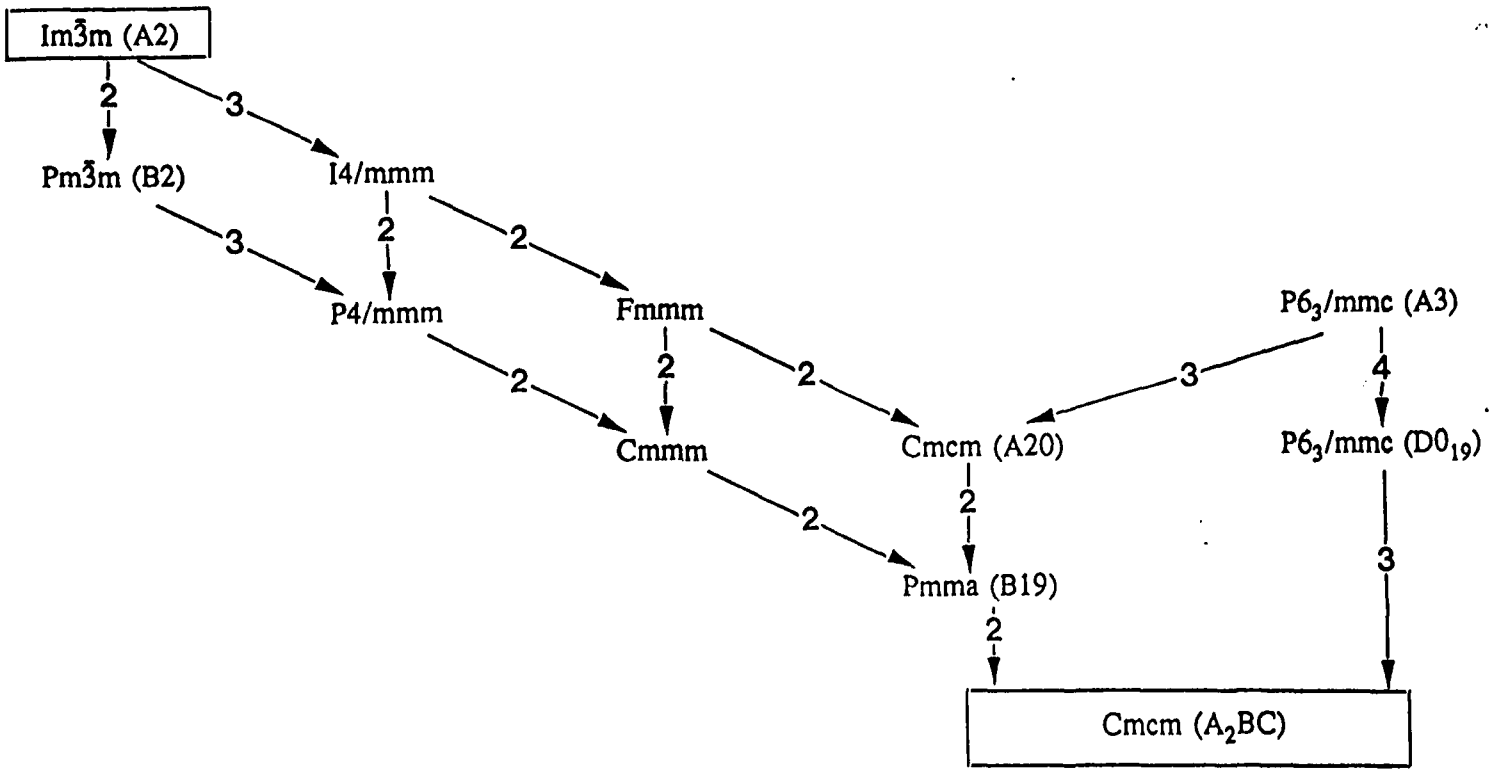

Fig. 2

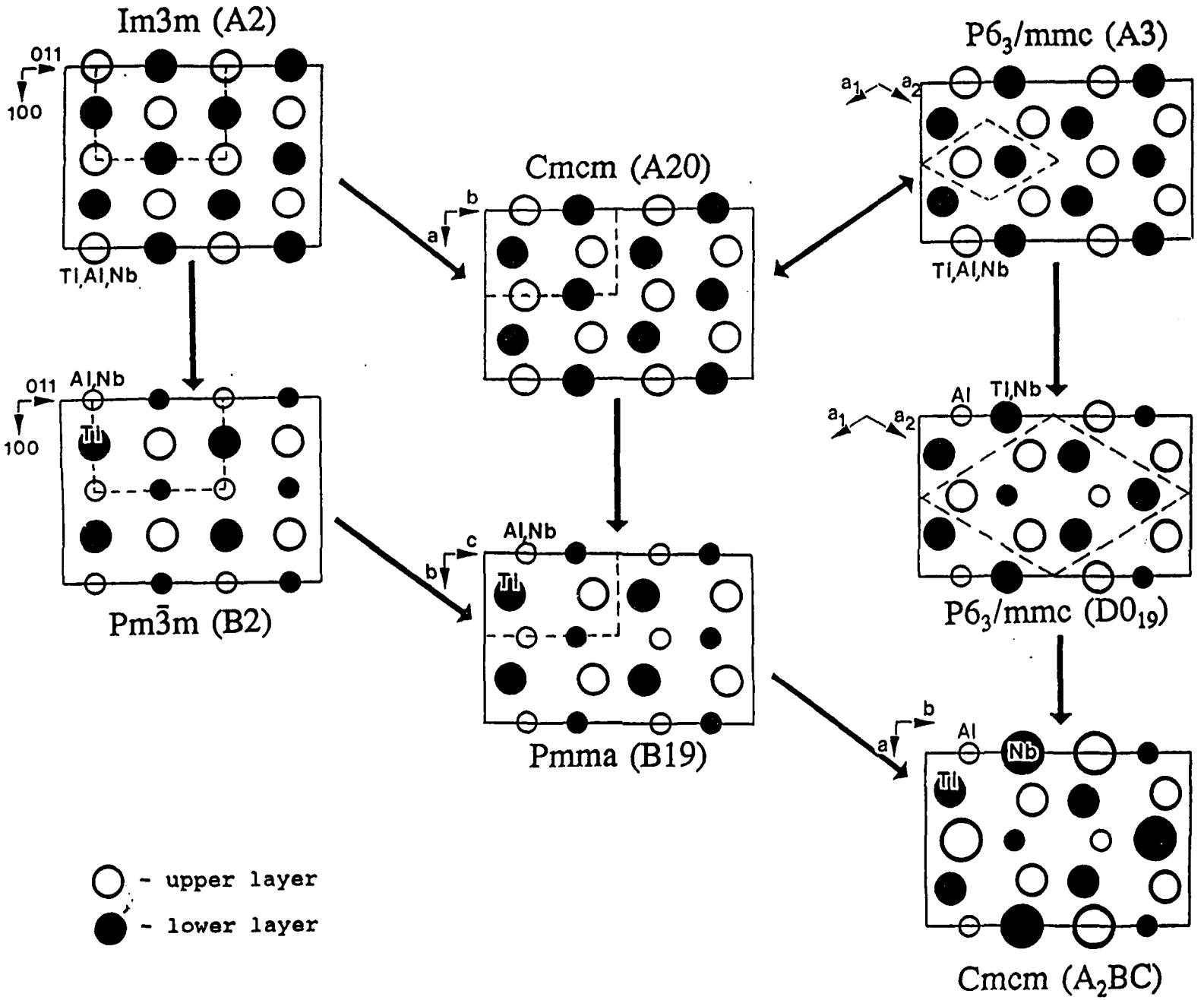
Im3m (A2)
011
100
Ti,Al,Nb
Cmcm (A20)
b
a
P6$_3$/mmc (A3)
a$_1$
a$_2$
Ti,Al,Nb
011
Al,Nb
100
Ti
Pm$\bar{3}$m (B2)
Al
Ti,Nb
a$_1$
a$_2$
P6$_3$/mmc (D0$_{19}$)
c
b
Al,Nb
Ti
Pmma (B19)
b
a
Al
Nb
Ti
Cmcm (A$_2$BC)
- upper layer
- lower layer

Fig. 3

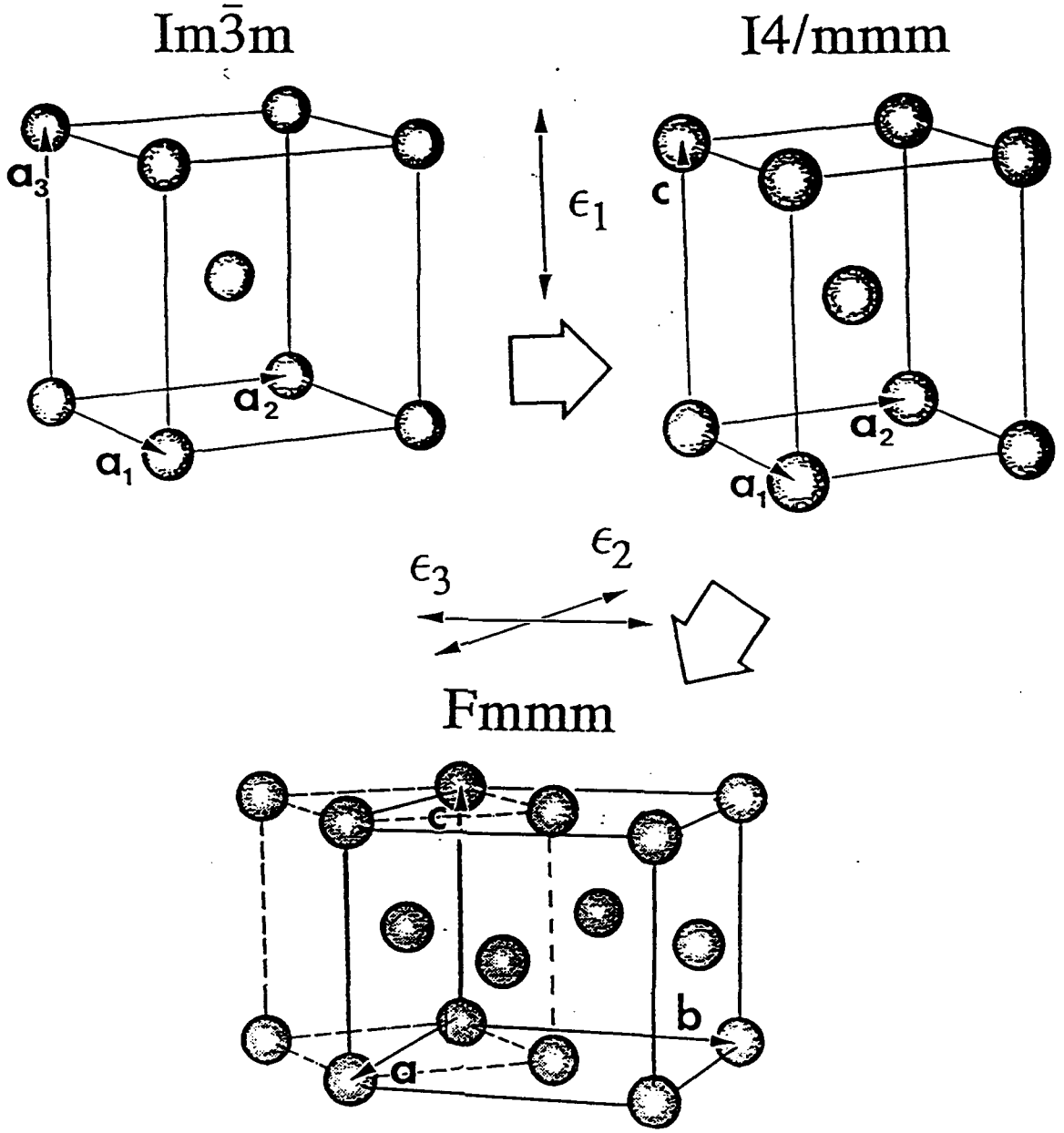
Im$\bar{3}$m
I4/mmm
a_3
a_2
a_1
ϵ_1
c
a_2
a_1
ϵ_3
ϵ_2
Fmmm
c
b
a

Fig. 4

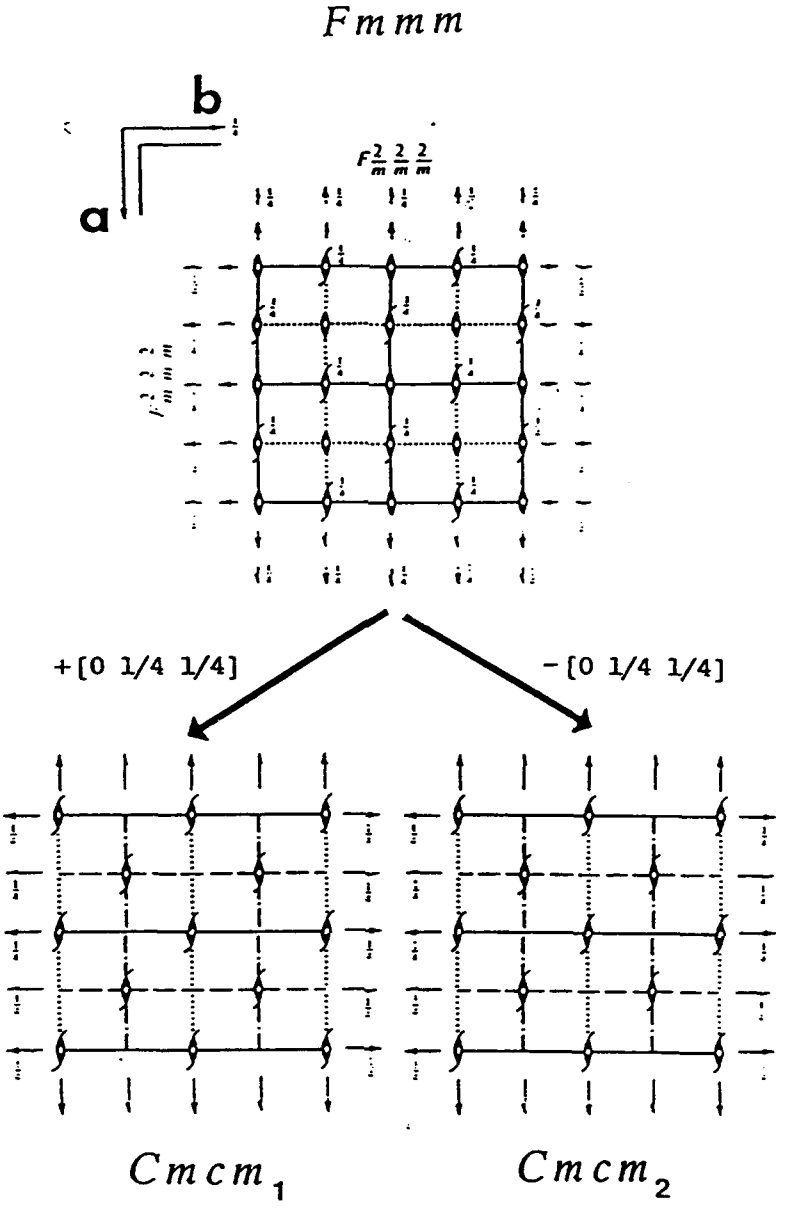

Fig. 5

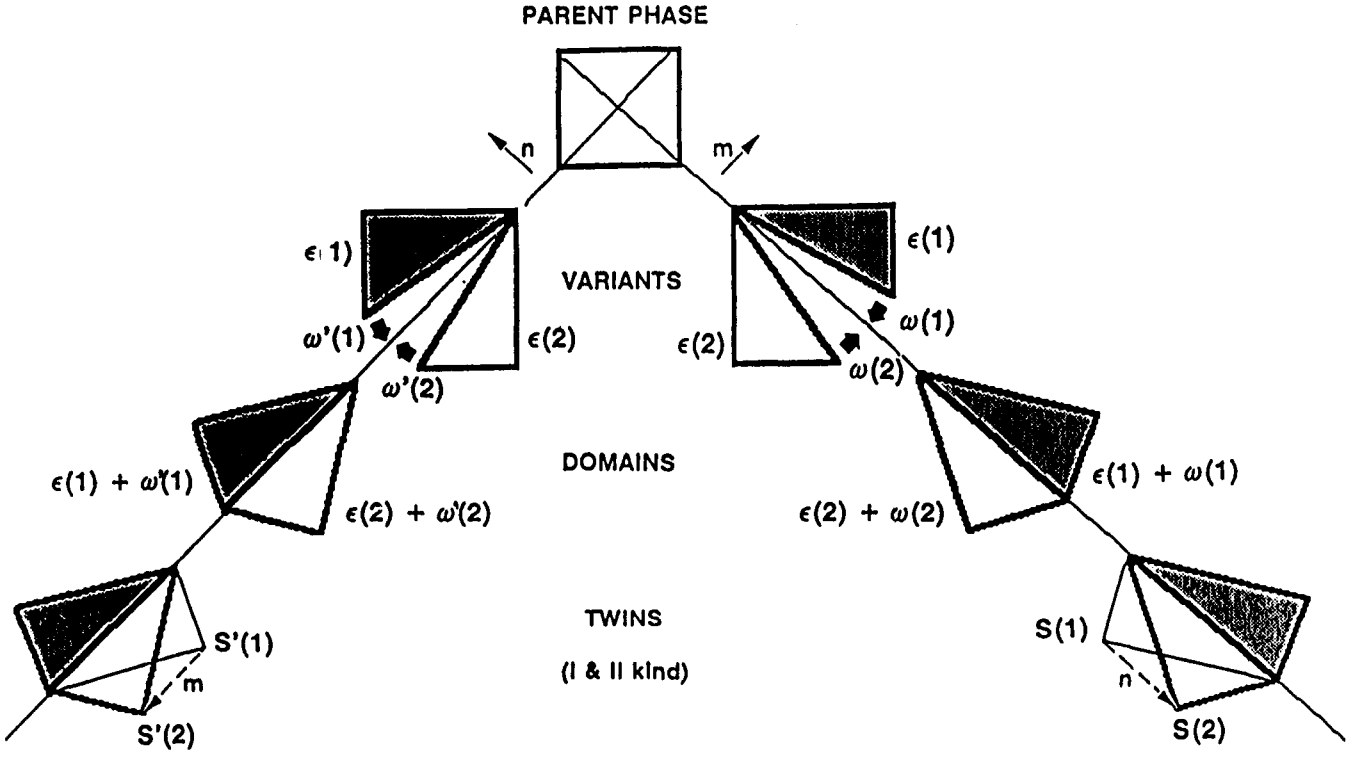
PARENT PHASE
n
m
ε(1)
VARIANTS
ω'(1)
ε(2)
ω'(2)
ε(1)
ω(1)
ε(2)
ω(2)
ε(1) + ω'(1)
DOMAINS
ε(2) + ω'(2)
ε(1) + ω(1)
ε(2) + ω(2)
TWINS
(I & II kind)
S'(1)
m
S'(2)
S(1)
n
S(2)

Fig. 6

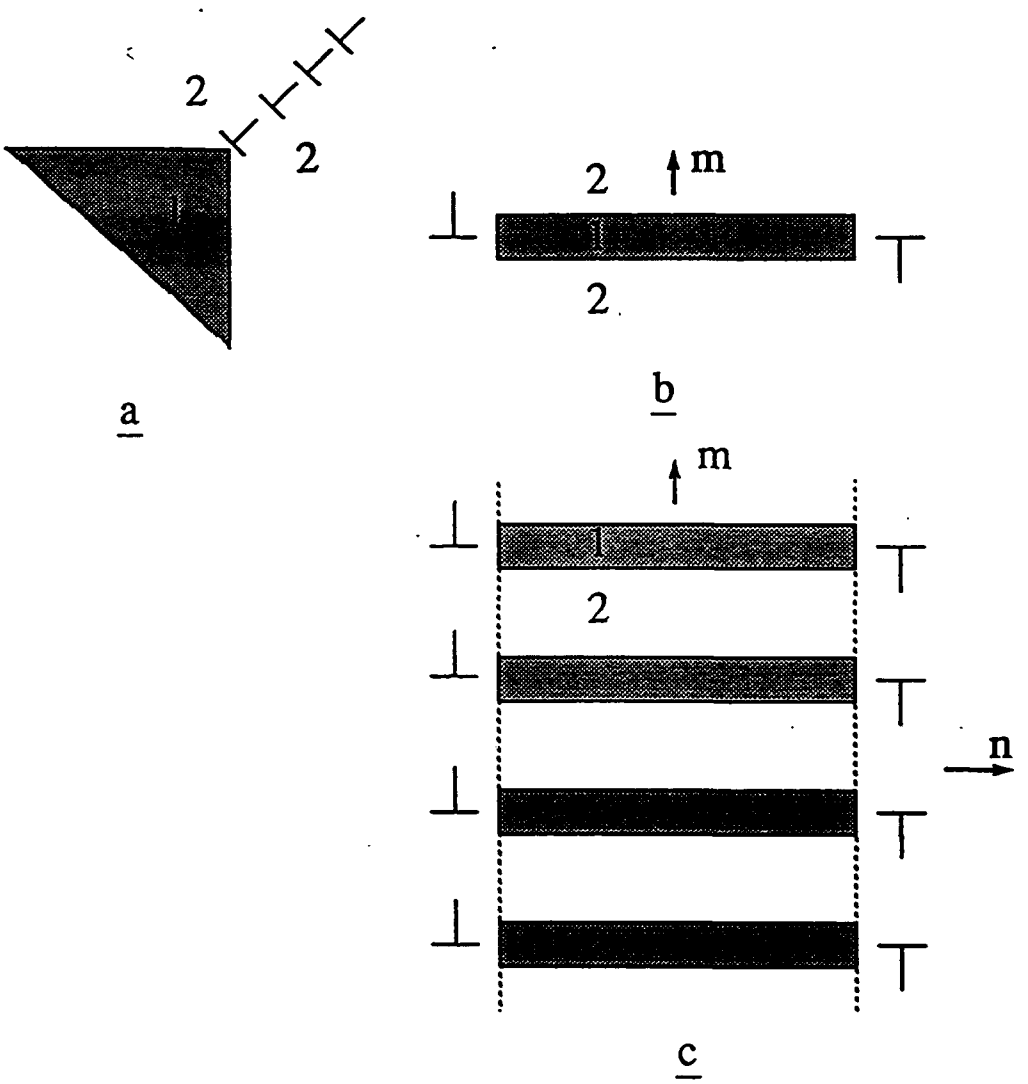

Fig. 7

Fig. 8

[12] [4] [3] [144]

$Im\bar{3}m(A2) \rightarrow$ Cmcm(A20) $\rightarrow$ $P6_3/mmc(DO_{19}) \rightarrow$ Cmcm(O)

$P6_3/mmc(A3) \rightarrow$

[2] [12] [2] [48]

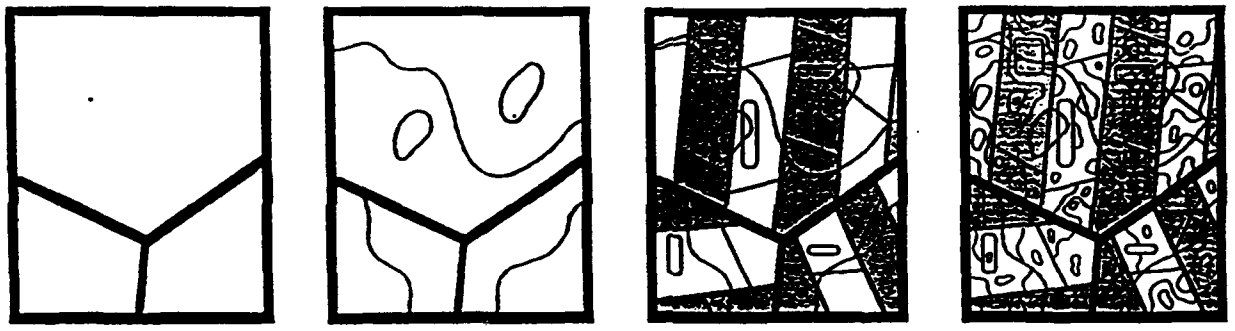

$Im\bar{3}m(A2) \rightarrow$ $Pm\bar{3}m(B2) \rightarrow$ Pmma(B19) $\rightarrow$ Cmcm(O)

[12] [2] [2] [48]

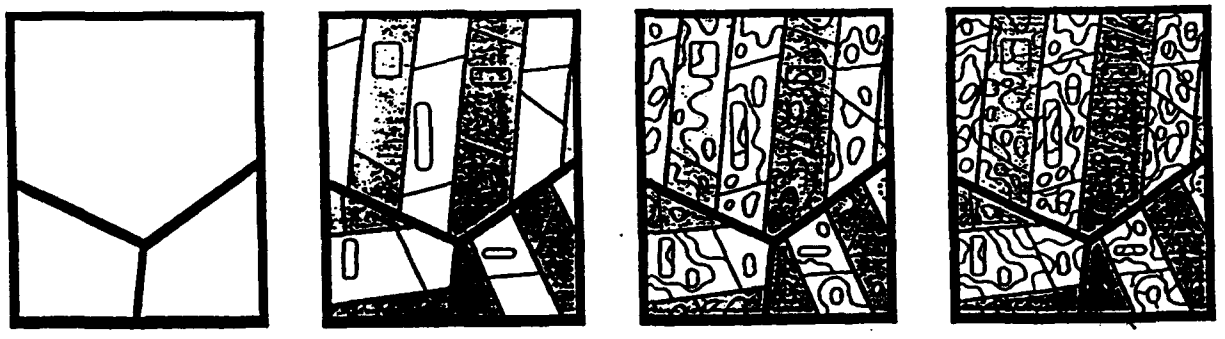

$Im\bar{3}m(A2) \rightarrow$ Cmcm(A20) $\rightarrow$ Pmma(B19) $\rightarrow$ Cmcm(O)

Fig. 9

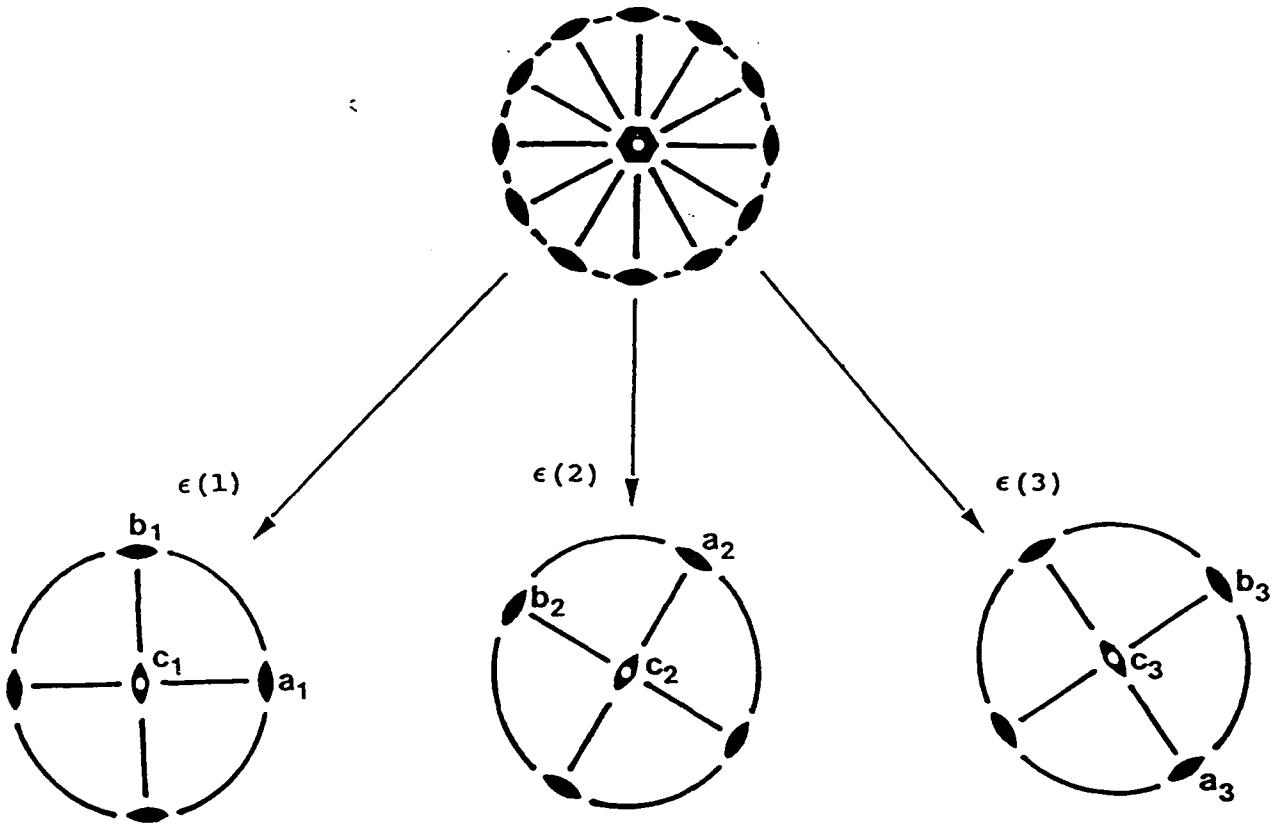

Fig. A1

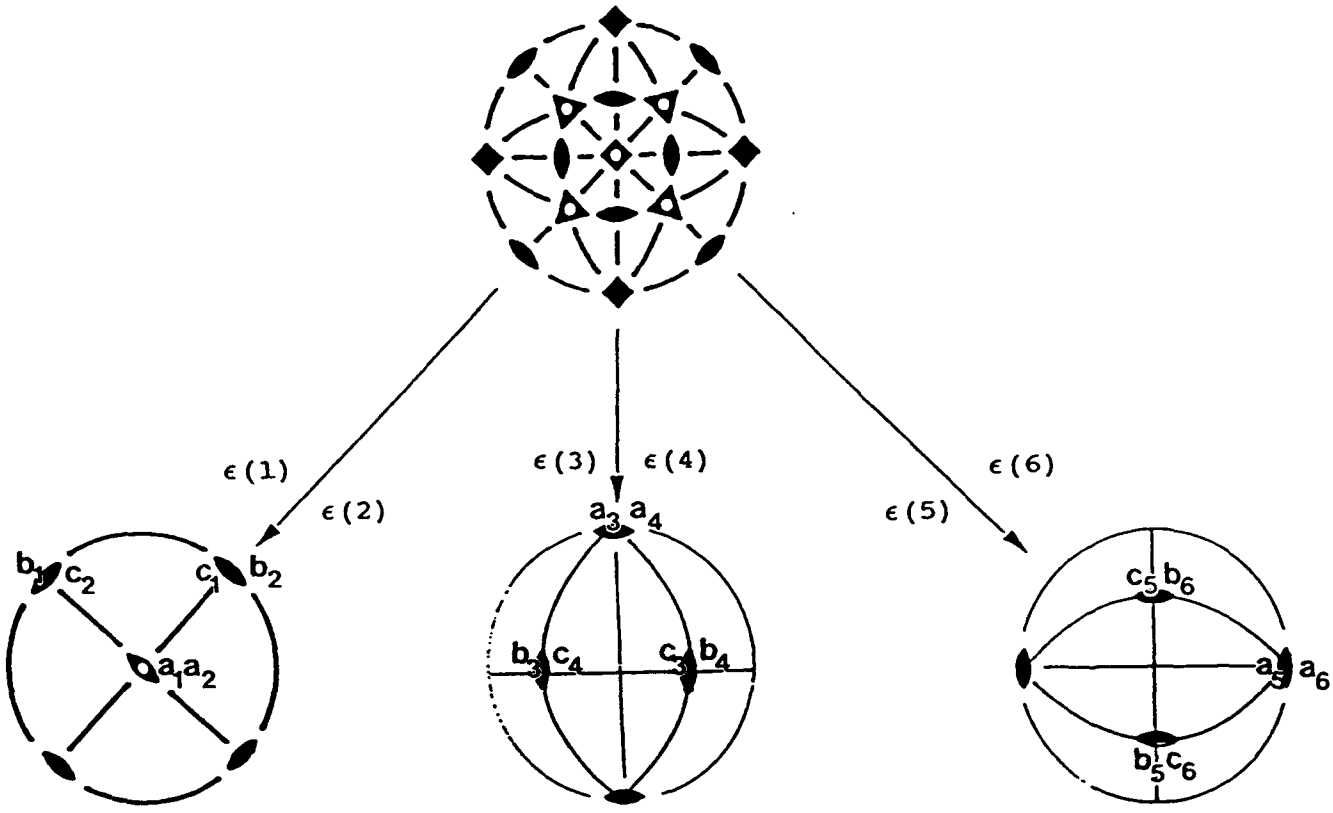

Fig. A2

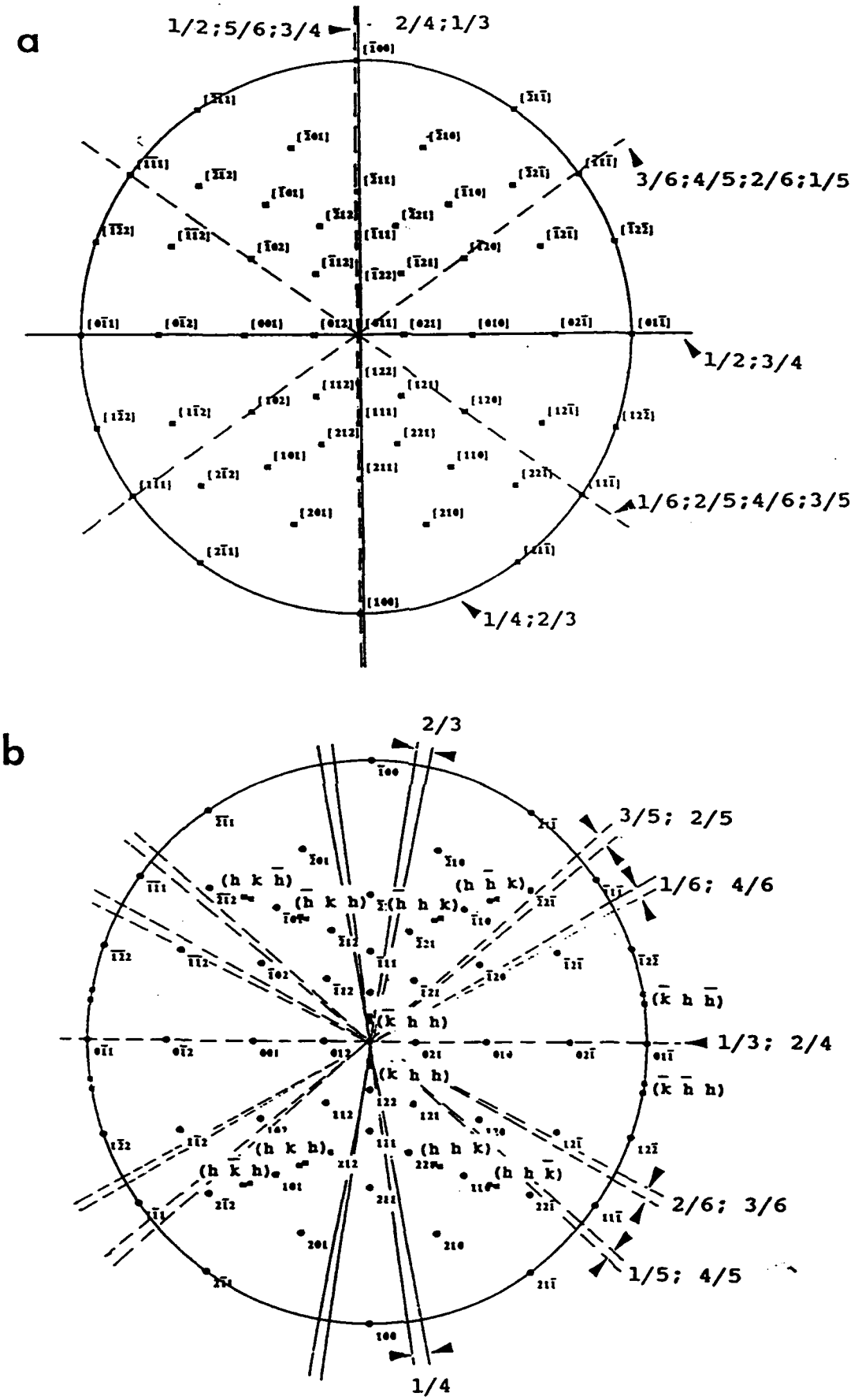
a
1/2;5/6;3/4
2/4;1/3
3/6;4/5;2/6;1/5
1/2;3/4
1/6;2/5;4/6;3/5
1/4;2/3
b
2/3
3/5; 2/5
1/6; 4/6
1/3; 2/4
2/6; 3/6
1/5; 4/5
1/4

Fig. A3

6

Submitted to Acta Met.

Transformation of BCC and B2 High Temperature Phases to HCP and Orthorhombic Structures in the Ti-Al-Nb System. Part II: Experimental TEM study of microstructures.

L. A. Bendersky and W. J. Boettinger

Metallurgy Division
National Institute of Standard and Technology
Gaithersburg MD 20899, USA

ABSTRACT

In Part I of this paper possible transformation paths that involve no long range diffusion and their corresponding microstructural details were predicted for Ti-Al-Nb alloys cooled from the high temperature BCC/B2 phase field into close-packed orthorhombic or hexagonal phase fields. These predictions were based on structural and symmetry relations between the known phases. In the present paper experimental TEM results show that two of the predicted transformation paths are indeed followed for different alloy compositions. For Ti-25Al-12.5Nb (at%), the path includes the formation of intermediate hexagonal phases, A3 and DO_{19}, and subsequent formation of a metastable domain structure of the low-temperature O phase. For alloys close to Ti-25Al-25Nb (at%), the path involves an intermediate B19 structure and subsequent formation of a translational domain structure of the orthorhombic (O) phase. The path selection depends on whether B2 order forms in the high temperature cubic phase prior to transformation to the close-packed structure. This paper also analyzes the formation of a two-phase modulated microstructure during long term annealing at 700°C. The structure forms by congruent ordering of the DO_{19} phase to the O phase, and then reprecipitation of the DO_{19} phase, possibly by a spinodal mechanism. The thermodynamics underlying the path selection and the two-phase formation are also discussed.

1. Introduction

In Part I [1] of this paper we have analyzed different phase transformation sequences and corresponding microstructures that may be possible in the course of transformations with no long-range diffusion (partitionless) of a BCC-based high temperature phase to close-packed phases for Ti-Al-Nb alloys. The analysis is based only on the crystallography of the equilibrium low and high temperature phases existing near the $(Ti,Nb)_3Al$ binary join. Based on formal maximal group/subgroup relations, possible connections spanning the high and low temperature phases (corresponding to high and low symmetry) have been found. These relations give different sequences involving symmetry-decreasing subgroups and one symmetry increasing-supergroup that might be considered to represent possible transformation paths. The transformation paths involve intermediate transitional structures, possibly metastable or unstable.

Assuming that the formal transformation steps actually occur as phase transitions, different transformation paths will result in different sequences of domain formation, i.e., in different final microstructures. The final single phase microstructures can be distinguished by the type and hierarchy of domain interfaces. Analysis of the interfaces is essential for understanding the transformation path, and is the major subject of this paper.

Transformation paths, derived from group/subgroup relations, can only be applied to transitions where no long range diffusion occurs, i.e. when a single phase transforms to a single phase of the same composition. For equilibrium transformation in multi-component systems, this can only occur at special compositions (consolute points) or for second or higher order transitions [2]. However partitionless transformations can also occur during cooling for first order transitions (for alloys with equilibrium multiphase fields) when sufficient undercooling of the high temperature phase is achieved that a limit of metastability is reached. This limit defines a temperature where the metastable undercooled phase becomes unstable and spontaneous

transformation occurs with no long-range diffusion requirement (congruent ordering) [3-5]. Experimentally, such congruent ordering could occur during continuous cooling if the cooling rate is fast enough to prevent competing transformations involving long-range diffusion. Clearly a mechanism for fast transformation kinetics must be available for these partitionless transformations; i.e., fast short-range diffusion in chemical (substitutional or interstitial) ordering or mobile defect motion producing the necessary atomic displacements in displacive (martensitic) ordering.

In this paper experimentally observed microstructures of three alloys from and near the pseudo-binary $(Ti,Nb)_3Al$ section will be analyzed. The alloys are Ti-25Al-12.5Nb (at%) (Alloy 1), Ti-25Al-25Nb (at%) (Alloy 2) and Ti-28Al-22Nb (at%) (Alloy 3). The alloys are close in composition to some alloys studied by different research groups in attempts to develop titanium aluminides for aerospace high temperature structural applications (see refs. 1 to 22 in [1]). We believe that the approach used here where the transitions are viewed as a sequence of symmetry changes will provide a unified view of the complex microstructural transitions in these materials. The microstructures studied, as represented by the distribution, type and morphology of interfaces induced by the transformations, will be compared with the interfaces predicted by the theoretical considerations of Part I [1]. The predictions represent idealized transformations, without taking into account such complications as the temporary coexistence of parent and transformed phases, or the mobility of the interfaces created. Therefore the predictions will be considered primarily as a point of reference for comparison to the details of the actual transformation process. The main goal of the paper is to demonstrate that the microstructures of the alloys studied correspond very closely to two of the possible transformation paths predicted:

for Alloy 1 - with intermediate hexagonal phases, ($Im\bar{3}m(A2) \rightarrow Cmcm(A20) \rightarrow P6_3/mmc(A3) \rightarrow P6_3/mmc(DO_{19}) \rightarrow Cmcm(O)$),

for Alloys 2 & 3 - with an intermediate orthorhombic B19 structure ($Pm\bar{3}m$(B2) → Pmma(B19) → Cmcm(O)).

In addition to the study of the diffusionless transformations, the effect of prolonged annealing, which results in a compositional phase separation, has been also investigated for the Ti-25Al-12.5Nb alloy. In this case the mechanism of microstructure formation becomes clear when the thermodynamic principles of both ordering transformations and phase separation in systems where both order and composition parameters variables are used [3,5].

2. Experimental

2.1. Specimen preparation

Three alloys with the compositions Ti-25Al-12.5Nb (at%) (Alloy 1), Ti-25Al-25Nb (at%) (Alloy 2) and Ti-28Al-22Nb (at%) (Alloy 3) were prepared by arc melting. A minimum of ten remelts was necessary to ensure mixing of the components. All samples received a homogenization treatment at 1400°C for three hours in a vacuum tight furnace under 2/3 atm of gettered Ar. During heat treatment samples rested on a Y_2O_3-coated Al_2O_3 substrate supported on a moveable pedestal which could be lowered out of the hot zone of the furnace into a lower chamber. The cooling rate of the samples during such cooling was estimated to be about 400°C/min. SEM microprobe of these samples using elemental standards gave the following compositions: (Alloy 1) Ti-24.7Al-12.6Nb (at%) (Alloy 2) Ti-23.2Al-25.8Nb (at%); and (Alloy 3) Ti-27.9Al-22.8Nb (at%). Typical oxygen, nitrogen and hydrogen levels for this procedure were less then 500, 350, 40 wppm, respectively as determined by inert gas fusion (O, N) and vacuum hot extraction (H).

For the study of the partitionless transformations, samples were examined after additional annealing at 1100°C for 4 days and cooling to room temperature at two rates: at about 400°C/min in the furnace described above or by water quenching. These latter samples were heat treated in another furnace in evacuated and He-backfilled quartz tubes after being wrapped in Ta foil. As the results will show, the 400°C/min cooling rate was slow enough to permit complete transformation to the orthorhombic phase for Alloy 1. However only partial transformation occurs for Alloys 2 and 3. Therefore samples of these two alloys were given a subsequent annealing at 700°C for 15 min in quartz tubes. To determine the phase equilibrium at 700°C, the samples annealed at 1100°C were additionally annealed at 700°C for different lengths of time, up to 26 days in quartz tubes.

TEM foils were prepared by a standard twin-jet electropolishing procedure using a 300 ml methanol, 175 ml n-butanol and 30 ml $HClO_4$ electrolyte at 0°C. Optical metallography was performed by mechanical polishing and subsequent etching with Kroll's reagent.

2.2 The problem of artifact structures in Ti alloy thin foil (TEM) specimens.

The formation of artifact structures in different Ti alloys during electropolishing of TEM specimen has been discussed in the literature [6-13]. Charging of thin foils by hydrogen in the course of electrochemical thinning was found to be possible. The concentration of hydrogen may be sufficient to cause formation of either different hydrides and/or hydrogen-stabilized martensites. Artifact structures such as fcc, fct, hcp and orthorhombically distorted α_2 have been reported. The amount of the accumulated hydrogen depends on a specimen's thickness prior to electropolishing, and on the type and temperature of the electrolyte. It was claimed [7] that the charged hydrogen may escape from a thin foil after electropolishing, unless the foil is protected by an oxide layer. If hydrogen escapes the specimen, the reversion of the hydride may

result in the formation of 1/2<111> dislocation loops in the BCC phase.

In order to be confident that microstructures observed by TEM in this study do not contain the described artifacts, several TEM specimens of the same material were prepared for comparison by two additional thinning techniques, presumably not affected by hydrogen contamination. The first technique was twin-jet electropolishing with non-acid electrolyte containing a solution of $CaCl_2$ in methanol [14]. The second technique was mechanical grinding to a 30 μm thickness with a dimpler followed by ion-milling. Specimens prepared by these two techniques show microstructures similar to those of the specimens prepared by an acid-based electrolyte.

3. High-temperature phases: microstructure after water quenching from 1100°C.

The identity of the high temperature phase was evident from the microstructural examination of specimens water quenched from 1100°C. Optical examination revealed large equiaxed grains that appeared a single phase. According to selected area electron diffraction (SAD) at room temperature, the phase has B2 order for all three alloys.

For Alloy 1 the presence of a high density of anti-phase boundaries (APBs) (observed using a dark-field image with a superlattice 100 reflection) suggests that at 1100°C the high temperature phase was disordered BCC. The cooling rate during quenching was fast enough to prevent formation of the low temperature phases but not the ordering and coarsening of the anti-phase domains (APDs). Typical of B2 ordering, the APBs have a two-domain interconnected morphology with isotropically curved interfaces. From these studies it is not clear whether the BCC to B2 transition in the Ti-Al-Nb system is first order (with a BCC+B2 two phase field) or second order.

For Alloys 2 and 3 no APBs due to the BCC→B2 ordering were observed after

quenching. This fact suggests that the B2 order for these compositions exists at 1100°C (in fact up to 1400°C [15, 16]).

We have referred here to the quenched-in phase as being cubic B2. However this is strictly correct only if local displacements of atoms from positions of cubic symmetry are ignored. The effect of such displacements are readily observed as an overall "tweed" contrast in TEM images for all three alloys (This tweed is known in the literature for different alloy systems as pre-martensitic, or pre-transformation phenomena [17]). Due to these displacements, the SAD patterns from all three alloys contain diffuse scattering: distortion of the cubic reflections, streaking along $<011>^*$ and $<1\bar{1}2>^*$ directions, and loci of diffuse intensity close to $1/2<011>^*$ and $1/2<1\bar{1}2>^*$ positions in reciprocal space. As will be seen later, these are the positions where reflections from different crystallographic variants of the O phase will occur. For Alloy 3 additional weak diffuse scattering near $1/2<111>^*$ positions is probably due to ω-type distortions [18,19]. In addition to the "tweed", defects similar in contast to dislocation loops are seen occasionally for all three alloys and are believed to be related to the nucleation mechanism of the low temperature phases.

4. Microstructures due to the diffusionless transformation of the high temperature cubic phase to the orthorhombic O phase.

4.1 Microstructure of Alloys 2 and 3 corresponding to the transformation path $Pm\bar{3}m$(B2) → Pnma(B19) → Cmcm(O).

From the transformation paths suggested by the symmetry considerations in Part I of the paper [1], the $Im\bar{3}m$(A2) → $Pm\bar{3}m$(B2) → Pnma(B19) → Cmcm(O) path (3.2) is the only one expected when B2 ordering precedes the transition to the close-packed structure. Here we will

demonstrate that the experimental evidence from TEM supports this formal supposition for both Alloys 2 & 3 which have the B2 structure as the high-temperature parent phase. The observed distribution and type of interfaces of the O phase correspond to those shown schematically in Fig. 9 of Ref. [1], with the exception that this schematic presumed the parent phase was BCC and thus includes the APBs due to the BCC→B2 ordering. Microstructures similar to those observed here, but with B2 APBs, have been observed recently for a Ti-24Al-15Nb (at%) alloy where the parent phase was indeed disordered BCC (Ref. 8 from [1]).

4.1.1. Formation of the plate-like domains of the O phase

For Alloys 2 and 3 the kinetics of transformation of the B2 phase to a low temperature phase was found to be relatively sluggish as is evident from optical micrographs, Fig. 1a, b. The micrographs show regions of partially transformed material, differing in their volume fraction according to the differences in cooling rates of the specimens. Annealing of the water quenched specimens (with 100% retained B2 phase) at 700°C for 15 min. was sufficient to produce complete transformation (Fig. 1c). Apparently the transformation proceeds by copious nucleation where the transformed regions grow uniformly outward until impingement. The transformation is partitionless without measurable difference in composition between the parent and transformed regions.

From TEM observations of the partially transformed specimens it is evident that the transformed regions have a complex microstructure of plate-like domains (Fig. 2). The smallest plates typically form an alternating sequence packed in a region named a polytwin in Part I. The polytwins themselves often have a plate-like shape and alternate with similar polytwin plates, as shown in Fig. 3a, b. Growth of the plate-like structure into the B2 phase matrix appears to have a common but ragged and diffuse transformation front (Fig. 2). Only occasionally were

independently grown single-domain plates observed. Therefore in most cases the growth of a plate is not independent but is correlated with the formation and growth of neighboring plates with variants able to accomodate transformation strains.

SAD (Figs. 3c and 4) combined with convergent beam (CB) electron diffraction from large plates that were occasionally observed and powder neutron diffraction [20] confirm the plates to be the O phase. No other phases were found in the samples that were continuously cooled or in those annealed at 700°C. From the SAD patterns of Figs. 4 a lattice correspondence between the B2 and the O phase is evident as the common one for BCC and close-packed structures [21]:

$$[001]_O \parallel [011]_c \text{ and } [100]_O \parallel [100]_c \qquad (1)$$

(c - cubic; o - orthorhombic).

The correspondence is the same as that used for the subgroup scheme of Part I. It gives six rotational variants of the orthorhombic phase (either B19 or O for path 3.2), each with its basal $(001)_O$ plane parallel to one of the six $\{110\}_c$ planes of the parent cubic structure. Small mutual rotations of the contacting variants are necessary to accommodate the transformation strains (self-strains) by creating stress-free interfaces (SFIs), as discussed in [1]. This results in an orientation relationship (OR) of domains slightly different from (1) and close to the OR known in the literature as the Burgers OR [21].

The microstructure has an average cubic symmetry due to the presence of all six rotational variants of the O phase. The symmetry is clearly seen in the SAD patterns of Fig. 4a, b, c showing (a) 4mm, (b) 3mm and (c) 2mm average Laue symmetries corresponding to the major zone axes of the cubic symmetry, $[100]_c$, $[111]_c$ and $[110]_c$. These average axes indicate the orientation of the parent (transformed) B2 phase lattice.

4.1.2. Stress accommodating morphology of the O phase.

All interfaces between the pairs of variants in and between the polytwin plates are expected to be SFIs, as discussed in Part I [1]. The pair of polytwins shown in Fig. 3 will be analyzed in order to demonstrate that the interfaces are indeed described as SFI. The analysis will be performed in coordinates of the parent cubic lattice. Two polytwin plates are seen in Fig. 3a, with the planar A-A interface between them (for a $[011]_c$ orientation of the thin foil, (Fig. 3c)). The A-A interface has $(01\bar{1})_c$ orientation and is "edge-on". The individual plates in the polytwins have nearly parallel inclined interfaces (B-B and C-C sets) between the variants. The interface traces are approximately $\pm 45°$ to the $[100]_c$ direction. The plates in each polytwin are nearly mirror related across the $(01\bar{1})_c$ plane, and therefore there is an apparent continuity of the plates across the A-A polytwin interface.

Dark field imaging with the 020_O reflection (Fig. 3b) proves that the plates labeled 5 and 5' in Fig. 3a from each polytwin belong to the same variant 5 (the variant labeling follows the scheme described in [1]). The variant is oriented with $[001]_O$ parallel to $[011]_c$ (the beam direction) and the 020_O, 200_O and 110_O reflections of the variant do not overlap with reflections from the other variants. Misorientation between the 5 and 5' plates (around a common $[001]_O$) is measured as about 10° (Fig. 3c). According to microdiffraction, the remaining two plate orientations are close to $<212>_O$ and belong to any pair chosen from among the 1, 2, 3 or 4 (not 6) variants [1].

If the structure shown in Fig. 3 is coherent and strain accommodating, the observed interfaces are expected to correspond to the SFIs calculated in [1]. Referring to Fig. A.3 in Appendix B of [1] (reproduced here as Figs. 3d,e) where the traces of the SFIs for the $[011]_c$ zone axis are given, we conclude (according to the measured angle of the trace and the widths of the B-B and C-C interface projections) that the B-B interface corresponds to $hh\bar{k}$ (or $hk\bar{h}$)

between variants 3/5 (or 2/5) and the C-C interface corresponds to $h\bar{k}h$ (or $h\bar{h}k$) between variants 1/5 (or 4/5) (Fig. 3d, e). The ambiguity of choice between the pair of variants in the polytwin plate can be resolved if one determines what side of the projected B-B and C-C interfaces intersect the upper and lower surfaces of the TEM foil. In order to have the line of intersection of the B-B and C-C planes lie within the A-A plane (as Fig. 3 suggests), the combination of variants must be either 4/5 and 2/5 or 1/5 and 3/5. These interfaces are irrational (twins of the II kind) and therefore their exact orientation depends on the lattice parameter of the orthorhombic phase at the temperature of transformation (Fig. 3e shows the spread of possible orientations for lattice parameters varying between Ti_2AlNb and DO_{19} phases, see ref. [1]).

The A-A interface consists of alternating segments that are structurally different. One type of segment is a $(01\bar{1})_c$ interface between 4 (or 1) and 2 (or 3) variants. This is a symmetric SFI (twin of the I kind). The second type of segment separating variant 5 (5') misoriented plates is a low angle symmetric boundary (~10°) which may be relaxed by forming a dislocation wall.

All high angle interfaces in the polytwin microstructure in Fig. 3 are thus shown to be SFIs. Observation of such an elastic energy accommodated arrangement of plates suggests an interacting process during their formation, i.e. a process where the presence of certain combination of variants in one polytwin plate influences the formation of variants in a neighboring plate. Formation of a strain accommodating arrangement of twins, of both the I and II kind, is an important phenomena in martensitic transformations [22-24].

4.1.3. Substructure of the O phase primary plates.

Closer examination of Fig. 3a, b reveals a substructure of a relatively high density of interfaces (defects) inside the plates of different variants of the O phase. The interfaces must be

of a translational type because they do not affect the positions of the reflections in each single variant. Dark field imaging was used to determine the R value using standard $\mathbf{R}\cdot\mathbf{g} = n$ ($n=0,\pm1,\pm2..$) invisibility criteria (R is the translation vector between two domains separated by the interface, g is an operating dark field reflection). Figs. 5a, b, c show three dark field images taken from a single variant oriented close to the $[110]_O$ zone axis (SAD pattern in Fig. 5d). Two types of interfaces, different in their displacement vector R and morphology, are seen in these images. The presence of these interfaces is in accord with transformation path 3.2 in [1].

The interfaces of the first type, with a wavy APB appearance, are visible with the superlattice reflections of the O phase, e.g., $\bar{1}10_O$ in Fig. 5b, but are invisible with the fundamentals, e.g., $\bar{2}20_O$ and $\bar{4}40_O$ in Fig. 5a and 5c. The second type has a distinct faceted appearance (clearly seen in Fig. 5a) and is visible with both the superlattice and some fundamental reflections, e.g., $\bar{1}10_O$ and $\bar{2}20_O$ (Fig. 5a,b). Both types are invisible with 002_O. For the $\bar{4}40_O$ reflection the faceted interfaces has only residual contrast (Fig. 5c). The experimental results on the visibility for both interfaces are summarized and analyzed for various displacement vectors in Table I.

TABLE 1

Experimental dark field visibilities and phase factors (R·g) for two types of interfaces forming substructure in the O phase in Alloys 2 and 3 (both g and R are in the O phase coordinates).

g (used in dark field)	002	$\bar{1}10$	$\bar{2}20$	$\bar{1}11$	$\bar{4}40$	400
Type I (curved interfaces)	i	v	i	v	i	i
R·g (R=1/2[0 1 0] or	0	1/2	1	1/2	2	0
R=1/2[1 0 0])	0	-1/2	1	-1/2	0	2
Type II (faceted interfaces)	i	v	v	v	r	i
R·g (R=1/4[0 1 2] or	1	1/4	1/2	1/4	1	0
R=1/4[0 1 0])	0	1/4	1/2	1/4	1	0

i - invisible; v - visible; r - residual.

Analysis of the R·g product for the first type suggests that the displacement vector R is $1/2[010]_O$. (C-centering of the Cmcm space group of the O phase makes the $1/2[100]_O$ vector an equivalent one.) This displacement vector is close to the antiphase vector between two differently ordered $4c_1$ and $4c_2$ sites in the pseudo-hexagonal $(001)_O$ plane of the O phase (Fig. 6a). Such ABPs may result after ordering of the B19 orthorhombic structure to the O phase structure (leading to a doubling of the a, b unit cell parameters) and are expected in the last step of the transformation path 3.2. The ordering requires a separation of the mixed (Al,Nb) site of the B19 (and B2) structure into predominantly Al ($4c_1$) and Nb ($4c_2$) sites in the O phase (see

Fig. 3 of [1]). Such ordering will produce a two domain interconnected morphology with no triple junctions as schematically shown in Fig. 9 of [1]. The morphology is similar to that seen in Fig. 5b, where the curved APB interfaces appear as either closed loops (with enclosed volume) or are attached to other interfaces. The presence of the $1/2[010]_O$ APBs provides the only evidence for the existence of the possible transient B19 structure.

The invisibility of the second type of interfaces with the 002 reflection suggests that their displacement vector, R_2, has a z-component that is either 0 or 1/2. Other visibility conditions (Table I) correspond to the $[0\ 1/4\ 1/2]_O$ (or $[0\ 1/4\ 0]_O$) displacement vector of a two-domain structure. Indeed, as Fig. 5a shows, no triple junctions of the faceted interfaces are seen, and the interfaces form either interconnected or closed volumes. The $[0\ 1/4\ 1/2]_O$ vector in the smaller unit cell of the orthorhombic Cmcm(A20) or Pmma(B19) structures (with a and b parameters half of the O phase) corresponds to an unique vector $[0\ 1/2\ 1/2]_{B19}$. As it has been discussed in [1], such displacement between domains is expected for the B2 to B19 transition, and therefore the faceted interfaces are due to the first step of the 3.2 transformation path.

The B2 to B19 (or similarly BCC to A20) transition is of a displacive type, with both homogeneous and heterogeneous (shuffle) transformation strain components [1]. The homogeneous strain determines the orientation of the six twin variants of the orthorhombic or hexagonal structure, as was discussed in section 4.1.1. The translational $[0\ 1/2\ 1/2]_{B19}$ domains result from shuffles acting in opposite directions ([25], Ref. 8 in [1]). An interface between such translational domains has the features of a stacking fault, and therefore structural relaxation of such interfaces is expected. This is supported by the observation of residual contrast for the $\bar{4}40_O$ reflection (Fig. 5c) suggesting small displacements in addition to $[0\ 1/4\ 1/2]_O$. (However some contribution to the contrast from the $\bar{2}20_O$ reflection to the $\bar{4}40_O$ in a systematic excited row cannot be ruled out.) The faceted interfaces were analyzed by trace analysis in order to find their orientations. Two different crystallographic planes for the facets were found: the basal

$(001)_O$ and close to the $\{221\}_O$.[1]

When the twin plates are thin, the faceted interfaces appear as a sequence of stacking fault planes rather than domain boundaries. Dark field imaging of the interfaces (Fig. 7a) shows that they are $(001)_O$ planes. The APBs are seen as stretched between the twin boundaries (Fig. 7b), probably because of surface energy considerations (balance of interfacial energies of APB and twin-type interfaces at a triple-junction).

4.2 Microstructure of Alloy 1 corresponding to the transformation path $Im\bar{3}m(BCC) \rightarrow Cmcm(A20) \rightarrow P6_3/mmc(A3) \rightarrow P6_3mmc(DO_{19}) \rightarrow Cmcm(O\ phase)$.

Alloys with compositions close to Alloy 1 exist at high temperature as a disordered BCC phase [15,16,26]. According to the theoretical considerations of [1], if the BCC does not order to B2 prior to the displacive transition to a close-packed structure, two transformation paths, 3.1 and 3.3, are possible. Here we will show evidence supporting the transformation path 3.1 for Alloy 1:

$$Im\bar{3}m(BCC) \rightarrow Cmcm(A20) \rightarrow P6_3/mmc(A3) \rightarrow P6_3mmc(DO_{19}) \rightarrow Cmcm(O\ phase).$$

The main feature of the path is the formation of intermediate hexagonal symmetry phases. This causes the O-phase rotational variants to be related to each other not only by the cubic symmetry of the parent phase but also by hexagonal symmetry.

4.2.1. Transformation to the coarse needle-like structure during continuous cooling.

For Alloy 1 the transformation kinetics are significantly faster than are those for Alloys 2

[1]Similar crystallographic planes have been observed in the 2H martensite of Cu-Al alloys. Because the unit cell of the martensite is different from that described here, the indices of the observed planes are different) [25].

and 3, and therefore cooling from 1100°C to room temperature at a rate of 400°C/min was slow enough to complete the transformation of the high temperature phase to the close-packed structure. The transformed microstructure has a morphology resembling a martensite structure when observed by optical metallography (Fig. 8). The TEM micrograph in Fig. 9 shows in more detail that the morphology is rather needle-like. The needles have very irregular interfaces (not resolved in Fig. 8), and no crystallographic habit plane. This is in great contrast to the mostly regular plate-like structure seen in Alloys 2 & 3. The blocky grains surrounding an elongated needle in Fig. 9 are probably cross-sections of needles oriented with their long axes parallel to the electron beam direction. The wavy character of the interfaces seems to be the result of impingement of needles during their independent growth. In a few regions, grains were found to be separated from each other by a thin layer identified as the BCC phase (Fig. 10). Enrichment of Nb in the BCC layer was detected by EDS for this and similar alloys [26]. The observed morphology suggests that near impingement, some diffusion does occur during the growth of the needles. We presume that in these regions the competing transformation with long range diffusion is marginally possible. Thus the cooling rate of these samples is on the lower limit for the dominance of the partitionless transformation.

Selected area diffraction from individual needles corresponds to the reciprocal lattice of the DO_{19} ordered hexagonal structure. The orientation relationship between different variants of the hexagonal structure and the previously existing BCC phase is clear from Fig. 11, which is taken from three grains that form a triple junction. Despite the different morphologies for Alloy 1 compared to Alloys 2 & 3, their SAD patterns are quite similar (Fig. 6b and 11). The present pattern is indexed as three variants of the DO_{19} phase (h) with $[10\bar{1}0]_h \| [111]_c$ and $(0001)_h \| (110)_c$. Similar to Alloys 2 and 3 this is the Burgers orientation relationship [21]. (Note that according to the structural relation between the DO_{19} and the O phases, $(0001)_h \rightarrow (001)_O$ and $[10\bar{1}0]_h \rightarrow [110]_O$).

Close examination of the SAD patterns reveals splitting of the spots and diffuse streaking in and normal to the $(0001)_h$ plane. These diffraction effects come from the substructure inside the needles, which is seen as dark contrast in Fig. 9. The nature of the spot splitting indicates the existence of orthorhombic distortions in the basal plane of the DO_{19} phase and suggests the presence of O phase domains. Therefore the hexagonal indexing that we use describes only the average symmetry and orientation of the needles.

The needle-like structure is not a stress accommodating plate-like structure as observed in Alloys 2 and 3 even though the orientation relationships are similar. This difference may perhaps be understood by considering the possibility that the transformation of the BCC phase of Alloy 1 may occur at higher temperature than Alloys 2 & 3 as indicated by the occurrence of some small level of long-range diffusion near impingement. At higher temperatures the ductility of the phases may be sufficient to accommodate the transformation stresses by plastic deformation and negate the requirement to form a stress accommodating structure. Indeed a dependence of morphology on cooling rate has been observed for alloys similar in composition to Alloy 1 [26] that range from those accommodating stress at high cooling rates to those similar to the morphologies described here at lower cooling rates. The occurrence of similar OR's in both diffusionless and diffusion controlled (precipitation) transformations is well known and is in fact observed in some other Ti-Al-Nb alloys [16].

4.2.2. Substructure of the needles.

Similar to the result found for Alloys 2 & 3, the substructure of the needles has two types of lattice defects associated with the translational domains. The defects (domain interfaces) have been imaged in dark field with different reflections belonging to three zone axes, $[11\bar{2}0]_h$, $[01\bar{1}0]_h$ and $[\bar{1}210]_h$, by tilting a single grain around the $[0001]_h$ direction, starting from the

$[11\bar{2}0]_h$ zone axis (Fig.12). As with Alloys 2 & 3, two types of defect are morphologically distinct: one has curved isotropic APB-type interfaces (Fig. 12h) and the other has planar interfaces. However the planar defects only occur in $(0001)_h$ planes for Alloy 1 (Fig. 12f) as compared to two different crystallographic planes for Alloy 2&3. The observed visibility conditions for both types of interface are summarized and analyzed for various displacement vectors R in Table 2.

The wavy isotropic interfaces are APBs between the domains formed by ordering of the disordered hexagonal structure to the DO_{19} structure [27]. According to Table 2 the APBs have $R=(1/6)<11\bar{2}0>_h$ displacement vectors (Fig. 6b). For the three such R vectors equivalent under the 6-fold symmetry operation, there are three different APBs and four distinct translational domains. (Compare this to the single APB and two domains observed in Alloys 2 & 3). When the APBs are imaged with superlattice reflections, only two of the three APBs are visible according to the R-g conditions. Therefore no triple junctions of the APBs can be seen. Comparison of the two dark field micrographs shown in Figs. 12e and 12h, show that some APB segments are visible for both of these imaging conditions (for $R=1/6[\bar{1}2\bar{1}0]_h$), while some segments are visible for only one of the imaging conditions in accord with Table 2.

The second type of defect, with a planar morphology, has the nature of a stacking fault displacement. These defects give rise to the $[0001]^*$ streaking. Invisibility of these defects was found invariably for the 0002 reflection and occasionally for the $1\bar{2}10$ and $2\bar{4}20$ reflections. The reason for this was found using dark field imaging of the same area oriented for different zone axes. Invisibility of the defects for the $[01\bar{1}0]$ zone axis orientation with 0002, $\bar{2}110$ and $\bar{4}220$ (Fig. 12g, h, i, respectively) and their visibility for $[11\bar{2}0]$ and $[\bar{1}210]$ zone axes orientations with $1\bar{1}00$, $2\bar{2}00$ (Fig. 12e, f, respectively) and $10\bar{1}0$ and $20\bar{2}0$ (Fig. 12k, l, respectively) suggest that the displacement vector R is $1/4[01\bar{1}0]_h$ as analyzed in Table 2. Because of the hexagonal symmetry of the DO_{19} phase, there are two additional crystallographically equivalent directions

$(1/4[10\bar{1}0]_h$ and $1/4[1\bar{1}00]_h)$ for the **R** vector. Regardless of this equivalence, the simultaneous invisibility of all planar defects for $10\bar{1}0$ and $20\bar{2}0$ for the $[01\bar{1}0]$ zone axis orientation (Fig. 12 h, i) proves that only one such **R** vector $(1/4[01\bar{1}0]_h)$ is present. Such deviation from hexagonal symmetry suggests that the preferred direction (or orthorhombic symmetry) existed prior to the formation of the hexagonal symmetry, which is consistent with the initial step of the path 3.1.

TABLE 2

Observed dark field visibility and calculated phase factor ($\mathbf{g}\cdot\mathbf{R}$) for two possible types of interface forming the substructure of the O phase in Alloy 1 (both **g** and **R** are in the DO_{19} phase coordinates).

g (used in dark field)	0002 (d,g)	$1\bar{1}00$ (e)	$2\bar{2}00$ (f)	$\bar{2}110$ (h)	$\bar{4}220$ (i)	$10\bar{1}0$ (k)	$20\bar{2}0$ (l)
curved interfaces	i	v	i	v	i	v	i
$\mathbf{R}\cdot\mathbf{g}$ ($\mathbf{R}=1/6[2\bar{1}\bar{1}0]$)	0	1/2	1	-1	-2	1/2	1
$\mathbf{R}\cdot\mathbf{g}$ ($\mathbf{R}=1/6[\bar{1}2\bar{1}0]$)	0	-1/2	-1	1/2	1	0	0
$\mathbf{R}\cdot\mathbf{g}$ ($\mathbf{R}=1/6[11\bar{2}0]$)	0	0	0	-1/2	-1	1/2	1
faceted interfaces	i	v	v	i	i	v	v
$\mathbf{R}\cdot\mathbf{g}$ ($\mathbf{R}=1/4[1\bar{1}00]$)	0	1/2	1	3/4	3/2	1/4	1/2
$\mathbf{R}\cdot\mathbf{g}$ ($\mathbf{R}=1/4[10\bar{1}0]$)	0	1/4	1/2	-3/4	-3/2	1/2	1
$\mathbf{R}\cdot\mathbf{g}$ ($\mathbf{R}=1/4[01\bar{1}0]$)	0	-1/4	-1/2	0	0	1/4	1/2

i - invisible; v - visible

The interfaces identified with the $1/4[1\bar{1}00]_h$ displacement vectors are similar to those of Alloys 2 & 3 and together with the similar OR indicate a similar displacive transition. In the case of Alloy 1 the phases are disordered: $Im\bar{3}m$(BCC) → Cmcm(A20) → $P6_3/mmc$(A3) whereas for Alloys 2 & 3 the path is ordered: $Pm\bar{3}m$(B2) → Pmma(B19). The presence of the disordered hexagonal A3 as an intermediate state is established by the presence of the $1/6<11\bar{2}0>_h$ APBs, which can only be due to the $P6_3/mmc$(A3) → $P6_3mmc$(DO_{19}) transition.

4.2.3. Congruent ordering of the DO_{19} to O phase.

The presence of domains of the O phase (as a part of the primary needle substructure) is manifest in the splitting of the DO_{19} reflections and in the complex contrast showing $[0001]_h$ directionality as seen in Figs. 12f, i, l. The domains with plate-like morphology can only clearly be seen in the $[0001]_h$ zone axis orientation where the domain interfaces are "edge-on", as shown in Fig. 13a. (In order to obtain maximum contrast, the TEM foil must be slightly off of the exact $[0001]_h$ zone axis in order to have a different excitation error and accordingly contrast for different domains.) In Fig. 13 two directions of interface trace, $<1\bar{1}00>_h$ (A-A) and $<11\bar{2}0>_h$ (B-B), are observed corresponding to $(11\bar{2}0)_h$ and $(1\bar{1}00)_h$ interfacial "edge-on" planes. The SAD patterns (Figs. 13b, c) were taken from areas with only one type of interface, A or B in Fig. 13a respectively. The corresponding SAD patterns are given in Figs. 13b and 13c. The patterns show splitting and streaking of reflections in directions normal to the interfaces. The SAD patterns from Fig. 13 can be reasonably well explained as belonging to two variants of the O phase, with coinciding (a) $(130)_{O(1)} \| (1\bar{3}0)_{O(2)}$ planes (A-A interfaces) and (b) $(110)_{O(1)} \| (1\bar{1}0)_{O(2)}$ planes (B-B interfaces) as seen in Fig. 14. SAD from a region of bright uniform contrast (upper left side of Fig. 13) shows the hexagonal symmetry of the pattern without the splitting of the peaks. This suggests that this region is untransformed DO_{19} phase.

In a single grain (needle) most often only one orthogonal set of such interfaces (plates) was observed, e.g. $(1\bar{1}00)_h$ and $(11\bar{2}0)_h$ in Fig. 13. Neighboring grains in the same $[0001]_h$ orientation have similar orthogonal sets of plates but rotated 60° or 120°. Occasionally the rotated sets are observed in different locations of the same grain, as is seen in Fig. 15. These sets of interfaces, related to each other by the hexagonal symmetry of the parent phase, belong to other pairs of variants of the orthorhombic phase. The presence of the O phase domains related to each other by the hexagonal symmetry clearly indicates the occurrence of the last step in the transformation path 3.1; viz., the DO_{19} to O phase transition. As was discussed in [1], the $\{1\bar{1}00\}_h$ and $\{11\bar{2}0\}_h$ interfaces are SFIs accommodating transformation strains in the hexagonal to orthorhombic symmetry transitions. In this transition the SFIs are always symmetric.

5. Decomposition of the metastable O phase in Alloy 1 after prolonged annealing at 700° C.

Annealing of specimens of Alloy 1 at 700°C for 26 days produces a third level of microstructure finer than that produced during the initial cooling from 1100°C. The coarser two levels of microstructure (shown in Figs. 9 and 13) are retained during this heat treatment.[2] The third level is contained within the second level shown in Fig. 13. A typical example of the second and third level microstructure is shown in Fig. 16. The structure within each first level needle remains coherent and preserves the average hexagonal symmetry and the ordering of the transient parent DO_{19} of path 3.1 as the SAD pattern in Fig. 16e shows.

Different dark field images (Fig. 16b, c, d) taken with the same diffuse $1\bar{1}00$ reflection but in a slightly different TEM foil orientation reveal fine scale domains and their interfaces

[2] The microstructure produced during cooling is more resistant to coarsening and recrystallization as compared to Alloys 2 & 3 under the same annealing conditions [16].

(tilting changes the excitation errors for different domains). Therefore the diffuse reflections are in fact clusters of a few reflections very close to each other (additional diffuse intensities from the presence of a high density of interdomain interfaces and lattice strain make it difficult to resolve them). The SAD pattern, Fig. 16e, can be explained by a structure consisting of either three variants of the O phase formed from the DO_{19} phase (as was observed in the specimens cooled from 1100°C, Fig. 13) or coexisting domains of the O and DO_{19} phases.

Because of experimental difficulties related to the similarity of the reciprocal lattices of the phases, the fineness of the domains and possible elastic distortions due to the coherency of interfaces, we were unsuccessful in providing direct TEM evidence of the identity and distribution of the phases. Analysis of the broadening and position of peaks in a neutron diffraction pattern obtained from a specimen similar to that of Fig. 16 has indicated the presence of both O and DO_{19} phases (unpublished research, [20]). Indirect evidence for the phase constitution can be obtained by analyzing the possible orientations for strain-free coherent interfaces which would be expected between the O phase domain variants or between domains of the DO_{19} phase and a variant of the O phase.

For a domain structure of the O phase formed from the DO_{19} phase, as was shown in [1] and confirmed experimentally in 4.2, the interfaces have locked-in symmetry and have either $\{1\bar{1}00\}_h$ or $\{11\bar{2}0\}_h$ planes (of the average hexagonal lattice). For contacting domains of the O and DO_{19} phases, the interface orientations depend on the lattice parameters at the temperature of formation, and in general are irrational (non-symmetric). Because the c-parameters of the O and DO_{19} phases are similar [20,28], the interfaces are expected to contain the $[0001]_h$ direction.

Measurement of the directions of the interface traces with respect to the average hexagonal lattice in Fig. 16 are sufficient to establish a significant deviation from the $\{1\bar{1}00\}_h$ and $\{11\bar{2}0\}_h$ planes despite the relatively large measurement error due to the diffuseness and shortness of the interface segments. We consider this deviation as evidence for the existence of

a coexisting two-phase mixture. Such non-symmetric interfaces are often seen lying parallel within a second level plate where the neighboring second level plate also has non-symmetric parallel interfaces but with different orientation. The observation is illustrated in Fig. 17 a,b where two dark field images (using the same cluster of reflections, $(4\bar{4}00)_h$, but with different small tilts of the TEM foil) show two second level plates, A and B, separately. The interface between them has a zig-zag shape but on average is close to the $(11\bar{2}0)_h$ plane (Fig. 17 c). The zig-zag shape is formed by two segments of interfaces between the DO_{19} and O phase domains located in neighboring second level plates A and B. The segments planes also seem to be in irrational orientation. The interpretation of the distribution of domains and phases in the microstructure of Fig. 17 is depicted schematically in Fig. 18 a, b. Another plausible two-phase morphology of domains with SFIs is shown schematically in Fig. 18c (and perhaps microstructurally in Fig. 16). In this case the DO_{19} phase forms zig-zag ribbons traveling continuously through the second level plates in a modulated manner. The DO_{19} phase ribbon-like domains have internal low angle boundaries (dislocation walls) and faceted SFIs with two variants of the O phase.

Therefore, the variety of interface orientations observed in Fig. 16 is due to the fact that the initial structure consisted of a three variant domain structure of the metastable O phase as seen in Fig. 15 (second level microstructure). Subsequent reformation of the hexagonal DO_{19} phase takes place in the plate-like structure of the O phase (corresponding to A and B plates in Fig. 17). The DO_{19} phase layers can have two equivalent stress-free habit planes for each variant of the O phase. The DO_{19} phase appears as a modulation of plates inside the orthorhombic phase domains. Because the 700°C annealing results in reprecipitation of the DO_{19} phase, Alloy 1 is believed to be in an equilibrium two-phase field at this temperature.

6. Thermodynamics of phase formation.

At the present time, neither the phase diagram nor its associated free energy functions are sufficiently well know to permit a priori prediction of the T_0 curves for the various BCC/B2 to close-packed transitions in the Ti_3Al-Nb_3Al pseudobinary section. These T_0 curves would provide the thermodynamic framework necessary to understand the partitionless transformations observed in the present work; viz., why there is a change in path from 3.1 to 3.2 for $(Ti,Nb)_3Al$ alloys as the Nb content is increased (from that of Alloy 1 to Alloys 2 & 3). However we can use the transformation path results of this paper, some knowledge of the ordering tendencies of BCC and HCP systems, and the limited phase diagram results from other researchers to construct a self-consistent pseudobinary section, a T_0 diagram, and a 700°C free energy-composition diagram as shown in Fig. 19. It will be seen that paths including and excluding the intermediate HCP phase are quite reasonable. The construction of the three diagrams was performed concurrently, adjusting curves to be consistent with the details described below.

The free-energy composition diagram (Fig. 19c) should be viewed as a superposition of BCC-based ordering diagram (BCC and B2) and an HCP-based ordering diagram (HCP, $D0_{19}$, B19, and O). The relative heights (energies) of these two subsidiary diagrams have been adjusted to be consistent with the fact that Nb is a beta (BCC) stabilizer; i.e., the HCP phase has a lower free energy at small Nb content than the BCC phase, and conversely at higher Nb content. In fact the intersection of the BCC and HCP free-energy curves (which gives the T_0 composition for the BCC to HCP transition) and the intersection of the BCC and B2 curve (which gives the composition for the BCC to B2 transition) were adjusted to agree with the experimental results of this paper. The individual BCC-based and the HCP-based free energy diagrams are sketched using reasonable assumptions about the ordering tendencies and preferred stoichiometries for the BCC- and HCP-based phases in this alloy system.

The BCC-based diagram is quite simple and consists of BCC and B2 curves. The BCC → B2 transition is assumed to be second order and thus the B2 free energy curve merges smoothly with that of the parent BCC curve and no two-phase BCC+B2 field exists in the phase diagram. (Thus the T_0 curve and the ordering critical curve are the same). It is reasonable to assume that the composition range of B2 stability exits at intermediate Nb content, probably centered around the Ti_2AlNb composition for the following reason. The two sublattices (or Wyckoff sites) of the B2 structures of Ti-Al-Nb are known to be preferentially occupied by Ti and a mixture of (Al,Nb) respectively (Ref. 21 in [1]). In the absence of competing non-BCC-based phases, the maximum order is most likely to be centered along the region of the ternary system where the atomic percent of Ti is equal to the sum of the atomic percents of Al and Nb. This region for maximum B2 order and hence for maximum stability intersects the $(Ti,Nb)_3Al$ section under consideration here at the Ti_2AlNb composition.[3] The maximum in the ordering curve is 1400°C or higher [15].

The free energy curves for the HCP-based phases, A3, B19, $D0_{19}$, and O, are more complex. The HCP → $D0_{19}$, HCP → B19, B19 → O and $D0_{19}$ → 0 transitions are all required to be first order transitions under equilibrium conditions [29]. For first order transitions, shapes for free energy vs. composition curves that contain end points and concave curvature have been described in detail by Soffa and Laughlin [5] and this shape was used for the orthorhombic ordering in Fig. 19c. The $D0_{19}$ and orthorhombic Ti_2AlNb phases are assumed to be the equilibrium phases at 700°C as indicated by the lowest common tangent, giving a tie line that would nearly lie in this pseudobinary section. Generally the tie lines will not lie in the $(Ti,Nb)_3Al$ section. If, after cooling, an O phase alloy finds itself at a composition and temperature with a concave free energy curve, spontaneous growth of composition fluctuations can occur. If the

[3]The possibility of achieving B2 order decreases as one moves from the TiAl composition to the TiNb composition because of the known positive heat of mixing of the BCC phase in the Ti-Nb binary.

local composition of a region of that alloy reaches the end point composition, then in that region the ordered phase will spontaneously disorder, in this case, to the $D0_{19}$ phase.

The B19 phase is an AB phase having only two Wyckoff sites with occupancies similar to B2 and would therefore be expected to have maximum stability in the same composition region where the B2 phase has maximum stability; i.e., along the 50% Ti line, which intersects the $(Ti,Nb)_3Al$ section near the Ti_2AlNb composition. Thus the B19 free energy curve is centered around this composition as indicated in Fig. 19c. The B19 phase has never been observed as an equilibrium phase in this system and is thus metastable at all temperatures and compositions and does not appear in the phase diagram. Finally the site occupancy of the ordered A_2BC orthorhombic phase [20] clearly indicates that its compositional range of stability should also be centered around Ti_2AlNb.

The $D0_{19}$ phase, an A_3B phase, is known to have a preference for Al on the B sites and a mixture of (Ti,Nb) on the A sites (Ref. 23 in [1]) in Ti-Al-Nb alloys. Thus stability of this phase with respect to HCP is expected across the entire $(Ti,Nb)_3Al$ section at 700°C and hence the free energy curve for $D0_{19}$ is drawn below the HCP. Near the composition Ti_2AlNb, it is likely that the B19 phase would have a lower free energy than $D0_{19}$ because of the presence of equal amounts of Al and Nb at this composition.

The pseudo-binary phase diagram section (Fig. 19a) was constructed using information on the BCC, HCP and $D0_{19}$ equilibria from the calculated binary Ti-Al and from isothermal sections of Ti-Al-Nb at 1100 and 1200°C [30]. The positions of phase boundaries between the $D0_{19}$, B2, and O phases at 900°C were taken from the 900°C isothermal section of ref. [31]. The maximum in the B2 to O transition was placed at 1000°C according to [16]. The remainder of the diagram was sketched to be consistent with Figs. 19 b and c.

The T_0 diagram (Fig. 19b) contains solid curves that correspond to the equilibrium two-phase fields in the phase diagram (Fig. 19a). The T_0 triple points (intersections of solid curves)

correspond to three-phase triangular regions in the phase diagram.[4] Also indicated are dashed extrapolations of the important BCC to HCP and BCC to B2 curves. A possible location for the T_0 curve for B2→B19 is also given. These dashed curves only have meaning if the high temperature BCC or B2 parent phase is retained for kinetic reasons during cooling through the higher T_0 curve(s).

We now discuss the observed results using these diagrams. Water-quenched samples of all three alloys in the present work are ordered B2. This rapid quench apparently suppresses the BCC→DO_{19} and the BCC→HCP transformations for Alloy 1 and permits access to the BCC to B2 ordering curve at ~900°C as shown in Fig. 19b. At a slower cooling rate (~400 K/s), the BCC→$D0_{19}$ transformation is bypassed for the kinetically simpler BCC→HCP transformation that requires only displacive ordering. Once the HCP phase forms, subsequent partitionless transformation to B2 is not possible. The formation of the HCP phase sets the stage for all of the subsequent transformations of Alloy 1. Alloys with higher Nb content can not escape ordering to the B2 at any cooling rate because the ordering temperature is relatively high. Indeed Alloy 2 is B2 at 1200°C. The presence of the B2 phase sets the stage for the subsequent transformations of Alloys 2 and 3. For Alloys 2 and 3 the transformation BCC→HCP is not possible because of the way the T_0 curve plunges to low temperature.

For simplicity of discussion, the subsequent transformation paths for each alloy are considered as occurring isothermally at 700° as indicated by the arrows in Fig. 19c starting from the HCP for Alloy 1 and from the B2 for Alloys 2 and 3 following the above discussion. The sequence for each alloy class undergoes partitionless transformation down a hierarchy of phases with decreasing free energy. One can see that for the alloys near the composition of Alloy 2, a B2→B19→O path is likely. On the other hand for alloys near the composition of Alloy

[4]The intersection point of two T_0 curves necessarily requires the intersection of a third T_0 at the same point.

1, an HCP→DO_{19}→O is likely. Thus we have constructed a set of thermodynamic relationships between the phases that is consistent with the experimentally observed paths for the partitionless transitions.

A later stage of transformation occurs for the low Nb content alloy shown in Fig. 19c that involves long-range diffusion. The concave curvature of the free energy curve indicates that the O phase formed for this composition by partitionless transformation is unstable on a longer time scale with respect to small fluctuations of composition (spinodal decomposition). This kind of process is termed conditional spinodal decomposition [3]. The Nb-poor regions of this decomposition will approach the end point of the O phase free energy curve and will spontaneously disorder (relative to the O phase) to the DO_{19} phase. This process is thought to lead to the third level of domain structure described in Section 5.

7. Conclusion

During cooling from 1100°C, the high temperature BCC-based phase of $(Ti,Nb)_3Al$ alloys decomposes into low temperature orthorhombic phase by two different partitionless paths depending on Nb content. Microstructurally the two paths are differentiated by the substructure of domain boundaries and the number of variants of the orthorhombic phase. For alloys with ~12.5 at% Nb, the transient formation of a hexagonal precursor occurs while at ~25 at% Nb ordering to the B2 precludes the hexagonal phase. In the latter case, defects are found that suggest the transient existence of a B19 phase. However the B19 phase itself was never observed in cooled samples. In the former case formation of the O phase from the ordered DO_{19} was observed along with defects indicating the hexagonal to the DO_{19} ordering. These two different paths are seen as feasible after an examination of subgroup/supergroup relations between the crystal structures of the various phases. The paths are also feasible based on

reasonable assumptions regarding the thermodynamic relationships among the free energy curves for the phases involved.

Detailed examination of the interfaces between the rotational domains/variants of the B2 to O phase transformation steps (for Alloys 2&3) and the DO_{19} to O phase transformation steps (for Alloy 1) showed they are determined by the minimization of elastic strain energy through the formation of stress-free interfaces with special orientations of twins of the I and II kind. For the Alloy 2&3 the twins are often arranged in a self-accommodating polytwin group consisting of three variants of the O phase.

A two-phase modulated microstructure is observed after long term annealing at 700°C of the Alloy 1. The structure morphology is determined first by a formation of the metastable O phase (by congruent ordering of the DO_{19} phase), and then by reprecipitation of the DO_{19} phase. The thermodynamics underlying the two-phase formation, possibly by a spinodal mechanism, are discussed.

Acknowledgement

The authors would like to thank F. S. Biancaniello for the alloy melting and the heat treatments and M. E. Williams for the TEM specimen preparation and the photographic work. The support of DARPA under Order #7469 is greatly appreciated.

References

1. L.A.Bendersky, A.Roytburd and W.J. Boettinger, Part I of this paper, this issue, p.?.

2. L.D.Landau and E.M.Lifshitz, Statistical Physics, Pergamon Press, London, 1980.

3. S.M.Allen and J.W.Cahn, Acta Met., 23, 1017 (1975); 24, 425 (1976).

4. A.G.Khachaturyan, T.F.Lindsey and J.W.Morris, Metall. Trans., 19A, 249 (1988).

5. W.A.Soffa and D.E.Laughlin, Acta Met., 37, 3019 (1989).

6. R.A.Spurling, Met. Trans., 6A, 1660 (1975).

7. G.M.Pennock, H.M.Flower and D.R.F.West, Metallography, 10, 43 (1977).

8. D.Banerjee and J.C.Williams, Scr. Met., 17, 1125 (1983).

9. D.Banerjee, C.G.Shelton, B.Ralph and J.C.Williams, Acta Met., 36, 125 (1988).

10. D.S.Shih, G.K.Scarr and G.E.Wasielewski, Scr. Met., 23, 973 (1989).

11. K.Muraleedharan, S.V.Nagender Naidu and D.Banerjee, Scr. Met., 24, 27 (1990).

12. R.A.Spurling, C.G.Rhodes and J.C.Williams, Met. Trans., 5, 2597 (1974).

13. H.J.Rack, D.Kalish and K.D.Fike, J. Mater. Sci. Eng., 6, 181 (1970).

14. R.A.Spurling, private communication.

15. L.A.Bendersky and W.J.Boettinger, Mat. Res. Soc. Symp. Proc., 133, p.45 (1989).

16. L.A.Bendersky, W.J.Boettinger and A.Roitburd, Acta Met., 39, 1959 (1991)

17. See papers in ASM Sumposium on Pretransformation Behavior Related to Displacive Transformations, L.E.Tanner and W.A.Soffa, Eds., Metall. Trans., 19A (1988)

18. R. Strychor, T.C. Williams and W.A. Soffa, Met. Trans., 19A, 1321 (1988).

19. L.A. Bendersky, W.J. Boettinger, B. Burton, F.S. Biancaniello, and C.B. Shoemaker, Acta. Metall. Mater, 38, 931 (1990).

20. B.Mozer, L.A.Bendersky, W.J.Boettinger and R.G.Rowe, Scr. Met., 24, 2363 (1990); B.Mozer, unpublished research, NIST, Gaithersburg, 1991.

21. Z.Nishiyama, Martensitic Transformation, Academic Press (1978)

22. D.S.Liberman in Phase Transformations, ASM, 1970, p.1.

23. T.Saburi and C.M.Wayman, Acta Metall., 27, 979 (1979).

24. S.Ichinose, Y.Funatsu and K.Otsuka, Acta Metall., 33, 1613 (1985).

25. F.C.Lovey, G.van Tendeloo and S.Amelinckx, Phys. Stat. Sol., 85, 29 (1984).

26. W.A.Baeslack III and T.Broderick, Scr. Met., 24, 319 (1990).

27. M.J. Marcinkowski in Electron Microscopy and Strength of Crystals, eds. G.Thomas and J.Washburn, Interscience, New York (1962), p.333.

28. H. T. Kestner-Weykamp, C. H. Ward, T. F. Broderick and M. J. Kaufman, Scr. Met. 23, 1697 (1989).

29. M. A. Krivoglaz and A.A. Smirnov, The Theory of Order-Disorder in Alloys, American Elsevier Publishing Co., New York, 1965, p.120.

30. U. R. Kattner and W. J. Boettinger, Mat. Sci. & Eng. A152 (1992), 9-17.

31. K. Muraleedharan, A.K. Gogia, T.K. Nandi, D. Banerjee and S. Lele, Met. Trans., 23A, 401 (1992).

FIGURE CAPTIONS

Fig.1 Optical micrographs of Alloy 3 specimens cooled from 1100°C at different cooling rates. Regions with different volume fractions tranformed according to (a) a higher and (b) a slower cooling rate. (c) Annealing of the water quenched specimens (with retained B2) for 15 min at 700°C was sufficient to produce complete transformation.

Fig.2 The TEM microstructure of the Alloy 3 specimen corresponding to Fig. 1a. The TEM image shows islands of transformed material, surrounded by a B2 phase matrix. The islands consist of a complex plate-like structure of the O phase. The phases do not differ in composition.

Fig.3 Higher magnification view of the plate-like structure of Fig. 2 showing the plates to be arranged into a larger size secondary plate (polytwin) which alternates with another variant of polytwin plate. (a) and (b) are dark-field images with the g_1 and g_2 reflections, indicated in the (c) $[011]_c$ SAD pattern. The g_2 reflection, 020_O, images a single variant (5) of the O phase. (d,e) show $[011]_c$ stereographic projections with superimposed calculated [1] traces of the (d) symmetric and (e) non-symmetric SFIs and the corresponding traces of the observed A-A, B-B and C-C interfaces of (a). The solid and dashed traces correspond to edge-on and inclined interfaces respectively.

Fig.4 A series of SAD patterns taken from an Alloy 2 specimen which was water quenched from 1100°C and then annealed at 700°C for 15 min. The selected area aperture was large enough to include numerous variants contributing to scattering. The patterns show average Laue symmetries (a) 4mm, (b) 3mm and (c) 2mm corresponding to the major zone axes of the cubic symmetry, [100], [111] and [110], respectively. The strongest reflections (consisting of several reflections from different variants of the O-phase) correspond to the fundamental BCC reflections and determine the orientation relationship

between lattices of the transformed B2 phase and the O phase variants.

Fig.5 Three dark field (a-c) images taken from a single variant plate in specimen of Alloy 3 continuously cooled from 1100°C. The dark field images are taken with the plate orientation close to the (d) $[110]_O$ zone axis using (a) $\bar{2}20_O$, (b) $1\bar{1}0_O$ and (d) $\bar{4}40_O$ reflections in approximately a two-beam condition. Two type of interfaces with different displacement vectors and morphology are observed. Both types are seen in (b) and only the faceted type in (a). In (c) only residual contrast from the faceted interfaces is seen. Arrow markers A and B identify the same places in all three micrographs.

Fig.6 [001] projections of the close-packed layers of the (a) O phase (according to [17]) and (b) DO_{19} phase (z=1/4 - empty circles; z=3/4 - filled circles). Small, medium and large size circles represent Al, Ti and Nb atoms, respectively. The displacement vectors of the type I (due to chemical ordering) and the type II (due to displacement) interfaces are shown.

Fig.7 Dark field images of (a) stacking fault (SF) type and (b) both SF and APB interfaces in thin plates of an O phase variant oriented with $[110]_O$ parallel to the electron beam. In (a) and (b) $2\bar{2}0_O$ and $1\bar{1}0_O$ reflections were used respectively.

Fig.8 Optical micrograph showing a needle-like transformed microstructure of Alloy 1 continuously cooled from 1100°C at 400°C/min.

Fig.9 Bright field TEM micrograph showing the the detailed morphology of the needles shown in Fig. 8. The needles have very irregular interfaces. Blocky grains between elongated needles are most probably cross-sections of the needles with their long axes normal to the TEM foil.

Fig.10 Thin (dark) layers of the BCC phase separating transformed phase grains. The dark-field image is taken with a DO_{19} reflection which is well separated from the BCC's. Dark contrast in the upper-left part of the photograph belongs to a different grain.

Fig.11 SAD pattern taken from three grains forming a triple junction in the Alloy 1 cooled from 1100°C. The pattern has $[10\bar{1}0]_h \| [111]_c$ (three 60° rotated $<10\bar{1}0>_h$ patterns around $[111]_c$) and $(0001)_h \| \{110\}_c$ in support of the Burgers OR found for the Alloys 2 & 3.

Fig.12 Series of dark field images taken from a single grain of the transformed Alloy 1 in the $[11\bar{2}0]_h$, $[01\bar{1}0]_h$ and $[\bar{1}210]_h$ zone axis orientations (SAD patterns of $[11\bar{2}0]_h$ and $[01\bar{1}0]_h$ patterns are shown in (a) and (b)). The sequence of orientations was obtained by tilting the grain around the $[0001]_h$ direction as shown in the stereographic projection (c). The dark field images are taken close to a two-beam condition using the following reflections: (d) 0002, (e) $1\bar{1}00$ and (f) $2\bar{2}00$ from the $[11\bar{2}0]_h$ ZA; (g) 0002, (h) $2\bar{1}\bar{1}0$ and (i) $4\bar{2}\bar{2}0$ from the $[01\bar{1}0]_h$ ZA; (k) $10\bar{1}0$ and (l) $20\bar{2}0$ from the $[\bar{1}2\bar{1}0]_h$ ZA.

Fig.13 (a) TEM dark field image of a continuously cooled Alloy 1 specimen, slightly off the $[0001]_h$ zone axis in order to give different excitation errors for different domains. Two orthogonal directions of the interface traces, $[1\bar{1}00]_h$ (A-A) and $[11\bar{2}0]_h$ (B-B), correspond to $(11\bar{2}0)_h$ and $(1\bar{1}00)_h$ interfacial planes between two variants of the O phase with coinciding $130_{O(1)}$ / $\bar{1}30_{O(2)}$ and $(110)_O$ / $(1\bar{1}0)_O$ planes. (b,c) SAD patterns taken from areas where only one type of interface is present (area A and B on Fig. 15a).

Fig.14 The superimposed $[001]_O$ diffraction patterns of two variants of the O phase rotated 120° to each other, with a coinciding row of (a) $130_{O(1)}$ and $\bar{1}30_{O(2)}$ (plane A) and (b) $110_{O(1)}$ and $1\bar{1}0_{O(2)}$ (plane B) reflections, corresponding to the experimental SAD of Fig. 15b, c, respectively. The kinematical intensities (size of the reflections) are calculated according to the O phase structure parameters in ref. [19].

Fig.15 Bright field image of a continuously cooled Alloy 1 specimen, slightly off the [0001] zone axis, where all three orthogonal sets of the O phase variant pairs (shown as A,B and C) rotated with respect to each other by 60° are observed in a single grain.

Fig.16 Microstructure of the Alloy 1 after annealing at 700°C for 26 days. Bright field (a) and

three dark field (b-d) images, all slightly different in a TEM foil tilt, show a complex morphology of coherent domains.

Fig.17 Two dark field images, a and b, taken with the same cluster of reflections $(4\bar{4}00)_h$ (c) but different in a small tilt (close to [0001]) show two second level plates, A and B, separated by a zig-zag shape interface close to the $(11\bar{2}0)_h$ plane. The zig-zag shape is formed by two segments of interfaces between the DO_{19} and O phase domains located in neighboring second level plates A and B. The segment planes are irrational orientations.

Fig.18 Schematic drawing showing the two-phase (O and DO_{19}) domain distribution based on interpretation of the experimental images (Fig. 16, 17). The two-phase structure is formed by re-precipitation of the DO_{19} phase from the initial O phase twinned plates (a). Two morphologies are shown: (b) one with a chess-board distribution of domains surrounded by SFIs. (c) another with the DO_{19} phase forms zig-zaged ribbons traveling continuously through the second level plates in a modulated manner. The DO_{19} phase ribbon-like domains have internal low angle boundaries (dislocation walls) and faceted SFIs with two variants of the O phase.

Fig.19 Schematic (a) pseudobinary equilibrium phase diagram, (b) T_0 diagram for partitionless transformations, and (c) 700°C free energy vs. composition curves for the Ti_3Al-Nb_3Al section of the Ti-Al-Nb system. The free energy diagram shows the superposition of the BCC (B2) and HCP ($D0_{19}$, B19, and O-phase) families of phases. For Alloy 2, an intermediate HCP or $D0_{19}$ phase cannot form during partitionless transformation from cubic to the O-phase.

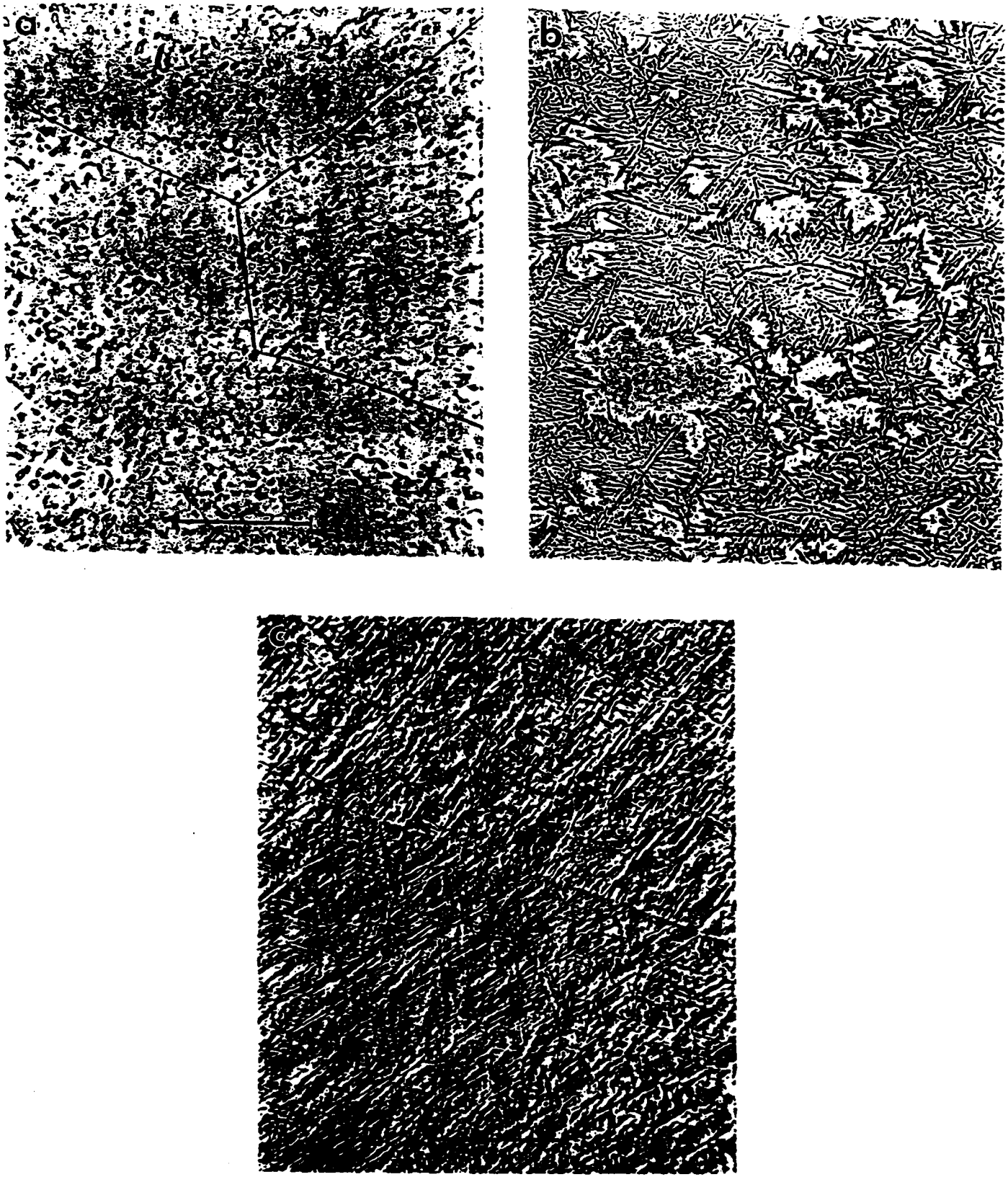

Fig. 1

Fig. 2

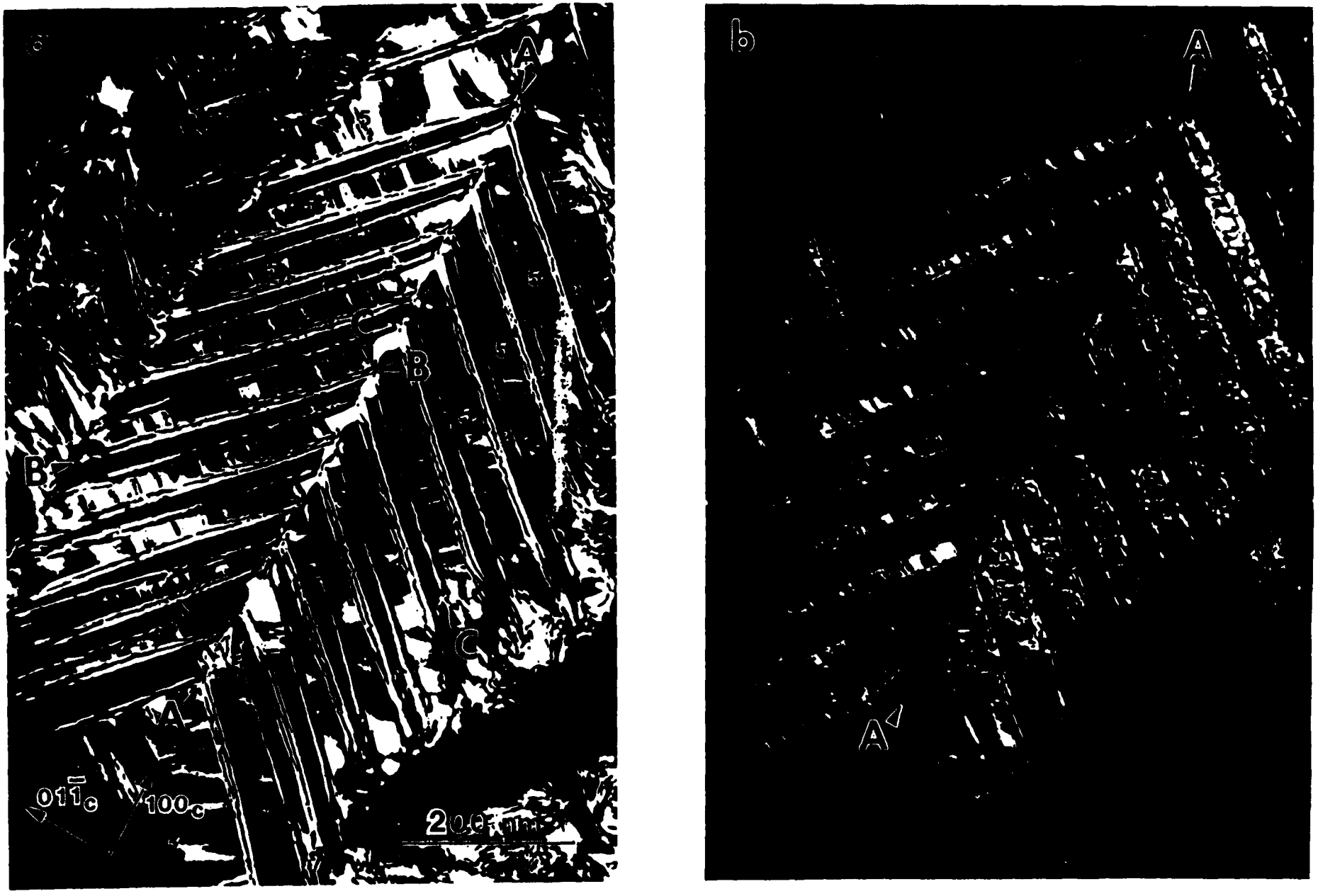

Fig. 3a,b

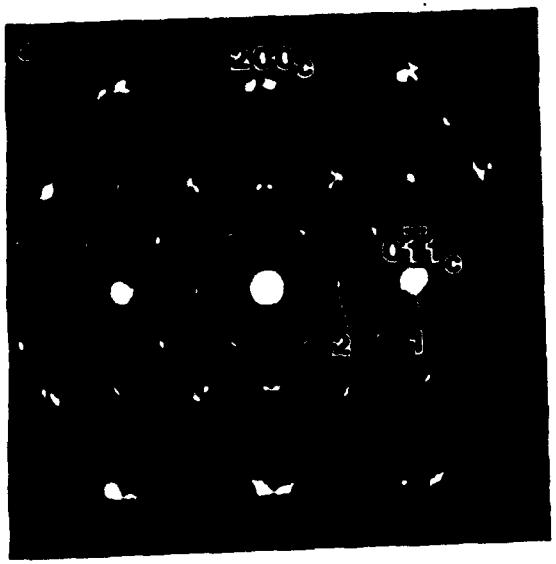

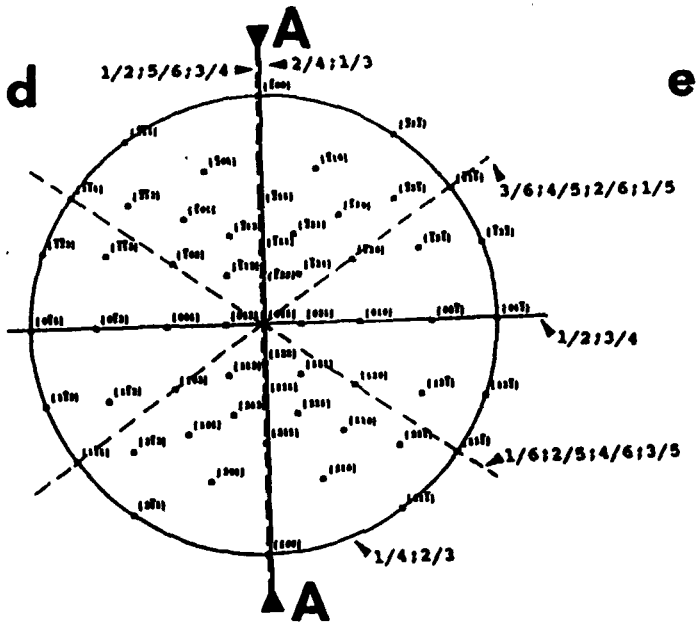
d
A
1/2;5/6;3/4
2/4;1/3
3/6;4/5;2/6;1/5
1/2;3/4
1/6;2/5;4/6;3/5
1/4;2/3
A

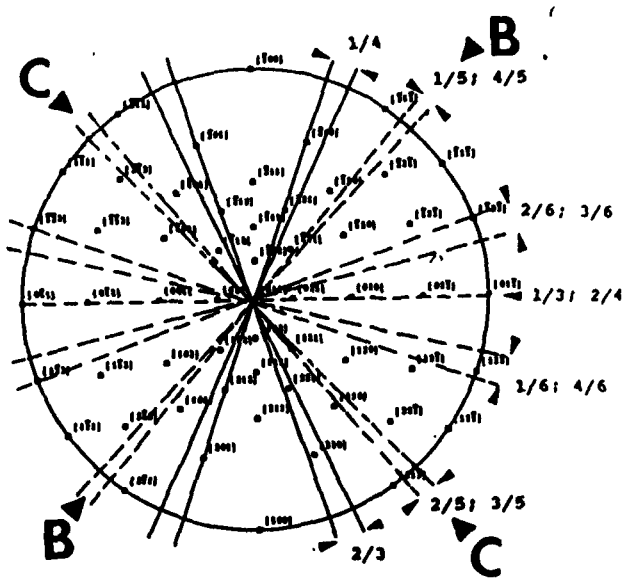
e
C
B
1/4
1/5; 4/5
2/6; 3/6
1/3; 2/4
1/6; 4/6
2/5; 3/5
2/3
B
C

Fig. 3 c,d,e

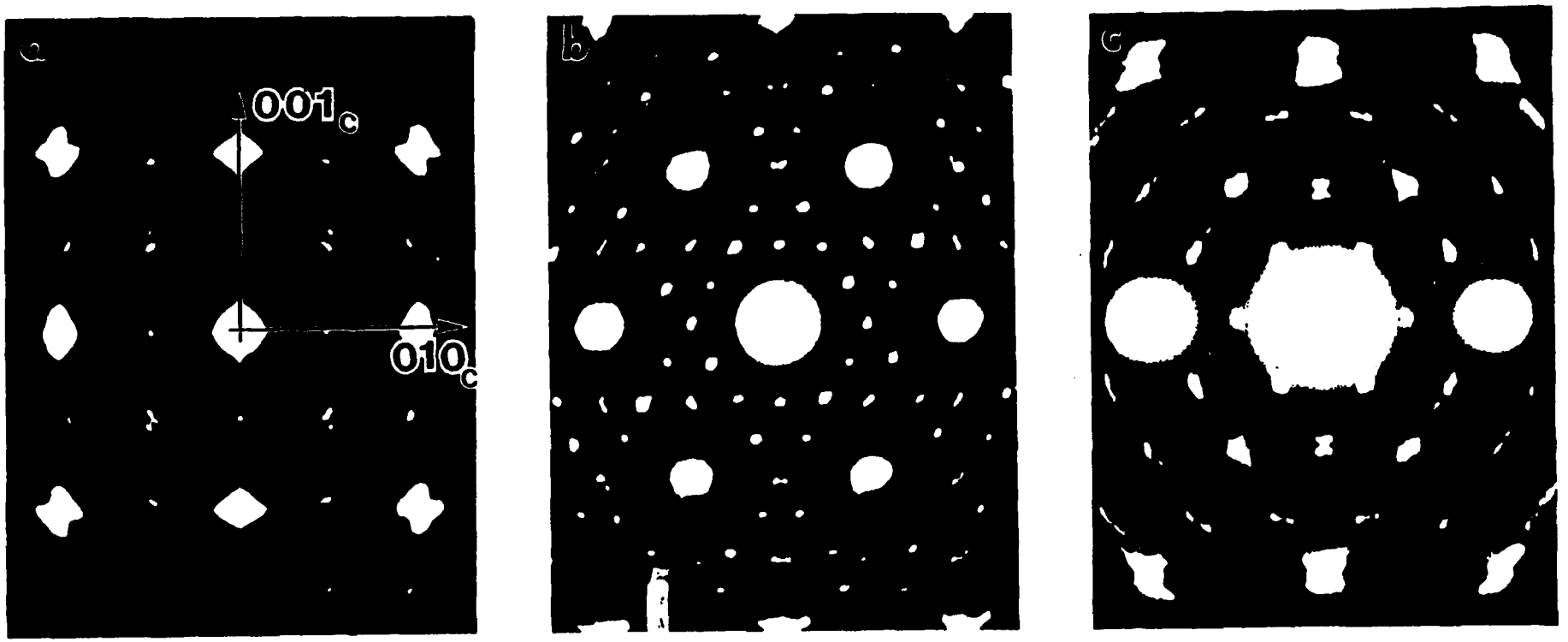

Fig. 4

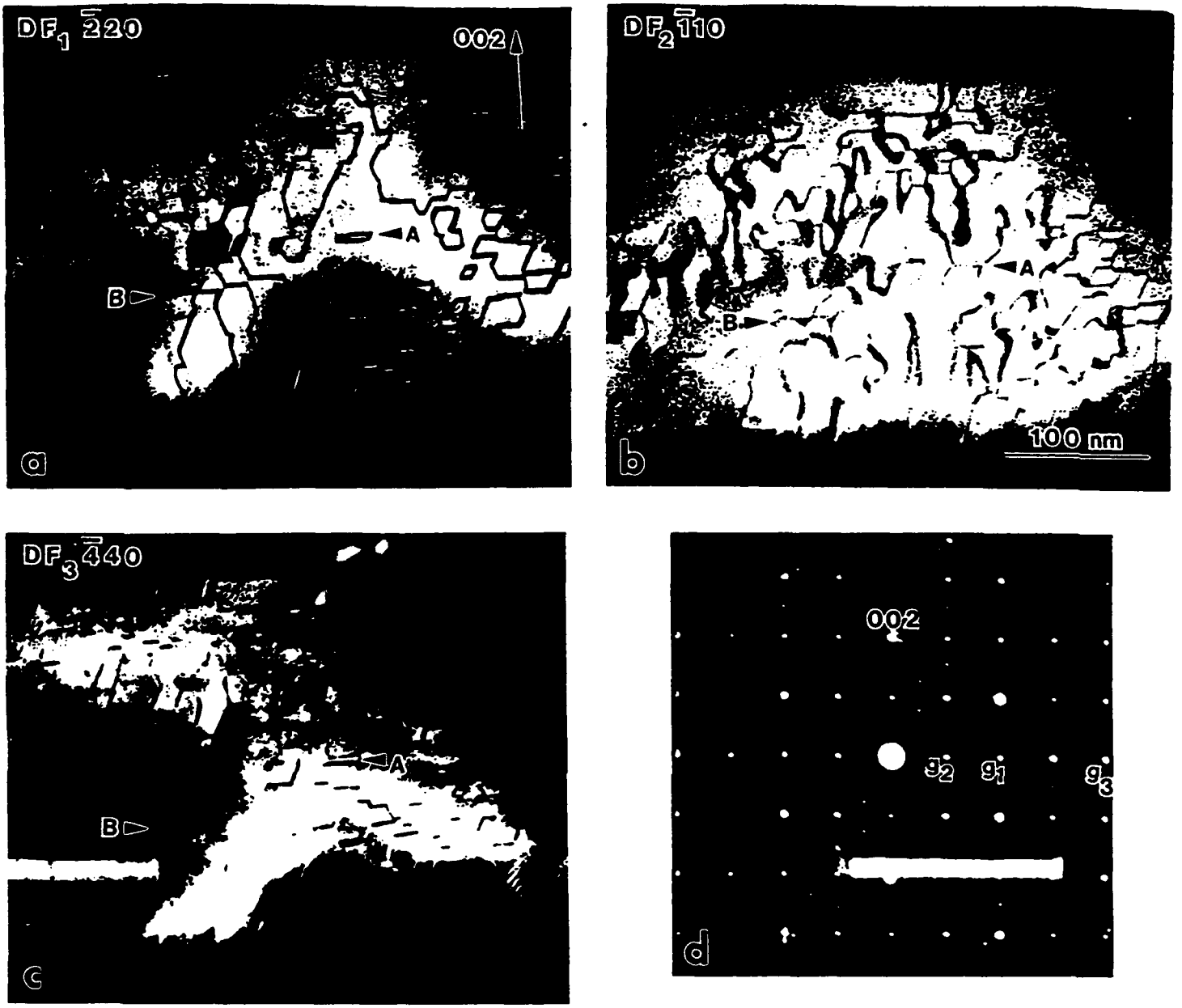
DF1 $\bar{2}$20
002
A
B
a
DF2 $\bar{1}$10
A
B
100 nm
b
DF3 $\bar{4}$40
A
B
c
002
g2
g1
g3
d

Fig. 5

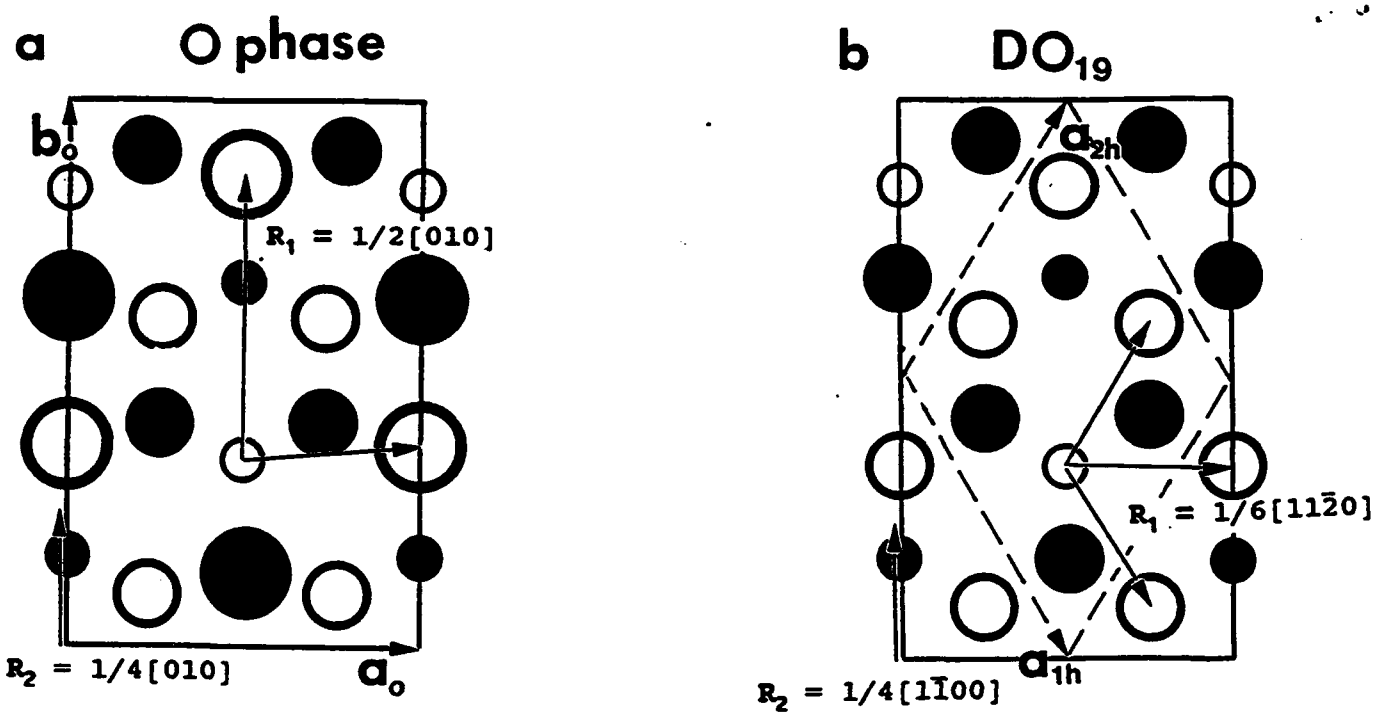
a
O phase
b_o
$R_1 = 1/2[010]$
$R_2 = 1/4[010]$
a_o
b
DO_{19}
a_{2h}
$R_1 = 1/6[11\bar{2}0]$
$R_2 = 1/4[1\bar{1}00]$
a_{1h}

Fig. 6

Fig. 7

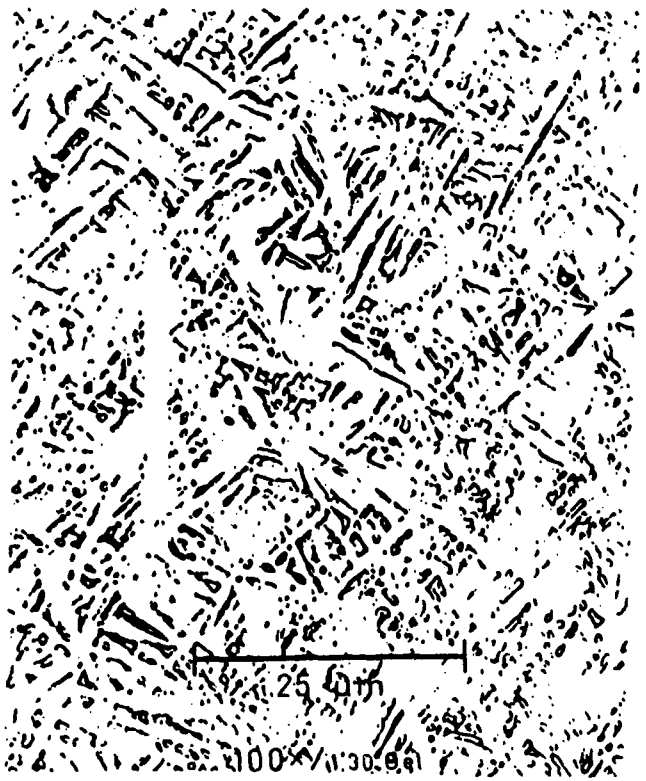

Fig. 8

Fig. 9

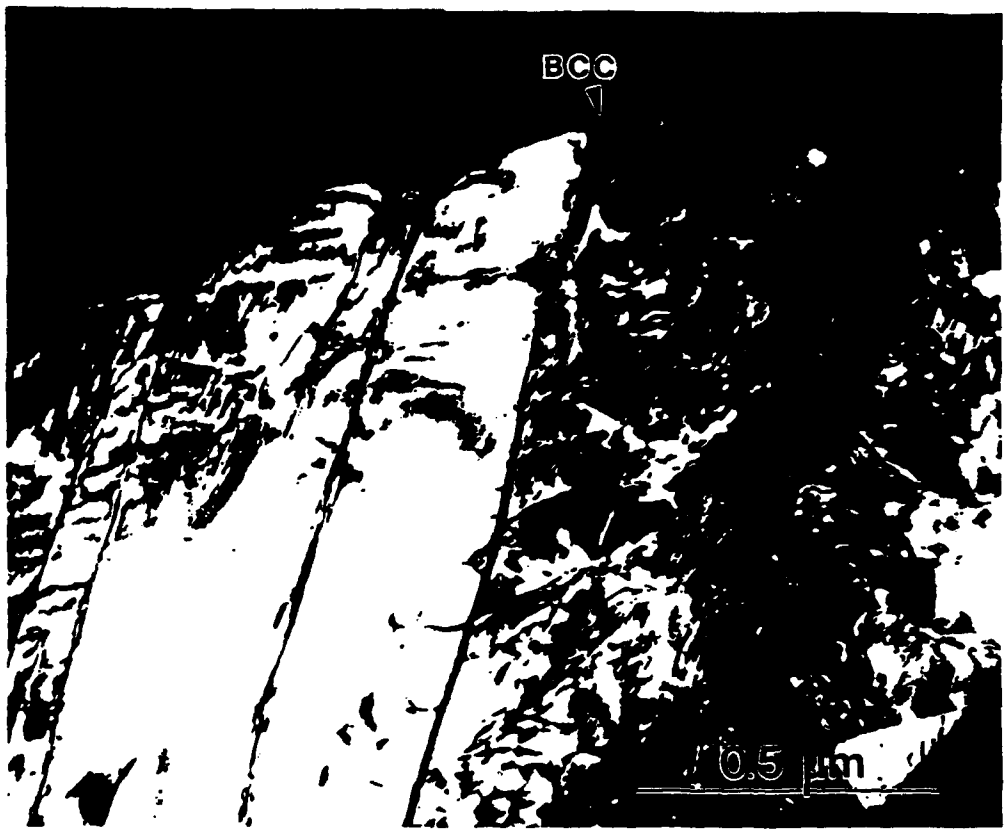

Fig. 10

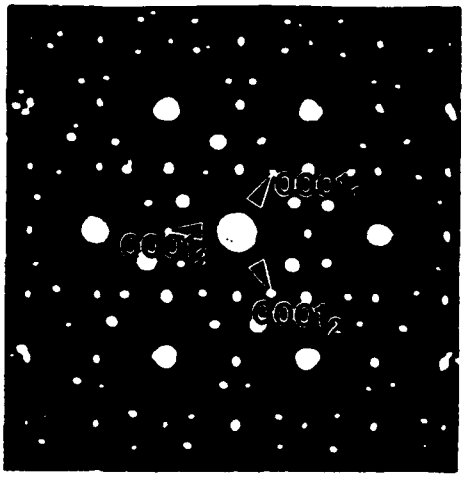

Fig. 11

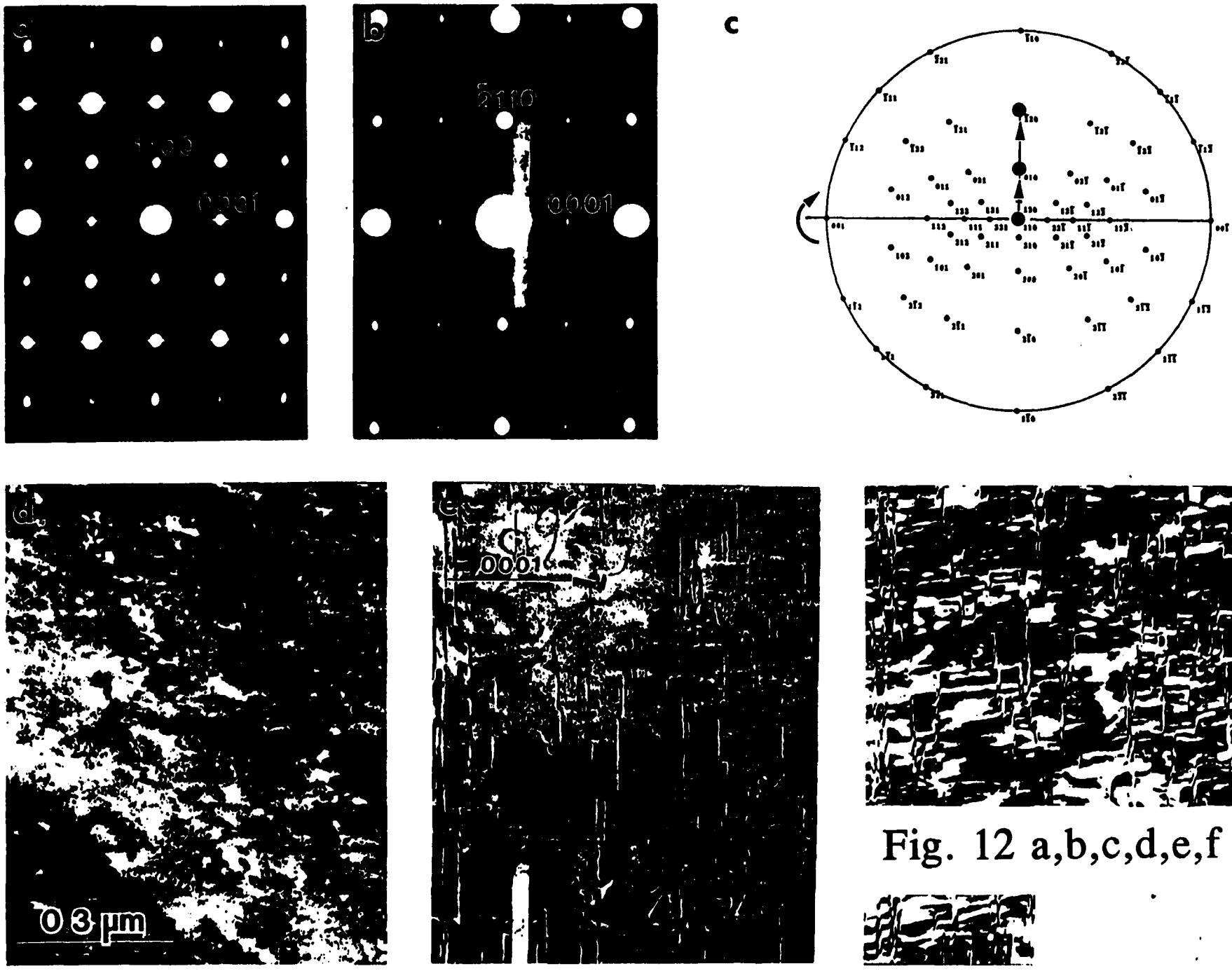

Fig. 12 a,b,c,d,e,f

Fig. 12 g,h,i,j,k,l

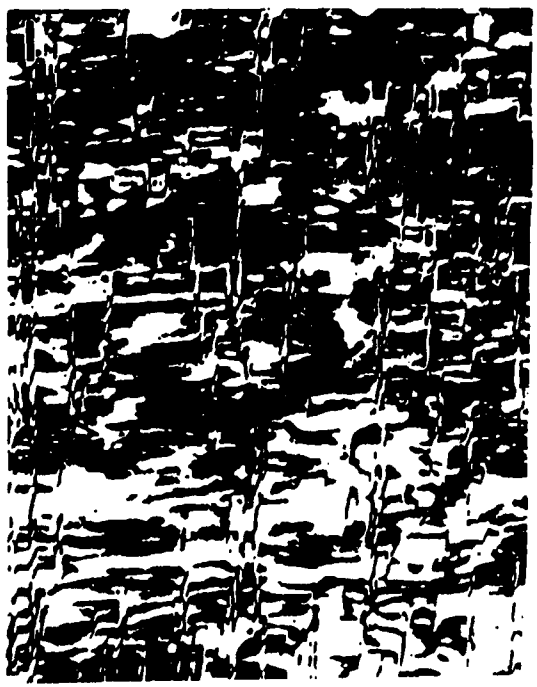

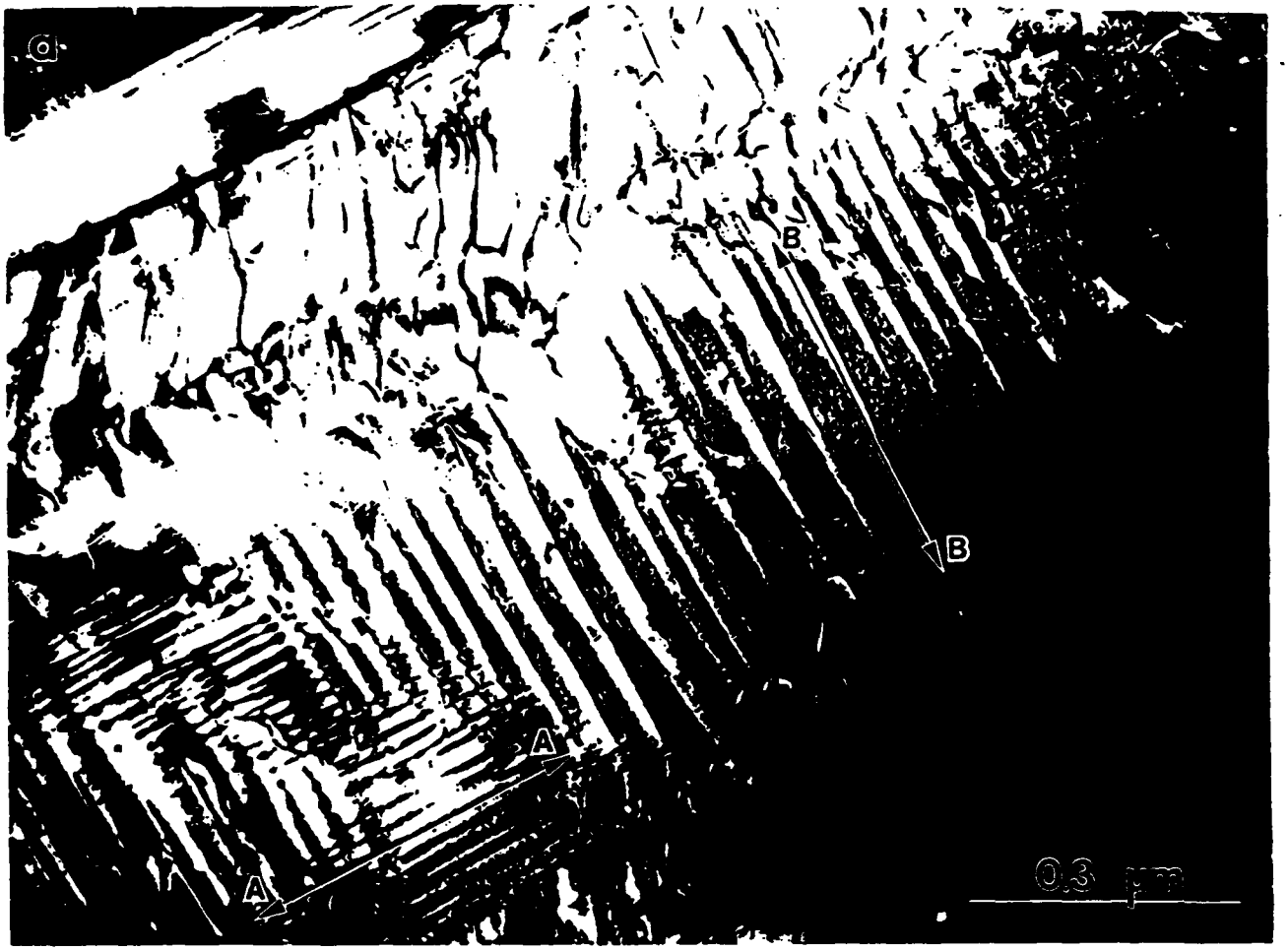

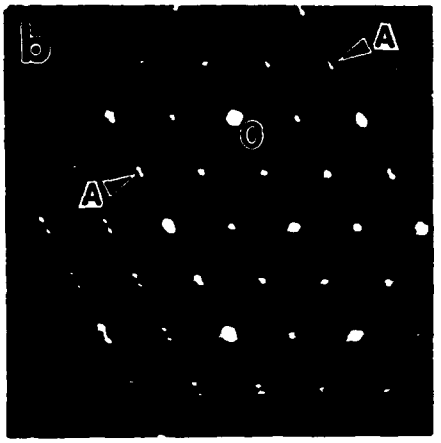

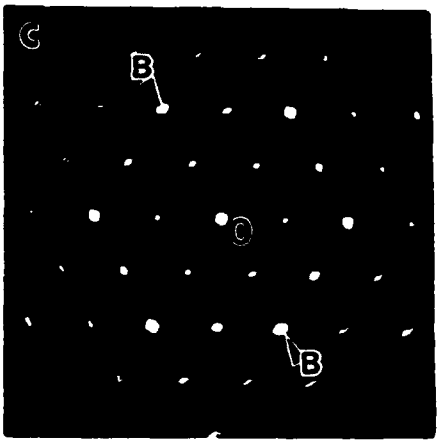

Fig. 13

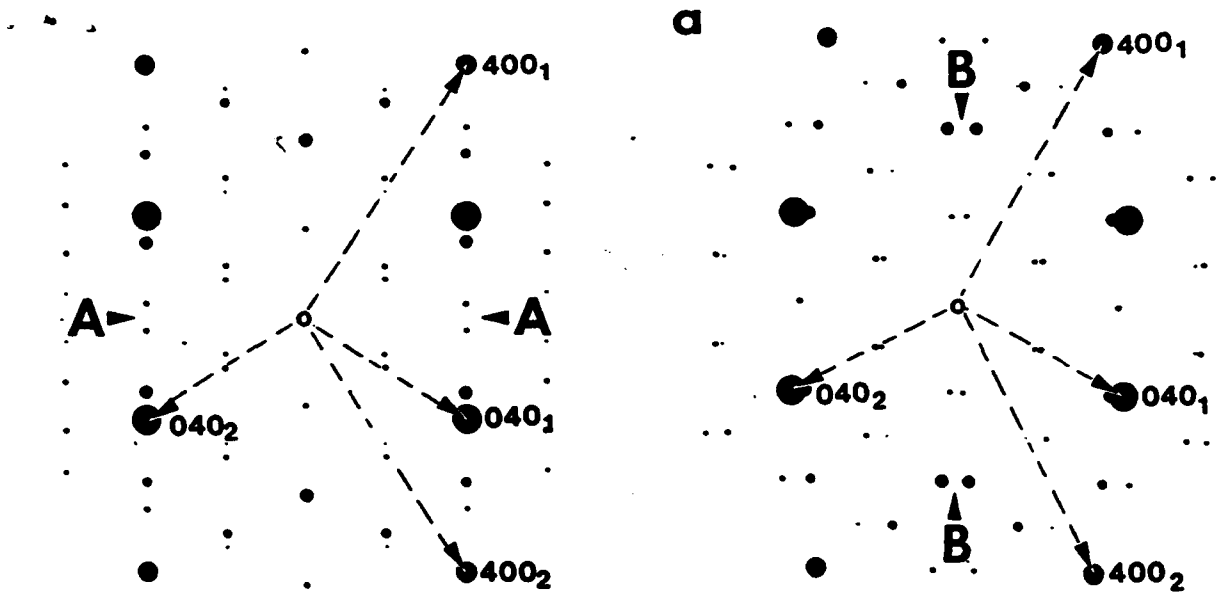

Fig. 14

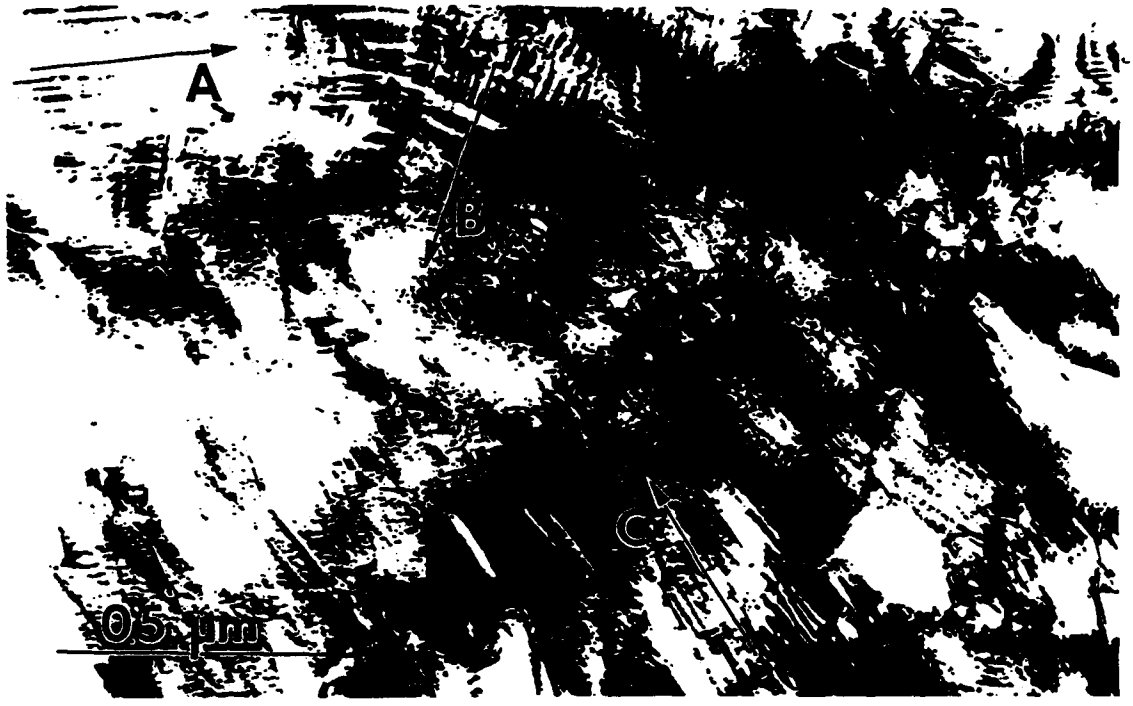

Fig. 15

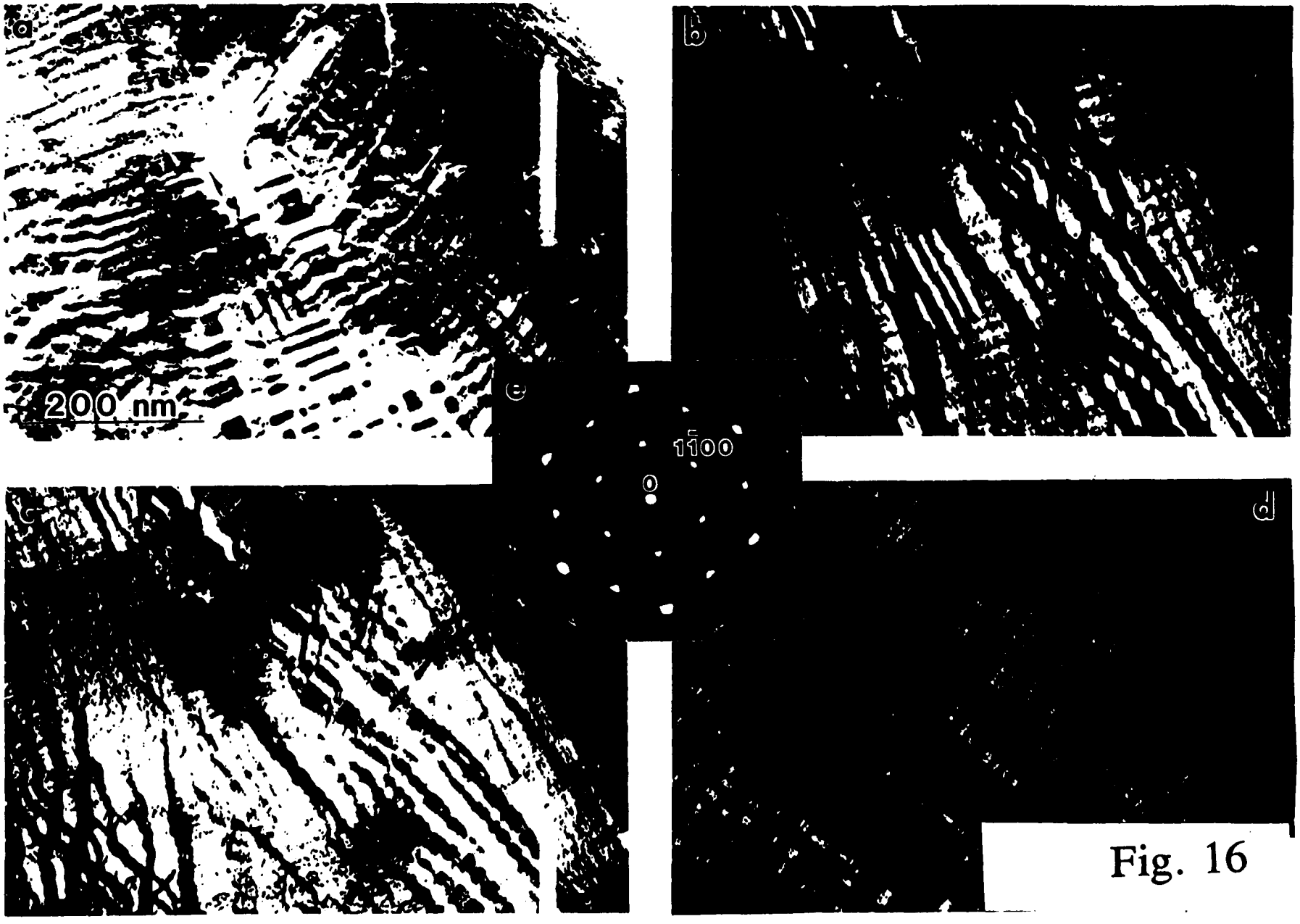

Fig. 16

Fig. 17

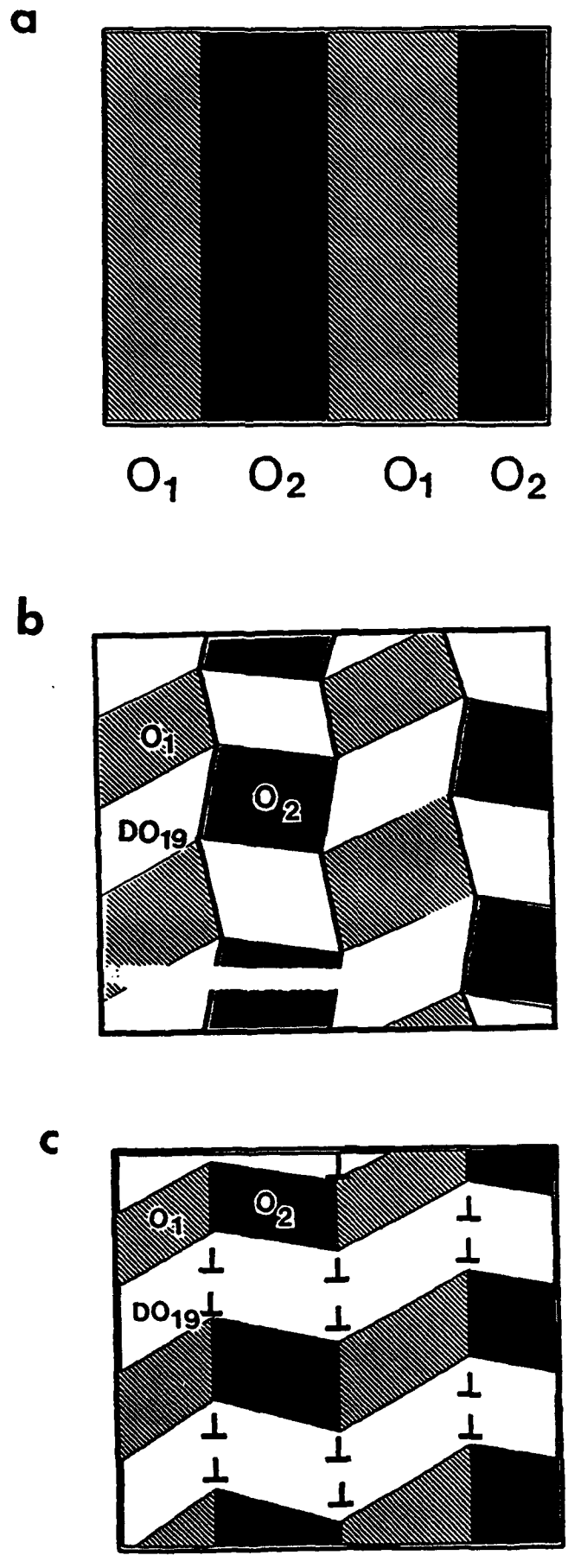

Fig. 18

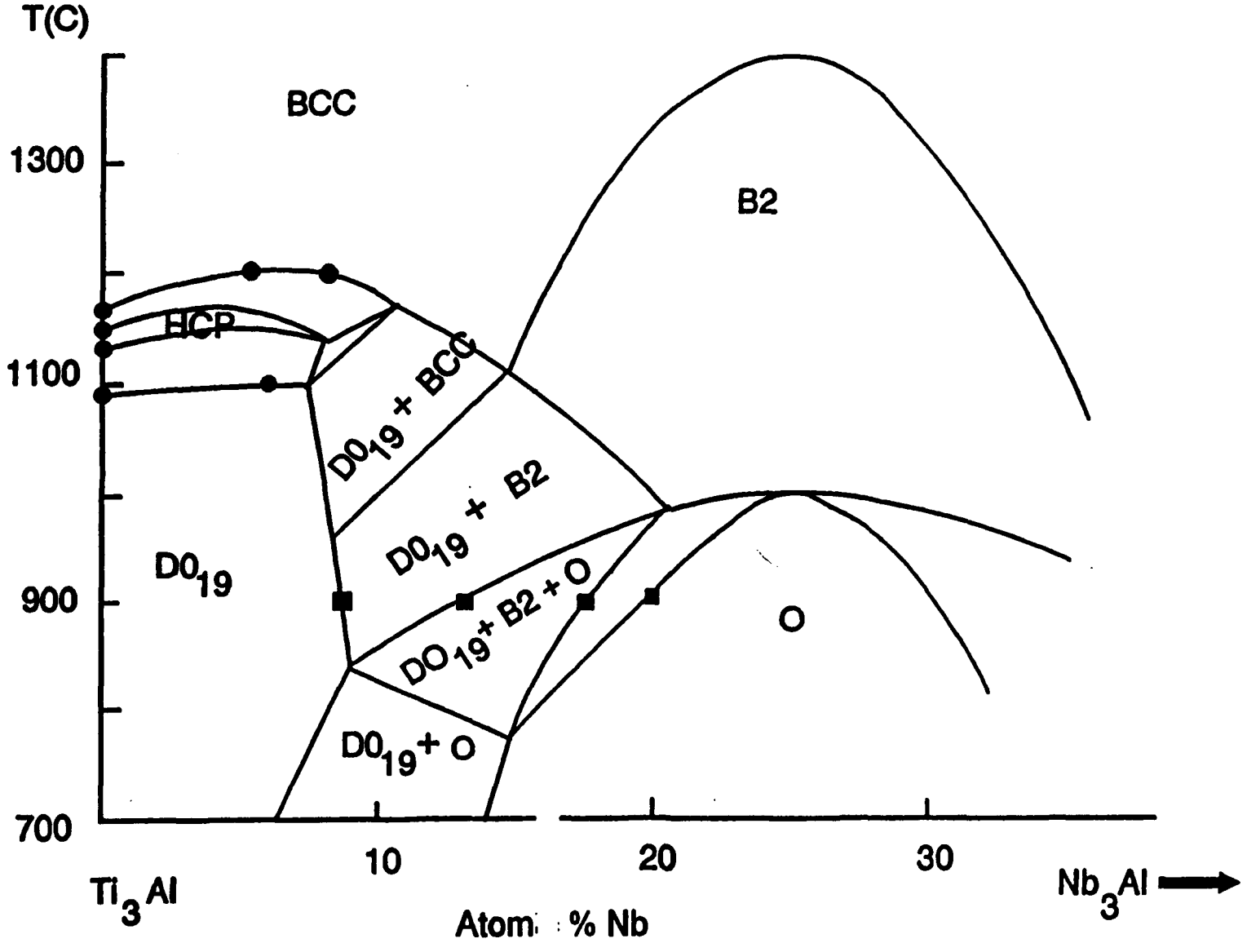
T(C)
BCC
1300
B2
HCP
1100
$D0_{19}$ + BCC
$D0_{19}$ + B2
$D0_{19}$
900
$D0_{19}$+ B2 + O
O
$D0_{19}$+ O
700
10
20
30
Ti_3Al
Nb_3Al
Atom % Nb

Fig. 19a

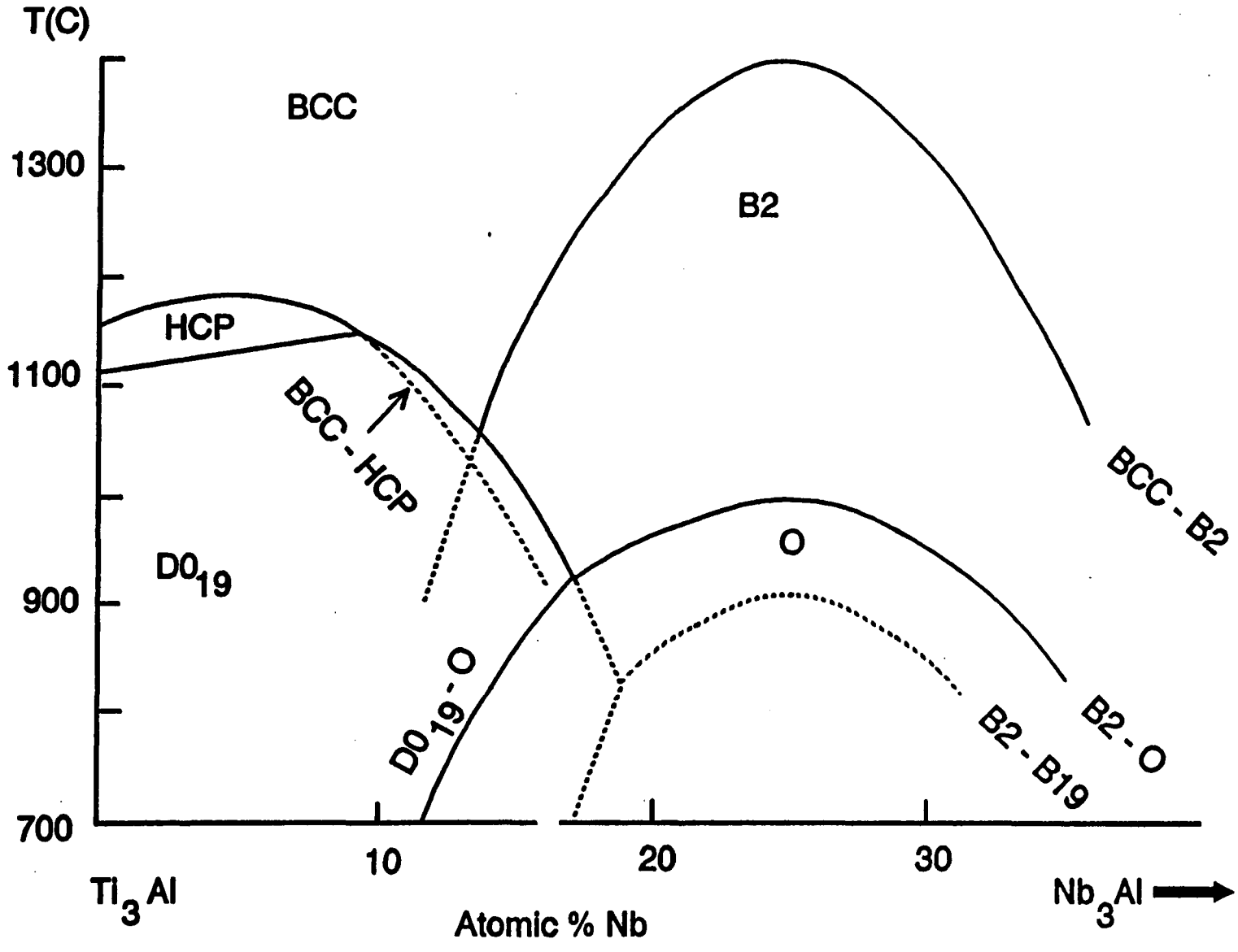
T(C)
1300
1100
900
700
BCC
B2
HCP
BCC - HCP
BCC - B2
D0 19
O
D0 19 - O
B2 - B19
B2 - O
10
20
30
Ti 3 Al
Nb 3 Al
Atomic % Nb

Fig. 19b

Scripta METALLURGICA et MATERIALIA
Vol. 24, pp. 2363-2368, 1990
Printed in the U.S.A.
Pergamon Press plc

NEUTRON POWDER DIFFRACTION STUDY OF THE ORTHORHOMBIC Ti_2AlNb PHASE

B. Mozer, L. A. Bendersky, W. J. Boettinger
Materials Science and Engineering Laboratory
National Institute of Standards and Technology
Gaithersburg, MD 20899

and

R. Grant Rowe
General Electric Corporate Research and Development
Schenectady, NY 12301

(Received September 17, 1990)
(Revised September 27, 1990)

Introduction

The Ti-Al-Nb system has stimulated considerable investigation as a possible lightweight, high temperature structural material. Blackburn and Smith [1,2] identified the alloy Ti-24 at% Al-11 at % Nb which has acheived a balance of room temperature ductility and elevated temperature rupture resistance. Depending on exact composition and heat treatment, this alloy may contain the ordered bcc B2 phase, the ordered hexagonal DO_{19} α_2-Ti3Al phase, and/or an orthorhombic phase. This orthorhombic phase was first discovered by Banerjee et al.[3] in coexistence with α_2 in a Ti-25at%Al-12.5at%Nb alloy that was furnace cooled from 1100°C. Convergent beam electron diffraction (CBED) established the mmm point symmetry and the Taft-Spence technique, which maximizes the x-ray fluorescence yield from specific crystal planes, was used to probe the nature of the site occupancy. They deduced the structure given in Table 1.

Table 1 - Cmcm Structure Deduced by Banerjee et al. [3]

Site	Atom	x	y	z
8g	Ti	1/4	-1/12	1/4
4c1	Al	0	1/6	1/4
4c2	Nb	0	-1/3	1/4

The Cmcm space group is a minimal subgroup of the $P6_3/mcm$ space group of α_2. It was previously established that Ti and Nb occupy the same site for dilute (5 at%) additions of Nb to the DO_{19} α_2 phase [4]. Thus the orthorhombic phase involves ordering of Ti and Nb in DO_{19}. The atomic positions above are in fact those of the hexagonal structure.

The composition range of the orthorhombic single phase field is quite broad in the 25 at% Al section and has been located by several investigators [5-6] although the boundaries with α_2 are subject to considerable doubt at present due the structural similarities of the two phases. The orthorhombic phase does not exist at high temperatures. At ~1100°C and above, alloys of this composition transform to the B2 phase. This research presents a structural refinement from single phase fine grain material prepared at 700°C.

Experimental Method

A sample with composition Ti-25at%Al-25at%Nb was prepared by repeated arc melting and was drop cast into a 32 mm dia cylindrical Cu mold. This cylinder was extruded at 1050°C

0036-9748/90 $3.00 + .00

to a 9.2 mm rod and ground to a 6 mm rod. Segments of the rod were wrapped in Ta and heat treated in a He-backfilled quartz tube at 1200°C for 1 hour followed by water quenching in order to recrystallize the B2 phase. Using similar encapsulation, the rods were heat treated at 700 °C for 228 h to form and equilibrate the orthorhombic phase. Samples were prepared for optical metallography and TEM. Electropolishing was performed at 0°C in an electrolyte containing 60% methanol, 35% butanol and 5% perchloric acid by volume.

Neutron powder diffraction was performed at room temperature with the high resolution five detector diffractometer, BT-1, at the NIST reactor [7] using the experimental conditions in Table 2. Four 2.5 cm long rods were bundled together with a common axis about which they were rotated during diffraction in order to reduce any preferred orientation effects that were caused by extrusion to at most, a fiber texture.

The data were analyzed with a code written by Prince [8] which allows the intensities from the five detectors to be processed simultaneously. The background was represented by a Chebychev polynomial function with up to six coefficients per detector. Six coefficients were used for the first detector and two coefficients were used for the remaining four detectors and were refined for each channel together with the profile and structural parameters. The scattering lengths used for the refinement are b(Ti)= -0.3438 Fermi (10^{-12} cm.), b(Al)=0.3449 Fermi, and b(Nb)=0.7054 Fermi [9].

Table 2 - Experimental Conditions Neutron Powder Diffraction

Monochromatic Beam	220 diffraction from Cu with a pyrolytic graphite filter to remove higher order contamination
Wavelength	0.1553(1) nm
Horizontal Divergences	10, 20, and 10 min. for the in-pile monochromator beam, and diffracted beam collimators, respectively.

Rietveld refinement was performed using the structure in Table 1 as the initial guess. First level refinement was performed to establish scale factor, background parameters, lattice parameters, and spectrometer zero. Subsequent refinements were performed to establish the atomic positions, and the temperature factors. For the first model, the Wyckoff sites were occupied by a unique atomic species having individual densities fixed according to the formula Ti_2AlNb. A correction was allowed for possible fiber texture which yielded a slight improvement. This model was not satisfactory in that the temperature factor for titanium was larger than acceptable for a simple alloy and the temperature factor for aluminum was negative.

To improve upon this model, we allowed the three sites to be occupied by combinations of the three atoms and refined the occupancies along with all the other parameters. The best refinement obtained was a model in which only aluminum occupied the 4c1 site and titanium and niobium were distributed on the 8g and 4c2 sites with the overall composition fixed according to the chemical formula. Another possible model was used following the suggestion of Banerjee et al.[3] in which different Wyckoff sites were assumed for the atomic species, their model Fig. 7(c) of Table 4. This model and modifications of it allowing each site to be occupied by a combination of all species gave a much poorer refinement in agreement with the analysis of [3].

Results

Fig. 1a shows a micrograph of the alloy after the 1200°C heat treatment. The alloy was single phase (B2 structure) with an 80 μm equiaxed grain size. Fig. 1b is an micrograph after the 700°C treatment. The alloy appears single phase with a 25 μm grain size. TEM examination (Fig. 2a) confirmed the microstructure as single phase grains but with irregular interfaces. This microstructure is believed to result from the isothermal martensitic formation and subsequent recrystallization of the the orthorhombic phase during the 700°C treatment. SAD and CBED (Fig. 2b,c) were consistent with the orthorhombic structure.

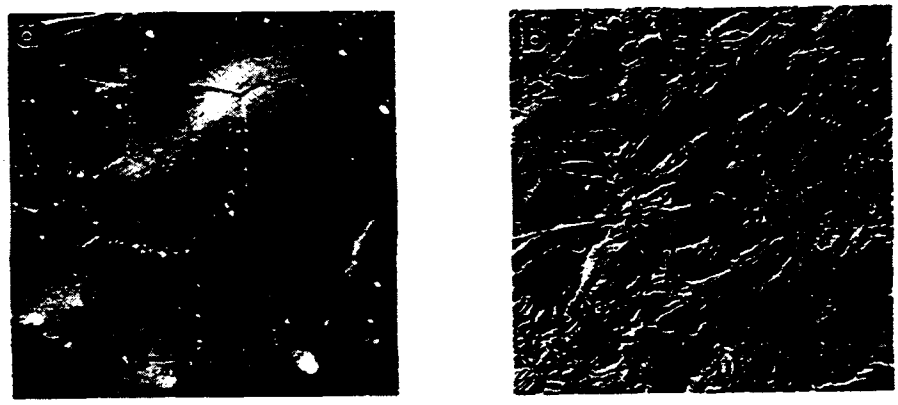

Fig. 1. (a) Optical Micrograph of alloy after 1200°C, 1 h treatment.
(b) Optical Micrograph of alloy after 700°C, 228 h treatment.

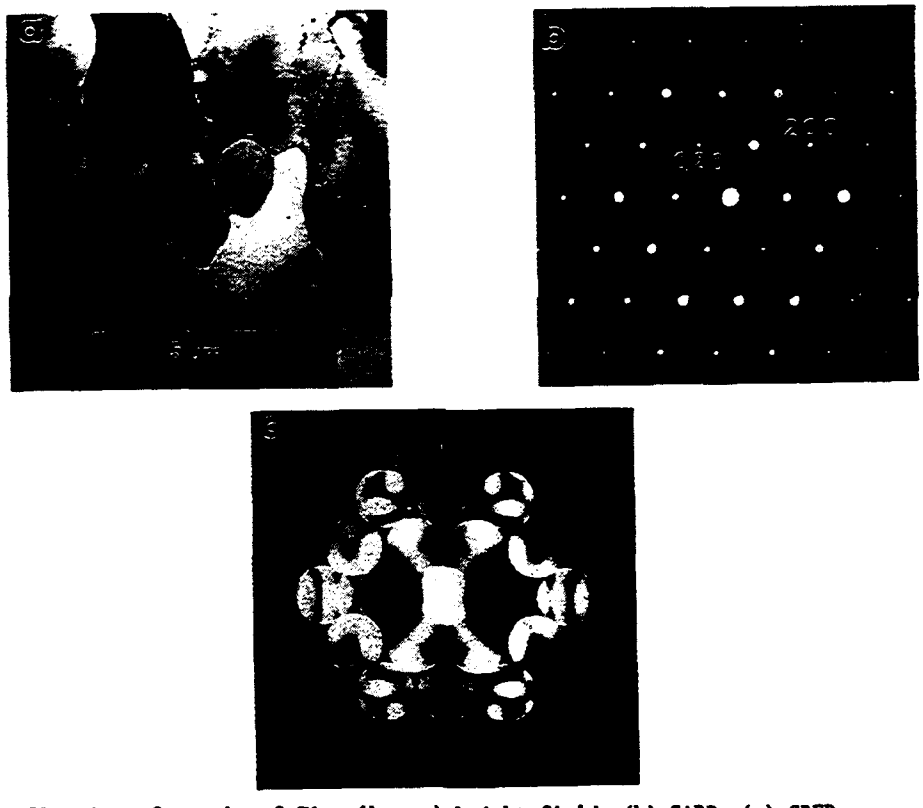

Fig. 2. TEM view of sample of Fig. 1b. a) bright field, (b) SADP, (c) CBED pattern consistent with mmm point symmetry.

The refinement of the powder neutron diffraction data of the orthorhombic phase of Ti_2AlNb was able to fix the model of the structure as one having only aluminum on the 4c1 site and a mixture of titanium and niobium on the 8g and 4c2 sites. The results of the refinement are given in Table 3. The agreement between observed and calculated intensities is shown in Fig. 3 for the five detectors of the spectrometer.

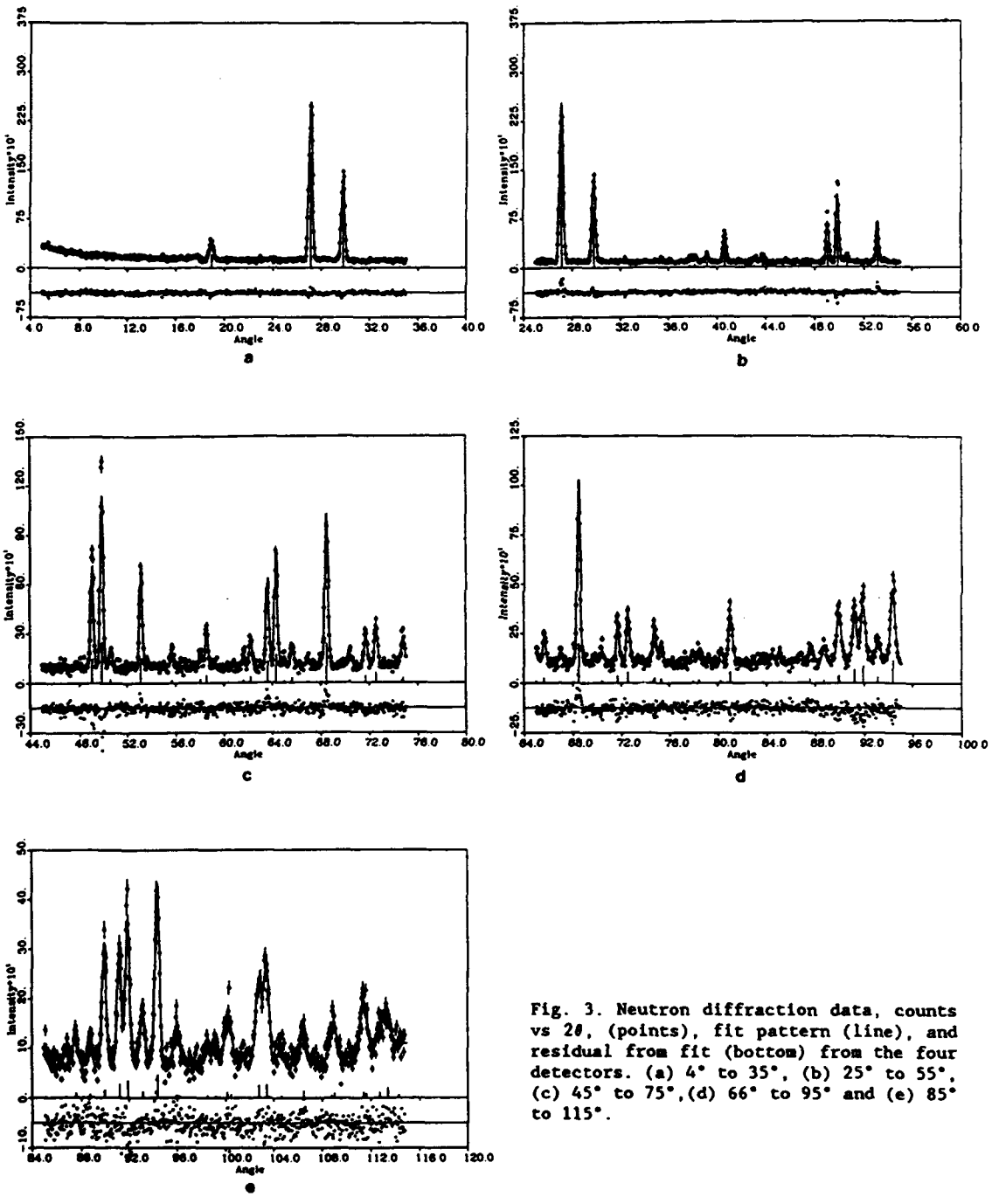

Fig. 3. Neutron diffraction data, counts vs 2θ, (points), fit pattern (line), and residual from fit (bottom) from the four detectors. (a) 4° to 35°, (b) 25° to 55°, (c) 45° to 75°,(d) 66° to 95° and (e) 85° to 115°.

Table 3- Summary of Neutron Powder Diffraction Refinement Results

Space Group Cmcm

Atom	Wyckoff Positions X	Y	Z	Temperature Factor	Relative Occupancy
Ti(8g)	0.2310(12)	-0.0959(6)	1/4	2.02(.14)	0.823(4)
Nb(8g)	0.2310(12)	-0.0959(6)	1/4	2.02(.14)	0.177(4)
Al(4c1)	0.0	0.1633(3)	1/4	0.48(.12)	0.5
Nb(4c2)	0.0	-0.3643(3)	1/4	0.62(.10)	0.323(4)
Ti(4c2)	0.0	-0.3643(3)	1/4	0.62(.10)	0.177(4)

Lattice Constants

a=0.60893(2) nm b=0.95694(4) nm c=0.46666(2) nm

Statistical Factors
Rn=10.53 Rp=11.21 Rw=14.98 Re=8.11
Chi=1.845

Notes. Figures in parentheses are standard deviations in the decimal figures. The temperature factor is in Angstroms squared. R factors are defined in A. Santoro, R.S. Roth, and D. Minor, Acta Crystallogr. Sect. B 33, 3945 (1977).

Discussion

The results of this neutron diffraction study confirm and refine the structure of the orthorhombic phase suggested by Banerjee et al. [3]. The structure is Cmcm (HgNa or Cd3Er) with a=0.60893(2) nm, b=0.95694(4) nm, and c=0.46666(2) nm. Ti(Nb) fills the 8g site, Al fills one 4c site, and Nb(Ti) fills another 4c site. The structure involves ternary ordering of the hexagonal DO_{19} phase. The binary DO_{19} phase (Fig. 4a) can be considered (in an orthorhombic cell) as a sequence of (100) planes of (Ti,Al)-Ti-(Ti,Al). For the ternary orthorhombic phase with composition Ti_2AlNb and with perfect order (Fig. 4b), the sequence is changed to (Nb,Al)-Ti-(Nb,Al); i.e., Nb replaces Ti on the 4c2 site. The ordering causes a break of the hexagonal symmetry and corresponding distortion of the unit cell; viz., contraction of the b and expansion of the a parameters. The c parameters of the two phases are essentially identical.

Compared to a random mixture of Ti and Nb on the Ti sites of α_2 DO_{19} Ti_3Al, the ternary ordering, Wyckoff positions, and distortion to the orthorhombic symmetry permit an increase of Al-Nb distances from .285-.289 nm to .302-.306 nm while slightly reducing the Al-Ti distances to .280-.285 nm. Estimates of Lennard-Jones potentials for Al-Ti and Al-Nb yield minima at interatomic distances of .279 and .292 nm respectively [10]. This is consistent with the tendency in the present case to form an ordered structure where the Nb atoms increase their distances from the Al atoms.

Even though the alloy has exact stoichiometric composition A_2BC - one atom per site, some mixing of Ti and Nb atoms on 8g and $4c_2$ sites was found. This reflects the equilibrium long range order present at 700°C where the alloy was equilibrated by the 228 hours of annealing. For the Al ($4c_1$) site no disorder was found. Although solubility limits also depend on the neighboring phase in the phase diagram, one might expect a narrow range of solubility along the TiAl-TiNb pseudobinary section and a wider range of solubility along the Ti_3Al-Nb_3Al section.

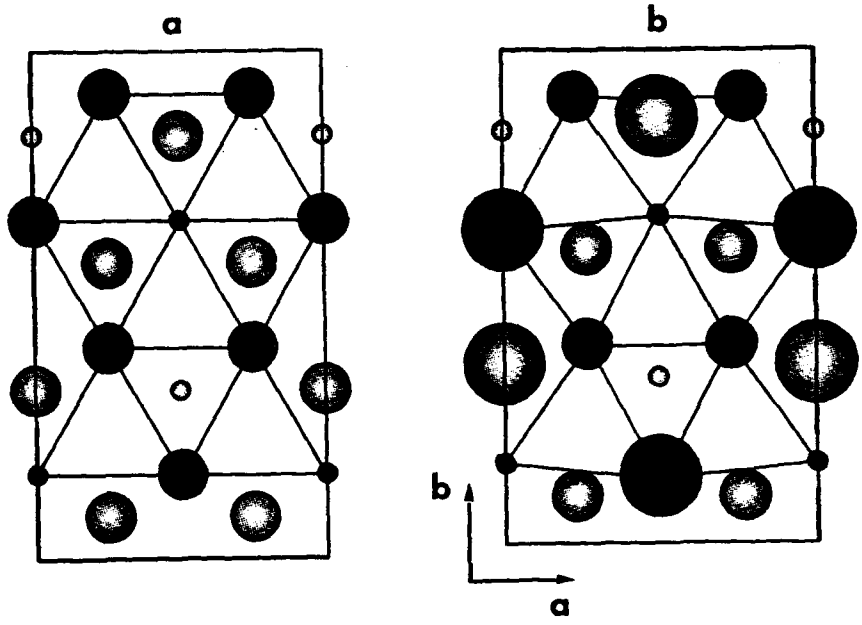

Fig. 4 [001] projection of layers at z=1/4 (dark) and 3/4 (light) of the (a) DO_{19} structure (using an orthorhombic cell) with small and medium size circles representing Al and (Ti,Nb) respectively and (b) the perfectly ordered orthorhombic structure with small, medium, and large size circles representing Al, Ti, and Nb respectively.

Acknowledgement

The authors would like to thank C.S. Choi, J. Stalick, A. Santoro for help with the Rietveld refinement. The support of DARPA under Order #7469 for LAB and WJB is greatly appreciated.

References

1. M. J. Blackburn and M. P. Smith, AFWAL-TR-81-4046, Interim Tech. Rept., May 1977-Dec. 1978, Contract #F33615-75-C-1167, June 1981.
2. M. J. Blackburn and M. P. Smith, U.S. Patent # 4,292,077, Sept. 29, 1981.
3. D. Banerjee, A. K. Gogia, T. K. Nandi and V. A. Joshi, Acta Met. 36, 871 (1988).
4. D. G. Konitzer, I. P. Jones and H. L. Fraser, Scripta Met. 20, 265 (1986).
5. H. T. Kestner-Weykamp, C. H. Ward, T. F. Broderick and M. J. Kaufman, Scr. Met. 23 1697 (1989).
6. R. G. Rowe, in High Temperature Aluminides and Intermetallics, ed. by S. H Whang, C. T. Liu, D.P. Pope and J. O. Stiegler, p.375, TMS-AIME, Warrendale PA (1990).
7. E. Prince and A. Santoro, Natl. Bur. Std. U.S. Tech. Note No. 1117, p.11, (1980).
8. E. Prince, Natl. Bur. Std. U.S. Tech. Note No. 1117, p.8, (1980).
9. G. Caglioti, A. Paoletti, and F. P. Ricci, Nucl. Instrum. 3, 223 (1958).
10. M. Enomoto and H. Harada, Met. Trans. 20A, 649 (1989).

8

Scripta METALLURGICA et MATERIALIA Vol. 24, pp. 1541-1546, 1990 Printed in the U.S.A. Pergamon Press plc

ORDERED ω-DERIVATIVES IN A Ti-37.5Al-20Nb at% ALLOY

L.A. Bendersky, B.P. Burton, W.J. Boettinger, F.S. Biancaniello
Metallurgy Division
NIST, Gaithersburg MD 20899
(Received May 14, 1990)
(Revised June 4, 1990)

Introduction

In recent studies of phase equilibria in the Ti-Al-Nb system, chemical ordering of an ω phase was reported for some alloys [1-3]. The Ti_4Al_3Nb alloy, cooled from a B2 phase field above 1100°C, has the following transformation path - B2 → ω" → $B8_2$ - which involves strongly coupled chemical and displacive order-disorder transitions.

The trigonal ($P\bar{3}m1$) ω" phase exhibits partial collapse of 111 planes of the B2 phase and reordering relative to its B2 parent [2]. Evidently the stable transformation path would be B2 → $B8_2$, but the observed path includes the metastable intermediate phase (ω"). Furthermore, ω" ($P\bar{3}m1$) is of lower symmetry than either B2 ($Pm\bar{3}m$) or $B8_2$ ($P6_3/mmc$), and it is of lower configurational entropy than $B8_2$. The $B8_2$ structure ($InNi_2$ prototype, [4]) was formed after prolonged annealing at 700°C. Both ω" and $B8_2$ structures were verified by means of transmission electron microscopy (TEM) and single crystal X-ray diffraction, and their structures are shown in the schematic drawing of Figure 1.

In the present work we report a new Ti-Al-Nb phase which is apparently a more ordered derivative of the $B8_2$ phase. The phase was found as fine precipitates in a $B8_2$ matrix. A possible structure of the new phase will be discussed based on the results of electron diffraction and high-resolution microscopy.

Experimental

An alloy with the Ti-37.5Al-20Nb (at%) composition was prepared by arc melting according to the procedure described in [2]. Three sets of specimens (HT1, HT2 and HT3) were studied in this work. HT1 was annealed at 1400°C for 3 hours and cooled at about 400°C/min. Specimen HT2 was prepared from one of the HT1 specimens by annealing at 1100°C for 25 hours followed by quenching in water. The HT2 specimen was prepared by encapsulating Ta foil-wrapped slices in evacuated He-backfilled quartz tubes. A third set of samples (HT3) was obtained by a heat treatment of some of the HT1 in similar tubes at 700°C for 18 days followed by a water quench.

All three specimens (HT1-HT3) were studied by transmission electron microscopy (TEM). TEM thin foils were prepared by standard twin-jet electropolishing using a 300 ml methanol, 175 ml n-butanol, 30 ml $HClO_4$ electrolyte at 0°C.

Microstructures at 1400°C, 1100°C and 700°C

All specimens cooled or quenched from 1400 and 1100°C (HT1, HT2 and HT3) contain two different microstructural scales - one resolved by optical metallography, and another only by TEM. The coarse scale represents the microstructure present at high temperature while the fine scale represents a phase transformation of the matrix during continuous cooling [2]. First we describe the coarse structure in order to indicate the equilibrium phases at temperature and second we identify the microstructure of the transformed matrix.

Optical metallography shows that the 1400°C samples (HT1) consist of large single phase grains. According to TEM analysis of its transformed structure (as will be evident later) the phase has the B2 structure. The 1100°C samples (HT2) consist of large grains of the same phase with blocky and needle-like precipitates (few tens of μm long) as shown in Fig.2a. The precipitates occurred in an irregular morphology, and TEM analysis indicates that they are an intergrowth of respectively σ and Li_0 phases. The 700°C (HT3) samples have needle-like precipitates finer that those in the HT2 specimens (Fig.2b and 3a), probably due

0036-9748/90 $3.00 + .00

to the lower precipitation temperature. As TEM analysis shows, the precipitates have a peculiar structure of thin layers of both DO_{19} and $L1_0$ phases (Fig.3b,c). The origin of this structure was not investigated in the present work.

The identity of the matrix phase at 1400 and 1100°C for the HT1 and HT2 specimens can only be inferred, whereas for the HT3 the actual 700°C phases are believed to be observed. Similar to our previous work [2] on a different composition we find the decomposition of a B2 phase during cooling from 1400°C and 1100°C temperatures to the ω" phase. No B2 APB's have been observed, indicating stability of the B2 order as high as 1400°C. The microstructure of the HT2 specimen indicates that the decomposition of the B2 phase occurs only below 1100°C during continuous cooling.

Crystallography of the new phase

Fig. 4a shows microstructure of the matrix of the HT3 specimen which consists of rotational (four) and translational (three for each rotational) domains of the ω-type phase. The structure is similar to that of the $B8_2$ phase found for the Ti_4Al_3Nb alloy [2] except for the presence of spherical (elipsoidal) precipitates uniformly distributed in the matrix. The precipitates can be imaged in dark-field separately from the matrix using reflections additional to those of the $B8_2$ phase (Fig. 4b). These reflections are in fact superlattice spots of the hexagonal reciprocal lattice of the $B8_2$ phase, as can be seen on a series of selected area diffraction (SAD) patterns taken from an area including all four rotational domains, Fig. 5a-c, (compared with those of only the $B8_2$ phase of the Ti_4Al_3Nb alloy, Fig. 5d-f).

From the SAD patterns and microdiffraction from individual domains it was found that the superlattice g vectors are $1/3\langle 11\bar{2}0\rangle^*$ of the $B8_2$ reciprocal lattice. This corresponds to a tripled hexagonal lattice of the precipitate phase: $a_p = 2a(\sin 60°)$; $c_p = c$ (a=0.458 nm, c=0.552 nm for the $B8_2$ phase [2]). Axes of the new cell with respect to the $B8_2$ are: $2a_{p1} = a_1 + 2a_2$, $a_{p2} = -2a_1 - a_2$, $c_p = c$.

The results on the crystallography of the new structure are directly confirmed by high resolution (HREM) imaging. Fig. 6 shows such an HREM image where two precipitates and the $B8_2$ matrix of one rotational domain, both in [0001] orientation, are imaged simultaneously. On that image the precipitates are translated with respect to each other by a.

Several structural models for the new phase can be suggested assuming further substitutional ordering of the $B8_2$ phase and a group/subgroup relation between the phases. The maximal non-isomorphic subgroup of the $B8_2$ $P6_3/mmc$ space group corresponding to our experimental results is centered hexagonal $H6_3/mmc$ which is equivalent to primitive hexagonal $P6_3/mcm$ with 90° rotated axes (and the c-glide plane) [5]. The subgroup has index [3] which gives the three translational variants (in fact observed in the HREM image, Fig 6). The index [3] also implies, based on the Landau-Lifschitz theory of phase transformation [6], that the ordering transformation is first order, which is consistent with the precipitation nature of the transformation.

Because the cell was tripled by the ordering, the number of atoms per unit cell is 18 (6 atoms per the $B8_2$ phase unit cell). For the cell with space group $P6_3/mcm$ and Pearson symbol hP18 we find a possible prototype phase, Ga_4Ti_5 [4]. This structure has four Wyckoff positions: (2)b 0,0,0; (4)d 1/3,2/3,0; (6)g_1 x_1,0,1/4; (6)g_2 x_2,0,1/4. For the $B8_2$ phase referred to these positions the g_1 site is occupied by Ti and g_2 by Al atoms in a double layer in Fig.1 [2]. We suggest that the observed ordering does not change the double layer, and therefore occurs entirely on a single layer. Based on the estimated compositions of the average matrix, $B8_2$ phase and precipitates, we suggest an ideal ordering on the single layer with Nb on (4)d and Al on (2)b positions. This gives a $(Ti_3Al_2)(AlNb_2)$ stoichiometry for the new phase, with occupancies Al (2)b, Nb (4)d, Ti (6)g_1, Al (6)g_2 and x_1 and x_2 slightly different from 1/3 and 2/3 of the ω-type.

Another possibility could be the Strukturbericht $D8_8$ structure, Mn_5Si_3 prototype, also with $P6_3/mcm$ space group but with 16 atoms per unit cell. For this structure the (2)b

position is vacant. The $(Ti_3Al_3)Nb_2$ stoichiometry has a good correspondence to mass balance requirements. Further HREM and X-ray diffraction work is in progress to find the correct structure.

Acknowledgement

The authors thank M.E.Williams for the TEM specimen preparation and L. Smith for the optical metallography. The work was supported by DARPA under order No. 6065.

References

1. R. Strychor, J.C. Williams and W.A. Soffa, Met. Trans. 19A, 225 (1988)
2. L.A. Bendersky, W.J. Boettinger, B.P. Burton, F.S. Biancaniello, C.B. Schumaker, to appear in Acta Met. (1990)
3. L.A. Bendersky and W.J. Boettinger, Proc. of 47th EMSA Meeting, San Francisco Press, Inc (1989) p.324
4. P. Villars and L.D. Calvert, "Pearson's Handbook of Crystallographic Data for Intermetallic Phases", Vol.1, ASM, Metals Park Oh (1985)
5. "International Tables of Crystallography", Vol. A, T. Hahn, ed., Reidel Publishing Co., Dordrecht (1978).
6. L.D. Landau and E.M. Lifschitz, "Statistical Physics", Pergamon, London (1976).

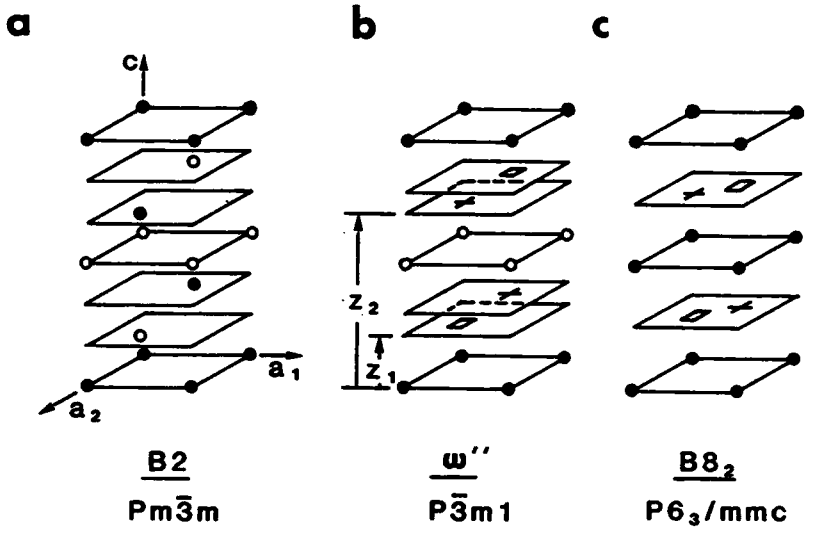

FIG. 1. Schematic drawing of (a) B2, (b) ω" and (c) $B8_2$ crystal structures. The B2 structure is shown as a stacking of (111) planes. Different symbols represent different occupancies. (From Ref. 2).

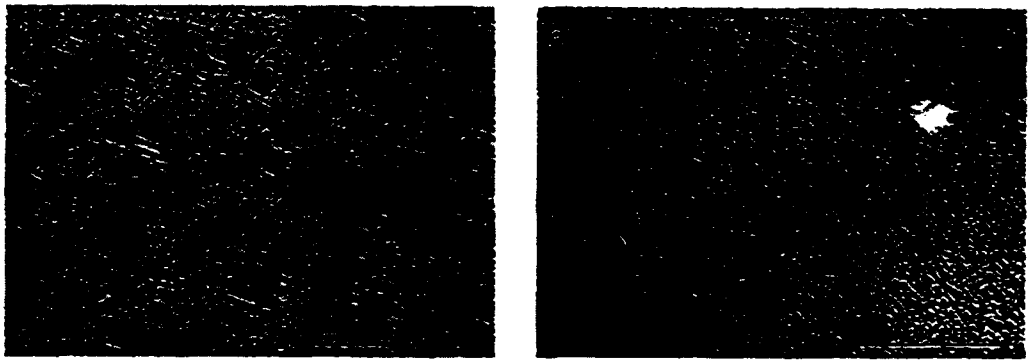

Fig. 2. Optical metallography of the (a) HT2 and (b) HT3 samples.

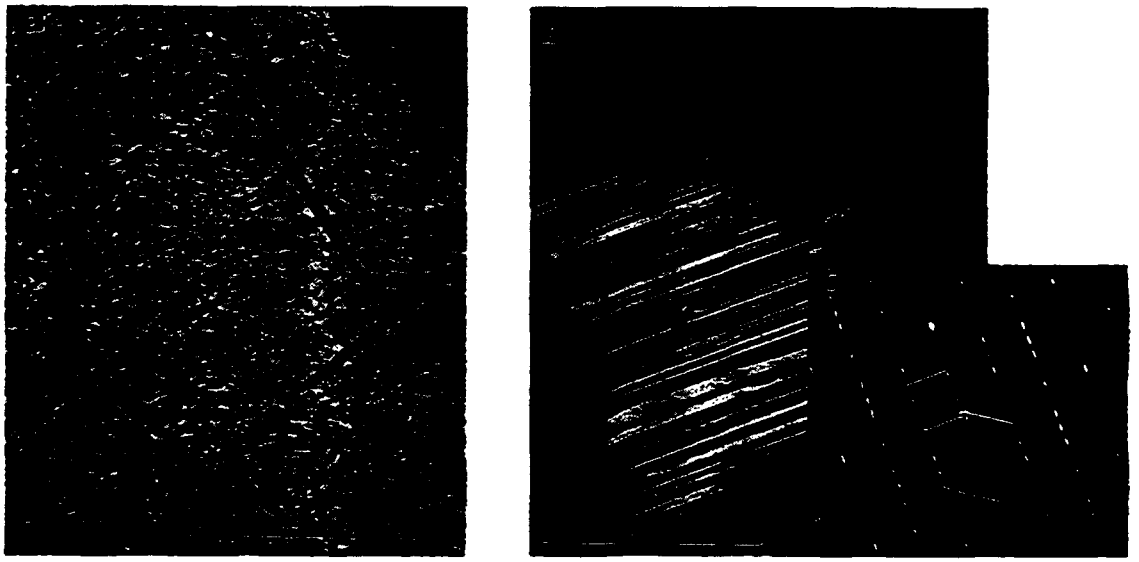

Fig. 3. TEM images of the needle-like precipitates in the HT3 (700°C) specimen matrix. (a) Low magnification image. (b) Internal structure of the precipitate and (c) the corresponding SAD pattern (smaller cell - the DO_{19} phase, [1120]; larger cell - the Ll_0 phase, [110]) showing alternating layers of the DO_{19} and Ll_0 phase and their orientation relationship.

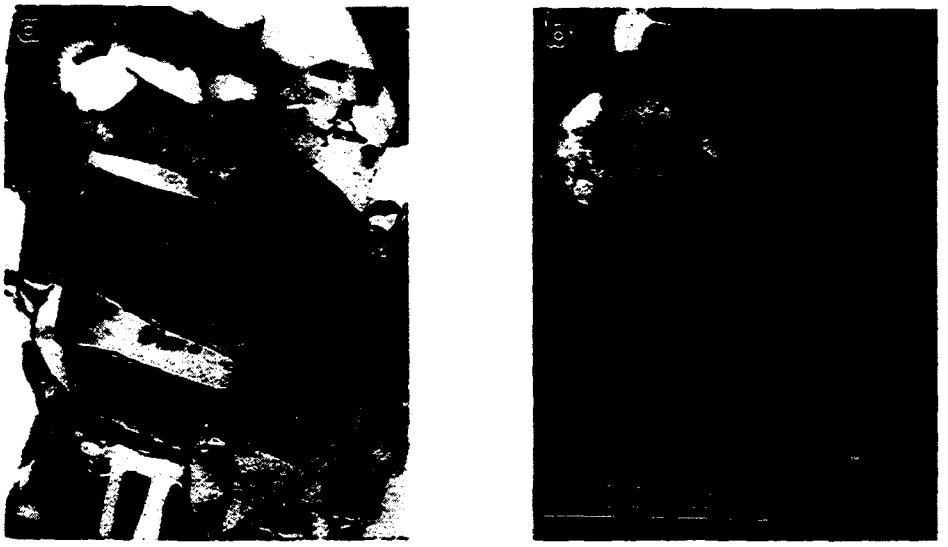

Fig. 4. Microstructure of the HT3 specimen matrix and spherical precipitates. (a) Bright-field image of several rotational and translational domains. (b) Dark-field image of the precipitates using superlattice (to $B8_2$) reflection.

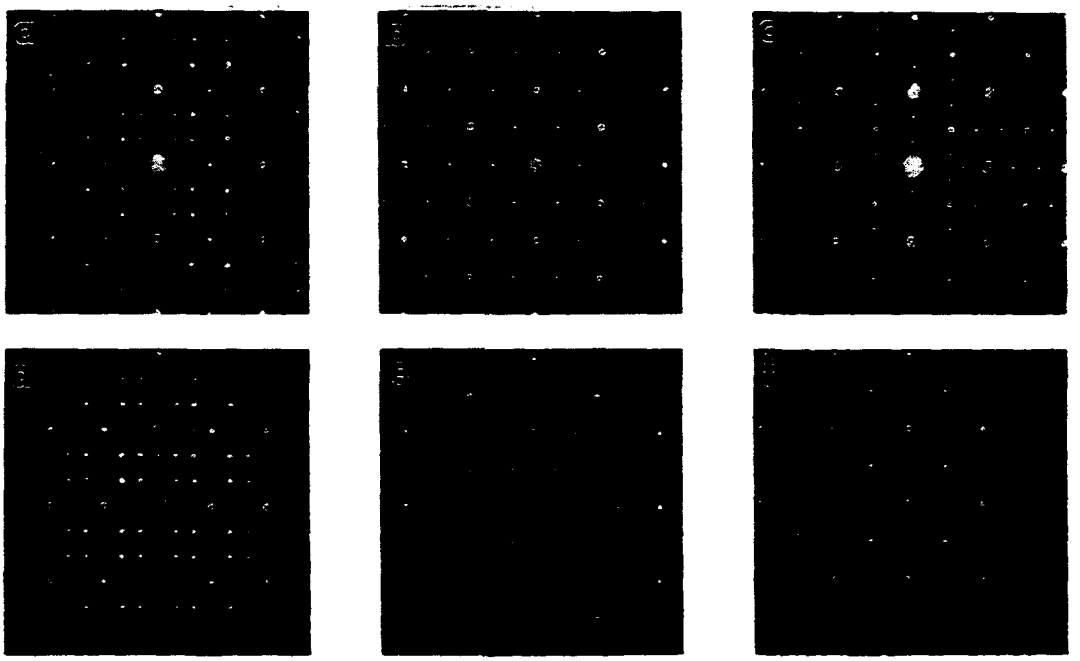

Fig. 5. (a-c) SAD patterns taken from the HT3 specimen and compared to those (d-f) from the $B8_2$ phase of the Ti_4Al_3Nb alloy. Zone axes using cubic indices are: (a,d) - <110>; (b,e) - <111>; (c,f) - <100>.

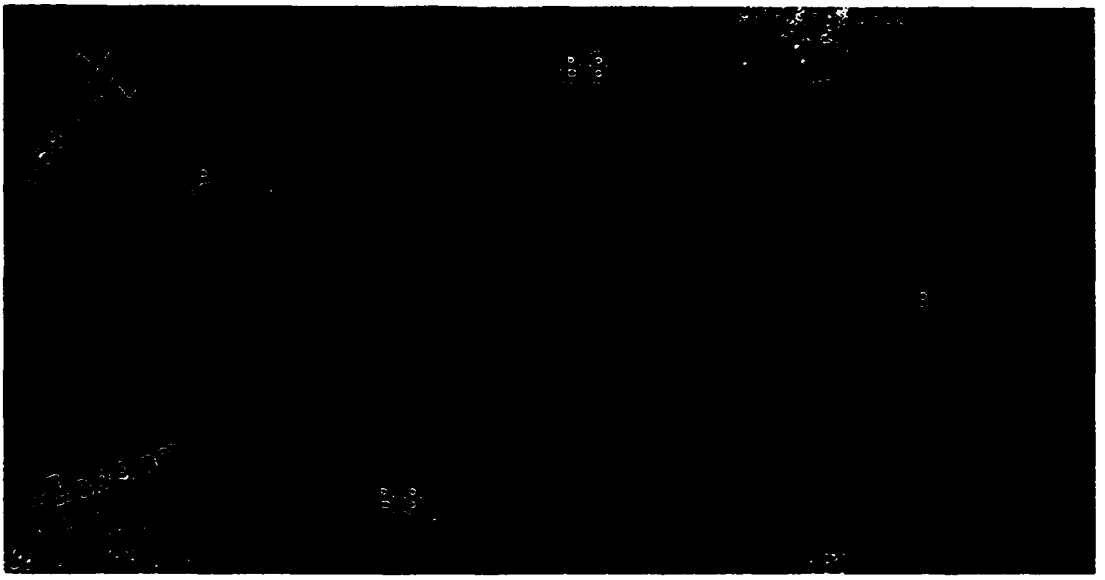

Fig. 6. HREM image of the $B8_2$ matrix and the precipitates (P) in an orientation of the [0001] parallel to the electron beam direction.

Materials Science and Engineering, A152 (1992) 41–47

Intermetallic Ti–Al–Nb alloys based on strengthening of the orthorhombic phase by ω-type phases

L. A. Bendersky, W. J. Boettinger and F. S. Biancaniello

Metallurgy Division, National Institute of Standards and Technology, Gaithersburg, MD 20899 (USA)

Abstract

The microstructure of an alloy, with composition Ti–30Al–20Nb (atomic percent), when annealed at temperatures between 700 and 900 °C for up to 18 days, consists of two intermetallic phases: orthorhombic Ti_2AlNb and ω-type $B8_2$ Ti_4Al_3Nb. The presence of the two phases in the microstructure is independent of the heat treatment path and, thus, the two phases appear to be in thermodynamic equilibrium. The potential for high strength alloys in this two-phase field, based on the combination of properties of the two different phases, is demonstrated by microhardness measurements.

1. Introduction

The need for low density structural materials with high temperature strength and low temperature ductility for aerospace applications has driven interest in titanium aluminides, especially those of the Ti–Al–Nb system. Different approaches have been utilized to produce microstructures composed of the following ordered intermetallic phases and their combinations: α_2-Ti_3Al (DO_{19}), α_2-Ti_3Al + γ-TiAl ($L1_0$) in the Ti–Al system, and α_2-Ti_3Al, α_2-Ti_3Al + β_0 (B2) in the Ti–Al–Nb system [1–3]. Very promising combinations of specific strength and rupture life at high temperature (up to 800 °C) have been achieved for an alloy with a composition close to Ti–24Al–11Nb (atomic percent) [3].

In a recent review by Rowe [3], it was indicated that the ordered O-Ti_2AlNb phase [4] may also have potential as an elevated temperature structural material. This phase has orthorhombic symmetry (*Cmcm*) which can be thought of as a ternary ordering of the α_2 lattice but also forms by a martensitic-type transformation from the high temperature B2 (β_0) phase [5, 6]. The O phase, either as a single phase or an O + β_0 structure, deforms more uniformly than the α_2 phase and exhibits higher specific strength and fracture toughness than α_2-based alloys [7].

Another ternary phase recently found in the Ti–Al–Nb system has a composition close to Ti_4Al_3Nb, and appears to occur in equilibrium with γ-TiAl and α_2-Ti_3Al phases at some temperatures [8, 9]. The ω phase forms readily from the high temperature B2 phase by a displacive transformation with subsequent chemical ordering. The ω phase has the $B8_2$ structure [9] which belongs to the class of ω-type phases. These ω-type phases lack the close-packed planes suitable for dislocation mobility. Depending on morphology and microstructure [10], the ω phase can either cause brittleness or be used as effective strengtheners (*e.g.* as with metastable ω-phase in some titanium and zirconium alloys).

Based on the compositions of the $B8_2$ and O phases, an equilibrium two-phase field between them was anticipated at elevated temperatures. Alloys in this two-phase field might exhibit the strengthening of the titanium aluminide (the O phase) by the stable ω-type phase. This combination of the ω-type and the orthorhombic phase has not been exploited in any of the previous work on titanium aluminides. The present paper presents some preliminary results which confirm the existence of the two-phase field and gives microstructures and preliminary properties of an alloy with Ti–30Al–20Nb (atomic percent) composition.

2. Experimental details

An alloy with composition Ti–30Al–20Nb (atomic percent) was prepared by arc melting and homogenizing at 1400 °C for 5 h in gettered argon. The homogenized specimens were subsequently heat treated at 1100 °C for 24 h, water quenched and then annealed at 900, 850, 800, 750 or 700 °C for different lengths of time. Annealing was performed by encapsulating tantalum foil-wrapped slices in evacuated and helium-backfilled quartz tubes. The microstructure of the alloys was studied mainly by means of transmission electron microscopy (TEM). TEM thin foils were prepared by standard twin-jet electropolishing procedure using a 300 ml methanol, 175 ml *n*-butanol and 30 ml

0921-5093/92/$5.00

$HClO_4$ electrolyte at 0 °C. Microhardness testing was performed on specimens prepared for optical metallography using a diamond pyramid indenter with a 1000 *g* load.

3. Displacive instabilities of the B2 structure

Both O and $B8_2$ phases have structural relations with the cubic B2 phase which can be described as combinations of displacive and chemical ordering. The displacive ordering for these two phases is represented by two fundamental modes: (1) shuffles of the $(110)_c$ planes in the $[1\bar{1}0]_c$ direction for the O phase and (2) shuffles (or collapse) of the $(111)_c$ planes in the $[111]_c$ direction for the $B8_2$ phase [4, 9]. These two modes are known to manifest themselves in the lattice dynamics of the b.c.c. (or B2) structure prior to the transformation by the softening of some elastic constants and the presence of anomalies in the phonon dispersion curve. These phenomena (often referred to in the literature as pre-martensitic) are readily observed in the tweed contrast and the diffuse scattering in TEM images and selected area diffraction (SAD) patterns taken from samples quenched from high temperature.

Such SAD patterns taken in a $[110]_c$ zone axis orientation are shown in Figs. 1(a) and 1(b) for specimens water quenched from 1100 °C for the Ti_2AlNb and Ti_4Al_3Nb alloys. Loci of diffuse intensity (in addition to distortion and streaking of the B2 reflections) are located at distinct point in reciprocal space, close to $1/2(1\bar{1}2)^*$ for the Ti_2AlNb and $1/3(1\bar{1}1)^*$, and $1/3(1\bar{1}2)^*$ for the Ti_4Al_3Nb alloys (arrows in Fig. 1). These are positions where reflections from different crystallographic variants of the corresponding low temperature phases are to be expected. For slowly cooled and fully transformed alloys such reflections (from six rotational variants of the O phase for Ti_2AlNb and four rotational variants of the $B8_2$ phase for Ti_4Al_3Nb) are seen in Figs. 2(a) and 2(b) where the SAD patterns are in a $[110]_c$ orientation. Figures 2(c) and 2(d) show images of the corresponding microstructures where (c) the O phase has a plate-like appearance and (d) the $B8_2$ phase has equiaxed grains.

For the Ti-30Al-20Nb (atomic percent) alloy, whose composition lies between the two alloys discussed above, both modes of the displacive transformation can be present simultaneously. Figure 3 shows a SAD pattern in a $[110]_c$ orientation from the B2 phase retained after water quenching from 1100 °C. (At 1100 °C a small amount of the DO_{19} phase is present, but the B2 phase has a composition close to the nominal composition of the alloy.) The diffuse scattering observed in the SAD patterns indeed represents both displacive modes with contributions of comparable intensity. Our preliminary results show that the relative amount of the two modes can be sensitive to the cooling history and to the local composition.

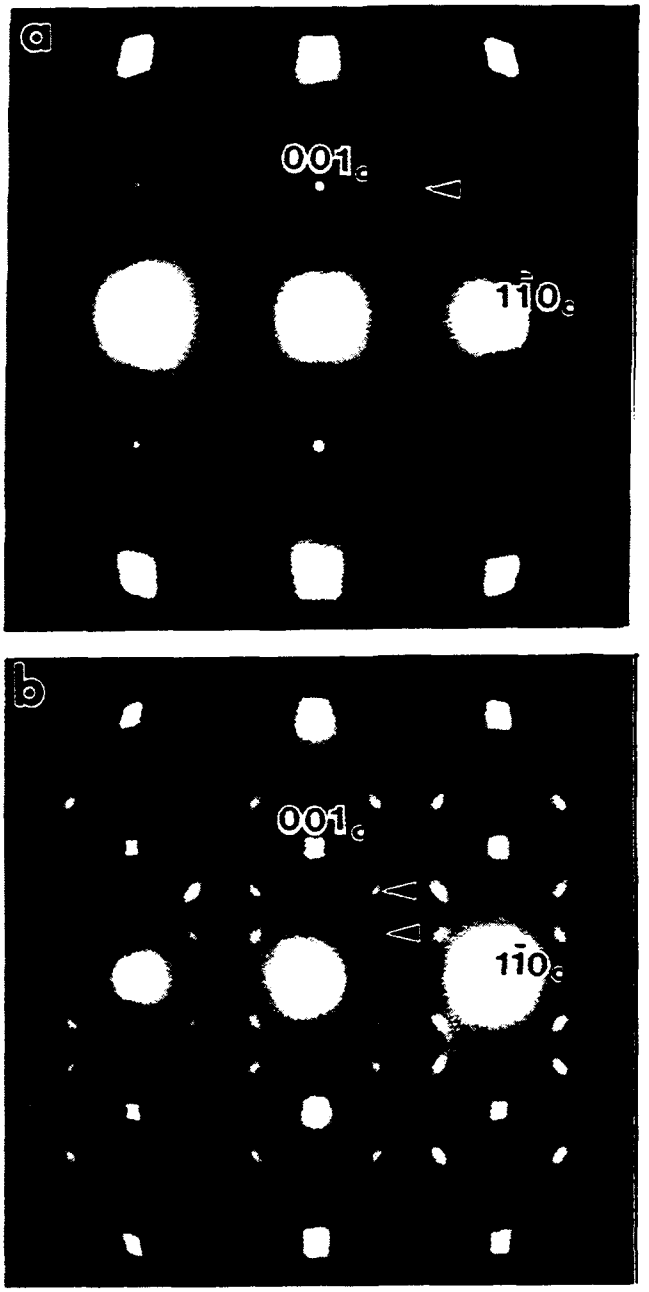

Fig. 1. SAD patterns in a $[110]_c$ zone axis orientation taken from the B2 phase of the (a) Ti_2AlNb and (b) Ti_4Al_3Nb alloys water quenched from 1100 °C.

4. Microstructures after annealing at elevated temperatures

Annealing at elevated temperatures (700–900 °C) produces a two-phase microstructure. As Figs. 4 and 5

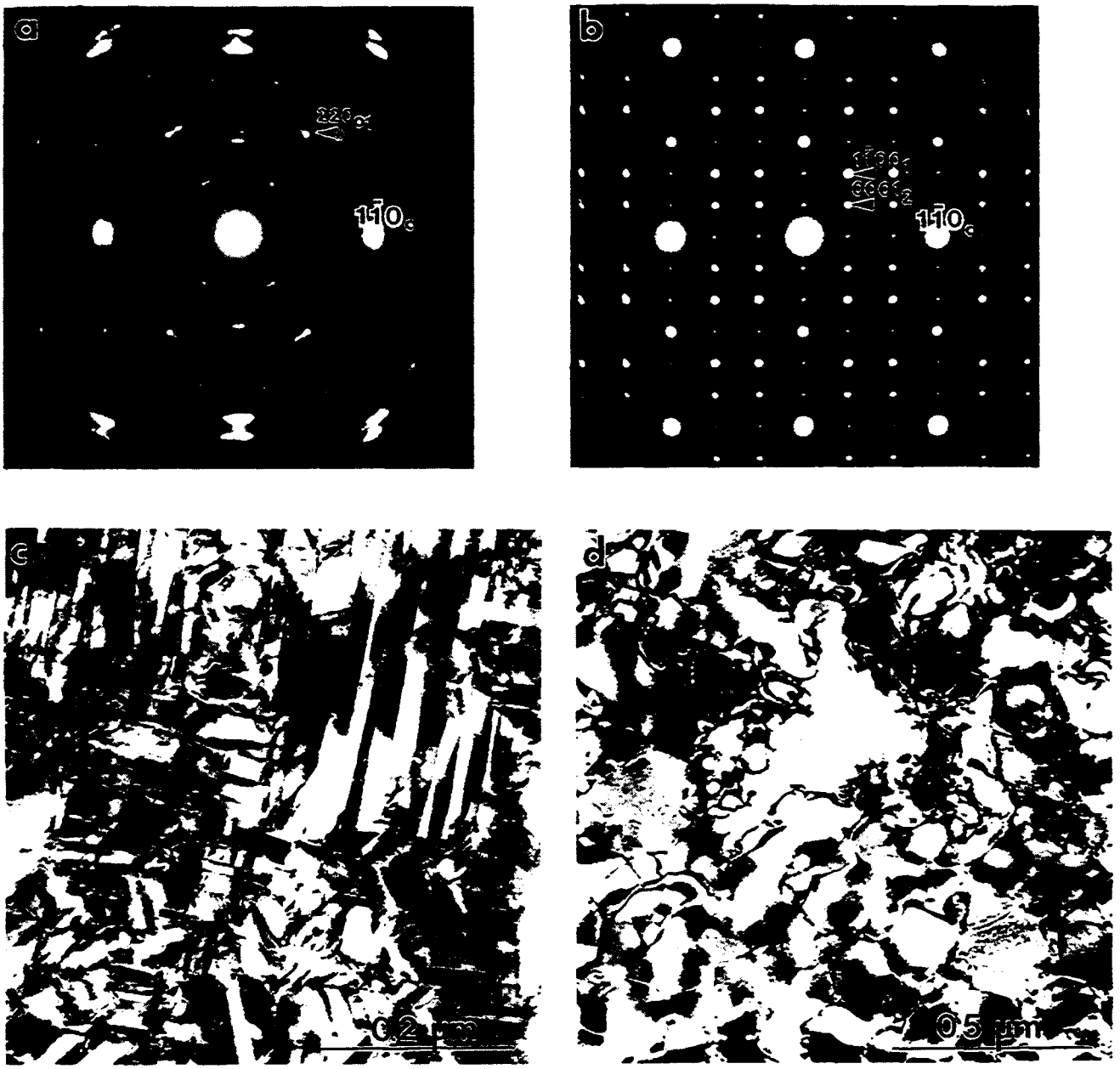

Fig. 2. SAD patterns from the multiple variants of (a) the O phase, Ti_2AlNb alloy and (b) the $B8_2$ phase, Ti_4Al_3Nb alloy in the $[110]_c$ orientation after slow cooling from the B2 region; (c) and (d) are the images of the corresponding microstructures.

show, the microstructure obtained for the Ti–30Al–20Nb alloy after annealing at 700 °C for 18 days consists of a homogeneous distribution of fine domains of both the O and $B8_2$ phases. The SAD patterns of Fig. 4, taken in (a) $[110]_c$ and (b) $[111]_c$ zone axis orientations, show the presence of reflections from both phases in orientation relationships (compared with the transformed B2 phase and with each other) which are the same as those in the SAD patterns of Figs. 2(a) and 2(b). The pattern in Fig. 4(a) is essentially a superposition of Figs. 2(a) and 2(b). The Fig. 4(b) pattern shows reflections of one of the $B8_2$ variants at the $1/3\langle 112\rangle_c$ position ($[0001]_\omega \| [110]_c$), and a triplet of surrounding reflections which belong to three variants of the O phase ($\langle 110\rangle_o \| [110]_c$). Figure 5(a) shows a bright field image of the microstructure in the $[110]_c$ orientation, and Figs. 5(b) and 5(c) shows dark field images of the microstructure taken with reflections belonging to a single variant of either (b) the O phase or (c) the $B8_2$ phase. Similar to the microstructures of

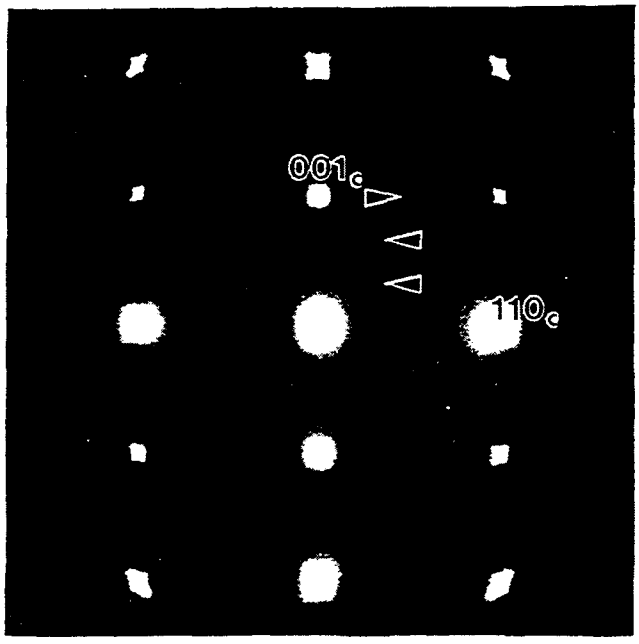

Fig. 3. SAD pattern in a $[110]_c$ orientation taken from the Ti–30Al–20Nb B2 phase retained after quenching in water from 1100 °C. The diffuse scattering in the SAD pattern (arrows) represents two displacive modes of transformation: the $\frac{1}{2}110$ $1\bar{1}0$ and the $\frac{1}{2}111$ $\bar{1}11$ modes.

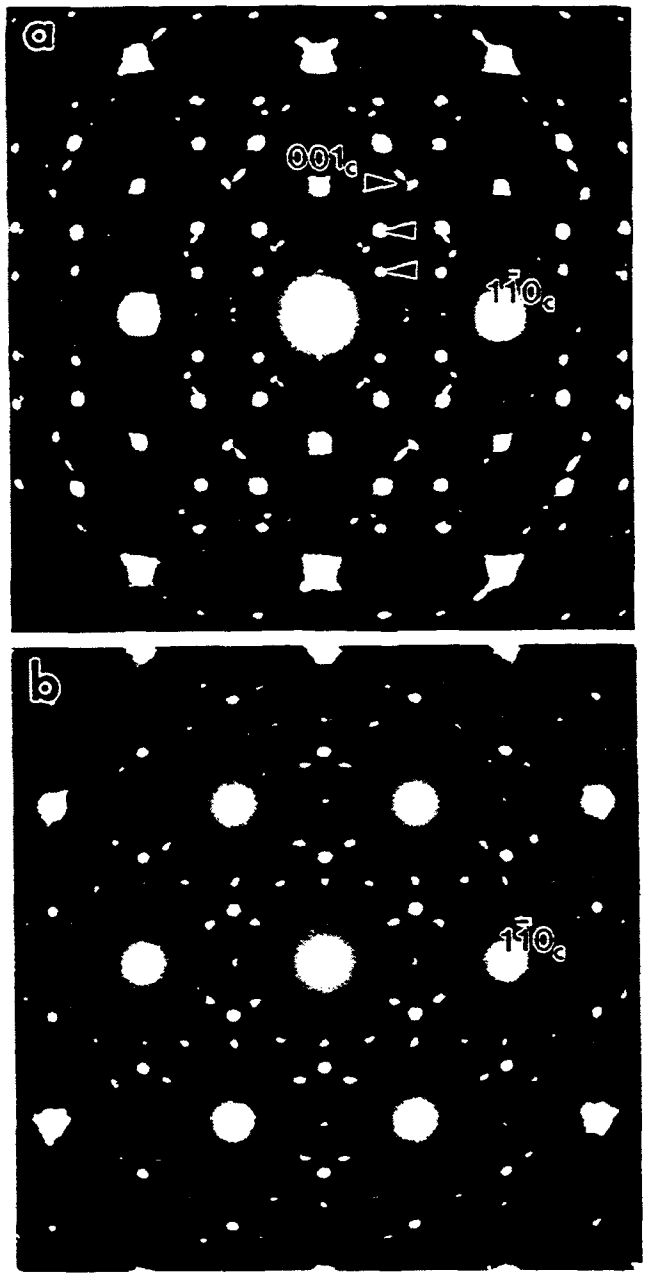

Fig. 4. SAD patterns taken from the Ti–30Al–20Nb alloy after annealing at 700 °C for 18 days in a $[110]_c$ (a) and a $[111]_c$ (b) zone axis orientation. The SAD patterns show the presence of reflections from both O and $B8_2$ phases in orientation relationships similar to those of the SAD patterns of Fig. 2 (a and b).

single phase alloys, the O phase appears in a plate-like form (Fig. 5(b)) whereas the $B8_2$ phase exists as round particles (Fig. 5(c)).

The two-phase structure is highly stable and resists to coarsening at temperatures where other Ti–Al–Nb alloys are structurally unstable after prolonged heat treatments. This instability can lead to premature failures [11, 12]. Compared with a single phase Ti_2AlNb alloy, the two-phase structure of the Ti–30Al–20Nb alloy remains fine after annealing for 18 days at 700 °C. The Ti_2AlNb alloy microstructure recrystallized after a few days (in some specimens after a few hours) at this same temperature [13]. Figure 6(a) shows a partially recrystallized region of the Ti_2AlNb alloy observed after 24 h of annealing at 700 °C where a large single grain is seen consuming an original fine-plate structure. Figure 6(b) shows another coarsening process in the Ti_2AlNb alloy which proceeds by thickening of some plates and disappearance of others.

The distribution of the O and $B8_2$ phases in the Ti–30Al–20Nb alloy can be controlled either by changes in cooling rate or by the temperature at which the quenched material is equilibrated. As preliminary results indicate, the microstructure can be very different for different heat treatment schedules. For example, Fig. 7 compares microstructures obtained by two different heat treatments, both with a final equilibration at 700 °C. The first one, Fig. 7(a), involved continuous fast cooling from 1400 °C to room temperature with subsequent annealing at 700 °C for 18 days. The second one, Fig. 7(b), involved slow cooling from 1100 to 700 °C and annealing at 700 °C for 5 days. Even though the second heat treatment was shorter, the O + $B8_2$ microstructure is noticeably coarser. Clearly the differences in microstructures are related to the

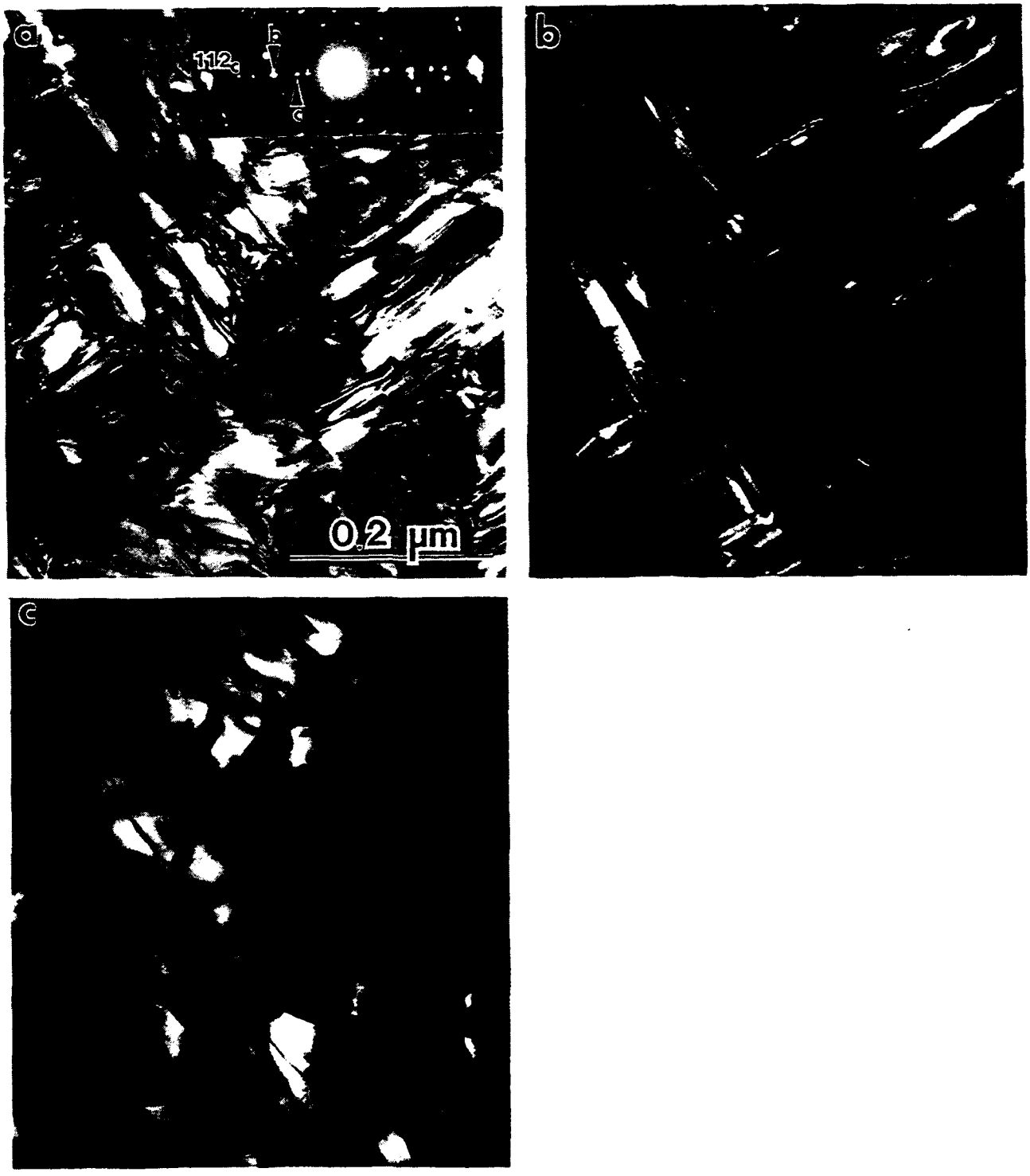

Fig. 5. The microstructure of the Ti–30Al–20Nb alloy after annealing at 700 °C for 18 days consisting of a homogeneous distribution of fine domains of the O and $B8_2$ phases. (a) Is a bright field image: (b) and (c) are dark field images taken with reflections belonging to a single variant of the O or $B8_2$ phases respectively.

competition between the formation of the O and $B8_2$ phase from the cubic phase. The details of this competition depend on the thermodynamic instability temperatures of the cubic phase and the formation kinetics for the two phases.

5. Microhardness

Preliminary room temperature microhardness tests were performed on the Ti–30Al–20Nb alloy following different heat treatments. The best result obtained so

far was for a specimen annealed at 700 °C for 18 days: 617–626 Vickers hardness (VHN) for a 1000 g load, without noticeable cracking. This hardness is higher than the best result found in the literature for alloys based on the orthorhombic phase, Ti–23.5Al–24Nb (308 VHN) [3], and for alloys based on the α_2

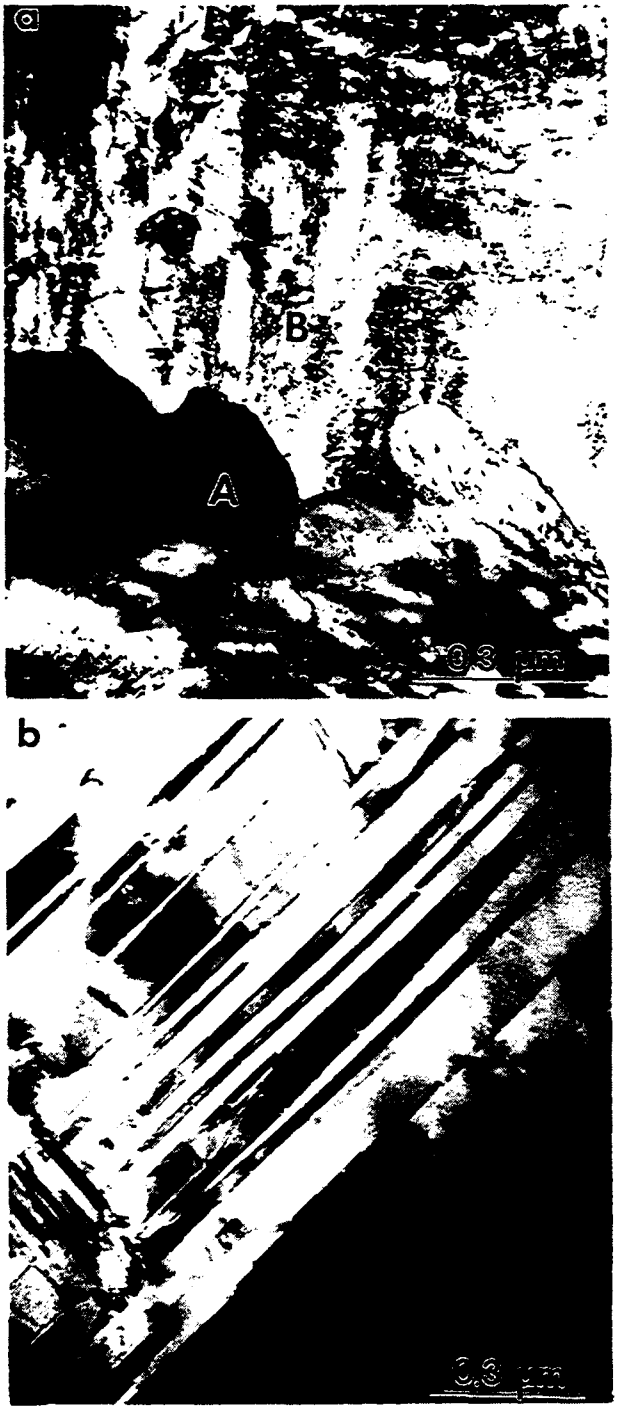

Fig. 6. Bright field images of a partially recrystallized region of the Ti_3AlNb alloy observed after 24 h annealing at 700 °C. (a) A large single grain A is consuming an original fine-plate structure B. (b) Another type of coarsening process proceeding by thickening of some plates and disappearance of others.

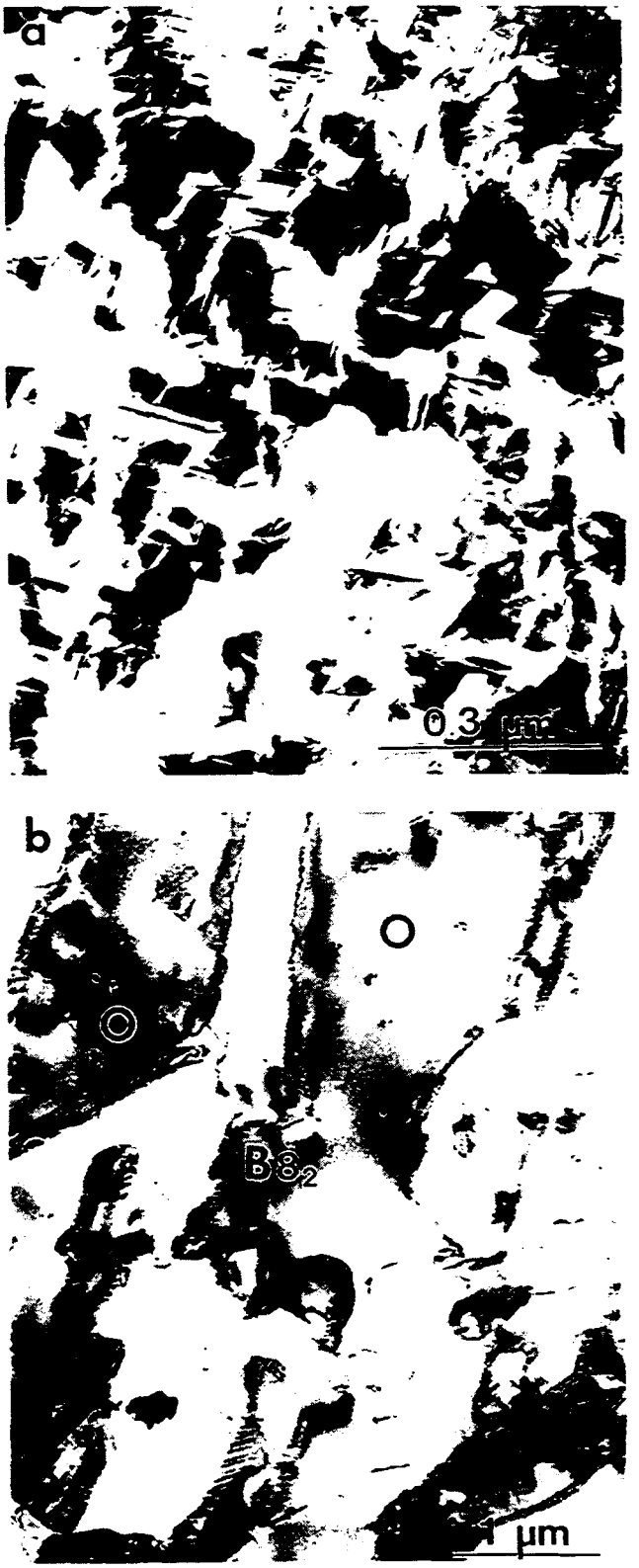

Fig. 7. Microstructures of the Ti–30Al–20Nb alloy obtained by two different heat treatments, both with a final equilibration at 700 °C. (a) After continuous fast cooling from 1400 °C to room temperature with subsequent annealing at 700 °C for 18 days. (b) After slow cooling from 1100 to 700 °C and subsequent annealing for 5 days.

phase, Ti–(24–26)Al–11Nb (470 VHN) [14, 15] and Ti–26.1Al–9.61Nb–2.9V–0.9Mo (440 VHN) [13].

6. Conclusions

The microstructure of an alloy with composition Ti–30Al–20Nb (atomic percent) has been analyzed in the present paper. When annealed at 700–900 °C for up to 18 days, the alloy consists of two intermetallic phases—orthorhombic Ti_2AlNb and ω-type $B8_2$ Ti_4Al_3Nb. The identity of the two phases in the microstructure is independent of heat treatment path. Thus, the two phases appear to be in thermodynamic equilibrium with each other between 700 and 900 °C. The potential for high strength based on the idea of combination of properties of the two different phases was demonstrated by microhardness measurements.

Acknowledgments

The authors acknowledge the effort of M. E. Williams and L. C. Smith. This research was partially supported under DARPA Order 7469.

References

1 C. T. Liu, A. I. Taub, N. S. Stoloff and C. C. Koch (eds.), *High-Temperature Ordered Intermetallic Alloys III, Materials Research Society Symposium Proceedings 133*, Materials Research Society, Pittsburgh, 1989.
2 O. Izumi (ed.), *Proc. Int. Symp. Intermetallic Compounds—Structure and Mechanical Properties*, Japan Institute of Metals, 1991.
3 R G. Rowe, in S. H. Whang, C. T. Liu, D. P. Pope and J. O. Stiegler (eds.), *High Temperature Aluminides and Intermetallics*, TMS–AIME, Warrendale, 1990, pp. 375–401.
4 D. Banerjee, A. K. Gogia, T. K. Nandi and V. A. Joshi, *Acta Metall., 36* (1988) 871.
5 B. Mozer, L. A. Bendersky, W. J. Boettinger and R. G Rowe, *Scr. Metall., 24* (1990) 2363.
6 L. A. Bendersky, W. J. Boettinger and A. Roitburd, in O. Izumi (ed.), *Proc. Int. Symp. Intermetallic Compounds—Structure and Mechanical Properties*, Japan Institute of Metals, 1991, p. 845.
7 R. G. Rowe, D. Konitzer, A. Woodfield and J. C. Chesnutt, in *Materials Research Society Symposium Proceedings 213*, Materials Research Society, Pittsburgh, 1990, p. 703.
8 R. Strychor, T. C. Williams and W. A. Soffa, *Met. Trans. A, 19* (1988) 1321.
9 L. A. Bendersky, W. J. Boettinger, B. Burton, F. S. Biancaniello and C. B. Shoemaker, *Acta Metall., 38* (1990) 931.
10 S. K. Sikka, Y. K. Vohra and R. Chidambaram, *Progr. Mater. Sci., 27* (1982) 245.
11 C. H. Ward, J. C. Williams and A. W. Thompson, *Scr. Metall., 24* (1990) 617.
12 R. G. Rowe and M. F. X. Gigliotti, *Scr. Metall., 24* (1990) 1209.
13 L. A. Bendersky, W. J. Boettinger and A. Roitburd, *Acta Metall., 39* (1991) 1959.
14 H. T. Weykamp, D. R. Baker, D. M. Paxton and M. J. Kaufman, *Scr. Metall., 24* (1990) 445.
15 W. A. Baeslack III and T. Broderick, *Scr. Metall., 24* (1990) 319.

Materials Science and Engineering, A152 (1992) 9–17

Thermodynamic calculation of the ternary Ti–Al–Nb system

U. R. Kattner* and W. J. Boettinger

Metallurgy Division, National Institute of Standards and Technology, Gaithersburg, MD 20899 (USA)

Abstract

Phase equilibria of the ternary Ti–Al–Nb system are dominated by the large range of homogeneity of (β-Ti,Nb), the binary intermetallic compounds of the Nb–Al and Ti–Al systems and the formation of two ternary compounds. The available ternary experimental data, together with a thermodynamic extrapolation of the ternary system from the binary systems, have been used to calculate the ternary phase diagram. The model descriptions of the Gibbs energies of most of these compounds are given by the existing calculations of the binary systems. In order to model a phase which is present in only one binary system, but has a ternary homogeneity range, a hypothetical phase with the same structure was analytically described for each binary system. Such a phase would, of course, be metastable in the other binary systems. Constraints on the Gibbs energies of formation were derived from the crystal structures of the corresponding ordered compounds. These same constraints were employed for the corresponding phases in the ternary system. In a final optimization step, ternary parameters were introduced and adjusted to the available experimental data. The as-derived description of the ternary Ti–Al–Nb system can be used to estimate single or multiphase fields and thermodynamic quantities where no experimental data are yet available. It is also useful as an indicator of problem areas for which additional experimental data are required.

1. Introduction

The Ti–Al–Nb system is of interest for the development of high temperature/low density intermetallic materials. Knowledge of stable and metastable phase relations in multicomponent materials provides valuable information for the development of processing strategies for these materials. Once derived, this thermodynamic description can be used to provide information which is not easily accessible through experimental techniques, such as metastable extensions or the temperatures where two phases have the same Gibbs energies at a given composition (T_0 curves).

Despite their importance, the phase relationships of this system are only partially known for certain temperature regimes [1–8]. From the available experimental data the following points can be determined.

(1) The intermetallic compounds of the binary Nb–Al and Ti–Al systems have relatively wide ranges of homogeneity in the ternary system.

(2) The compounds $NbAl_3$ and $TiAl_3$ form a continuous ($D0_{22}$) solid solution.

(3) At least two ternary compounds exist near the compositions Ti_2AlNb and Ti_4Al_3Nb.

(4) The (β-Ti,Nb) phase with b.c.c. structure orders to the (β_0-Ti,Nb) with B2 (CsCl) structure.

(5) A miscibility gap may exist in the ordered (β_0-Ti,Nb) phase.

The available ternary experimental data, together with a thermodynamic extrapolation of the ternary system from the binary systems, have been used to calculate the ternary phase diagram. This attempt at modeling the Ti–Al–Nb system must be viewed as preliminary. However, it provides a basis for the combination of data from several sources in a thermodynamically consistent manner and indicates composition and temperature regimes where further experimentation is essential. A continued interchange between calculation and experimentation is the quickest route to the true diagram.

2. History of calculations of the Ti–Al–Nb system

Previous calculations of the Ti–Al–Nb system were based on the then accepted calculations of the binary systems and available experimental data. In a first calculation of the Ti–Al–Nb system [9], the thermodynamic descriptions of the binary systems of Nb–Al and Ti–Al by Murray [10, 11] and of Ti–Nb by Kaufman and Bernstein [12] were used. Since this calculation, the experimental data and thermodynamic descriptions of the binary Ti–Al and Nb–Al systems have been subject to revision. For the calculation of the Nb–Al system, Murray [10] used phase diagram as well

*Also at: Department of Materials Science and Engineering, University of Wisconsin-Madison, Madison, WI 53706, USA.

0921-5093/92/$5.00

as thermodynamic data to derive the thermodynamic description for this system. A re-evaluation of the experimental data for this system suggested that some of the thermodynamic data are inconsistent with the phase diagram data. The calculation based on this re-evaluation yielded a simplified thermodynamic description and a more accurate fit between the calculated and experimental phase boundaries [13]. For the Ti–Al system, new experimental results showed that (α-Ti) is in equilibrium with the liquid phase and higher liquidus temperatures were established for the composition range of 35–80 at.% Al. These changes in the experimental phase diagram are reflected by a series of calculations in the literature (see Kattner *et al.* [14] for a summary).

Since the accuracy of the thermodynamic descriptions of the binary systems is crucial for the calculation of a ternary phase diagram, the most recent calculations of the binary Nb–Al and Ti–Al systems were used for a new approximation of the Ti–Al–Nb system. These three calculated binaries are shown in Fig. 1.

3. Available experimental data

The available experimental data for the Ti–Al–Nb system are sparse when compared with the complexity of this system. Most of the experimental information is available for the isothermal section at 1200 °C. The tie-line data of refs. 6 and 15 are in good agreement and establish the phase boundaries with sufficient accuracy. The data of ref. 2 for the (β-Ti,Nb)–Nb_3Al–Nb_2Al and Nb_2Al–TiAl–(Ti,Nb)Al_3 three-phase equilibria are in general agreement with the phase boundaries indicated by refs. 6 and 15. It is noteworthy to mention that the tie-line data of ref. 6 indicate an isolated single-phase area near the composition $Nb_{10}Al_{45}Ti_{45}$. This single phase is believed to have the B2 (CsCl) structure. It is also known that the (β-Ti,Nb) phase undergoes an ordering transition from the disordered b.c.c. structure to the ordered B2 structure (β_0-Ti,Nb) in the ternary system [1, 3, 6]. The occurrence of two single-phase fields with the same crystal structure is suggestive of a miscibility gap.

Most of the experimental data which are available for the 1100 °C section determine the (β-Ti,Nb)–Ti_3Al boundary. The data of Perepezko [7] show a relatively wide two-phase area, while the data of Muraleedharan and Banerjee [4] show a relatively narrow one. Further experimental data report a tie-line for (β_0-Ti,Nb)–Nb_2Al [1], as well as data for two tie-triangles (β_0-Ti,Nb)–Nb_2Al–TiAl [16] and (β_0-TiNb)–Ti_3Al–TiAl [5]. The compositions of the (β_0-Ti,Nb) phase reported for these two three-phase equilibria are contradictory to the extrapolation of the phase boundary data given by Perepezko [7]. This conflict can be resolved if the assumption is made that two single-phase areas of the (β_0-Ti,Nb) phase also exist at this temperature. In this case one (β_0-Ti,Nb) would be

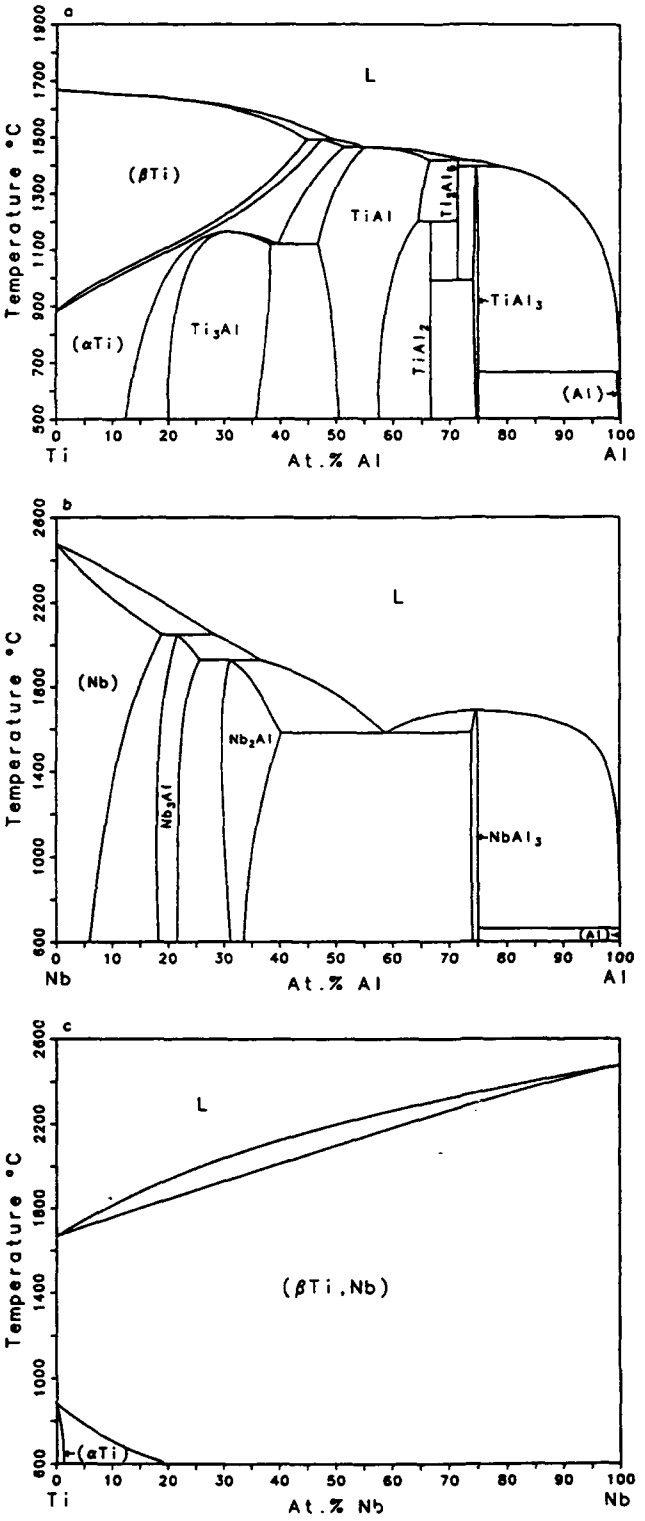

Fig. 1. The calculated binary phase diagrams. (a) Ti–Al, (b) Nb–Al and (c) Ti–Nb.

observed in the three-phase equilibria [8], while the other (β_0-Ti,Nb) was observed by Perepezko [7].

For temperatures other than 1200 and 1100 °C, only few tie-line data are available. For 700 °C, Bendersky *et al.* [8] reported tie-line data between (β-Ti,Nb) and Ti_2AlNb, and Bendersky *et al.* [5] reported data between Ti_4Al_3Nb and TiAl in equilibrium with a trace of Ti_3Al.

Experimental data involving the liquid phase are available only for the $TiAl_3$-rich part of the quasibinary $NbAl_3$–$TiAl_3$ section [6]. Based on the observation of primary fields of crystallization and preliminary differential thermal analysis (DTA) results, Perepezko *et al.* [6] proposed an estimated liquidus projection.

Experimental results have established the existence of two ternary compounds: Ti_2AlNb [17] and Ti_4Al_3Nb [5]. The Ti_2AlNb compound has an orthorhombic ordered structure. It is based on ternary ordering of the $D0_{19}$ structure of Ti_3Al which is an ordered derivative of h.c.p. The Ti_4Al_3Nb compound has the $B8_2$ (Ni_2In) structure and is believed to have a relatively small range of homogeneity. Neither ternary compound was observed in alloys that were annealed at 1100 °C [5, 8] or higher temperatures. Bendersky *et al.* [8] reported the occurrence of the Ti_2AlNb compound in samples that were annealed at and below 970 °C, and the Ti_4Al_3Nb compound was observed in samples that were annealed at 700 °C [5].

4. Analytical description of the phases

The phases considered in the calculation of the Ti–Al–Nb system are the disordered solution phases (liquid, (β-Ti,Nb), (α-Ti) and (Al)), the ordered intermetallic compounds of the Nb–Al and Ti–Al binaries (Nb_3Al, Nb_2Al, $(Ti,Nb)Al_3$, Ti_3Al, TiAl, $TiAl_2$ and Ti_2Al_5) and the ordered ternary compounds (Ti_2AlNb and Ti_4Al_3Nb). Since the transition between disordered (β-Ti,Nb) and ordered (β_0-Ti,Nb) is believed to be a second-order transition, and in order to keep the analytical description as simple as possible, these two structures will not be distinguished in the present calculation; both are represented as the (β-Ti,Nb) phase.

For the calculation of phase equilibria, the Gibbs energies (G) of the phases present must be expressed as analytical functions of the variables of interest, *i.e.* composition and temperature. For the calculation of the ternary system, the type of equation (model) for the phases existing in the binaries has been predetermined by the thermodynamic description used in the calculation of the binary systems. In all three binary systems the disordered solution phases were described with quasi-subregular solution models. The ranges of homogeneity of the ordered intermetallic compounds were described with a sublattice model, considering two or more sublattices and allowing substitution to occur on at least one of them. Phases for which few data were available on their homogeneity ranges were assumed to be stoichiometric. For the present calculation, the program PMLFKT by Lukas *et al.* [18] was used. In this program the different model descriptions can all be treated with an equation of the form

$$G^i = \sum_l a^l \sum_k y_k (G_k + RT \ln(y_k)) + \sum_j A_j y_p y_q v_p^{m-1} v_q^{n-1} + \sum_{jj} B_{jj} y_p^m y_q^n y_r^o$$

with

$$v_p = y_p + (1 - y_p - y_q)$$

and

$$v_q = y_q + (1 - y_p - y_q)$$

where i is the phase index; l is the sublattice index; k, p, q, r are the species indices; j is the polynomial index (binary terms); jj is the polynomial index (ternary terms); G^i is the molar Gibbs energy of phase i; a^l is the fraction of sublattice l in phase i; y_k, y_p, y_q, y_r are the concentration of species, referred to 1 mole of sublattice sites; G_k is the Gibbs energy of species k; A_j is the Gibbs energy coefficients of binary polynomial terms; B_{jj} is the Gibbs energy coefficients of ternary polynomial terms; and m,n,o are the exponents of polynomial terms. The G_k, A_j and B_{jj} parameters are either constant or linear functions of the temperature. The exponents m, n and o as well as the indices p, q and r are given individually for each j or jj.

The first term on the right-hand side of eqn. (1) represents the Gibbs energies of the species and their contribution to the configurational entropy, the second and third term are binary and ternary polynomial interaction energies, respectively. The polynomial interaction terms consist of two types (as seen in Table 1). Terms involving products of concentrations on different sublattices correspond to the energy of formation of the phase with only one species present on each sublattice. Terms involving products of concentrations on the same sublattice correspond to the change in energy owing to the mixing of the species on this sublattice.

The above equation reduces to the binary quasi-subregular solution model if only one sublattice ($l = 1$ and $a^1 = 1.0$) is considered. In this case the species concentration, y_k, is identical to the elemental concentration, x_k, and therefore, the variable x_k is used instead of y_k, and with

$$v_1 = x_1 + (1 - x_1 - x_2) = x_1$$

TABLE 1. Thermodynamic description of the Ti–Al–Nb system (all quantities are given in J mol^{-1})

Multiplier	Parameter G_k, A_j or B_{ij}
Liquid	
x_{Nb}	0.00
x_{Al}	0.00
x_{Ti}	0.00
$x_{Nb}x_{Al}v_{Nb}^{2}$	$-103737.10+29.45904\,T$
$x_{Nb}x_{Al}v_{Nb}v_{Al}$	$-289716.20+87.97006\,T$
$x_{Nb}x_{Al}v_{Al}^{2}$	$-127713.10+58.51102\,T$
$x_{Ti}x_{Al}v_{Ti}$	$-120521.00+41.11378\,T$
$x_{Ti}x_{Al}v_{Al}$	$-104619.40+41.11378\,T$
$x_{Ti}x_{Nb}$	13058.26
$x_{Nb}x_{Al}x_{Ti}$	−100000.00
(β-Ti,Nb)	
x_{Nb}	$-30000.00+10.90910\,T$
x_{Al}	$-628.00+6.65980\,T$
x_{Ti}	$-14146.00+7.28800\,T$
$x_{Nb}x_{Al}v_{Nb}$	$-133982.50+41.69422\,T$
$x_{Nb}x_{Al}v_{Al}$	$-125401.50+41.69422\,T$
$x_{Ti}x_{Al}$	$-129396.70+40.06310\,T$
$x_{Ti}x_{Nb}$	13075.00
$x_{Nb}^{2}x_{Al}x_{Ti}$	$-80000.00+60.00000\,T$
$x_{Nb}x_{Al}^{2}x_{Ti}$	$-180000.00+60.00000\,T$
$x_{Nb}x_{Al}x_{Ti}^{2}$	$-70000.00+60.00000\,T$
(α-Ti)	
x_{Nb}	$-13000.00+9.70910\,T$
x_{Al}	$-5151.40+9.61780\,T$
x_{Ti}	$-18316.00+10.89840\,T$
$x_{Nb}x_{Al}$	$-120000.00+40.00000\,T$
$x_{Ti}x_{Al}v_{Ti}$	$-139823.40+45.39174\,T$
$x_{Ti}x_{Al}v_{Al}$	$-107753.60+21.02630\,T$
$x_{Ti}x_{Nb}$	13075.00
$x_{Nb}x_{Al}x_{Ti}$	−115000.00
(Al)	
x_{Nb}	$-8000.00+8.70910\,T$
x_{Al}	$-10711.00+11.47280\,T$
x_{Ti}	$-12316.00+10.79840\,T$
$x_{Nb}x_{Al}$	$-185783.30+92.57490\,T$
$x_{Ti}x_{Al}$	$-124269.60+43.89675\,T$
$x_{Ti}x_{Nb}$	13075.00
Nb_3Al (two sublattices)	
Niobium sublattice: $a^{Nb}=0.75$	
y_{Nb}^{Nb}	$-24500.00+10.35910\,T$
y_{Al}^{Nb}	$-3148.80+7.86305\,T$
y_{Ti}^{Nb}	$-13688.50+8.16560\,T$
$y_{Nb}^{Nb}y_{Ti}^{Nb}$	9806.25
Aluminum sublattice: $a^{Al}=0.25\,T$	
y_{Nb}^{Al}	$-24500.00+10.35910\,T$
y_{Al}^{Al}	$-3148.80+7.86305\,T$
y_{Ti}^{Al}	$-13688.50+8.16560\,T$
$y_{Al}^{Al}y_{Nb}^{Al}$	$-8675.01+2.47012\,T$
$y_{Nb}^{Al}y_{Ti}^{Al}$	3268.75
$y_{Ti}^{Al}y_{Al}^{Al}$	−4000.00
Polynomial terms between species on different sublattices	
$y_{Nb}^{Nb}y_{Al}^{Al}$	$-35518.50+6.93617\,T$
$y_{Al}^{Nb}y_{Nb}^{Al}$	$35518.50-6.93617\,T$
$y_{Ti}^{Nb}y_{Al}^{Al}$	$-26000.00+7.00000\,T$
$y_{Al}^{Nb}y_{Ti}^{Al}$	$26000.00-7.00000\,T$
$y_{Nb}^{Nb}y_{Ti}^{Nb}y_{Al}^{Al}$	−6000.00
Nb_2Al (three sublattices)	
Niobium sublattice: $a^{Nb}=0.53333340$	
y_{Nb}^{Nb}	$-22666.70+10.17567\,T$
y_{Al}^{Nb}	$-3989.00+8.26413\,T$
y_{Ti}^{Nb}	$-13536.00+8.45813\,T$
$y_{Al}^{Nb}y_{Ti}^{Nb}$	8046.15
$y_{Ti}^{Nb}y_{Al}^{Nb}$	−10000.00
Aluminum sublattice: $a^{Al}=0.33333330$	
y_{Nb}^{Al}	$-22666.70+10.17567\,T$
y_{Al}^{Al}	$-3989.00+8.26413\,T$
y_{Ti}^{Al}	$-13536.00+8.45813\,T$
$y_{Al}^{Al}y_{Nb}^{Al}$	$-5499.82+1.66825\,T$
$y_{Nb}^{Al}y_{Ti}^{Al}$	5028.85
$y_{Ti}^{Al}y_{Al}^{Al}$	−6000.00
Niobium sublattice: $a^{Nb}=0.13333330$	
y_{Nb}^{Nb}	$-22666.70+10.17567\,T$
Polynomial terms between species on different sublattices	
$y_{Nb}^{Nb}y_{Al}^{Al}y_{Nb}^{Nb}$	$-46895.30+10.46569\,T$
$y_{Al}^{Nb}y_{Nb}^{Al}y_{Nb}^{Nb}$	19747.45
$y_{Al}^{Nb}y_{Al}^{Al}y_{Nb}^{Nb}$	$-27148.69+10.46569\,T$
$y_{Ti}^{Nb}y_{Al}^{Al}y_{Nb}^{Nb}$	$-35200.00+6.20000\,T$
$y_{Al}^{Nb}y_{Ti}^{Al}y_{Nb}^{Nb}$	$-35200.00+6.20000\,T$
$(Ti,Nb)Al_3$ (two sublattices)	
(Ti,Nb) sublattice: $a^{TN}=0.25$	
y_{Nb}^{TN}	$-8000.00+8.70910\,T$
y_{Al}^{TN}	$-10711.00+11.47280\,T$
y_{Ti}^{TN}	$-12316.00+10.79840\,T$
$y_{Nb}^{TN}y_{Al}^{TN}$	12500.00
$y_{Ti}^{TN}y_{Al}^{TN}$	12500.00
$y_{Nb}^{TN}y_{Ti}^{TN}$	3268.75
Aluminum sublattice: $a^{Al}=0.75$	
y_{Nb}^{Al}	$-8000.00+8.70910\,T$
y_{Al}^{Al}	$-10711.00+11.47280\,T$
y_{Ti}^{Al}	$-12316.00+10.79840\,T$
$y_{Al}^{Al}y_{Nb}^{Al}$	$-56592.56+33.80652\,T$
$y_{Al}^{Al}y_{Ti}^{Al}$	$-61849.46+36.53370\,T$
$y_{Nb}^{Al}y_{Ti}^{Al}$	9806.25
$y_{Nb}^{Al}y_{Al}^{Al}y_{Ti}^{Al}$	−100000.00
Polynomial terms between species on different sublattices	
$y_{Nb}^{TN}y_{Al}^{Al}$	$-50131.90+12.18287\,T$
$y_{Al}^{TN}y_{Nb}^{Al}$	$50131.90-12.18287\,T$
$y_{Ti}^{TN}y_{Al}^{Al}$	$-40349.60+10.36525\,T$
$y_{Al}^{TN}y_{Ti}^{Al}$	$40349.60-10.36525\,T$
$y_{Nb}^{TN}y_{Ti}^{TN}y_{Al}^{Al}$	$-17000.00+6.00000\,T$
Ti_2Al_5 (stoichiometric compound)	
1	$-361654.70+145.66830\,T$
$TiAl_2$ (stoichiometric compound)	
1	$-165313.20+66.80632\,T$
TiAl (two sublattices)	
Titanium sublattice: $a^{Ti}=0.5$	
y_{Nb}^{Ti}	$-8000.00+8.70910\,T$
y_{Al}^{Ti}	$-10711.00+11.47280\,T$
y_{Ti}^{Ti}	$-12316.00+10.79840\,T$
$y_{Ti}^{Ti}y_{Al}^{Ti}v_{Ti}^{Ti}$	$-102978.40+7.79282\,T$

TABLE 1 (*continued*)

Multiplier	Parameter G_k, A_j or B_{ij}
Titanium sublattice: $a^{Ti}=0.5$ (*continued*)	
$y_{Ti}^{Ti}y_{Al}^{Ti}v_{Al}^{Ti}$	$-24001.71+7.79282\,T$
$y_{Nb}^{Ti}y_{Ti}^{Al}$	6537.50
$y_{Nb}^{Ti}y_{Al}^{Ti}y_{Ti}^{Ti}$	-40000.00
Aluminum sublattice: $a^{Al}=0.5$	
y_{Nb}^{Al}	$-8000.00+8.70910\,T$
y_{Al}^{Al}	$-10711.00+11.47280\,T$
y_{Ti}^{Al}	$-12316.00+10.79840\,T$
$y_{Nb}^{Al}y_{Al}^{Al}$	$-60000.00+11.00000\,T$
$y_{Al}^{Al}y_{Ti}^{Al}$	$-28311.63+10.85167\,T$
$y_{Nb}^{Al}y_{Ti}^{Al}$	6537.50
Polynomial terms between species on different sublattices	
$y_{Nb}^{Ti}y_{Al}^{Al}$	$-42000.00+8.00000\,T$
$y_{Al}^{Ti}y_{Nb}^{Al}$	$42000.00-8.00000\,T$
$y_{Ti}^{Ti}y_{Al}^{Al}$	$-37445.10+16.79376\,T$
$y_{Al}^{Ti}y_{Ti}^{Al}$	$37445.10-16.79376\,T$
$y_{Nb}^{Ti}y_{Ti}^{Ti}y_{Al}^{Al}$	-20000.00
Ti_3Al (two sublattices)	
Titanium sublattice: $a^{Ti}=0.75$	
y_{Nb}^{Ti}	$-13000.00+9.70910\,T$
y_{Al}^{Ti}	$-5151.40+9.61780\,T$
y_{Ti}^{Ti}	$-18316.00+10.89840\,T$
$y_{Nb}^{Ti}y_{Al}^{Ti}$	-30000.00
$y_{Ti}^{Ti}y_{Al}^{Ti}$	$-71277.87+25.46998\,T$
$y_{Nb}^{Ti}y_{Ti}^{Ti}$	9806.25
Aluminum sublattice: $a^{Al}=0.25$	
y_{Nb}^{Al}	$-13000.00+9.70910\,T$
y_{Al}^{Al}	$-5151.40+9.61780\,T$
y_{Ti}^{Al}	$-18316.00+10.89840\,T$
$y_{Nb}^{Al}y_{Ti}^{Al}$	3268.75
Polynomial terms between species on different sublattices	
$y_{Nb}^{Ti}y_{Al}^{Al}$	$-38000.00+7.00000\,T$
$y_{Al}^{Ti}y_{Nb}^{Al}$	$38000.00-7.00000\,T$
$y_{Ti}^{Ti}y_{Al}^{Al}$	$-29633.60+6.70801\,T$
$y_{Al}^{Ti}y_{Ti}^{Al}$	$29633.60-6.70801\,T$
$y_{Nb}^{Ti}y_{Ti}^{Ti}y_{Al}^{Al}$	-9400.00
Ti_2AlNb (three sublattices)	
Titanium sublattice: $a^{Ti}=0.5$	
y_{Nb}^{Ti}	$-13000.00+9.70910\,T$
y_{Ti}^{Ti}	$-18316.00+10.89840\,T$
$y_{Nb}^{Ti}y_{Ti}^{Ti}$	-10000.00
Niobium sublattice: $a^{Nb}=0.25$	
y_{Nb}^{Nb}	$-13000.00+9.70910\,T$
y_{Ti}^{Nb}	$-18316.00+10.89840\,T$
Aluminum sublattice: $a^{Al}=0.25$	
y_{Al}^{Al}	$-5151.40+9.61780\,T$
Polynomial terms between species on different sublattices	
$y_{Nb}^{Ti}y_{Nb}^{Nb}y_{Al}^{Al}$	$-38000.00+7.00000\,T$
$y_{Ti}^{Ti}y_{Ti}^{Nb}y_{Al}^{Al}$	$-29633.60+6.70801\,T$
$y_{Ti}^{Ti}y_{Nb}^{Nb}y_{Al}^{Al}$	$-34000.00+7.00000\,T$
$y_{Nb}^{Ti}y_{Ti}^{Nb}y_{Al}^{Al}$	$34000.00-7.00000\,T$
Ti_4Al_3Nb (stoichiometric compound)	
1	$-480000.00+180.00000\,T$

and

$$v_2 = x_2 + (1 - x_1 - x_2) = x_2$$

the equation can be rewritten as

$$G^i = x_1(G_1 + RT\ln(x_1)) + x_2(G_2 + RT\ln(x_2)) + \sum_j A_j x_1^m x_2^n$$

In order to provide a thermodynamic description of a binary phase whose compositional stabilities extend into the ternary region, the Gibbs energies of the counter phases in the other binaries need to be estimated. These complimentary phases are not stable in the respective binaries under ordinary conditions. For the Nb-Al and Ti-Al systems, the Gibbs energies of formation of the stable phases were used to estimate the Gibbs energy of formation of the hypothetical metastable compounds. The phases in the Ti-Nb system exhibit no ordering tendency. Therefore, the Gibbs energy of formation of the ordered compounds was set to zero for the Ti-Nb system and the total excess Gibbs energy was set equal to that of the disordered compounds.

In the analytical descriptions of the ordered intermetallic compounds of the Nb-Al and Ti-Al systems, the number of parameters in the description was minimized by using constraints for the different Gibbs energies of formation. If, in an ordered compound, all the elements are assumed to occur on all sublattices of this compound, this compound will exist over the entire composition range. The structures of most of these compounds are ordered derivatives of the structures of the pure elements. For complete substitution, *i.e.* at the composition of one of the pure elements, the degree of ordering in these compounds must be zero and the Gibbs energy of these compounds must then be equal to the Gibbs energy of the pure elements of the corresponding crystal structure. This implies constraints for the Gibbs energy of formation of the substitutional atoms. The same constraints were applied to the thermodynamic quantities of the hypothetical metastable compounds in the respective binaries.

Because the homogeneity range of the ternary Ti_4Al_3Nb compound is believed to be small, this phase is modeled as stoichiometric. The structure of the ordered Ti_2AlNb phase can be derived through additional ordering of titanium and niobium on the titanium sublattice of Ti_3Al. It was therefore modeled as a solution phase with three sublattices (the titanium, niobium and aluminum sublattices). This phase reveals a significant range of homogeneity with respect to titanium and niobium, but the range of homogeneity with respect to aluminum is smaller. It was, therefore, assumed that niobium and titanium atoms mix only on the titanium and niobium sublattices and no mixing occurs on the aluminum sublattice. Thus, the Ti_2AlNb compound composition is constrained to $(Ti,Nb)_3Al$. For complete substitution on either the titanium or niobium sublattice, the degree of ordering must again be zero and the Gibbs energy of formation must then be identical to the corresponding binary Ti_3Al and Nb_3Al phases with the $D0_{19}$ structure.

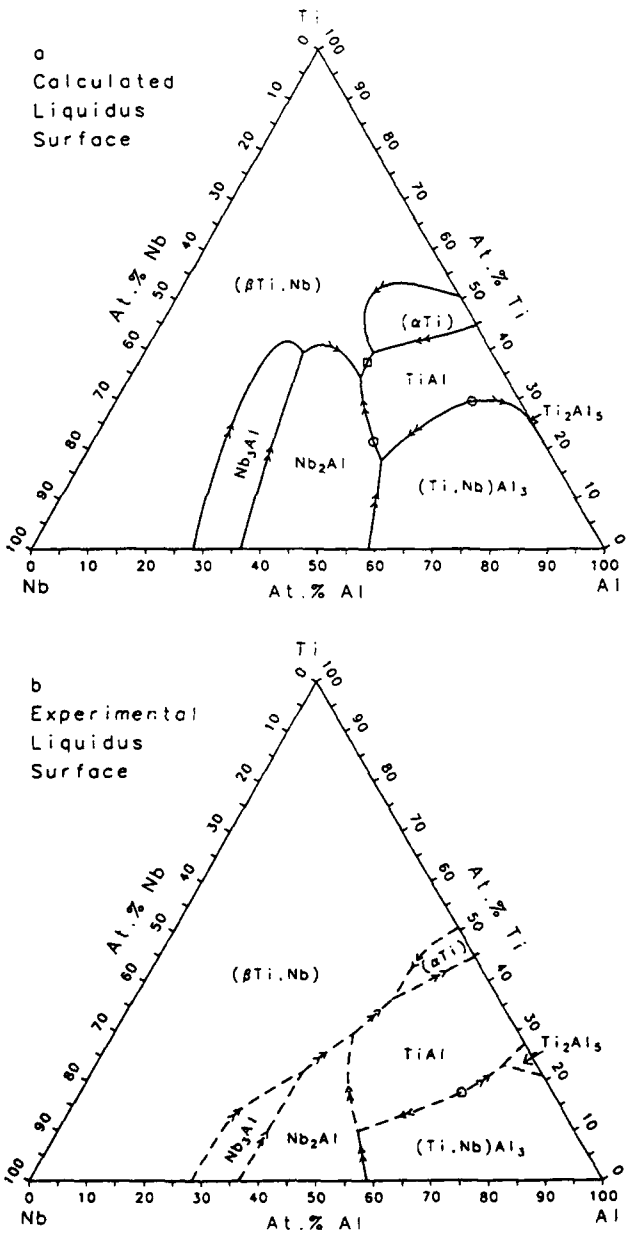

Fig. 2. The liquidus projection (circles, maximum; squares, minimum). (a) Calculated. (b) Initially, after Perepezko *et al.* [6], the composition of liquid of the binary three-phase equilibrium was taken from the binary calculations.

No attempt was made to develop a miscibility gap in the (β_0-Ti,Nb) phase in order to fit the data of Perepezko *et al.* [6]. For the present calculation, the simplification of treating the (β-Ti,Nb) and (β_0-Ti,Nb) as one disordered phase has the consequence that this miscibility gap would have to occur in the (β-Ti,Nb) phase. In the three binary systems, the (β-Ti,Nb) phase only forms a miscibility gap in the Ti-Nb system at a relatively low temperature. However, the experimental data suggest that the ternary miscibility gap occurs on the (Ti,Al)-rich side of the system at relatively high temperatures. In order to obtain the specific curvature of the Gibbs energy needed for the formation of a miscibility gap, the number of ternary polynomial terms would have to be increased. Considering the simplifications already introduced for the analytical description of the (β/β_0-Ti,Nb) phase, increasing the number of polynomial terms is not justified.

At the beginning of the calculation, attempts were made to use a least squares method in order to adjust the Gibbs energy coefficients of the polynomial terms. Since the amount of available data with respect to the number of adjustable terms is relatively small and most of these data cover only the temperature interval between 1100 and 1200 °C, the results of the least squares fitting could only be used as initial values for trial and error calculations. In the trial and error method the values of the adjustable parameters are estimated. The change of the phase boundaries between two steps of the calculation is used to estimate new values in order to adjust the calculated phase boundaries to the experimental results. The reported values of the adjustable parameters were estimated by such a trial and error approach.

5. Results and discussion

The thermodynamic description of the Ti-Al-Nb system is given in Table 1. This description was used to calculate the liquidus projection, several isothermal sections and an isopleth. The calculated liquidus projection is compared with a preliminary projection estimated by Perepezko *et al.* [6] in Fig. 2. The calculated 1400 °C section is shown in Fig. 3. The calculated

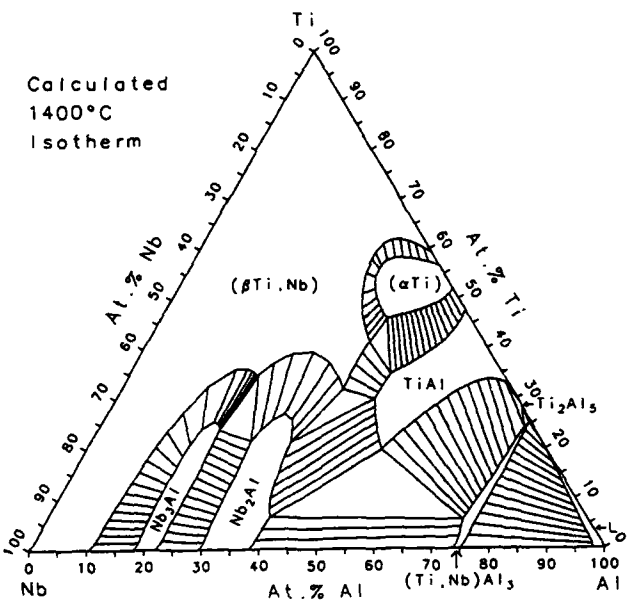

Fig. 3. Calculated isothermal section at 1400 °C.

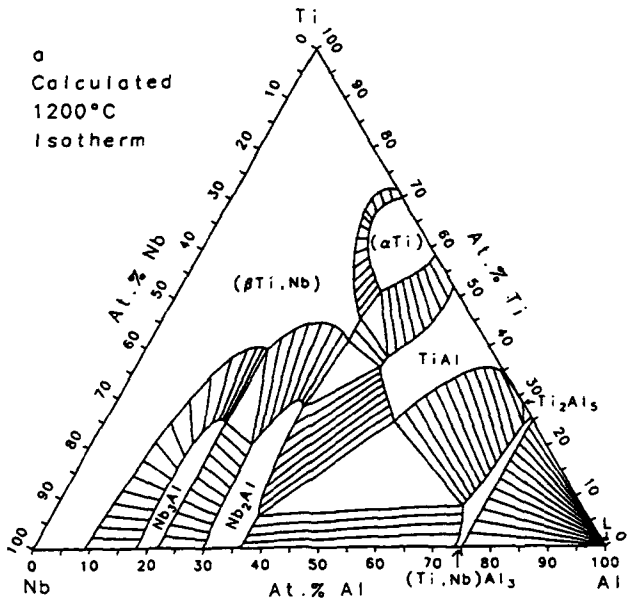

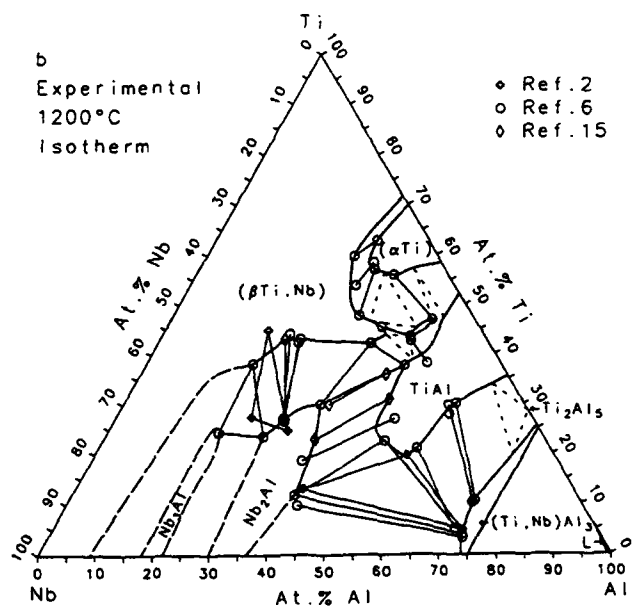

Fig. 4. Isothermal section at 1200 °C. (a) Calculated. (b) Experimental data and phase boundaries.

isothermal sections at 1200, 1100 and 700 °C are compared with the experimental tie-line and phase boundary data as shown in Figs. 4–6. The isopleth at 25 at.% Al with the experimental data is shown in Fig. 7.

The calculated and the estimated experimental liquidus projections as given in Figs. 2(a) and 2(b) are in qualitative agreement. The calculation predicts correctly the phases occurring in the invariant four-phase equilibria. However, the liquidus temperatures predicted by the calculation for the primary TiAl region are lower than the temperatures from first experimental results [6]. This has as a consequence that the temperature of the calculated three-phase equilibrium $L+(\alpha\text{-Ti})+TiAl$ decreases with increasing niobium concentration while the first experimental results indicate that the temperature increases. A ternary eutectic ($L \rightarrow Nb_2Al+(Ti,Nb)Al_3+TiAl$) is predicted for the invariant equilibrium involving $L+Nb_2Al+(Ti,Nb)Al_3+TiAl$, but the experimental results indicate that it is a transition-type reaction ($L+(Ti,Nb)Al_3 \rightarrow Nb_2Al+TiAl$). The calculation gives a maximum for the three-phase equilibrium $L+Nb_2Al+TiAl$ close to the eutectic composition. Small changes of Gibbs energies of the compounds involved in this equilibrium could shift this maximum closer to or even beyond the eutectic composition. In the latter case, the invariant equilibrium would then be a transition type and the maximum would occur in the metastable three-phase equilibrium.

The calculated 1400 °C section reveals a large range of homogeneity for (β-Ti,Nb). This is in agreement with experimental results [1], which indicate that this range of homogeneity is even larger. The calculated and experimental phase boundaries agree fairly well at 1200 and 1100 °C, while the calculated tie-line directions deviate from those experimentally determined. The increased range of homogeneity observed for the $(Ti,Nb)Al_3$ phase in the ternary system was well matched by the calculation at 1200 °C. In the present calculation the temperature of the binary eutectoid (α-Ti) $\rightarrow Ti_3Al+TiAl$ decreases initially with increasing niobium concentration. This results in an isolated ternary (α-Ti) phase field between Ti_3Al and TiAl.

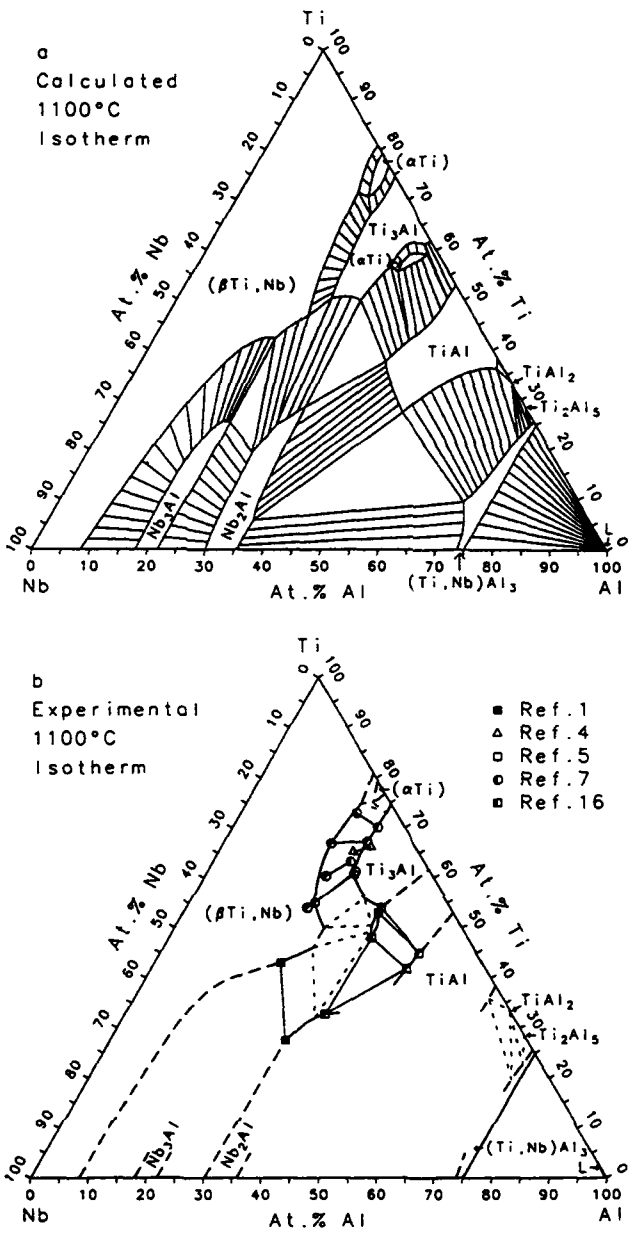

Fig. 5. Isothermal section at 1100 °C. (a) Calculated. (b) Experimental data and phase boundaries.

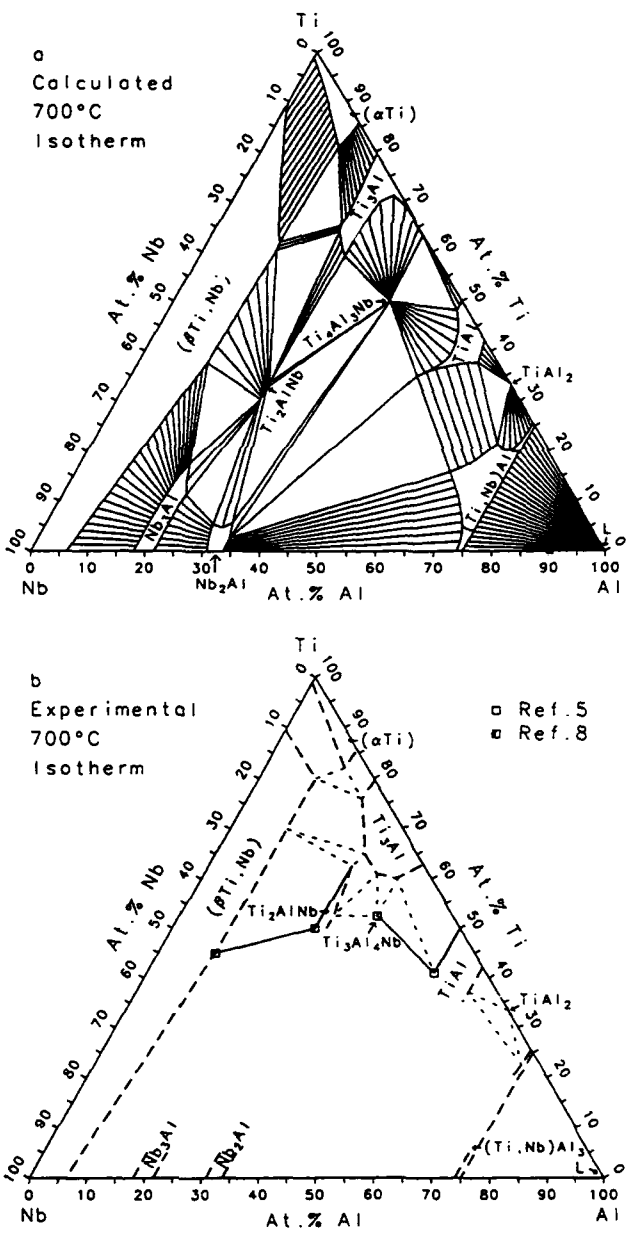

Fig. 6. Isothermal section at 700 °C. (a) Calculated. (b) Experimental data and phase boundaries.

The agreement between the calculated isothermal section at 700 °C and the experimental data is poor. The single-phase region of the phase denoted by Ti_2AlNb exists in the present calculation at an excessively high niobium content and, in fact, does not include the stoichiometric composition of Ti_2AlNb. Thus the important $(\beta\text{-Ti,Nb}) + Ti_3Al + Ti_2AlNb$ three-phase equilibrium also exists at an excessively high niobium content. With the current thermodynamic description of the $(\beta\text{-Ti,Nb})$ phase, the phase boundaries of the $(\beta\text{-Ti,Nb})$–Ti_3Al, $(\beta\text{-Ti,Nb})$–Ti_2AlNb and $(\beta\text{-Ti,Nb})$–Nb_3Al equilibria have very similar slopes and small changes in the Gibbs energy of the Ti_2AlNb compound would result in different topologies for this section. Further experimental effort is needed to establish the phase boundaries for this isothermal section.

The process of adjusting the Gibbs energy coefficients of the polynomial terms showed that the phase relationships obtained from the calculation are extremely sensitive to small changes in the Gibbs energies. Similar behavior had been previously observed during the calculation of the Ti–Al binary system [14, 19]. The fact that small changes in the Gibbs energies

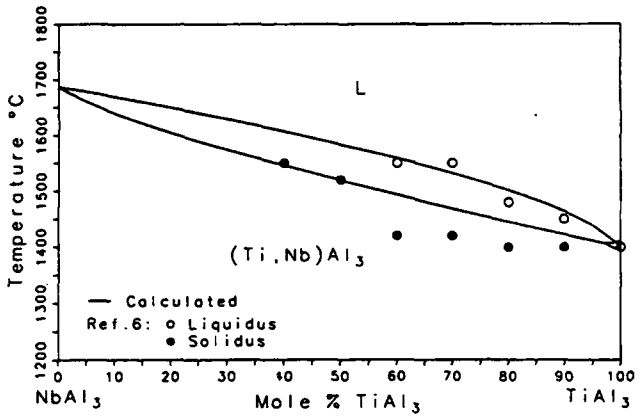

Fig. 7. Calculated isopleth at 25 at.% Al and experimental data. Note that this section is quasibinary, except on the $TiAl_3$-rich side.

result in different phase relationships may not only help to explain the experimental difficulties in determining the accurate phase diagram for the Ti-Al-Nb system, but also explain the difficulties of obtaining a satisfactory thermodynamic descripton for the phases in this system. A change in the thermodynamic description of one phase affects all the phase equilibria involving that phase. In the trial and error calculation it is advisable to modify only a few parameters between two steps of the calculation in order to clearly recognize the effects of the modifications on the locations of the calculated phase boundaries. To model the wide homogeneity ranges of the ordered intermetallic compound a large number of adjustable parameters had to be included. This large number of adjustable parameters makes the trial and error method for the adjustment of these parameters relatively inefficient. A straightforward method of adjusting all of the parameters simultaneously is the least squares method [20]. However, in order to apply this method successfully, more experimental data are needed. These data are not only needed to constrain the phase boundaries at certain temperatures, but even more importantly, to establish the change of the phase boundaries over a larger temperature interval.

6. Conclusion

The calculated phase diagrams of the Ti-Al-Nb ternary systems are undoubtedly subjected to large uncertainties owing to the lack of sufficient thermodynamic and phase equilibria data to fix the model parameter values and the complicated phase relationships. However, they do provide valuable and useful information for alloy development and indeed suggest experiments to be carried out in critical compositional and temperature regions in order to elucidate the phase equilibria of this technologically important system.

Acknowledgments

The authors wish to thank Dr. H. L. Lukas of the Max-Planck-Institut für Metallforschung (Stuttgart, FRG) for providing the software used in the present assessment, Professor J. H. Perepezko of the University of Wisconsin-Madison for helpful discussions and Professor Y. A. Chang of the University of Wisconsin-Madison for critically reading the manuscript. This research was partially supported (W.J.B.) under DARPA Order 7469.

References

1 L. A. Bendersky and W. J. Boettinger, *Mater. Res. Soc. Symp. Proc., 11* (1989) 45.
2 K. Kaltenbach, S. Gama, D. G. Pinatti, K. Schulze and E.-Th. Henig, *Z. Metallkd., 80* (1989) 535.
3 H. T. Kester-Weykamp, C. H. Ward, T. F. Broderick and M. J. Kaufman, *Scr. Metall., 32* (1989) 1697.
4 K. Muraleedharan and D. Banerjee, *Metall. Trans. A, 20* (1989) 119.
5 L. A. Bendersky, W. J. Boettinger, B. P. Burton, F. S. Biancaniello and C. B. Shoemaker, *Acta Metall. Mater., 38* (1990) 931.
6 J. H. Perepezko, Y. A. Chang, L. E. Seitzman, J. C. Lin, N. R. Bonda, T. A. Jewett and J. C. Mishurda, in *Proc. Symp. High Temperature Aluminides and Intermetallics*, Indianapolis, ASM/TMS-AIME, Metals Park, OH, 1990, p. 19.
7 J. H. Perepezko, private communication, 1990.
8 L. A. Bendersky, W. J. Boettinger and A. Roytburd, *Acta Metall. Mater., 39* (1991) 1959.
9 U. R. Kattner, unpublished results, 1988.
10 J. L. Murray, Alcoa report, 1987.
11 J. L. Murray, *Metall. Trans. A, 19* (1988) 24.
12 L. Kaufman and H. Bernstein, *Computer Calculation of Phase Diagrams*, Academic Press, New York, 1970.
13 U. R. Kattner and H. L. Lukas, unpublished results, 1990.
14 U. R. Kattner, J.-C. Lin and Y. A. Chang, *Metall. Trans. A., Feb.* (1992) accepted for publication.
15 D. T. Hoelzer and F. Ebrahimi, in E. D. Verink Jr., *Processing and Protection of High Temperature Structural Materials, Annual Report*, University of Florida, Gainesville, FL, 1990, p. 26.
16 L. A. Benderski, private communication, 1991.
17 D. Banerjee, A. K. Gogia, T. K. Nandi and V. A. Joshi, *Acta Metall., 36* (1988) 871.
B. Mozer, L. A. Bendersky, W. J. Boettinger and R. G. Rowe, *Scr. Metall. Mater., 24* (1990) 2363.
18 H. L. Lukas, J. Weiss and E.-Th. Henig, *CALPHAD, 6* (1982) 229.
19 J. C. Lin, T. Jewett, J. C. Mishurda, Y. A. Chang and J. H. Perepezko, Second Annual Report, supported by DARPA through ONR contract (0014-86-K-075), 1988.
20 H. L. Lukas, E.-Th. Henig and B. Zimmermann, *CALPHAD, 1* (1977) 225.

Scripta METALLURGICA et MATERIALIA
Vol. 25, pp. 1993-1998, 1991
Printed in the U.S.A.

Investigation of the Phase Constitution of Al_2TiTa

W. J. Boettinger, A. J. Shapiro, J. P. Cline, F. W. Gayle,
L. A. Bendersky and F. S. Biancaniello
Materials Science and Engineering Laboratory
National Institute of Standards and Technology
Gaithersburg, MD 20899

(Received May 21, 1991)

Introduction

Recently the composition Al_2TiTa has been identified as a basis for further alloy development during a search of γ titanium aluminide alloys having increased oxidation resistance and solidus temperature (1). At 1100°C this composition consists of γ phase (TiAl containing Ta) and σ phase (Ta_2Al containing Ti) (2,3). McCullough et al.(4) obtained evidence by high temperature x-ray diffraction for the transformation of a similar composition (Al-28at%Ti-27at%Ta) to HCP and BCC phases above 1450°C. Weaver et al. (5) found an alloy Al-24at%Ti-25at%Ta to be BCC and σ at 1450°C. In the present paper the compositions and crystal structures of the equilibrium phases present in an Al_2TiTa alloy for temperatures between 1200 and 1550°C are determined. Based on the series of phase transformations found above 1325°C, significant opportunities exist to alter the microstructure of the $\gamma + \sigma$ two phase mixture which is stable below 1325°C.

Experimental

Arc melted buttons were prepared from 99.99% pure components. Several remelts were necessary to ensure dissolution of the Ta before the buttons were solidified into a rod shape. Pieces approximately 1 cm x 1 cm x 1 cm in size were used for heat treatment. Due the excellent oxidation resistance, a few samples were heat treated in air to facilitate water quenching, while the majority of the samples were heat treated in gettered Ar. The Ar furnace was equipped with a support pedestal which could be lowered into a cold chamber. Cooling rates for these samples were estimated at 400°C/min. Heat treatment procedures were varied as experience with the alloy was obtained. Generally a 1400°C/3 h treatment followed by a 1525°C/1 h treatment was used to eliminate casting microsegregation. Without the initial treatment partial melting was sometimes observed at 1525°C. Subsequent isothermal holds for times up to 23 h were used to establish equilibrium at the various temperatures.

Samples for optical metallography were etched in 3:1:1 solution of lactic, nitric and hydroflouric acids. Scanning electron microscopy (SEM) microprobe analysis was performed using unetched samples and elemental standards. All reported compositions are the mean of at least three measurements. Bulk composition results obtained using broad area scans showed approximately ± 1 at% macrosegregation from piece to piece and an average composition of Al-25.8at%Ti-25.9at%Ta.

Selected samples were prepared for transmission electron microscopy (TEM) by electropolishing in a solution containing 30 cc perchloric acid, 175 cc butyl alcohol and 300 cc ethyl alcohol. Differential thermal analysis (DTA) was performed in gettered Ar up to 1500°C to establish a basis for the choice of heat treatment temperatures. To determine the structures of the phases that decomposed during cooling, high temperature x-ray powder diffraction patterns were obtained at 1300, 1400 and 1475°C in gettered He from 0.4 mm thick slices of as-cast material which were spot welded to a Ta heater strip. Temperatures were measured by a thermocouple spot welded to the back of the heater strip.

1993
0036-9748/91 $3.00 + .00

Results

Microprobe and DTA Results - The results of the microprobe analysis of the phase compositions are given in Table 1 and Fig. 1 for the samples treated in Ar. Compositions of phases present in samples treated in air showed no significant deviations from those in Table 1. The four distinct branches in Fig. 1 show conclusively that four distinct phases occur. Of the phases found to be present at the various temperatures only σ and γ exist at room temperature. The phases labeled β and α decompose on a fine microstructural scale during cooling from the temperature of equilibration. In these cases the microprobe beam was spread to cover regions large enough to average over the fine decomposition structure.

Table 1 - Summary of Microprobe Results

Temp.	Phase	%Ti	%Ta	%Al	Heat Treatment (°C)
1550	β	25.7	25.0	49.3	1550/1h
1525	β	25.7	25.0	49.3	1400/3h; 1525/2h
1500	β	24.7	26.2	49.1	1400/3h; 1500/2h
	α	26.0	22.3	51.7	
1475	β	25.2	26.1	48.7	1400/3h; 1475/4h
	α	26.4	22.3	51.3	
1450	β	24.9	27.3	47.8	1400/3h; 1550/1h; 1450/5h
	α	26.0	22.6	51.4	
1425	β	24.7	27.8	47.5	1400/3h; 1525/1h; 1425/18h
	α	25.8	22.9	51.3	
1400	β	24.4	28.0	47.6	1400/3h; 1525/1h; 1400/18h
	α	26.1	23.1	50.8	
	σ	14.1	43.4	42.5	
1375	α	27.6	21.5	50.9	1400/3h; 1550/1h; 1375/18h
	σ	15.4	43.4	41.2	
1350	α	29.5	20.0	50.5	1400/3h; 1550/1h; 1350/16h
	σ	17.5	40.0	42.5	
1330	α	29.2	20.8	50.0	1400/3h; 1525/1h; 1330/18h
	σ	16.3	43.4	40.3	
	γ	29.5	16.9	53.6	
1300	σ	29.7	16.3	54.0	1400/3h; 1525/1h; 1300/18h
	γ	15.3	44.1	40.6	
1200	σ	14.3	46.0	39.7	1200/23h
	γ	31.5	14.1	54.4	

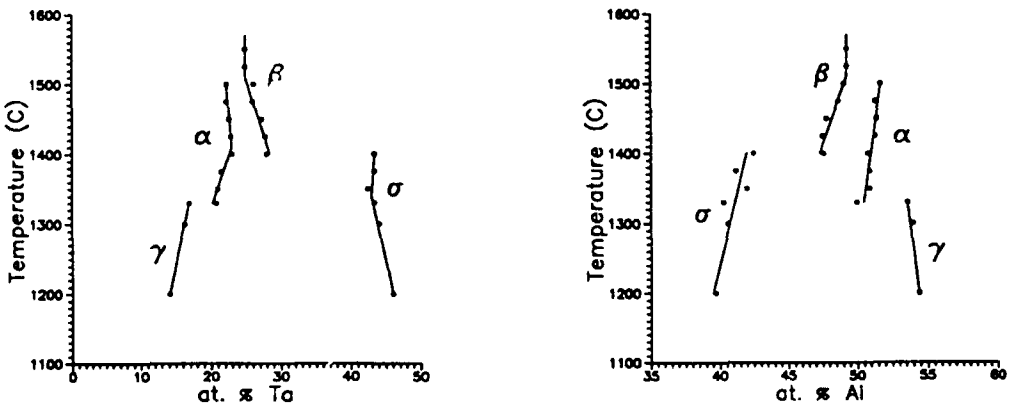

Fig. 1. Composition of phases observed in Al-25at%Ti-25at%Ta at various temperatures. a) Ta content. b) Al content.

With the exception of isolated compositions and temperatures (i.e., reactions with zero degrees of freedom), equilibrium demands that a single alloy composition that lies in an n-phase region at some temperature must pass into a region with n+1 or a n-1 phases during heating or cooling. The data in Table 1 and Fig. 1 shows that the adjoining solid phase fields for Al-25at%Ti-25at%Ta during cooling are β, $\beta+\alpha$, $\beta+\alpha+\sigma$, $\alpha+\sigma$, $\alpha+\sigma+\gamma$, and $\sigma+\gamma$. The three phase regions should exist over a range of temperatures but are apparently quite narrow as each was observed only at one temperature. In Fig. 1 changes in the slope of the curves for each phase should occur when the curve crosses into an adjoining region. In some cases enough data is present to observe these changes.

Examination of DTA heating curves for this alloy showed a flat baseline from below 1100°C up to a pair of strong endothermic peaks with onsets at 1325 ± 15°C and 1385 ± 10°C. On heating the onset of an endothermic DTA peak should occur whenever a new phase begins to form. Comparison of these temperatures with Fig. 1 indicate that these onsets correspond to the formation of α and β phases respectively during heating.

Microstructures - The microstructures typical of these six multiphase fields are shown in Fig. 2. The large grain size and the associated fine decomposition structure seen in samples cooled from the single phase β region is shown in Fig. 2a. For samples annealed in the $\alpha+\beta$ region, two distinct microstructures occur. Initial β treatment and annealing in the two-phase field produces the α phase (light) on the boundaries and in the interior of the β grains as shown in Fig. 2b. On the other hand, direct heating to the two-phase field produces the equiaxed two-phase structure of Fig. 2c.

A sample annealed for 18 h at 1400°C contains a three phase structure of α (gray), β (dark) and σ (bright) as shown in Fig. 2d. A two phase $\alpha+\sigma$ microstructure found at 1350°C is shown in Fig. 2e. Fig. 2f shows a three-phase α(gray)+γ(dark)+σ(bright) structure. Backscattered SEM images were essential to metallographically differentiate between α and γ. Note the parallel boundaries in some regions where α and γ touch. These are similar to the $(111)_\gamma \parallel (0001)_\alpha$ boundaries observed for $\alpha+\gamma$ structures in binary Ti-Al alloys. Finally a $\gamma+\sigma$ structure obtained at 1300°C is shown in Fig. 2g.

Crystal Structures - The crystal structures of γ and σ were confirmed directly by room temperature x-ray diffraction and selected area diffraction and microdiffraction in the TEM to be the same as the binary γ-TiAl phase and the binary σ-Ta_2Al phase. To determine the structures of the phases identified by microprobe as β and α, samples water-quenched from 1550 and 1450°C were examined by TEM respectively. Fig. 2h shows the morphology revealed by TEM of the β phase sample after quenching. BCC and HCP phases are identified by microdiffraction. Viewed at lower magnification, the BCC phase appears to be the matrix and is probably retained from the high temperature heat treatment and the HCP phase formed during cooling from 1550°C. On the other hand quenching from 1450°C failed to retain the high temperature phases. TEM examination revealed only the presence of the room temperature phases σ and γ. The γ phase however contained antiphase boundaries and {111} faults that were not present in γ phase which was cooled from temperatures where it was in equilibrium ($\leq$ 1330°C). This suggests that the γ with defects formed during quenching. In agreement with (5), these APB's and faults suggested that this γ phase formed from an FCC parent. Confirmation was sought using high temperature x-ray diffraction.

Consistent with the heat treatment results, high temperature x-ray patterns at 1300°C confirmed the presence of σ and γ. The γ phase disappeared in the pattern obtained at 1400°C and no FCC was observed. At this temperature as shown in Fig. 3, the pattern contains lines from tetragonal σ, and new lines associated with HCP α, and a trace of BCC β. Lines from the Ta heater strip (BCC, a=0.333nm) are also seen. Rietveld refinement of the lattice parameters using a sample displacement correction established the following lattice parameters: σ(tet), a=0.9987nm, c=0.5263nm; α(hex), a=0.2935nm, c=0.4670nm. X-ray scans at higher temperature (1475°C) were plagued by excessive grain growth but the presence of BCC (a=~0.325nm) and HCP was apparent.

In the recently refined Ti-Al binary phase diagram, the HCP phase was found to exist with up to 48 at% Al at 1430°C (6,7). The HCP α phase found here has composition ~Ti-51at%Al-23at%Ta and lattice parameters close to the binary α phase. Thus we conclude that the α phase present in this alloy between ~1325C and ~1500°C belongs to the solution phase based on α-Ti with Al and Ta additions. Also the β phase observed here likely belongs to the solution phase based on β-Ti and Ta. These results on the presence of HCP and BCC phase at high temperature in alloys of this general composition agree with (4).

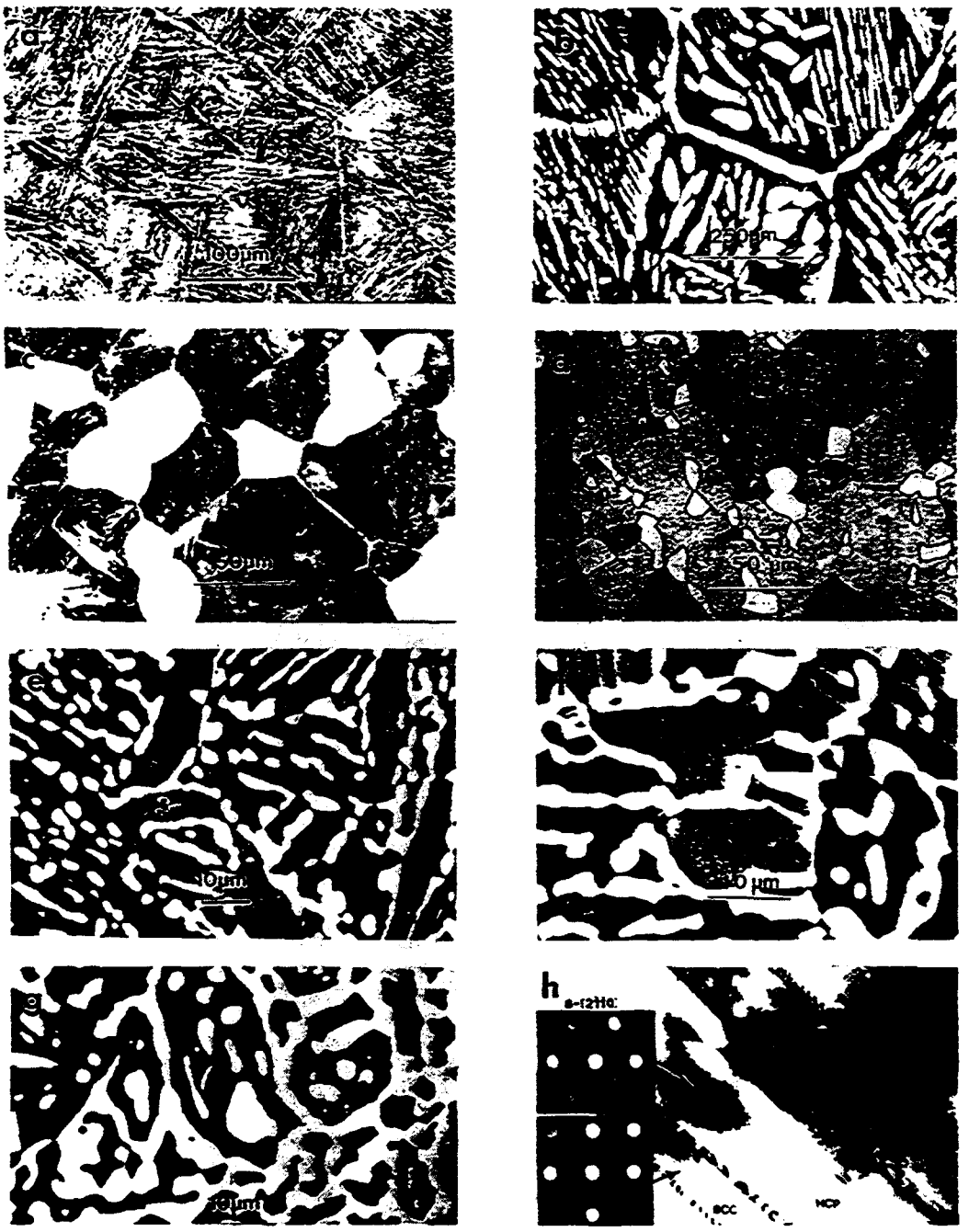

Fig. 2. a) Optical. Decomposed β phase. 1525°C. b,c) Optical. β(dark)+α(light). 1450°C. d) Optical. β(dark)+α(gray)+σ(light). 1400°C. e) Backscattered SEM α(dark)+σ(light). 1350°C. f) Backscattered SEM, α(gray)+σ(light)+γ(dark). 1330°C. g) Backscattered SEM. σ(light)+γ(dark). 1300°C. h) TEM of a sample water quenched from 1550°C showing retained BCC phase and HCP plates.

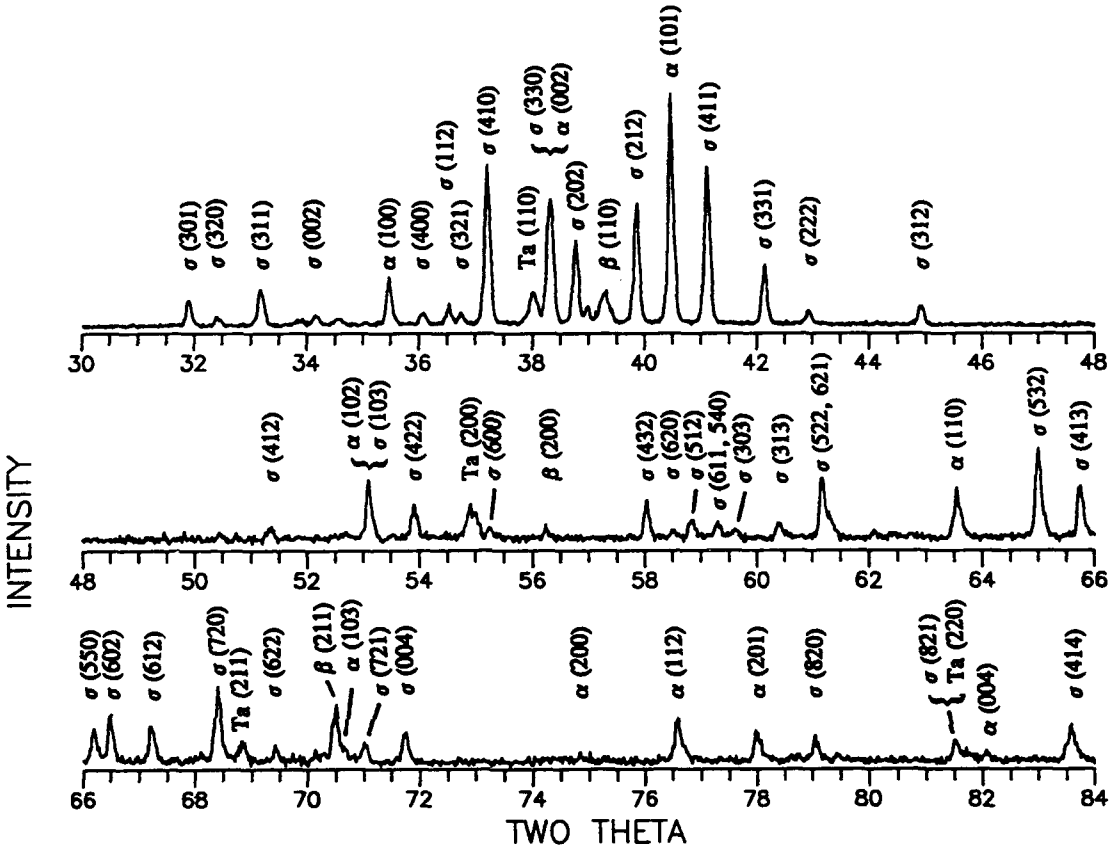

Fig. 3. X-ray diffraction pattern obtained at 1400°C showing the presence of HCP α along with tetragonal σ and a trace of BCC β. Lines from the Ta strip heater are also observed. Sample displacement is 0.33 mm. Intensity scale for data between 48° and 84° is doubled.

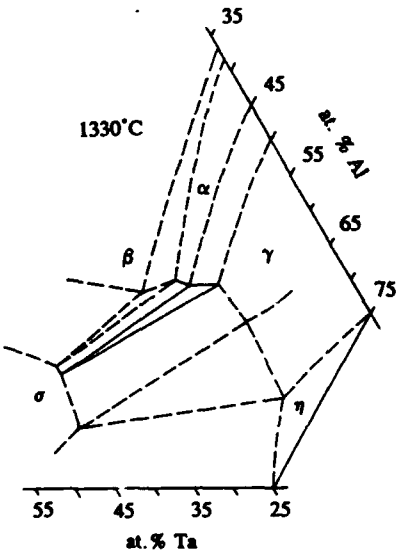

Fig. 4. Estimated partial isothermal section of the Ti-Ta-Al ternary system at 1330°C. Data for the $\alpha+\gamma+\sigma$ three phase triangle was measured at this temperature. The location of the $\alpha+\beta+\sigma$ triangle is estimated from higher temperature data. The $\sigma+\gamma+\eta$ triangle is include to complete the topology and is taken from the data of (3) for 1100°C.

Discussion

The data obtained in the present study involves only one composition. However, partial isothermal sections of the Ti-Al-Ta system can be estimated. Consistent with Table 1, isothermal sections in the temperature range between 1200 and 1550°C involve two three-phase triangles, $\alpha+\beta+\sigma$ and $\alpha+\gamma+\sigma$. These triangles and their associated two-phase fields shift through the composition studied as the temperature is varied to produce the observed equilibria.

An estimate of an isothermal section at 1330°C is given in Fig. 4. First the measured data for the three-phase triangle between α, γ, and σ at 1330°C was plotted. Next an estimate for the position of the three-phase triangle between α, β, σ at 1330°C was performed. This triangle was only observed at 1400°C for the studied composition but would be expected to shift to lower Al content as the temperature is reduced based on the behavior of the β phase in the Ti-Al binary. The triangle was assumed to have the same size and orientation as that measured at 1400°C. Its position was estimated using the following procedure. Extrapolation of the compositions of the α and β phases from the temperature range between 1400 and 1500°C to 1330°C using Fig. 1 establishes a metastable tie line at 1330°C between α and β which contains the studied composition. The end points of this tie line and the limits of the $\alpha+\beta$ field at 1330°C in the Ti-Al binary were used to sketch a two-phase field in the isothermal section which extend from the binary Ti-Al to the composition range of interest. The three-phase $\alpha+\beta+\sigma$ triangle was then shifted from its position at 1400°C so that the ends of the $\alpha+\beta$ side of the triangle coincided with the sketched $\alpha+\beta$ boundaries.

The basic topology of Fig. 4 should exist up to the solidus. Preliminary thermodynamic calculations of the liquidus surface (8) show two four-phase reactions involving $L+\alpha+\beta+\sigma$ and $L+\alpha+\gamma+\sigma$. At temperatures just below these invariant reactions, the same two three-phase fields, $\alpha+\beta+\sigma$ and $\alpha+\gamma+\sigma$, will form. These triangles likely persist down to the temperature range studied. Clearly the estimate given in Fig. 4 needs verification and quantification by experiment on other alloy compositions.

The upper limits of stability of the $\gamma+\sigma$ structure in the Al_2TiTa composition has been established as 1325°C. The phase changes which occur between 1325° and 1550°C provide the opportunity to change the $\gamma+\sigma$ microstructure by heat treatment and to perhaps effect improvements in low temperature toughness and/or high temperature creep resistance. For example a β or an $\alpha+\beta$ heat treatment can be done on this alloy to adjust the grain size. Furthermore casting microsegregation can be completely removed by a β treatment. Appropriate heat treatment can also be determined to produce coarse or fine σ within the γ matrix.

Summary

The composition Al_2TiTa transforms from a structure of γ (TiAl) and σ (Ta_2Al) during heating above 1325°C to various multiphase structures composed of σ, α(HCP) and β(BCC). Between 1425°C and 1500°C the alloy is two phase $\alpha+\beta$ and between 1525°C and 1550°C the alloy is single phase β.

Acknowledgement

The authors thank Leonard C. Smith for the metallography. This research was partially supported (WJB, LAB) under DARPA Order #7469.

References

1. R. Perkins, Lockheed Missiles and Space Co., Palo Alto, CA, unpublished research.
2. S. Sridharam and H. Nowotny, Z. Metallkunde 74, 468 (1983).
3. S. Das, T.J. Jewett, J. C. Lin and J. H. Perepezko, in Microstructure/Property Relationships in Titanium Alloys and Titanium Aluminides, Y. -W. Kim, J. A. Hall and R. R. Boyer, TMS-AIME, Warrendale, OH, 1991, in press.
4. C. McCullough, J. J. Valencia, C. G.. Levi, R. Mehrabian, M. Maloney and R. Hecht, submitted to Acta Met.
5. M. L. Weaver, S. L. Guy, R. K. Stone and M. J. Kaufman, Mat. Res. Soc. Symp. Proc. 213, (1991), in press.
6. J. C. Mishurda, J.-C. Lin, Y. A. Chang and J. H. Perepezko, Mat. Res. Soc. Symp. Proc. 133, 57 (1989).
7. C. McCullough, J. J. Valencia, C. G.. Levi, R. Mehrabian, Acta Met. 37, 1321 (1989).
8. U. Kattner, NIST, Gaithersburg, MD, unpublished research.

Materials Science and Engineering, A155 (1992) 33–44

Application of ternary phase diagrams to the development of $MoSi_2$-based materials

William J. Boettinger

Metallurgy Division, National Institute of Standards and Technology, Gaithersburg, MD 20899 (USA)

John H. Perepezko and Peter S. Frankwicz

Department of Materials Science and Engineering, University of Wisconsin–Madison, Madison, WI 53706 (USA)

Abstract

A review of the literature reveals ternary phase diagram data for a number of systems involving $MoSi_2$. Although incomplete, this literature provides the initial basis for a rational approach to alloy design. For example, one can assess the high temperature stability of various artificially introduced reinforcements, such as niobium or SiC in an $MoSi_2$ matrix and the possibilities for the development of stable two-phase microstructures in quasibinary alloys in the $MoSi_2$–$TiSi_2$ and $MoSi_2$–$TaSi_2$ systems. Revised phase diagrams for these latter systems are presented that indicate the absence of the $C11_b$-to-C40 high temperature polymorphic transformation in pure $MoSi_2$.

1. Introduction

The application of ternary and higher order phase diagrams to problems of alloy and composite processing and design provides significant improvement over the use of binary diagrams. In this paper a critical review is presented for selected ternary and higher order phase diagrams involving $MoSi_2$. Many of the literature citations in this article were obtained from the bibliography of Prince [1, 2]. As examples, the $MoSi_2$–Nb and $MoSi_2$–SiC composite system are examined using the relevant ternary diagrams in conjunction with the concept of the ternary diffusion path to describe the reaction layers that may or may not form in composites based on an $MoSi_2$ matrix reinforced with these materials. The bulk of the paper is then concerned with phase diagrams based on pairs of disilicides, especially those involving multiphase alloys that combine the tetragonal $C11_b$ structure of $MoSi_2$ and the hexagonal C40 structure to determine whether any opportunities for microstructural manipulation exist through solidification or heat treatment. Finally, new phase equilibria data is presented on the $MoSi_2$–$TiSi_2$ and $MoSi_2$–$TaSi_2$ systems which precludes the possibility of an equilibrium C40-to-$C11_b$ polymorphic transition in pure $MoSi_2$.

2. Application of ternary diagrams to composite design: diffusion paths

2.1. $MoSi_2$–Nb

Figure 1 shows the 800 °C isothermal section of the Mo–Nb–Si diagram according to ref. 3. Isothermal sections of ternary phase diagrams contain three different kinds of regions. In the figure, black areas represent regions where alloys consist of only one phase. For example, niobium and molybdenum dissolve completely in each other as a b.c.c. solid solution. Other single-phase regions are: Mo_3Si; a continuous solution from Nb_5Si_3 to Mo_5Si_3; $NbSi_2$ having the C40 structure, which is different from the $MoSi_2$ structure; and silicon. Between single-phase regions are two-phase regions which contain tie-lines whose ends are the compositions of the saturated phases in an equilibrium coexisting mixture. Finally there are triangular regions (tie-triangles) in which three phases are in equilibrium with compositions given by the corners. Each side of the triangle is a limiting tie-line of the adjacent two-phase field. Every isothermal section of a ternary system is made from combinations of single-phase, two-phase and three-phase regions. Such a section is required for each temperature to describe the alloy system completely. It is useful to note the narrow two-

0921-5093/92/$5.00

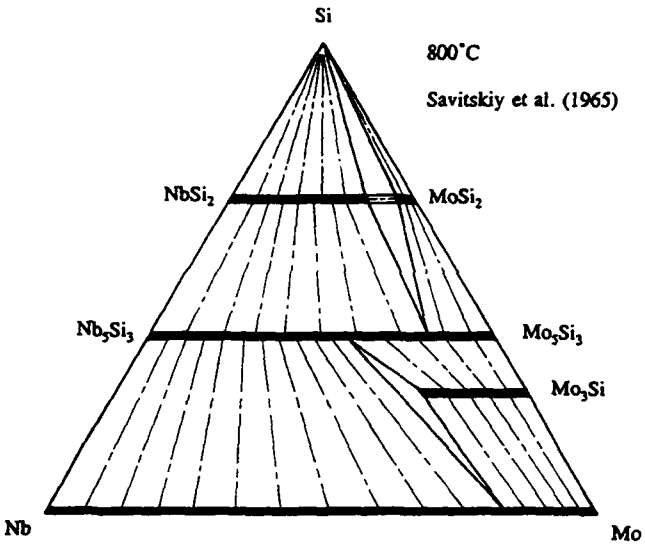

Fig. 1. Mo–Si–Nb isothermal section at 800 °C [3]. The composition widths of the compounds are schematic.

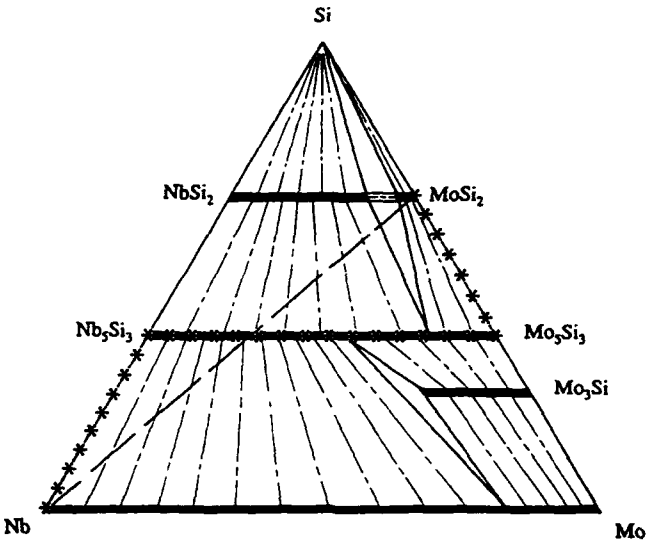

Fig. 2. Schematic diffusion path observed for the reaction between niobium and $MoSi_2$ at 1200 and 1500 °C by Lu *et al.* [5] superimposed on the ternary triangle of [8] at 800 °C, which is the only one available.

phase region between the disilicides in Fig. 1. This is a common feature of disilicide equilibrium that is discussed in considerable detail below.

The analysis of reaction layers in composites requires the use of these diagrams in conjunction with the "diffusion path". A thorough discussion of these paths is available in the work of Kirkaldy and Young [4]. Lu *et al.* [5] have recently formed composites of either plates or wires of niobium in $MoSi_2$ and examined the reaction layers and the mechanical properties between 1200 and 1500 °C. In diffusion couples they found a reaction layer consisting of niobium-rich $(Nb,Mo)_5Si_3$ and molybdenum-rich $(Nb,Mo)_5Si_3$ compounds. If one obtains microprobe data across a reaction layer and plots the compositions on the ternary triangle, a graph of the diffusion path is obtained. The path observed at these temperatures is shown superimposed on the available 800 °C section in Fig. 2; it runs from the pure niobium corner into the single-phase b.c.c. region (dissolving a very small amount of silicon) and then jumps across the two-phase field following a tie-line to Nb_5Si_3. The jump occurs at positions in the sample corresponding to the location of the boundary between the phases. The path then runs across the Nb_5Si_3 and Mo_5Si_3 region and jumps from the Mo_5Si_3 to the $MoSi_2$ region. One can calculate the path and the rate of thickening of the layers using the phase diagram if the diffusion coefficients for all the phases are available and if the interfaces remain parallel. Indeed diffusion data are often obtained by doing such experiments.

Three simple points can be made about diffusion paths. First, compositions obtained from microprobe that lie in two- or three-phase fields must be properly interpreted. The compositions of single phases occurring in diffusion couples must (under all practical cases) lie in single-phase regions of the phase diagram. Experimental contradiction is often seen owing to the imperfect spatial resolution of the microprobe measurements traversing interfaces or owing to regions of fine microstructure that are two phase. These two-phase regions are caused by morphological instability of the initially planar interfaces and must be analyzed separately. Second, because a line connecting the two compositions of the two reacting materials must contain the average composition, the diffusion path must zigzag across this line to conserve mass within the reaction zone. The path must lie on both sides of the connecting line. Finally the route that the path takes across the ternary triangle is related to the identity of the fast-diffusing species. Note that the ends of the diffusion path, near the $MoSi_2$ end and the niobium end, both point either toward or away from the silicon corner. This fact indicates that the silicon is the fastest-diffusing species. For example, if the path had left the niobium corner in a direction toward molybdenum, molybdenum would have been indicated as the fast diffuser in the b.c.c. phase.

The microstructure and diffusion path observed in the reaction zone after hot isostatic pressing (HIP) of commercial grade $MoSi_2$ in a niobium HIP can at 1450 °C is shown in Fig. 3. Similar paths are reported in another paper in these proceedings [6]. This path is different from that shown in Fig. 2. Microprobe analysis performed on this sample shows that the path goes from niobium to Nb_5Si_3 to $NbSi_2$ and across the join to

$MoSi_2$. The micrograph shows, from left to right, pure niobium, a layer of Nb_5Si_3, a two-phase layer of Nb_5Si_3 and $NbSi_2$ with a diminishing volume fraction of Nb_5Si_3, a single-phase region of $(Nb,Mo)Si_2$ with an increasing molybdenum content, and finally $MoSi_2$. Typical of commercial $MoSi_2$ the dark regions within the $MoSi_2$ contain silicon-rich material as either SiO_2 or elemental silicon. If a line were drawn between pure niobium and pure $MoSi_2$, it would be seen that the path would violate mass conservation. One possible explanation involves the realization that the material contained within the HIP can contain excess silicon. If the line is drawn between niobium and a point within the two-phase field between $MoSi_2$ and silicon, the path can satisfy the requirement of mass conservation. Thus the reaction path and the identity of the phases within the reaction layers can depend on the quality of the $MoSi_2$ powder.

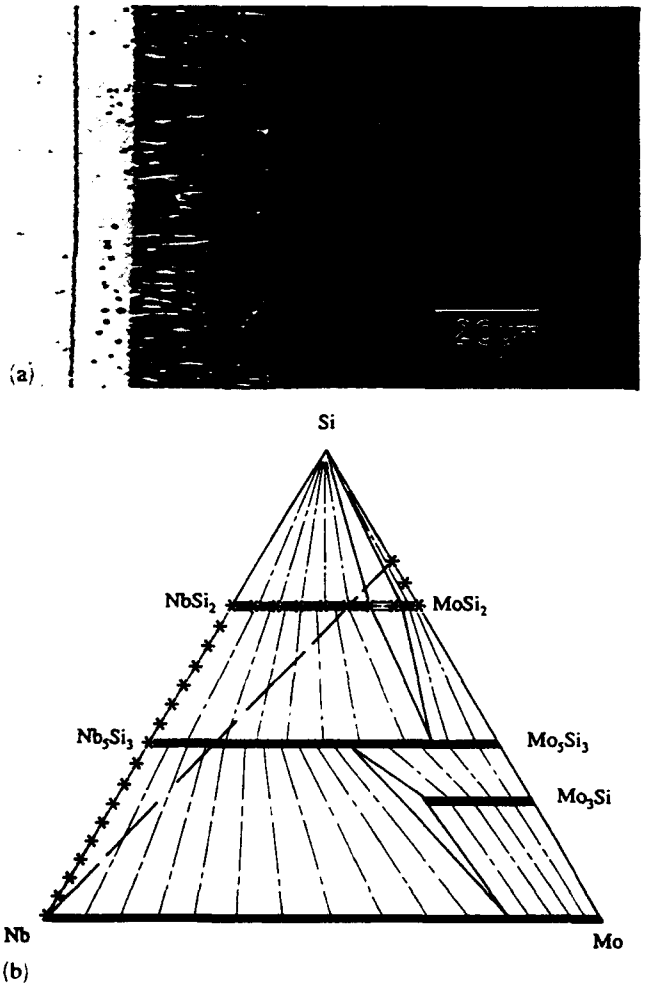

Fig. 3. (a) Microstructure and (b) schematic diffusion path, observed after HIP treatment at 1450 °C between a niobium container (left, white) and commercial purity $MoSi_2$ powder with silicon-rich inclusions (right). The light-gray phase is Nb_5Si_3, and the medium-gray phase is $(Nb,Mo)Si_2$.

A significant detail has been omitted in the above discussion regarding $(Nb,Mo)_5Si_3$. The microstructure and microprobe data presented by Lu *et al.* [5] showed the existence of two $(Nb,Mo)_5Si_3$ phases, *i.e.* two discrete interlayers are observed in the diffusion path: one niobium-rich and the other molybdenum-rich. Thus, on the assumption that there is no fourth component contamination, the phase diagram at the temperature of the HIP treatment (1450 °C) must contain a two-phase field across the $(Nb,Mo)_5Si_3$ composition. This observation is indeed supported by the fact that Nb_5Si_3 has a polymorphic transition from a low temperature form ($D8_l$) to a high temperature form ($D8_m$) at temperatures reported from about 1650 to about 1950 °C depending on the exact stoichiometry [7]. The high temperature form has the same crystal structure as Mo_5Si_3 and a complete solution is possible between Nb_5Si_3 and Mo_5Si_3 at high temperatures. However, the low temperature form of Nb_5Si_3 has a different crystal structure from Mo_5Si_3. Therefore despite the uncertainty of the polymorphic transition temperature, which needs to be clarified, it seems likely that the shape of the diagram (Fig. 1) must be revised to include a two-phase field across the $(Nb,Mo)_5Si_3$ composition at low temperatures as shown schematically in Fig. 4. This is a good example of the current incomplete state of the database for ternary systems involving $MoSi_2$. The available information provides a starting point for analysis but many details remain to be clarified.

2.2. $MoSi_2$–SiC

Considerable research has been focused toward the formation of composites of $MoSi_2$ with additions of

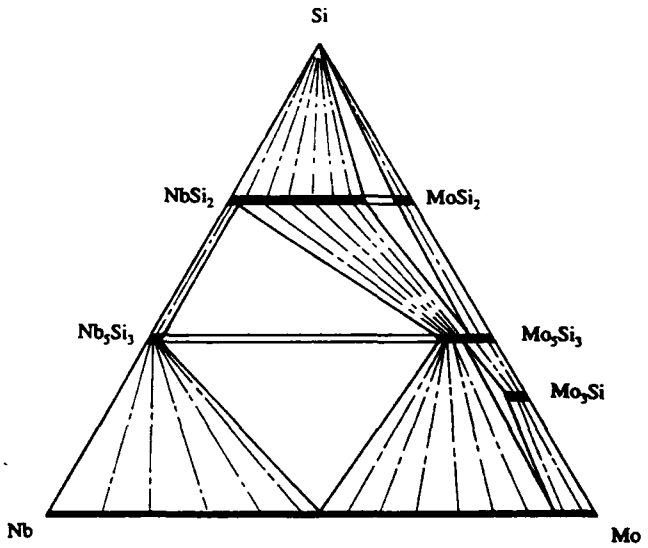

Fig. 4. Schematic Mo–Si–Nb ternary system which reflects the fact that Nb_5Si_3 and Mo_5Si_3 have different crystal structures below 1650 °C. A two-phase field is thus required along the $(Nb,Mo)_5Si_3$ section.

SiC. These additions are known to be thermodynamically stable. No dissolution or reaction layer occurs with the diffusional bonding of the starting materials. The Mo–Si–C ternary diagram [8] is consistent with these observations. As shown in Fig. 5(a), a narrow two-phase field (indicated by the single tie-line) exists between $MoSi_2$ and thus a two-phase mixture is stable at 1600 °C.

One might ask whether SiC could be used in a duplex mixture of $MoSi_2$ and Mo_5Si_3 (Mo_3Si_2 according to older literature). According to this figure, a composite of $MoSi_2$, Mo_5Si_3 and SiC would not be thermodynamically stable at 1600 °C. No three-phase triangle exists at this temperature for these three phases. The ternary phase (Mo–Si–C) indicated in the diagram would form in these composites at 1600 °C. At lower temperatures, however, the triple composite would be stable. For example using diffusion couple results at 1200 °C, van Loo *et al.* [9] have shown that a three-phase field does exist between $MoSi_2$, Mo_5Si_3 and SiC. The existence of a four-phase reaction $MoSi_2$ + ternary phase → Mo_5Si_3 + SiC at some temperature between 1200 and 1600 °C is necessary to make the diagrams of refs. 8 and 9 consistent. The temperature of this reaction would be the upper operating limit for the triple composite.

Interesting possibilities may exist in $MoSi_2$–SiC system for controlled microstructural designs based on melt processing. $MoSi_2$ has been melt processed by plasma spraying [10] and by cold-hearth melt spinning [11]. Thus the consideration of solidification structures is important. Figure 5(b) shows the liquidus surface for Mo–Si–C alloys. Note the quasi-binary eutectic reaction at the liquidus valley at 1900 °C between $MoSi_2$ and SiC where the liquid will naturally freeze into a mixture of $MoSi_2$ and SiC phases. A detailed examination of this reaction is described in more detail in ref. 12.

3. Disilicide quasi-binary systems

The data in the literature on the relative solubilities and two-phase fields (generally at 1300 °C) of various disilicides when combined with $MoSi_2$ [3, 13] are summarized in Fig. 6. Referring to Fig. 1, the alloys under consideration contain phases that maintain a constant silicon level but vary the refractory metal content for example between $NbSi_2$ and $MoSi_2$. A section of this type is termed a quasi-binary section if all of the tie-lines at the various temperatures lie in the plane of the section. In this case the section obeys the rules of construction of an ordinary binary phase diagram with $MoSi_2$ and the other disilicide as the components. Most familiar is the alloying of $MoSi_2$ with WSi_2 which are both tetragonal $C11_b$ and which form a complete solid solution across the diagram. Combinations of $MoSi_2$ with disilicides that have the hexagonal C40 structure necessarily require the formation of a two-phase field between the $C11_b$ and C40 phases with various ranges of solubility. For example, Fig. 6 shows that $CrSi_2$ is soluble in $MoSi_2$ up to 40 mol.%. Beyond this level of addition a two-phase region exists between the $C11_b$ structure and the C40 structure. (This high level of solubility is not confirmed in the present work (see Fig. 17).) The solubility data in the literature are also shown for combinations of $MoSi_2$ with $TiSi_2$, $TaSi_2$, and $NbSi_2$. $TiSi_2$ has the orthorhombic C54 structure rather than the C40 structure. Thus a second two-phase region occurs between the C40 and C54 phases in this quasi-binary section. As part of an ongoing study, it was necessary to determine the accuracy of these data on binary disilicide interactions and to measure how these solubilities change with temperature. Such solubility changes would provide the opportunity for heat treating these alloys to bring out precipitates within the different phases for possible use in strengthening.

Nowotny *et al.* [14] also examined quasi-ternary sections at 1300 °C that combine three disilicides as shown in Fig. 7. These diagrams obey all the geometrical rules followed by a "real" ternary diagram. One can see that the dominant second phase for the formation of natural composites with $MoSi_2$ is the C40 phase. For example the addition of $TaSi_2$ and $TiSi_2$ to $MoSi_2$ yields various compositions of the C40 phase which can occur in equilibrium with the $C11_b$ phase. This may allow the development of two-phase alloys with controlled matching of expansion coefficients or interfacial interatomic distances. One can see that the C40 phase is ubiquitous in these combinations of disilicides and, despite some quantitative errors known to exist in these figures, it is clear that the C40 phase is extremely important as a second phase in two-phase microstructures of disilicide systems.

3.1. $MoSi_2$–$TiSi_2$

Experiments were conducted on $MoSi_2$–$TiSi_2$ alloys to resolve conflicting data in the literature. The diagram of Fig. 8 [15] shows $MoSi_2$ with a polymorphic transition from $C11_b$ to the C40 phase on heating above 1860 °C. The $C11_b$ structure has limited solubility of $TiSi_2$ in $MoSi_2$. The diagram shows the C54 form of $TiSi_2$ and a large homogeneity range for the C40 phase. The accuracy of this diagram is suspect because of the curvature of the boundary between the C40 and (C40 + $C11_b$) phase fields near 1860 °C. (No heat of transformation data is available to check this slope.) The liquidus data are for the C40 phase except near the $TiSi_2$ side of the diagram. There is no liquidus for the $C11_b$ phase because of the supposed poly-

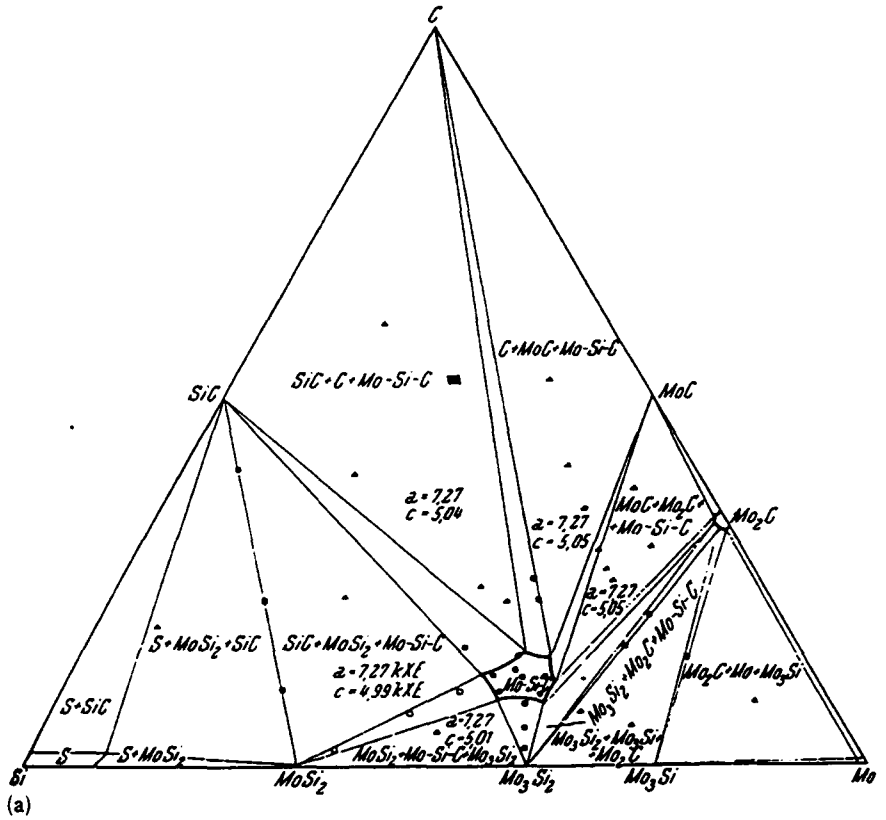

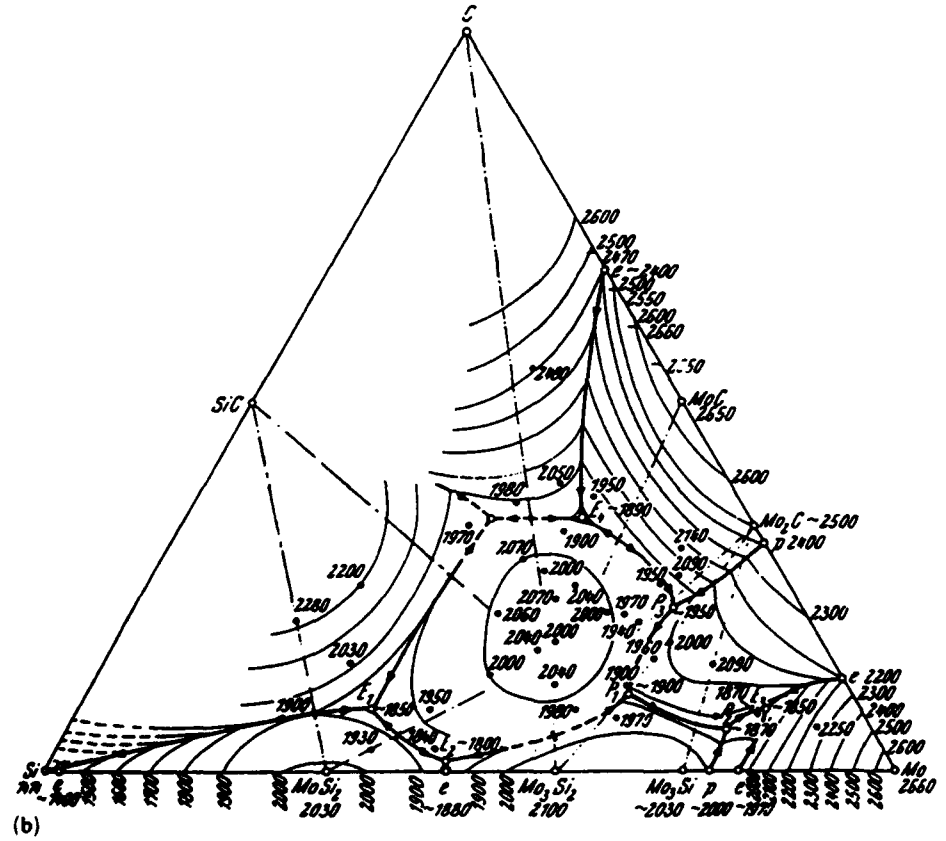

Fig. 5. Mo–Si–C ternary diagrams according to ref. 8: (a) isothermal section at 1600 °C showing stable two-phase field between $MoSi_2$ and SiC; (b) liquidus projection showing eutectic reaction between $MoSi_2$ and SiC. The phase designated Mo_3Si_2 is now referred to as Mo_5Si_3.

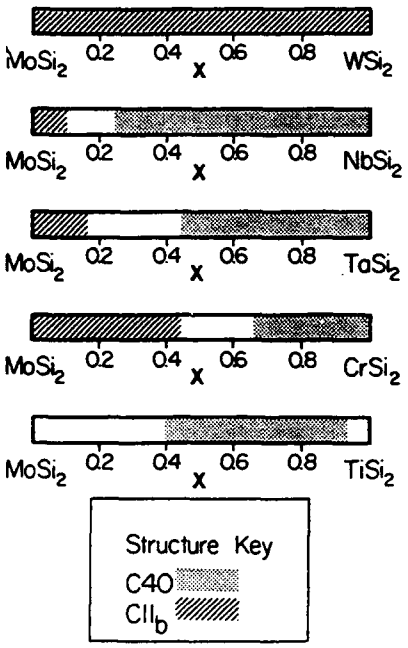

Fig. 6. Homogeneity range in mole fraction and two-phase fields for various combinations of disilicides at 1300 °C (800 °C for $MoSi_2$-$NbSi_2$) [3, 13]. See Fig. 17 for revised results.

morphic transformation of the $C11_b$ on heating above 1860 °C.

Contrary to this diagram, Fig. 9 shows the liquidus surface projection of the $MoSi_2$-$TiSi_2$-$TaSi_2$ quasi-ternary system [13]. Unfortunately Kudielka and Nowotny [13] never showed a graph of the binary system along the $MoSi_2$-$TiSi_2$ edge. However, one can see the presence of a binary peritectic reaction, liquid + $C11_b \rightarrow$ C40, at about 1750 °C and about 83 mol.% $TiSi_2$ on the binary edge of the ternary triangle. In the present work the existence of this peritectic reaction is confirmed albeit at a different composition and temperature.

The $MoSi_2$-$TiSi_2$ quasi-binary diagram as determined in the present work is shown in Fig. 10. The experiments used to determine this diagram used alloys prepared from research purity elements by arc melting the pure elements in gettered argon with several remelts to ensure homogeneity. The revised diagram features the peritectic formation of the C40 $(Mo,Ti)Si_2$ phase. The microstructure of a cast sample of $MoSi_2$-4mol.%$TiSi_2$ (Fig. 11) shows a classical peritectic microstructure [16] where the first phase to solidify forms plates of the $C11_b$ phase (white phase), and the region between the plates solidifies as the lower temperature phase (dark phase) with some slight readjustment in the solid state to approach completion of the peritectic reaction. The temperature for the peritectic reaction, liquid + $C11_b \rightarrow$ C40, was determined by the heat treatment of samples in gettered helium or argon

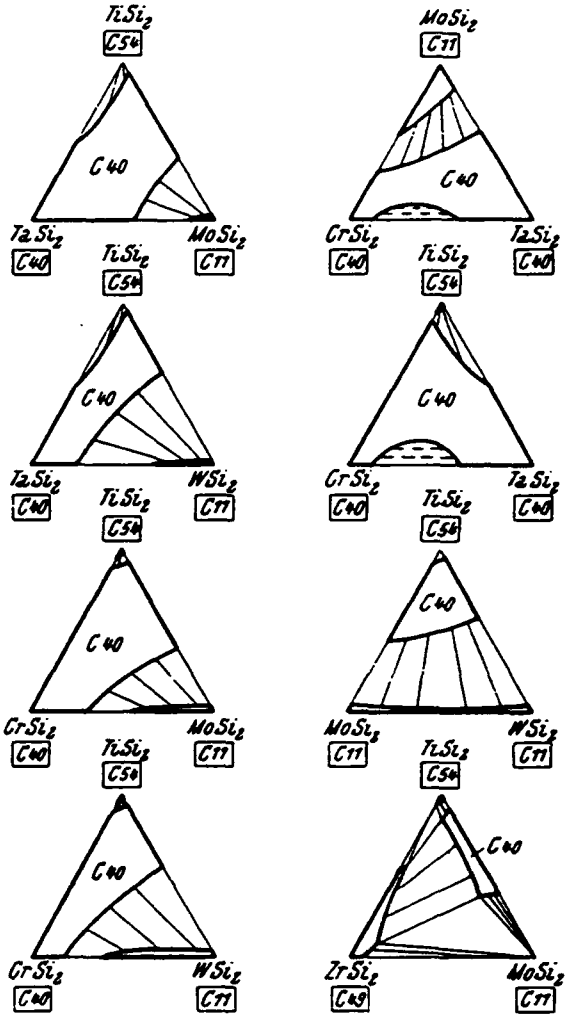

Fig. 7. Quasi-ternary isothermal sections at 1300 °C of various combinations of disilicides showing the omnipresence of the C40 phase according to ref. 14.

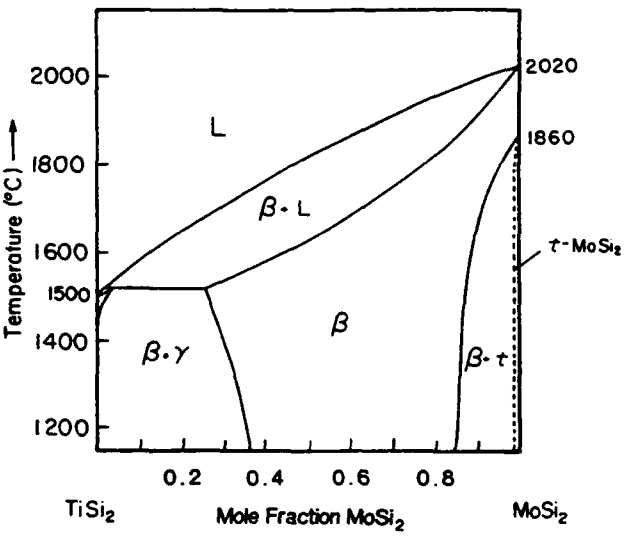

Fig. 8. Quasi-binary $MoSi_2$-$TiSi_2$ diagram according to ref. 15. β, C40; γ, C54; t, $C11_b$.

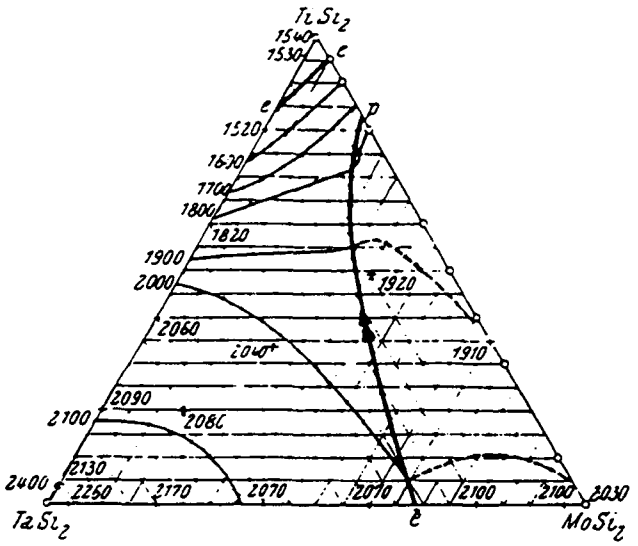

Fig. 9. Quasi-ternary liquidus surface [13] for $MoSi_2$–$TiSi_2$–$TaSi_2$ that shows a peritectic reaction, liquid + $C11_b$ → C40, on the $MoSi_2$–$TiSi_2$ binary edge and a eutectic reaction, liquid → C40 + $C11_b$, on the $MoSi_2$–$TaSi_2$ binary edge.

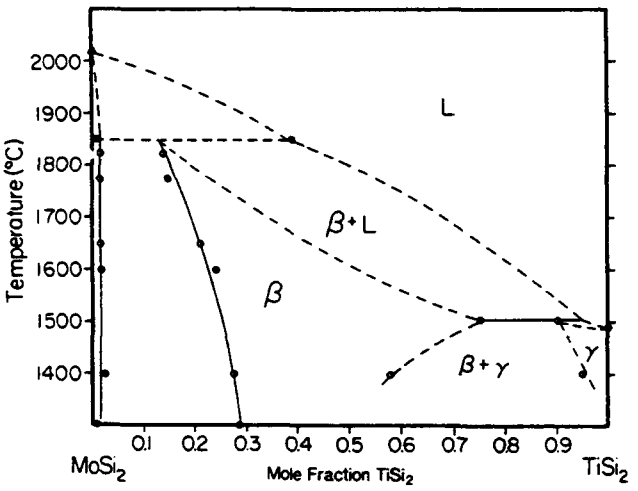

Fig. 10. $MoSi_2$–$TiSi_2$ quasi-binary diagram obtained through this research.

at successively higher temperatures until an indication of partial melting was observed metallographically after quenching at about 400 °C min^{-1}. The liquidus composition at the peritectic temperature was estimated from microprobe data taken from this quenched liquid. The peritectic temperature for the other peritectic reaction, liquid + C40 → C54, near the $TiSi_2$ side of the diagram, was determined by differential thermal analysis measurements. The data points shown for the subsolidus regions were determined by microprobe analysis of samples heat treated in gettered helium and quenched at about 400 °C min^{-1}. Elemental standards were used to quantify the microprobe results. The very

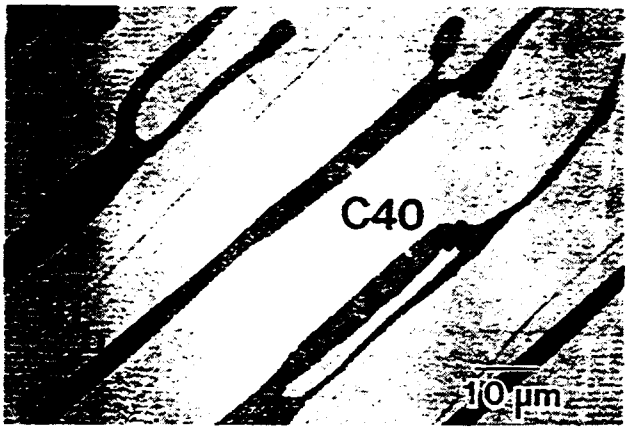

Fig. 11. Backscattered scanning electron micrograph of the as-cast alloy, $MoSi_2$–4mol.%$TiSi_2$, showing a peritectic structure consisting of primary plates of $C11_b$ (light) and interplate C40 phase (dark).

limited solubility of $TiSi_2$ in $MoSi_2$ is confirmed as well as the existence of a wide C40 region in the middle of the diagram.

3.1.1. The $C11_b$-to-C40 polymorphic transformation in pure $MoSi_2$

The experimentally determined $MoSi_2$–$TiSi_2$ diagram and the solidification path analysis [17] indicates the absence of the $C11_b$-to-C40 transformation in pure $MoSi_2$. An $MoSi_2$ polymorphic transition is shown in the current evaluation of the binary Mo–Si system [7]. Figure 12 compares the general shape of the phase boundaries of the $MoSi_2$–$TiSi_2$ diagram found in the literature (Fig. 8) with those measured in the present work. The diagram in the literature contains the polymorphic transformation in pure $MoSi_2$ that gives rise to a two-phase region between C40 and $C11_b$ with $TiSi_2$ additions. The key difference between the diagram in the literature and the revised diagram of this work is an increase in the polymorphic transformation temperature to above the melting point of $MoSi_2$. The upper part of the ($C11_b$ + C40) two-phase field is thus metastable and the peritectic reaction, liquid → $C11_b$ + C40. is naturally generated. If one were to extrapolate the experimentally measured boundaries of the ($C11_b$ + C40) phase field upward in temperature in the revised $MoSi_2$–$TiSi_2$ diagram (Fig. 10), there is no possibility that the boundaries can converge at the $MoSi_2$ terminus axis at a temperature below the melting point of $MoSi_2$ ($T_m \approx 2020$ °C).

The possible arrangements for the free energy *vs.* temperature behavior for the liquid, $C11_b$ and C40 phase for pure $MoSi_2$ are shown schematically in Fig. 13. In this figure the lowest curve at any temperature represents the stable equilibrium phase and the intersections of the free-energy curves correspond to the

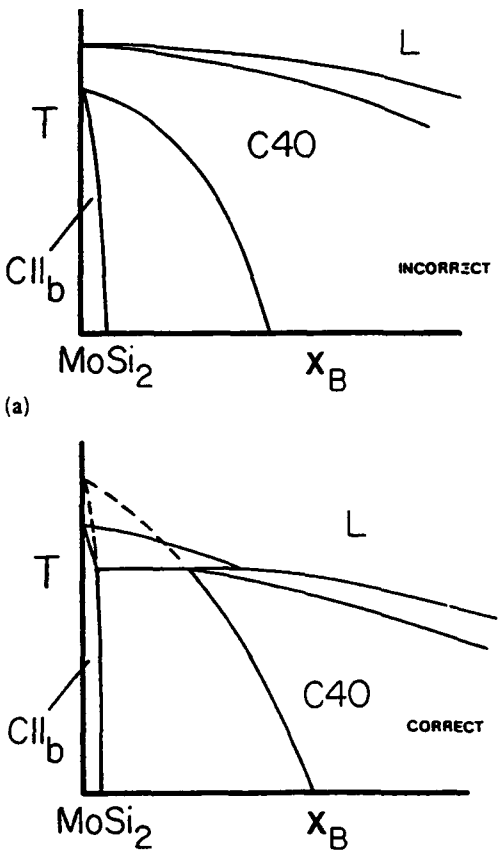

Fig. 12. Schematic representation of two possibilities for the $MoSi_2$–$TiSi_2$ quasi-binary diagram. The polymorphic transformation of pure $MoSi_2$ from $C11_b$ to C40 is (a) below and (b) above the melting point. (b) shows the phase relationships determined in this work.

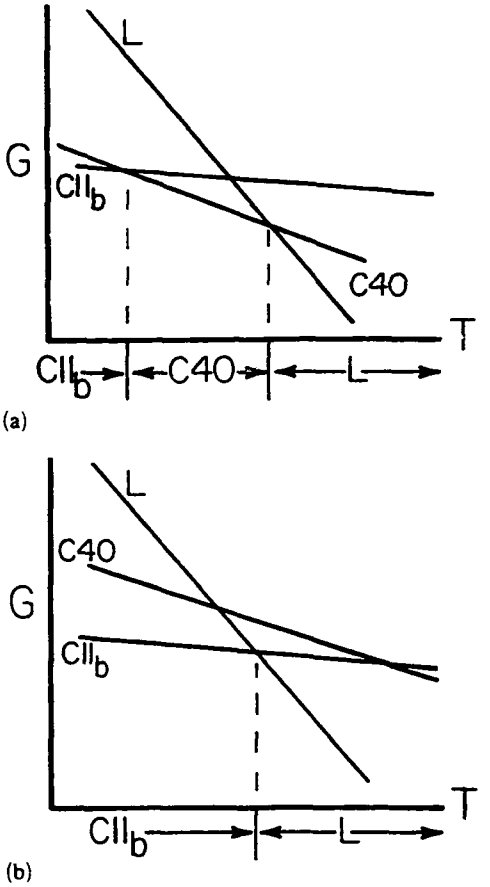

Fig. 13. Possible arrangements for the free-energy *vs.* temperature curves for the liquid, $C11_b$ and C40 phase for pure $MoSi_2$. The polymorphic transformation of pure $MoSi_2$ from $C11_b$ to C40 is (a) below and (b) above the melting point. (b) is the correct situation as determined in this work for pure $MoSi_2$.

transition temperatures. If, for pure $MoSi_2$, the $C11_b$ phase transformed to the C40 structure during heating below the melting point, one would have the relationships shown in Fig. 13(a). On the contrary, if the $C11_b$ structure is stable to the melting point, then the free-energy relationships would exist as in Fig. 13(b). In the latter case, the polymorphic transition would be metastable and would occur above the melting point. Similarly in this case the liquid-to-C40 transition would occur below the $C11_b$ melting point. The relationships shown in Fig. 13(a) can be obtained from those of Fig. 13(b) by merely raising the free-energy curve for the C40 phase relative to the liquid and $C11_b$ phases. Addition of solute alters the phase stability as happens with the addition of $TiSi_2$ or, as shown below, for $TaSi_2$. It is also clear how, in a rapid liquid quenching operation such as plasma spraying, the formation of a metastable $MoSi_2$ C40 phase can occur directly from the melt if the undercooling takes the melt below the metastable melting point of the C40 phase (the intersection of the C40 and liquid free-energy curves). This melting point may be only a few degrees Celsius below the melting point of the $C11_b$ phase. The conditions required for the formation of metastable phases during rapid solidification have been discussed elsewhere [17].

3.1.2. Powder processing of $MoSi_2$–$TiSi_2$

In the present study, limited experiments were performed involving powder processing of these high purity arc cast samples. The ingots were reduced to −325 mesh powder and HIP processed in argon at 200 MPa at 1750 °C for 1 h in a tantalum can. The microstructure of this HIP-processed sample as well as the fracture behavior after Vickers indentation with a 100 kgf load are shown in Fig. 14. An equiaxed structure of grains of $C11_b$ and grains of C40 phases is detected through backscattered contrast in the scanning electron microscope (and confirmed by microprobe). Some residual porosity is also evident. The region around the indent is chipped and various cracks are evident. Measurement of crack length as a function of load (10–100 kgf) showed a consistent fracture

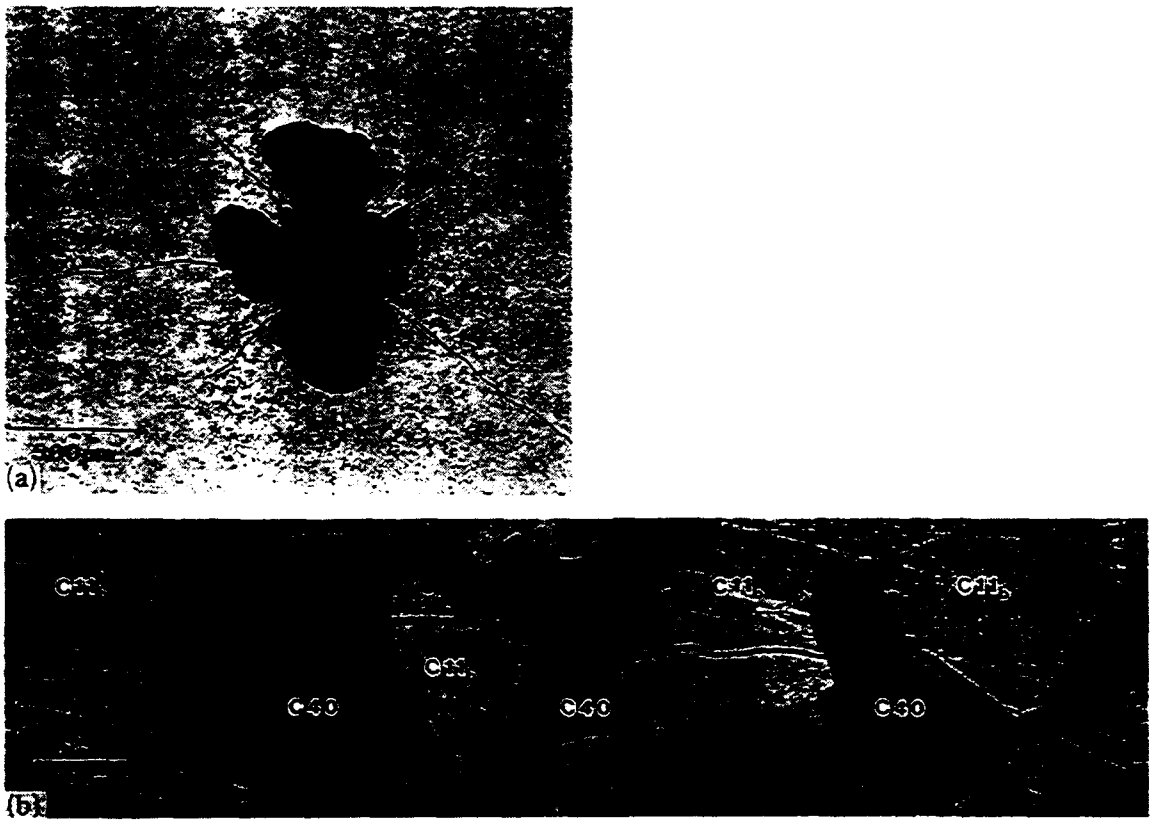

Fig. 14. HIP-processed $MoSi_2$–10 mol.%$TiSi_2$ showing a 100 kgf Vickers indentation. An equiaxed structure of grains of $C11_b$ and grains of C40 phases is detected through backscattered contrast in the scanning electron microscope. Cracks associated with the indentation are used to determine the fracture toughness and the interaction of the crack with the two-phase microstructure.

toughness value typical of pure $MoSi_2$. The crack path shows little deflection as it passes through the different phases except at the end of the crack where it deflects down a grain boundary between the $C11_b$ and the C40 phases. Thus there appears to be no dramatic effect of the two-phase microstructure on toughness, at least in this equiaxed morphology. However, it is evident that the two-phase structure can be manipulated into other morphologies and size scales. No tests were performed to determine whether this combination of phases can yield any improvement in creep behavior.

The alloying of $MoSi_2$ with $TiSi_2$ does not appear to impair the intrinsic oxidation resistance of $MoSi_2$. In preliminary oxidation tests, arc-melted ingots of $MoSi_2$ with 3 and 18 mol.% $TiSi_2$ held 10 h at 1300 °C in air exhibit oxidation resistance behavior similar to that of an unalloyed $MoSi_2$ control sample.

3.2. $MoSi_2$–$TaSi_2$

Figure 9 shows a eutectic reaction between $MoSi_2$ and $TaSi_2$. If real, this feature would have been interesting for melt processing and would have provided the capability to produce a fine dispersion of $C11_b$ and C40 phases from the melt. However, arc-cast samples of this composition with about 30 mol.% $TaSi_2$ contained no eutectic microstructure. The samples froze as a single-phase C40 with essentially no microsegregation. Similar to the $MoSi_2$–$TiSi_2$ alloys, arc-cast alloys containing less $TaSi_2$ exhibit the same classic peritectic structure where the $C11_b$ phase forms first and the C40 phase forms between the $C11_b$ plates (Fig. 15(a)). Figure 15(b) shows the results of aging the arc-melted material at 1600 °C for 4 h. Because the composition of the C40 phase produced by solidification contains more $MoSi_2$ than is present in the C40 phase at 1600 °C, needles of the $C11_b$ precipitate in the C40. These precipitates appear as parallel plates and thus an orientation relation exists between the $C11_b$ and C40 phases. Transmission electron microscopy examination found the interface plane to be $(110)_{C11_b} \| (0001)_{C40}$ with $(002)_{C11_b} \| (10\bar{1}0)_{C40}$ as was expected from the known relationship between the $C11_b$ and C40 structures. Annealing at 1300 °C (Fig. 15(c)) produces the same microstructure but with much finer plates.

The summary of the revised phase diagram, which includes microprobe work on heat-treated-and-quenched samples, is shown in Fig. 16. Instead of a eutectic reaction between $C11_b$ and C40, a minimum

Fig. 15. Micrographs of $MoSi_2$–10 mol.% $TaSi_2$: (a) backscattered scanning electron micrograph of as-cast material; (b) backscattered scanning electron micrograph of material which had been heat treated for 4 h at 1600 °C; (c) optical micrograph of material which had been heat treated for 110 h at 1300 °C.

in the liquidus surface has been placed at about 30 mol.% $TaSi_2$ because no coring of alloys is observed for samples cast in this range. The boundaries of the ($C11_b$ + C40) two-phase region are documented through microprobe measurements. The lower temperature data are shown as broken curves to reflect uncertainties in the data due to the slow diffusion of tantalum in samples that have not reached equilibrium at 1300 °C with a 100 h heat treatment. The liquidus construction is only suggested at this time. The points (indicated by crosses) are the liquidus data taken along the quasi-binary $MoSi_2$–$TaSi_2$ edge of Fig. 9. When extrapolated to the pure disilicides, they are about 100 °C too high. The proposed liquidus is constructed parallel to the data points. In conclusion, the $MoSi_2$-rich end of this diagram contains a similar peritectic reaction as does the $MoSi_2$–$TiSi_2$ diagram of Fig. 10. Similar to the $MoSi_2$–$TiSi_2$ system, there is no way that the ($C11_b$ + C40) two-phase field can extend to give a polymorphic transformation in pure $MoSi_2$ before melting occurs.

Figure 17 shows the revised version of Fig. 6 which includes the solubilities of the $C11_b$ and C40 phases as determined in the present work at 1300 °C. Included are data for $MoSi_2$–$CrSi_2$ that were obtained by microprobe analysis of samples heat treated at 1375 °C for 98 h. Clearly the large solubility of $CrSi_2$ in $MoSi_2$ shown in Fig. 6 is not confirmed. The limited solubilities of the various disilicides in $MoSi_2$ even at elevated temperatures (at least for $TiSi_2$ and $TaSi_2$) would limit the potential for the precipitation of C40 phase within a matrix of $C11_b$, but there are some capabilities for the reverse situation of developing structures based on the precipitation of $C11_b$ precipitates in a C40 matrix.

In this paper, only the addition of refractory metals that substitute for molybdenum have been considered. Another strategy for manipulation of the metallurgical structure of the alloys can be obtained through the substitution of aluminum for silicon. The isothermal section of the Mo–Si–Al diagram has been measured [18] and contains a two-phase field between a $C11_b$ and a C40 phase. This C40 phase has the composition $Mo(Si,Al)_2$.

4. Conclusions

Ternary diagrams are necessary to understand the reactions that occur in various composites based on $MoSi_2$ and are very useful to develop strategies for alloy design. Existing phase diagram information gives some useful general trends in disilicide systems. Further research is needed to improve the accuracy and reliability of these data before any detailed analysis of heat treatment of monolithic alloys or analysis of diffusion paths for reaction with reinforcements is possible. Parts of the $MoSi_2$–$TiSi_2$ and $MoSi_2$–$TaSi_2$ quasi-binary diagrams have been measured. The phase equilibria exhibited in these systems lead to the conclu-

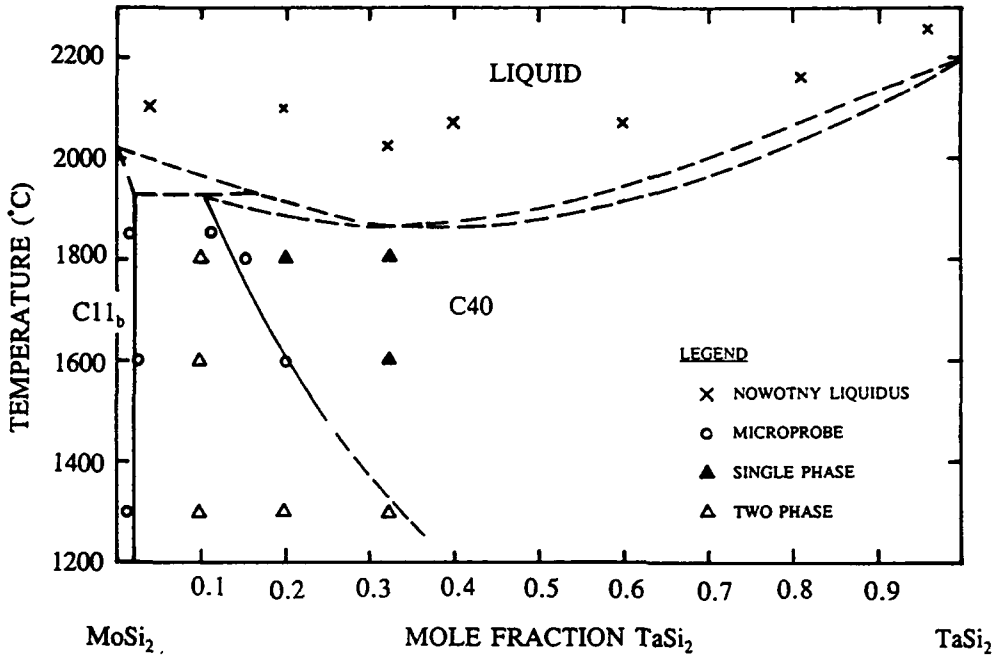

Fig. 16. $MoSi_2$–$TaSi_2$ quasi-binary diagram obtained through this research.

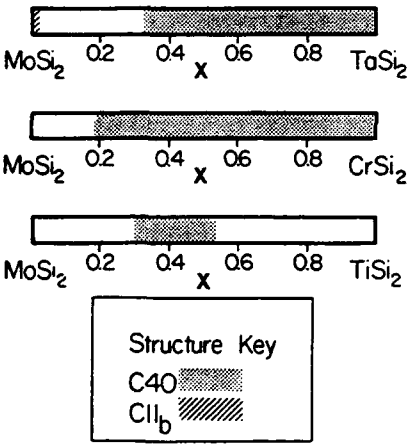

Fig. 17. Revised homogeneity range (in mole fraction) and two-phase fields at 1300 °C for various combinations of disilicides obtained through this work.

sion that there is no C40 high temperature polymorph in pure $MoSi_2$.

Acknowledgments

This research was partially supported by the Defense Advanced Research Projects Agency (DARPA) Order 7469 (W.J.B.) and DARPA–US Army Research Office Grant DAAL 03-90-6-0183 (J.H.P. and P.S.F.). The efforts of F. S. Biancaniello, D. E. Harne, A. J. Shapiro, L. E. Smith, J. Wallace and M. E. Williams are greatly appreciated.

References

1 A. Prince, *Multicomponent Alloy Bibliography 1955–1973*, Metals Society, London, 1978.
2 A. Prince, *Multicomponent Alloy Bibliography 1974–1977*, Metals Society, London, 1981.
3 E. M. Savitskiy, V. V. Baron, M. I. Bychkova, S. A. Bakuta and E. I. Gladyshevskiy, *Izv. Akad. Nauk SSSR, Met., 2* (1965) 159.
4 J. S. Kirkaldy and D. J. Young, *Diffusion in the Condensed State*, Institute of Metals, London, 1987, p. 382.
5 T. C. Lu, A. G. Evans, R. J. Hecht and R. Mehrabian, *Acta Metall. Mater., 39* (1991) 1853.
6 N. S. Stoloff and D. E. Alman, *Mater. Sci. Eng. A, 155* (1992).
7 T. B. Massalski (ed.), *Binary Alloy Phase Diagrams*, American Society for Metals, Metals Park, OH, 1990, p. 2666.
8 H. Nowotny, E. Parthe, R. Kieffer and F. Benesovsky, *Monatsh. Chem., 85* (1954) 255.
9 F. J. J. van Loo, F. S. Smet, G. D. Rieck and G. Verspui, *High Temp.—High Pressures, 14* (1982) 25.
10 H. Herman and R. Tiwari, *Mater. Sci. Eng. A, 155* (1992).
11 A. Basu, A. Ghosh and R. Ray, *Metallurgical Society of AIME Fall Meet., 1991.*
12 H. Deve, J. Yang, A. G. Evans and C. Levi, *Mater. Sci. Eng. A, 155* (1992).
13 H. Kudielka and H. Nowotny, *Monatsh. Chem., 87* (1956) 471.
14 H. Nowotny, H. Kudielka and E. Parthe, *Proc. Plansee Semin.*, Metallwerk Plansee, Reutte, 1956, p. 166.

15 V. N. Svechnikov, Yu. A. Kocherzhinsky and L. M. Yupko, *Dokl. Akad. Nauk, Ukrain, RSR, 6A* (1972) 566.
16 P. S. Frankwicz and J. H. Perepezko, in L. A. Johnson, D. P. Pope and J. O. Stiegler (eds), *High Temperature Ordered Intermetallic Alloys IV, Materials Research Society Symp. Proc.*, Vol. 213, Materials Research Society, Pittsburgh, PA, 1991, p. 169.
17 J. H. Perepezko and W. J. Boettinger, in C. H. Bennett, T. B. Massalski and B. C. Giessen (eds.), *Alloy Phase Diagrams, Materials Research Society Symp. Proc.*, Vol. 19, Materials Research Society, Pittsburgh, PA, 1983, p. 223.
18 C. Brukl, H. Nowotny and F. Benesovsky, *Monatsh. Chem.*, 92 (1961) 967.